CONTRIBUTION TO STRUCTURAL VULNERABILITY QUANTIFICATION

Benjamin Richard

HABILITATION À DIRIGER DES RECHERCHES DE L'UNIVERSITÉ PARIS SACLAY

Spécialité : **Génie Civil**

Présentée par

Benjamin Richard

CONTRIBUTION TO STRUCTURAL VULNERABILITY QUANTIFICATION

FROM THE REPRESENTATIVE VOLUME ELEMENT TO THE MEMBER SCALE

soutenue publiquement le 17 Novembre 2016, devant le jury composé de :

Pr Alain COMBESCURE	*Président*
Pr Filip FILIPPOU	*Rapporteur*
Pr Christian LABORDERIE	*Rapporteur*
Pr Pierre LEGER	*Rapporteur*
Pr Stephen MAHIN	*Examinateur*
Dr Jean-François SEMBLAT	*Examinateur*
Pr Frédéric RAGUENEAU	*Garant*

Acknowledgements

Je me suis interrogé un certain temps pour savoir dans quelle langue j'allais rédiger ces remerciements. Ne parvenant pas à me décider, mes remerciements seront exprimés en français et en anglais.

Il a été si rare d'avoir l'occasion de remercier les personnes qui ont contribué, de près ou d'un peu plus loin, à faire en sorte que ce travail ait pu voir le jour que je vais donc profiter pleinement de celle-ci pour le faire. Tout d'abord, j'aimerais remercier Filip Filippou, Pierre Léger et Christian Laborderie d'avoir accepté la lourde tâche de rapporter ce mémoire. Bénéficier de leur expertise a été pour moi un honneur. Plus particulièrement, j'aimerais remercier Filip Filippou et Pierre Léger pour avoir pu se libérer et pour être venus d'outre-Atlantique. Je leur en suis sincèrement reconnaissant. J'aimerais également remercier Christian Laborderie pour les nombreux échanges que nous avons eus. La proximité de nos thématiques de recherche rendent nos discussions toujours plus passionnantes.

J'aimerais également remercier Alain Combescure pour avoir accepté de présider le jury. Je lui en suis très reconnaissant. Now it is time to switch in English... I met Steve Mahin at the occasion of the first TINCE conference in Cachan and we naturally discussed about the SMART 2013 project which was ongoing at this period. I particularly appreciated our exchanges during the TINCE conference and even more, during the defence. I am very grateful he accepted to join the evaluation panel while coming from quite far. Back to French... Je remercie Jean-François Semblat pour avoir accepté de faire partie de mon jury et plus généralement, pour les échanges très enrichissants que nous avons dans le cadre de l'Association Française de Génie Parasismique (AFPS).

Je ne saurais oublier Frédéric Ragueneau, mon garant. Nous nous sommes connus au cours de sa mobilité au LCPC alors que je commençais ma thèse. A cette époque, il avait accepté de m'encadrer et depuis, nous avons continué à travailler ensemble. Sur le plan scientifique, il a su me transmettre la passion de la mécanique et me faire découvrir bien des choses dans le domaine du Génie Civil. Sur d'autres plans, il m'a appris à encadrer des étudiants et, en particulier, à trouver le juste milieu entre laisser l'étudiant libre de suivre ses intérêts et imposer un cadre strict. Ce compromis est toujours délicat à établir mais il est fondamental.

Je souhaite maintenant remercier l'ensemble de mes étudiants. Rien n'aurait été possible sans eux ! Je pense tout d'abord à mes doctorants : Romain, Maxime, Ejona et Thomas. Je ne peux oublier Chaymaa et Santosh qui viennent de commencer leur thèse qui, j'en suis certain, sera une aventure intellectuelle dont ils garderont un inoubliable souvenir. Je ne saurais oublier mes post-doctorants : Eliass et plus récemmement, Alessandro. Enfin, je pense également à mes stagiaires longs : Stefano et Francesco. Je les remercie tous les deux pour la qualité des travaux qu'ils ont accomplis durant leur séjour au CEA. Enfin, je souhaite également remercier l'ensemble des stagiaires de Master avec qui j'ai travaillé à différents stades de ma vie professionelle : Sébastien, Maxime, Benjamin, Sebastian, Roxane, Nicolas, Eleni, Romili, Mikel et je suis très heureux de pouvoir continuer à travailler avec ceux qui ont fait le choix de poursuivre dans le domaine de la recherche !

Vient le tour des collègues avec qui j'ai pris beaucoup de plaisir à travailler. Je pense évidemment à mon entourage proche au sein du Service d'Etudes Mécaniques et Thermiques mais pas seulement ! Je pense aussi aux nombreux collègues et collaborateurs avec qui j'ai eu la chance d'échanger et de travailler dans différents cadres au cours de ces six dernières années. En parti-

culier, ceux du secteur Génie Civil du LMT Cachan, ceux de l'IFSTTAR à Marne la Vallée, du laboratoire 3SR à Grenoble ou encore de l'INSA à Lyon.

Parce que sans moyen aucune activité de recherche ne peut avoir lieu, je tiens à remercier les partenaires qui soutiennent mes activités de recherche. Je pense plus particulièrement aux partenaires industriels comme EDF ou AREVA ou encore aux partenaires institutionnels comme l'IRSN.

Je souhaite aussi témoigner des échanges très fructueux que j'ai pu avoir avec les membres du Groupe Jeunes de l'AFPS, et plus particulièrement avec les membres du Bureau. La dynamique qui est présente au sein du Groupe Jeunes est très positive et très enrichissante. Les activités auxquelles j'ai pu participer m'ont fait découvrir d'autres métiers du Génie Parasismique. Enfin, je souhaite également remercier l'ensemble des membres du Groupe Jeunes pour l'ambiance aussi studieuse qu'agréable qui y règne.

Je souhaite enfin remercier tous mes proches, parfois venus de loin pour assister à ma soutenance, et également ma famille non seulement pour son soutien dans les moments difficiles mais aussi et surtout, pour la joie de vivre qu'elle dégage. Parce que je m'en voudrais d'oublier quelqu'un, j'ai préféré ne citer personne car je sais que chacun se reconnaîtra, qu'il soit ici ou ailleurs.

Abstract

This memoir is the synthesis of research activities I have conducted over the past decade aiming at improving the numerical description of some dissipative mechanisms at the material scale and quantifying the vulnerability of reinforced concrete structures. The main objectives of the research presented in this dissertation are: (i) to improve both the predictive capabilities and the numerical robustness of the time integration strategies of the continuous constitutive model when dealing with the cyclic behavior of quasi-brittle materials subjected to either long-term or short-term loadings, (ii) to improve numerical techniques capable of describing the discontinuous nature of cracking and related local dissipative phenomena, and (iii) to contribute to the definition of large-scale experimental campaigns and to organize international workshops aiming to better understand the complex behavior of reinforced concrete structures when subjected to extreme loadings, such as earthquakes. In the first part, we focus on the development and validation of a continuous constitutive model to describe the mechanical behavior of quasi-brittle materials subjected to cyclic loadings. Simplified strategies are also derived from full three-dimensional approaches to serve probabilistic techniques aiming at taking into account uncertainties and updating mechanical models. In the second part, some light is shed on some developments aiming at better quantifying the cracking features. Then, the results of experiments designed to assess the dynamic response of strongly asymmetric reinforced concrete structures are presented. The experimental data have led to numerical studies shared with the international scientific community. The lessons learned from this research is then employed to design research projects we plan to work on over the next few years.

Keywords: constitutive model, quasi-brittle materials, steel/concrete interface, discrete element approach, strong discontinuities, earthquake engineering, seismic margins

Forwords

In this memoir, a summary of my research activities carried out between 2007 and 2016 is given. The contributions reported in this document could not have been reached without the existence of stimulating joint project frameworks, several fruitful scientific collaborations with other research teams, as well as with Masters and Ph.D. students whom I have advised. For the sake of conciseness, the collaborative frameworks within which I have been working for the past decade are summed up hereafter. This report is outlined in two main parts, in which the main results are described and discussed.

The first part is devoted to the numerical description of some dissipative mechanisms characterizing the cyclic response of quasi-brittle materials when subjected to cyclic loading. The scale of the representative volume element is mainly considered. In addition, some light is shed on the development of nonlinear computational strategies, low in time consumption, that serve a probabilistic analysis to quantify the probability of exceeding a given limit state. The major part of the contributions presented in this section were obtained within the framework of my Ph.D. thesis at LCPC and was supported by the ANR-APPLET project. The most recent developments, in which the concept of a regularized unilateral effect is introduced, have been carried out in the context of Maxime Vassaux's Ph.D. (in collaboration with ENS Cachan) thesis, supported by the FUI-ILMAB research project.

In the second part, the results presented aim at better quantifying the vulnerability of both existing and new reinforced concrete structures when subjected to different types of loadings. The developments in connection with the estimation of the cracking features have been carried out within the framework of Maxime Vassaux's Ph.D., in the case of the discrete elements strategy, and Ejona Kishta's Ph.D. (in collaboration with ENS Cachan and supported by CEA), in the case of the enhanced kinematics approach. For this latter topic, improvements of the global crack path following algorithm have been obtained during the one-year internship of Francesco Riccardi (a student at the Politecnico Milan-ENPC), supported by the CEA and IRSN. Mikel Balmaseda's Master's thesis (supported by the Paris Saclay SEISM Institute) has also contributed to assessing the relevancy of the approach. On the other hand, the assessments in connection with the dissipative capability of reinforced concrete structures, aiming at better identifying the damping/damage relationship and the effect of corrosion on the bearing capacity of an existing bridge, were made in the context of Romain Crambuer's Ph.D. thesis (in collaboration with ENS Cachan), supported by the CEA, and Sebastien Epaillard's Master's thesis (in collaboration with Polytech' university at Lille, France), supported by the European-FP7 project Sustainable Bridges, respectively. Last, the seismic assessments of a torsion-sensitive reinforced concrete structure aiming at quantifying the seismic margins and validating the best-estimate nonlinear assessment approaches have been carried out within the frameworks of the one-year internship of Stefano Cherubini's (a student at Tor Vergata University at Roma, Italy-ENPC, France) and of a collaboration with Paolo Martinelli (Associate Professor at the Politecnico Milan, Italy). This work has been supported by the CEA and EDF, under the umbrella of the IAEA. The influence of the thermal break components has been numerically and experimentally analyzed within the framework of the European-FP7 project SERIES. The visiting Ph.D. student Sebastian Crijanovschi (Technical University "Ghoerghe Asachi" at Iasi, Romania) contributed in part to the analysis. The CEA and IRSN partially supported this work.

Contents

1 Introduction **18**

2 Modeling of some mechanisms occurring in quasi-brittle material failure process **24**
2.1 Introduction . . . 24
2.2 Theoretical framework . . . 25
2.2.1 Generalized standard materials . . . 25
2.2.2 Spherical/deviatoric split . . . 26
2.2.3 Coupled damage/plasticity . . . 30
2.2.4 The regularized unilateral effect . . . 33
2.3 Concrete behavior: Critical review . . . 36
2.3.1 Softening description, asymmetry between tension and compression, and regularization . . . 36
2.3.2 Material parameters and identification . . . 38
2.3.3 Main features . . . 39
2.4 Steel/concrete interface behavior . . . 42
2.4.1 Full 3D approach . . . 42
2.4.2 Simplified approach . . . 49
2.5 Summary . . . 55

3 Quantification of the vulnerability of reinforced concrete structures **58**
3.1 Introduction . . . 58
3.2 Quantification of cracking features . . . 59
3.2.1 Discrete element strategy . . . 59
3.2.2 Enhanced kinematics approach . . . 70
3.3 Structural dissipation capability . . . 85
3.3.1 Effect of cracking on damping . . . 85
3.3.2 Effect of corrosion on the ductility . . . 89
3.4 Probabilistic analysis . . . 94
3.4.1 Driving ideas . . . 94
3.4.2 Equational framework . . . 96
3.4.3 Numerical examples . . . 99
3.5 Structural assessment of torsion-sensitive structures subjected to extreme loading 102
3.5.1 Seismic margins assessment . . . 102
3.5.2 Influence of thermal breakers on the seismic response of an asymmetric reinforced concrete structure . . . 115
3.6 Summary . . . 130

4 Conclusions and outlook **134**

List of Figures

2.1 Control of the crack closure effect — uniaxial cyclic tension loading path. 40
2.2 Uniaxial tension/compression loading path. 41
2.3 Biaxial response — experimental data from Kupfer et Gerstle (1973). 41
2.4 Steel/concrete interface constitutive law — local results. 47
2.5 Finite element mesh — reinforced concrete beam. 48
2.6 Damage pattern — after corrosion and before the mechanical loading for different corrosion degrees. 48
2.7 Damage pattern — after corrosion and after the mechanical loading for different corrosion degrees. 49
2.8 Local and structural responses after the four-point bending tests. 50
2.9 Local results — monotonic loading — uncorroded. 53
2.10 Local results. 53
2.11 Structural results — load/midspan displacement. 54
2.12 Damage pattern. 55

3.1 Description of the setup for the contact mechanism. 60
3.2 Numerical comparison of the cyclic direct tension test performed by Nouailletas (2013). 62
3.3 Sequential description of the global/local analysis strategy. 62
3.4 Experimental setup of the PCT3D test as in Feist et Hofstetter (2007b). 64
3.5 Spatial discretizations considered for the refined re-analysis of the PCT3D. . . . 64
3.6 Results obtained after the re-analysis of the PCT3D test by means of the global/local post-processing strategy. 65
3.7 Fraction of closed cracks versus the maximum crack strain. 66
3.8 Fraction of closed cracks versus the maximum crack strain. 67
3.9 Drawings of the CEOS.fr shear wall. 67
3.10 Description of the loading histories. 68
3.11 Finite element mesh used for the reinforced concrete shear wall. 68
3.12 Experimental–numerical comparaison of the load/relative displacement of the shear wall under cyclic loading. 69
3.13 Numerical and experimental principal strains — experimental–numerical comparisons. 70
3.14 Numerical results — cyclic tension test. 77
3.15 Numerical results — cyclic tension test. 78
3.16 Crack path around the notch — gray finite elements having enhanced kinematics are highlighted in gray. 80
3.17 Normal component of the displacement discontinuity around the notch — gray finite elements having enhanced kinematics are highlighted in gray. 80
3.18 Isovalues of the temperature-like field. 82

3.19 Isovalues of the temperature-like field for different meshes — root element plotted in red. . . . 82
3.20 Comparison between online tracking strategies — gray area = strong discontinuity kinematics activated. . . . 84
3.21 Loading setup according to Schlangen (1993) — SEN plain concrete beam. . . . 85
3.22 Experimental–numerical comparisons — SEN plain concrete beam. . . . 85
3.23 Description of the loadings — loading factor = percentage of maximum force. . . . 87
3.24 Uniaxial reverse cyclic responses. . . . 88
3.25 Equivalent viscous damping ratio versus loading factor. . . . 90
3.26 Description of the Ornskoldsvik bridge. . . . 91
3.27 Loading setup of the Ornskoldsvik bridge. . . . 91
3.28 Finite element mesh of the Ornskoldsvik bridge — concrete in blue; reinforcing bars in red; elastic platen in purple; elastic areas and CFRP bars in geen. . . . 92
3.29 Experimental–numerical comparison of load–midspan displacement response. . . . 93
3.30 Experimental–numerical comparison of the failure mechanism. . . . 93
3.31 Sensitivity of the load–midspan displacement with respect to steel cross section reduction. . . . 94
3.32 Sensitivity of the load–midspan displacement to the bond properties. . . . 94
3.33 Classic experimental designs in a two-dimensional physical space. . . . 96
3.34 Initial and final positions of the proposed adaptive experimental design — application to the star configuration. . . . 97
3.35 Structural system — the dimensions are in meters. . . . 100
3.36 15,000 samples computed by the Monte Carlo simulation method. . . . 102
3.37 Results from the updating strategy. . . . 103
3.38 Comparison between design and response spectra — 2% and 5% damping — magnitude equal to 5.5. . . . 104
3.39 Picture of SMART 2013 specimen fixed on the AZALEE shaking table, ready to be tested. . . . 105
3.40 Formwork drawing of the SMART 2013 test specimen — dimensions in millimeters. 106
3.41 Summary of the measurement points. . . . 107
3.42 Experimental observations of the degradation process of the SMART 2013 specimen. 108
3.43 Robustness indicators — design level — numerical–experimental comparisons. . . . 113
3.44 Robustness indicator — displacement based indicator — Northridge after shock. 114
3.45 Picture of ENISTAT mock-up. . . . 117
3.46 Sketch of the specimen geometry — dimensions in millimeters. . . . 118
3.47 Picture of a thermal break component. . . . 119
3.48 Drawing of the DF type 1 thermal break component. . . . 119
3.49 Drawing of the DF type 2 thermal break component. . . . 119
3.50 Drawing of the ESI thermal break component. . . . 120
3.51 Measurement points. . . . 120
3.52 Seismic loading in the X direction — comparison between the target response spectrum with the synthetic one — PGA scaled at 0.1 g. . . . 122
3.53 Seismic loading in the Y direction — comparison between the target response spectrum with the synthetic one — PGA scaled at 0.1 g. . . . 122
3.54 Cracking pattern — input signal with a PGA = 0.8 g. . . . 123
3.55 DIC results — input signal with a PGA = 0.2 g — opening at the 1^{st} floor — shear wall #3. . . . 123
3.56 Qualitative representation of the overall relative displacement of the 2^{nd} floor — amplification factor equal to 1500. . . . 124
3.57 Maximum engineering stress versus seismic ground motion level — shear wall #1. 125

3.58 Maximum engineering stress versus seismic ground motion level — shear wall #2. 125
3.59 Maximum engineering stress versus seismic ground motion level — thermal breaks DF type 1 — shear wall #3. 126
3.60 Finite element mesh of the shaking table and the mock-up — red: shear walls; white: plates; yellow: beams; red: column; green: foundation; gray: shaking table. 126
3.61 Acceleration time histories — experimental–numerical comparison — run #28. . 129
3.62 Floor response spectra — experimental–numerical comparison — run #28. . . . 129

4.1 Principle of the enhanced microplane approach. 136
4.2 Experimental setup of the IDEFIX experiments. 137

List of Tables

2.1 Closed-form expressions of the consolidation functions' first derivatives — # 1 = strategy presented in Section 2.2.2, # 2 = strategy presented in Section 2.2.3, # 3 = strategy presented in Section 2.2.4. 37
2.2 Closed-form expressions for the damage variables — # 1 = strategy presented in Section 2.2.2, # 2 = strategy presented in Section 2.2.3, # 3 = strategy presented in Section 2.2.4. 38
2.3 Sets of material parameters — # 1 = strategy presented in Section 2.2.2, # 2 = strategy presented in Section 2.2.3, # 3 = strategy presented in Section 2.2.4. . . 39

3.1 Summary of the constitutive equations characterizing the anisotropic continuum damage model. 72
3.2 Summary of the constitutive equations characterizing the anisotropic discrete damage model. 75
3.3 Specimen specifications and loading characteristics — E_c = Young's modulus for the concrete — f_{cm} = Compressive strength of the concrete — f_{tm} = Tensile strength of the concrete — Values in brackets stands for the coefficients of variation. 87
3.4 Statistical parameters and distributions of the random variables. 101
3.5 Results. 101
3.6 Identification of the probabilistic model — LN = Lognormal; COV = Coefficient Of Variation; std = Standard Deviation. 102
3.7 Seismic loading procedure — DL = design level; MS = Main Shock; AS = After Shock — percentages are computed, for a given test sequence, as the ratio between the PGA of a run and the nominal PGA. 108
3.8 Teams involved in the SMART 2013 international benchmark—Part 1. 110
3.9 Teams involved in the SMART 2013 international benchmark—Part 2. 111
3.10 Mechanical parameters of the thermal break components. 120
3.11 Target PGAs of all the bi-directional seismic runs. 121
3.12 Experimental–numerical comparison of the eigenfrequencies — damaged structural state. 128

1 Introduction

Nowadays, the concept of structural performance has become common, not only for design engineers but also for stakeholders. Looking for efficient structures requires paying attention to three criteria: (i) ensuring a satisfactory level of sustainability at the material scale, (ii) ensuring serviceability, and (iii) ensuring structural safety regarding external loadings. The issues related to the aforementioned requirements become of higher importance when dealing with sensitive facilities such as the ones devoted to the energy production. The design of civil engineering structures having a satisfactory level of performance over their life-cycle requires the ability to assess their structural behavior when subjected to various kinds of loadings, which can be either long-term or short-term. Furthermore, structural assessments at the design level become less and less sufficient: it is crucial to understand how reinforced concrete structures behave in the beyond-design range in o rder to quantify the strength provisions. To illustrate this, in 2010 French regulators increased the safety requirements regarding the seismic loading in the case of classical civil engineering structures. This trend can also be noticed at a higher scale. In 2011, following the Tohoku earthquake Ide *et al.* (2011) which took place in 2011 in Japan, the European Commission required that all its member states demonstrate the safety level of their nuclear facilities, not only at the design level but also in the beyond-design regime.

Except for some slender structures that may reach a failure state because of second-order effects, most civil engineering buildings are solid. In this case, nonlinearities can be explained by local dissipative mechanisms occuring at the material scale. For instance, we can mention concrete cracking, steel reinforcement yielding, and bond failure. As a consequence, it is important to have trustworthy and efficient constitutive laws which may be used for a refined analysis up to failure. To ensure a satisfactory predictive capability, several material parameters should be identified. Due to the presence of uncertainties, it is becoming more and more crucial to define a possible set of structural responses instead of a unique result. In other words, taking into account uncertainties and making possible their propagation through a mechanical model are very helpful for both design engineers and stakeholders. The efficiency of a probabilistic approach depends not only on its way of estimating the failure probability, but also on the relevancy of the nominal mechanical models used to describe the structure under study. In addition, because it is necessary to compute several mechanical responses for statistical purposes, efficient simplified strategies should be considered. This task is far from being straightforward because it requires the understanding of the local mechanisms which are of secondary importance. Nowadays, the most matural approaches are based upon a continuous description of the constitutive materials. For instance, constitutive models expressed within the frameworks of continuum damage mechanics or plasticity theory have reached a certain confidence level even though some questions remain open. How can the material parameters related to nonlinear processes be identified? How can local cracking features be quantified? It is not rare that similar questions arise, especially when safety requirements are expressed in terms of local quantities, such as crack openings or spacings. Tackling these issues requires being able to explicitly describe the discontinuous nature of the displacement field. Despite the fact that various numerical strategies have been explored and developed in the literature over the past decades, the efficiency of such strategies

has not been generally assessed for the case of large-scale structures. Indeed, the complexity of the local dissipative mechanisms, which are usually coupled, requires not only their robust identification at the material scale but also the understanding of their consequences at the structural scale. Especially in the case of extreme loadings, such as earthquakes, additional phenomena appear due to their dynamic nature. Among the most known, we can mention the resonance or damping, which both play an important role when dealing with the design or structural assessment of reinforced concrete structures. Therefore, appropriate testing strategies, such as shaking table tests, must be considered in order to better understand and describe the complex dynamic responses of a given structure. The experimental data obtained by means of such experimental techniques can then be used by the international scientific community in order to demonstrate and assess the efficiency of advanced nonlinear strategies. Indeed, because of the challenges currently faced, and the fact that the computational practices are varied, it is crucial to create international opportunities to allow scientific exchanges and brainstorming sessions to move forward.

In view of the conclusions and issues mentioned above, our research activities have been conducted with the following objectives in view:

1. To improve both the predictive capabilities and the numerical robustness of the time integration strategies of the continuous constitutive model when dealing with the cyclic behavior of quasi-brittle materials subjected to either long-term or short-term loadings;

2. To improve numerical techniques capable of describing the discontinuous nature of cracking and related local dissipative phenomena;

3. To contribute to the formulation of large-scale experimental programs and associated collaborative international projects aimed at better understanding the complex behavior of reinforced concrete structures when subjected to extreme loadings, such as earthquakes.

To reach the aforementioned objectives, this report is split into two different parts. *In the first part*, publications related to three research topics are summarized. We focus on the development of constitutive laws to describe the cyclic behavior of concrete-like materials, on the formulation of a steel/concrete interface constitutive model accounting for refined mechanisms based upon more or less simplified frameworks and then, on the improvements of probabilistic approaches. *In the second part*, several works aiming at quantifying the vulnerability of reinforced concrete structures are presented. The first item is related to the development and improvement of refined strategies to quantify cracking features. Then, some contributions aimed at taking into account uncertainties and efficiently updating an initial probabilistic model are described. Last, experimental studies aiming at estimating not only the dissipative capability of reinforced concrete components but also the design provisions with respect to extreme loadings are presented.

Because the beyond-design behavior of civil engineering structures is locally driven by that related to concrete, we first focus on that specific case. Among the available approaches developed over the past decades, the isotropic continuum damage mechanics has been considered because it allows nonlinear computations at the member scale. The initial theoretical background which lies in decreasing the elastic properties of concrete in a progressive and continuous way has been enhanced with the aim of handling the complex case of cyclic loadings. The first idea consists in splitting the difficulties related to the crack opening/closing and local sliding between the lips of the cracks. This consideration has been implemented by a spherical/deviatoric split of the Helmholtz energy. The feedback we got from this first attempt showed the inability of the approach to deal with highly damaging cyclic loadings, mainly due to the fact the initial stiffness could not be fully recovered when switching from tension to compression. The second idea lies

in describing the fact that cracking is localized in tension and much more diffuse in compression. In other words, damage has been used in tension and plasticity in compression. Both descriptions have been continuously linked by introducing a linear crack closure function. Despite the fact that satisfactory results could be obtained in the case of cyclic bending-dominated loadings within a fully three-dimensional framework, the constitutive law failed to handle the case of a reinforced concrete structure subjected to shear-dominated loading, such as shear walls. We observed a lack of numerical robustness of the local time-integration strategy when dealing with this kind of loading. The main conclusion from these first attempts is that the way of describing the unilateral effect has been identified as playing a crucial role, not only to ensure a good numerical robustness of local time-integration strategies but also to reach a satisfactory description of the mechanical responses when subjected to cyclic loading. As a consequence, the concept of regularized unilateral effect has been introduced in recent developments. This strategy is still based on the use of a crack closure function in order to manage the unilateral effect. However, the function does not link the total stress and total strain anymore. Rather, it allows making a $\mathcal{C}^1$ junction between the stress and strain rates when switching from tension to compression. In addition, the choice of the crack closure function has also been improved, especially thanks to physical considerations. This way, the resulting continuous constitutive model has been successfully tested on several structural case studies, such as reinforced concrete beams and shear walls subjected to cyclic loadings.

Another quasi brittle-like "material" having a noticeable influence on the mechanical response of reinforced concrete structures is the steel/concrete interface. Indeed, specific dissipative phenomena occur at this location during the loading process. The understanding of the behavior of such a region is of primary importance because it drives the redistribution of the load between the concrete and the reinforcing steel bars under a cracked condition. In addition, this region may be a preferential location for the development of reinforced concrete pathologies such as corrosion. The prediction of the performance level of a reinforced concrete structure over its life cycle requires being able to satisfactorily understand how this area behaves under complex loadings. Among the available approaches to tackle this issue, we first focused on the development of a refined constitutive law which can be used within a three-dimensional framework based upon the use of zero-thickness finite elements. Despite the fact that this strategy provides pretty nice results, its principal limitation lies in the quasi-inability of meshing all the interface areas with zero-thickness finite elements. This step is far from being straightforward, and the resulting nonlinear analyses are generally time consuming. In order to overcome this drawback, we simplified this refined constitutive law in order to make it compatible with the multifiber finite element framework. We explored a way of coupling a steel fiber constitutive law with a numerical model of the steel/concrete interface. Despite the fact that an increase in the computational cost related to the multifiber analysis has been noticed, this strategy allows satisfactorily quantifying the mechanical response of reinforced concrete structures subjected to complex loadings.

In order to make accurate estimations of the cracking features possible, we focused on the improvement of numerical strategies based upon an explicit description of the cracking. The first approach explored was the discrete element method. This strategy lies in a particle-based description of the media, each particle being linked by beam-like elements with a brittle behavior. To make this model capable of handling cyclic loadings, two additional mechanisms were introduced: contact and frictional sliding, which are of primary importance when dealing with the cyclic response of concrete-like materials. Besides these physical considerations, strong nonlinearities in connection with these two mechanisms lead to numerical difficulties related to the time-integration algorithm. Furthermore, to ensure the rigorous fulfillment of the momentum

balance equation, it is necessary to consider implicit strategies, even though this is unusual in the case of this kind of method. A time integration algorithm coupling, in a strong way, the well-know sawtooth approach (to handle fracture nonlinearities) with a predictor–correction numerical scheme (to handle contact and frictional sliding nonlinearities) has been developed and the benefits we could get from its use have been highlighted. Especially the numerical results become almost independent of the time-step. Then, the particle model has been used not only in the context of a postprocessing strategy to quantify in a refined way the cracking features, but also as a virtual testing machine to complement the set of available mechanical tests in order to improve the way of identifying the material parameters of continuous constitutive laws. This latter could not have been handled if the particle model had not exhibited strong predictive capabilities. However, the use of such strategies remains difficult in the case of large-scale structures.

To overcome this drawback, one of the possibilities lies in enhancing the displacement field by a discontinuous term allowing for cracking description. This approach has been considered within a local framework in order to ensure its low-intrusiveness in the computational software. Furthermore, this framework allows refining the crack description by taking into account several fracture mechanisms: mode I, mode II and mixed mode I+II. The classical continuum constitutive laws are naturally replaced by traction/separation relationships. Based upon an anisotropic damage framework, a mixed mode traction/separation law has been formulated and tested at the member scale. As a major drawback of this kinematically enhanced approach, the geometrical $\mathcal{C}^0$-continuity of the crack path is not ensured. Therefore, the use of tracking strategies is recommended. One of the best known algorithms consists in solving a heat conduction-like problem. The iso-temperature-like lines are used to enforce the continuity of the crack path. However, in its original formulation, the global tracking strategy leads to an ill-posed discrete problem that needs the addition of an algorithmic conductivity term which is generally user-defined and therefore decreases the predictive capability of the approach. To overcome this drawback, we introduce a new interpretation of the boundary value problem to solve, based upon techniques classically used in computational fluid mechanics. The relevancy of this alternative approach has been assessed though numerical comparisons with the previous technique.

The developments and improvements of computational strategies to handle cracking need always to be complemented by experimental data. We have especially focused on the estimation of the dissipative capabilities of reinforced concrete structures subjected to either long-term or short-term loadings. In the first case, the refined steel/concrete constitutive law has been used in order to predict the structural consequences of corrosion, which is one of the most damaging pathologies. A 40-year old reinforced concrete bridge has been analyzed and the numerical results obtained at the member-scale confirmed some conclusions given in the published literature. The dissipative capability of the bridge appeared to be drastically reduced as well as its overall ductility. These results made us think corrosion should have a great influence on the dynamic response of reinforced concrete structures when subjected to an extreme loading. Furthermore, another parameter which is highly influenced by the degradation state is the damping ratio. Often considered as a tuning parameter when dealing with dynamic analysis, an analytical experimental study involving reinforced concrete beams was carried out in order to derive a damage/damping relation. The experimental measurements were then compared with numerical results, allowing discriminating different hysteretic schemes to manage the energy dissipation due to the frictional sliding mechanism.

On the other hand, despite the fact that local cracking mechanisms may be understood and reproduced, the predictive capability of a given model is highly dependent on the way of identi-

fying the set of material parameters. It is rare that the material parameters can be considered as being deterministic, indeed, uncertainties should be taken into account. To reach this objective, probabilistic approaches have been developed over the past decades. Based upon the definition of a satisfactory structural model, the responses corresponding to a set of realizations of material parameters should be computed. Due to the large number of responses needed to compute statistical estimators, the issue of the computational efficiency appears in a natural way. In addition, the probabilistic model should be able to be updated based upon new pieces of information. Within the framework of our research activities, we paid attention to both these issues.

Structural assessments need to be compared with the output from large-scale experimental studies. Within the framework of earthquake engineering, this becomes essential when dealing with strongly asymmetric reinforced concrete structures. Indeed, asymmetry creates coupled torsional/bending effects, which are usually quite complex to take into account. We analyzed this issue in two structural case studies, aiming at providing some answers to different challenges. First, the case of a reinforced concrete structure designed according to the rules allowed in France in the nuclear industry was analyzed. A wide experimental study based upon shaking table tests was realized in order to assess the seismic margins available. The experimental results formed the basis for an international benchmark, named SMART 2013. This benchmark was the opportunity for the international earthquake engineering community to exchange views about their common scientific concerns. Engineers and researchers sat down around the same table and could exchange views and reach a consensus. On the other hand, in a more industrial context, the issue of thermal insulation and efficiency has become of primary importance. To reduce energy loss, innovative structural components called thermal break elements have been developed. They are introduced at the shear wall–slab junction, an area where thermal bridges are often located. However, the effect of these new components on the dynamic behavior of strongly asymmetric reinforced concrete structures have not been well-established. Therefore, shaking table tests were carried out to obtain some answers to this issue. The experimental measurements have been complemented by nonlinear time history analysis. The results allow concluding that the thermal break elements have almost no influence on the overall behavior of this kind of reinforced concrete structure.

2 Modeling of some mechanisms occurring in quasi-brittle material failure process

2.1 Introduction

The family of quasi-brittle materials includes those which exhibit different strength properties, depending on the type of the loading they are subjected to. As an example, the most used material in civil engineering is nowadays concrete. Ductile in compression and brittle in tension, this material exhibits complex local dissipative mechanisms during its failure process. In addition to its strong asymmetry in tension/compression, concrete is a material that is sensitive to the hydrostatic pressure and exhibits dilatancy phenomenon in the case of quasi-static loadings. Its physics becomes more complex when dealing with cyclic loading. Indeed, a part of the elastic energy is released due to the frictional sliding occurring between the lips of the cracks (also known as the hysteresis effects) and the elastic stiffness is recovered when switching from a tension stress state to a compression state (also known as the unilateral effect). From these observations, it can be concluded that concrete modeling is still a paradigm which motivates the national and international scientific community and makes this area an intense and fascinating research field.

Most of the structures in civil engineering are not made of concrete alone: steel reinforcing bars are used to withstand tension forces that cannot be balanced if concrete were used alone. Reinforced concrete is therefore a composite material that is able to withstand many types of complex loadings. However, the strength properties of such a composite material are mainly dependent on the properties of the bond between the steel reinforcing bars and the surrounding concrete. This specific area may exhibit complex dissipative mechanisms when dealing with a structural response that is close to the failure state. Indeed, either a brittle or a more progressive loss of the bond appears at the steel/concrete interface. Both types of degradation mechanisms are often called mode-I and mode-II failure modes respectively. The presence of passive (stirrups) or active (prestressing force) modifies the variations of the bond properties, allowing a mixed mode failure mode. Furthermore, the steel/concrete interface may be a preferential area in which some pathologies appear. For instance, it is the case of corrosion, which involves the creation of rust products that swell, leading to the presence (locally) of tensile stresses responsible for cracking if the tensile strength is overcome, coupled with a reduction in the the steel cross section.

In this chapter, a summary of our contributions to providing some answers to the complex issue of the modeling of quasi-brittle materials is presented. First, we focus on the case of concrete modeling, a research topic we have been dealing with for six years now. The objective of our research is to improve the constitutive laws to improve the numerical description of the complex behavior of concrete under cyclic loading. Both the progressive improvements of the initial constitutive law formulated within the framework of my Ph.D. thesis and the remaining limitations we are working on are presented. Second, the case of the steel/concrete interface

modeling is considered. A full three-dimensional formulation allowing a refined description of the most preponderant dissipative mechanisms is presented. This formulation is based upon the use of zero-thickness finite elements and therefore may lead to some difficulties when dealing with the mesh generation. In order to overcome this drawback, a strategy, within the framework of the multifiber approach, aiming at embedding the contribution of the steel/concrete interface to the constitutive law of the steel reinforcing bars has been explored. This work has also been motivated by the fact that simplified strategies are needed when dealing with probabilistic studies, requiring hundreds of computations.

2.2 Theoretical framework

2.2.1 Generalized standard materials

The formulation of a constitutive law can be realized in several ways. Given a specific material, some authors make the choice of expressing its constitutive law by fitting experimental data obtained from elementary mechanical tests, whereas others consider dedicated theoretical frameworks in order to avoid physical inconsistencies. In our research, we have chosen to use the theoretical framework of irreversible thermodynamic processes Lemaitre *et al.* (2009). Indeed, this approach offers an energetic framework that ensures well-known principles coming from physics will be a priori fulfilled. Considering a representative volume element (RVE) of the material to be described, it is assumed that its thermodynamical state can be represented by a given set of variables, which are collected into a scalar functional, called the state potential. Each variable allows for the description of a macroscopic deformation mechanism. Among the different possibilities which exist to express the state potential, the most convenient is to express it as the sum of strain-based terms. Indeed, this strategy allows simplifying the time integration of the underlying constitutive law when dealing with its numerical implementation.

Assuming the state potential is represented by the Helmholtz free energy Ψ, an admissibility condition can be obtained from the first and second principles. This condition is called the Clausius–Duhem–Truesdell inequality and should be fulfilled for all loading processes of the RVE in order to make possible the description of the evolution of its thermodynamic state. This condition can be expressed as follows, in the case of small perturbations and an isothermal strain process:

$$\mathcal{D} = \underline{\underline{\sigma}} : \dot{\underline{\underline{\epsilon}}} - \rho\dot{\Psi} \geq 0 \tag{2.1}$$

where $\underline{\underline{\sigma}}$ is the second-order Cauchy stress tensor, $\underline{\underline{\epsilon}}$ the second-order strain tensor, and ρ the mass density of the considered material. $\mathcal{D}$ is called the intrinsic dissipation and should remain positive or null. To move forward, it is assumed that the Helmholtz free energy is a convex and $\mathcal{C}^2$-differentiable function of the strain tensor and a given set of variables allowing the description of macroscopic degradation mechanisms:

$$\Psi = \Psi(\underline{\underline{\epsilon}}, (\alpha_k)_{k=1,\cdots,n}) \tag{2.2}$$

where α_k is an internal variable related to the k^{th} macroscopic mechanism to be described and n the total number of mechanisms the constitutive law takes into accounts. It should be noted that the mathematical nature of the variable α_k depends on the physical properties characterizing the mechanism it represents. Combining Equations 2.1 and 2.2 and assuming a constant mass density, the intrinsic dissipation can be expressed as follows:

$$\mathcal{D} = \left(\underline{\underline{\sigma}} - \rho\frac{\partial\Psi}{\partial\underline{\underline{\epsilon}}}\right) : \dot{\underline{\underline{\epsilon}}} - \rho\sum_{k=1}^{n}\frac{\partial\Psi}{\partial\alpha_k}\dot{\alpha}_k \geq 0 \tag{2.3}$$

The inequality 2.3 should be fulfilled for all loading paths, the first state law can be deduced as follows:

$$\underline{\underline{\sigma}} = \rho \frac{\partial \Psi}{\partial \underline{\underline{\epsilon}}} \tag{2.4}$$

Similarly, dual variables can be associated each α_k as follows:

$$A_k = \rho \frac{\partial \Psi}{\partial \alpha_k} \tag{2.5}$$

From Equations 2.4 and 2.5, it can be seen that two sets of variables $\mathcal{P} = (\underline{\underline{\epsilon}}, (\alpha_k)_{k=1,\cdots,n})$ and $\mathcal{F} = (\underline{\underline{\sigma}}, (A_k)_{k=1,\cdots,n})$ have been introduced and are linked with each other through the state potential Ψ. These two sets of variables define the thermodynamic state of the RVE and represent the sets of the state variables and the thermodynamic forces, respectively. However, it is necessary to add conditions in order to describe when and how this state will evolve during a given loading process. To achieve these goals, a dissipation potential f is introduced, often expressed in the $\mathcal{F}$ space. It can be interpreted as a threshold criterion (or a loading surface) that defines the time when the internal variables will flow. The flow rules define the way the internal variables flow. They are built from the maximum plastic dissipation principle, which postulates that the admissible variables A_k are the ones that maximize the intrinsic dissipation under the constraint of being inside the loading surface Eckart (1948). Under these assumptions, the admissible thermodynamic forces are defined as follows:

$$A_k = \underset{f(A_k^\star)\leq 0}{\mathbf{Argmin}} \left\{ -\mathcal{D}(A_k^\star) \right\} \tag{2.6}$$

Equation 2.6 can be solved by introducing a Lagrangian functional $\mathcal{G}(.) = -\mathcal{D}(.) + \dot{\lambda} f(.)$, where $\dot{\lambda}$ is a Lagrange multiplier. The stationarity conditions of the Lagrangian allow defining the flow rules as follows:

$$\frac{\partial \mathcal{G}(A_k)}{\partial A_k} = 0 \implies -\dot{\alpha}_k + \dot{\lambda} \frac{\partial f(A_k)}{\partial A_k} = 0 \implies \dot{\alpha}_k = \dot{\lambda} \frac{\partial f(A_k)}{\partial A_k} \tag{2.7}$$

Complementary conditions, also called Karush–Kuhn–Tucker's conditions, are naturally obtained:

$$\dot{\lambda} \geq 0 \quad f(A_k) \leq 0 \quad \dot{\lambda} f(A_k) = 0 \tag{2.8}$$

Conditions 2.8 are crucial to manage the loading/unloading response of the RVE. However, some materials fail to fulfill gradient-based flow rules having the general expression shown in Equation 2.7. In order to overcome this drawback, it is common to introduce a new potential g, called the pseudo-potential of dissipation, which will be used to define the flow rules Halphen et Quoc Son (1974). A material which exhibits dissipative mechanisms that flow according to a pseudo-potential of dissipation is qualified as being generalized. In such a case, the potential of dissipation f is used to know when the internal variables flow and the pseudo-potential of dissipation is used to know how they flow.

2.2.2 Spherical/deviatoric split

Driving ideas

Quasi-brittle materials exhibit different dissipative mechanisms according to the type of stress state they are subjected to. Assuming that cracking is mainly responsible for the energy dissipation and consequent material nonlinearities, it seems necessary to accurately describe the local

mechanisms that are connected with the way a cracked area behaves. The first mechanism to be considered is the cracking itself. Following the progressive growth of cavities at the mesoscopic scale, macroscopic cracks appear in a more or less localized way, depending on the stress state (tension or compression). Note that the pure shear stress state, which is an extreme case, corresponds to a coupled tension/compression stress state in different observation directions. This first mechanism can be described by isotropic continuum damage theory, introducing a unique scalar damage variable d (ranging continuously from 0 to 1) for reasons of thermodynamical consistency Mazars (1984); Marigo (1985). A second mechanism which plays an important role when dealing with cyclic loadings is the frictional sliding Ragueneau (1999). This is related to the fact that frictional forces appear between the crack lips. This mechanism must be taken into account in order to accurately capture the internal damping when dealing with the low-velocity dynamics. To do so, a second-order tensor $\underline{\underline{\epsilon}}^{\pi}$ has been introduced. In connection with the aforementioned mechanisms, corresponding hardenings have also been introduced in order to treat the loading/unloading response of the RVE. Following the same idea as the one proposed by Gabet *et al.* (2008), both mechanisms are included in the thermodynamic state potential through a spherical/deviatoric split of the functional. In the present formulation, the frictional sliding mechanism has only been introduced on the deviatoric part since it is mainly related to the friction. Furthermore, the damage has not been introduced in the negative part of the spherical part of the energy. This strategy allows, partially, taking into account the crack/closure effect Mazars *et al.* (1990). A summary of the constitutive equations proposed is presented in the next paragraphs.

The state potential

The state potential is chosen as the Helmholtz free energy, split into a spherical part and a deviatoric part. It can be expressed as follows:

$$\rho\Psi = \frac{1}{2}\left\{\frac{\kappa}{3}\mathbf{tr}^2\underline{\underline{\epsilon}} + 2\mu\underline{\underline{\epsilon}}^d : \underline{\underline{\epsilon}}^d\right\} \tag{2.9}$$

where $(.)^d = (.) - \frac{1}{3}\mathbf{tr}(.)\underline{\underline{\delta}}$ with $\underline{\underline{\delta}}$ Kronecker's tensor, and κ and μ the bulk coefficient and Coulomb's modulus respectively. This strategy has been proposed in order to describe cracking, frictional sliding and the unilateral effect according to the physical motivations presented above. Cracking is introduced by considering a scalar damage variable d ranging from 0 (virgin material) to 1 (fully broken material). The thermodynamic state potential becomes as follows:

$$\rho\Psi = \frac{1}{2}\left\{\underbrace{(1-d)}_{Damage}\frac{\kappa}{3}\mathbf{tr}^2\underline{\underline{\epsilon}} + 2\underbrace{(1-d)}_{Damage}\mu\underline{\underline{\epsilon}}^d : \underline{\underline{\epsilon}}^d\right\} \tag{2.10}$$

The spherical part of the Helmholtz free energy is split into a positive part and negative part, allowing to cancel, at least partially, the effect of damage when the volumetric strain becomes negative. This consideration allows obtaining the following expression for the state potential:

$$\rho\Psi = \frac{1}{2}\left\{\frac{\kappa}{3}(\underbrace{(1-d) < \mathbf{tr}\underline{\underline{\epsilon}} >_+^2 + < \mathbf{tr}\underline{\underline{\epsilon}} >_-^2}_{Unilateral\ effect}) + 2(1-d)\mu\underline{\underline{\epsilon}}^d : \underline{\underline{\epsilon}}^d\right\} \tag{2.11}$$

where $< . >_+$ and $< . >_-$ stands for the positive and negative parts of $(.)$, respectively. This strategy for the description allows accounting for a partial unilateral effect. The last mechanism included in the formulation is the frictional sliding, which is characterized by the internal sliding second-order tensor. Because frictional sliding is mainly related to mode II, this mechanism acts

on the deviatoric part of the free Helmholtz energy. Hence, the state potential can be formulated as follows:

$$\begin{aligned}\rho\Psi =&\frac{\kappa}{6}((1-d)<\mathbf{tr}\underline{\underline{\epsilon}}>_+^2+<\mathbf{tr}\underline{\underline{\epsilon}}>_-^2)+\\&(1-d)\mu\underline{\underline{\epsilon}}^d:\underline{\underline{\epsilon}}^d+\underbrace{d\mu(\underline{\underline{\epsilon}}-\underline{\underline{\epsilon}}^\pi)^d:(\underline{\underline{\epsilon}}^d-\underline{\underline{\epsilon}}^\pi)^d}_{Internal\ sliding}\end{aligned} \tag{2.12}$$

Finally, hardening mechanisms are added to the free Helmholtz energy. An isotropic hardening in connection with damage is assumed, whereas a kinematic one is assumed when dealing with internal sliding. The thermodynamic state potential becomes

$$\begin{aligned}\rho\Psi =&\frac{\kappa}{6}((1-d)<\mathbf{tr}\underline{\underline{\epsilon}}>_+^2+<\mathbf{tr}\underline{\underline{\epsilon}}>_-^2)+\\&(1-d)\mu\underline{\underline{\epsilon}}^d:\underline{\underline{\epsilon}}^d+d\mu(\underline{\underline{\epsilon}}-\underline{\underline{\epsilon}}^\pi)^d:(\underline{\underline{\epsilon}}^d-\underline{\underline{\epsilon}}^\pi)^d\}+H(z)+\frac{\gamma}{2}\underline{\underline{\alpha}}:\underline{\underline{\alpha}}\end{aligned} \tag{2.13}$$

where H is the consolidation function, z the isotropic hardening variable, γ a material parameter to be identified, and $\underline{\underline{\alpha}}$ the kinematic hardening second-order tensor.

The state equations

State equations can be deduced from Equation 2.12 by differentiating it with respect to each state variable. The stress/strain relation is deduced as follows:

$$\underline{\underline{\sigma}}=\frac{\partial\rho\Psi}{\partial\underline{\underline{\epsilon}}}=\frac{\kappa}{3}\left((1-d)<\mathbf{tr}\underline{\underline{\epsilon}}>_+ +<\mathbf{tr}\underline{\underline{\epsilon}}>_-\right)\underline{\underline{\delta}}+2(1-d)\mu\underline{\underline{\epsilon}}^d+2d\mu(\underline{\underline{\epsilon}}-\underline{\underline{\epsilon}}^\pi)^d \tag{2.14}$$

The frictional stress that is related to the internal sliding is defined as follows:

$$\underline{\underline{\sigma}}^\pi=\frac{\partial\rho\Psi}{\partial\underline{\underline{\epsilon}}^\pi}=2(1-d)\mu\underline{\underline{\epsilon}}^d+2d\mu(\underline{\underline{\epsilon}}-\underline{\underline{\epsilon}}^\pi)^d \tag{2.15}$$

The rate Y of the release of damage energy is obtained from its classical expression:

$$Y=-\frac{\partial\rho\Psi}{\partial d}=\underbrace{\frac{\kappa}{6}<\mathbf{tr}\underline{\underline{\epsilon}}>_+^2+2\mu\underline{\underline{\epsilon}}^d:\underline{\underline{\epsilon}}^d}_{Damage}-\underbrace{2\mu(\underline{\underline{\epsilon}}-\underline{\underline{\epsilon}}^\pi)^d:(\underline{\underline{\epsilon}}^d-\underline{\underline{\epsilon}}^\pi)^d}_{Internal\ sliding} \tag{2.16}$$

We can see that Y is composed of two contributions: one related to the damage and the other related to the internal sliding. Finally, the thermodynamic forces associated with the isotropic hardening and the back stress are computed by differentiating the thermodynamic state potential with respect to the corresponding variables:

$$\underline{\underline{X}}=\gamma\underline{\underline{\alpha}} \tag{2.17}$$

$$Z=\frac{dH(z)}{dz} \tag{2.18}$$

The potentials of dissipation

In order to allow the definition of the pseudo-time from which the dissipative mechanisms (damage and frictional sliding) become active, two potentials of dissipation have to be introduced. Regarding the isotropic damage, the threshold surface is expressed in terms of the energy rate $\bar{Y}$ as follows:

$$f_d = \bar{Y} - (Y_0 + Z) \tag{2.19}$$

where Y_0 is an initial threshold which must be overcome. $\bar{Y}$ is the strain energy variable that drives the damage. To define different behaviors in tension and compression, the total strain is split into two contributions. The first one refers to direct extensions $\underline{\underline{\epsilon}}^{\mathbf{Dir}}$ whereas the second one refers to indirect extensions $\underline{\underline{\epsilon}}^{\mathbf{Ind}}$. The direct extension second order tensor is defined as follows:

$$\underline{\underline{\epsilon}}^{\mathbf{Dir}} = <\underline{\underline{\epsilon}}>_+ \mathcal{H}(<\underline{\underline{\epsilon}}>_+ : <\underline{\underline{\sigma}}>_+) \tag{2.20}$$

where $\mathcal{H}$ stands for the Heaviside function. The indirect extension second order tensor is defined by removing the direction extension contribution from the total strain tensor:

$$\underline{\underline{\epsilon}}^{\mathbf{Ind}} = \underline{\underline{\epsilon}} - \underline{\underline{\epsilon}}^{\mathbf{Dir}} \tag{2.21}$$

Corresponding energy rates are introduced in order to express the threshold surface related to damage:

$$Y^{\mathbf{Dir}} = \frac{1}{2}\underline{\underline{\epsilon}}^{\mathbf{Dir}} : \underline{\underline{\underline{\underline{C}}}} : \underline{\underline{\epsilon}}^{\mathbf{Dir}} \tag{2.22}$$

$$Y^{\mathbf{Ind}} = \frac{1}{2}\underline{\underline{\epsilon}}^{\mathbf{Ind}} : \underline{\underline{\underline{\underline{C}}}} : \underline{\underline{\epsilon}}^{\mathbf{Ind}} \tag{2.23}$$

where $\underline{\underline{\underline{\underline{C}}}}$ is the fourth order Hooke tensor. Finally, the threshold surface is expressed as follows:

$$f_d = \bar{Y} - (Y_0 + Z) = Y^{\mathbf{Dir}} + \beta Y^{\mathbf{Ind}} - (Y_0 + Z) \tag{2.24}$$

where β is a material parameter allowing the setting up of the shape of the biaxial response. Regarding the frictional sliding mechanism, the threshold surface is chosen as a J_2-plasticity based surface:

$$f_\pi = J_2(\underline{\underline{\sigma}}_\pi - \underline{\underline{X}}) \tag{2.25}$$

where $J_2(.)$ is the second invariant of $(.)^d$. One can note that $f_\pi \geq 0$ for all loading paths. This means an energy balance occurs between two consecutive thermodynamic states from the damage mechanism to the frictional sliding one.

The flow rules

Flow rules are introduced for both dissipative mechanisms. In the case of damage, an associative flow is assumed, whereas in the case of frictional sliding, a non-associative flow is assumed in order to describe the nonlinearities related to the hysteretic responses when dealing with the loading/unloading paths. The flow rules driving the damage and the isotropic hardening variables follow the normality rule:

$$\begin{cases} \dot{d} = \dot{\lambda}_d \dfrac{\partial f_d}{\partial \bar{Y}} = \dot{\lambda}_d \\ \dot{z} = \dot{\lambda}_d \dfrac{\partial f_d}{\partial Z} = -\dot{\lambda}_d \end{cases} \tag{2.26}$$

where $\dot{\lambda}_d$ is the Lagrange multiplier related to the damage. We can note that $\dot{d} + \dot{z} = 0$, which means that d and z are flow-coupled. The flow rules related to the frictional sliding mechanism require the consideration of a pseudo-potential of dissipation ϕ_π. According to the proposal made by Armstrong et Frederick (1996), the following pseudo-potential is considered:

$$\phi_\pi = f_\pi + \frac{a}{2}\underline{\underline{X}} : \underline{\underline{X}} \tag{2.27}$$

where a is a material parameter which drives the energy dissipation during a loading/unloading cycle. Now the flow rules can be defined, employing the normality rule with respect to ϕ_π:

$$\begin{cases} \underline{\underline{\dot{\epsilon}}}^\pi = \dot{\lambda}_\pi \dfrac{\partial \phi_\pi}{\partial \underline{\underline{\sigma}}^\pi} \\ \underline{\underline{\dot{\alpha}}} = -\dot{\lambda}_\pi \dfrac{\partial \phi_\pi}{\partial \underline{\underline{X}}} \end{cases} \tag{2.28}$$

where $\dot{\lambda}_\pi$ is the Lagrange multiplier related to frictional sliding.

2.2.3 Coupled damage/plasticity

Driving ideas

In the continuation of the work presented in Section 2.2.2, new efforts were made in order to overcome some of the identified drawbacks related to the proposed constitutive equations. In particular, the objectives of this new line of research were to consider a full unilateral effect when switching from tension to compression and to include the internal sliding mechanism in tension. Indeed, quasi-brittle material RVEs tend to reach their failure state in tension prior to reaching it in compression. Hence, frictional sliding may be significant in tension Yazdani et Schreyer (1990) and need to be taken into account. In order to achieve the aforementioned objectives, isotropic damage is used in tension and plasticity is used in compression. The use of plasticity in compression is frequent in the field of soil mechanics when nonlinearities, dilatancy and permanent strains must be described Jason *et al.* (2006). The behavior of tension and compression can be split into two distinct parts by considering the sign of the Cauchy stress tensor in 1D (or a related quantity in 3D). Since hysteretic phenomenon are linked with frictional sliding, this mechanism is considered in tension, allowing a realistic description not only of hysteretic loops but also of permanent strains in tension. The unilateral effect is also taken into account using a closure function, which ensures the continuity of the stress/strain relation whatever the loading path. With these assumptions, one can state that the behavior of an RVE is accurately represented in tension (brittleness, hysteretic loops and permanent strains) and roughly described in compression (nonlinearity and permanent strains).

The state potential

The state potential has been chosen as the Helmholtz free energy. Similarly to the work presented in Section 2.2.2, this strategy makes the numerical implementation easier, since the state laws will not have to be inverted. The starting point of the Helmholtz free energy is the following expression:

$$\rho\Psi = \frac{1}{2}\left\{(1-d)\underline{\underline{\epsilon}} : \underline{\underline{\underline{\underline{C}}}} : \underline{\underline{\epsilon}} + d(\underline{\underline{\epsilon}} - \underline{\underline{\epsilon}}^\pi) : \underline{\underline{\underline{\underline{C}}}} : (\underline{\underline{\epsilon}} - \underline{\underline{\epsilon}}^\pi) + \gamma \underline{\underline{\alpha}} : \underline{\underline{\alpha}}\right\} + H(z) \tag{2.29}$$

We can note that the spherical/deviatoric split introduced in Section 2.2.2 is no longer employed. Furthermore, expression 2.30 allows taking into account both damage and frictional sliding mechanisms, which are necessary when dealing with the cyclic response of a quasi-brittle material

RVE. In order to consider a full unilateral effect, a closure function η is introduced. The way of including it in the state potential is driven by the fact that when $\underline{\underline{\epsilon}}^{\pi} = \underline{\underline{0}}$, Hooke's constitutive law is recovered. In accordance with this observation, the state potential is enhanced as follows:

$$\rho\Psi = \frac{1}{2}\left\{(1-d)\underline{\underline{\epsilon}} : \underline{\underline{\underline{\underline{C}}}} : \underline{\underline{\epsilon}} + d(\underline{\underline{\epsilon}} - \eta\underline{\underline{\epsilon}}^{\pi}) : \underline{\underline{\underline{\underline{C}}}} : (\underline{\underline{\epsilon}} - \underline{\underline{\epsilon}}^{\pi}) + \gamma\underline{\underline{\alpha}} : \underline{\underline{\alpha}}\right\} + H(z) \tag{2.30}$$

The closure variable η should range from 1 (opened crack) to 0 (closed crack). Finally, the nonlinearities related to the diffuse cracking process of the quasi-brittle material RVE when subjected to a compressive stress state are considered by including a dedicated energy rate in the state potential. Because of the diffuse nature of cracking when dealing with compression, a plasticity based approach is employed. The expression for the Helmholtz free energy becomes:

$$\begin{aligned}\rho\Psi =& \frac{1}{2}\left\{(1-d)(\underline{\underline{\epsilon}} - \underline{\underline{\epsilon}}^{p}) : \underline{\underline{\underline{\underline{C}}}} : (\underline{\underline{\epsilon}} - \underline{\underline{\epsilon}}^{p}) + d(\underline{\underline{\epsilon}} - \eta\underline{\underline{\epsilon}}^{\pi} - \underline{\underline{\epsilon}}^{p}) : \underline{\underline{\underline{\underline{C}}}} : (\underline{\underline{\epsilon}} - \eta\underline{\underline{\epsilon}}^{\pi} - \underline{\underline{\epsilon}}^{p}) + \gamma\underline{\underline{\alpha}} : \underline{\underline{\alpha}}\right\} + \\ & H(z) + G(p)\end{aligned} \tag{2.31}$$

where $\underline{\underline{\epsilon}}^{p}$ is the second order tensor representing the permanent strains in compression, G is a consolidation function allowing the description of the softening, and p is the isotropic hardening variable associated with the plastic strain variable, which can also be interpreted as the cumulative plastic strain.

The state equations

The state potential being now well-defined, the state equations can be derived from expression 2.31 by differentiating it with respect to the state variables. The first state equation, linking Cauchy's stress tensor with the total strain second-order tensor, is:

$$\underline{\underline{\sigma}} = \frac{\partial\rho\Psi}{\partial\underline{\underline{\epsilon}}} = -\frac{\partial\rho\Psi}{\partial\underline{\underline{\epsilon}}^{p}} = (1-d)\underline{\underline{\underline{\underline{C}}}} : (\underline{\underline{\epsilon}} - \underline{\underline{\epsilon}}^{p}) + d\underline{\underline{\underline{\underline{C}}}}(\underline{\underline{\epsilon}} - \eta\underline{\underline{\epsilon}}^{\pi} - \underline{\underline{\epsilon}}^{p}) \tag{2.32}$$

An important feature of expression 2.33 is the fact that when $\eta = 0$, Hooke's constitutive law is recovered. The frictional stress $\underline{\underline{\sigma}}^{\pi}$ can be defined as follows:

$$\underline{\underline{\sigma}}^{\pi} = -\frac{\partial\rho\Psi}{\partial\underline{\underline{\epsilon}}^{\pi}} = \eta d\underline{\underline{\underline{\underline{C}}}} : (\underline{\underline{\epsilon}} - \eta\underline{\underline{\epsilon}}^{\pi} - \underline{\underline{\epsilon}}^{p}) \tag{2.33}$$

Note that the closure variable η acts as a multiplicative part of the internal sliding tensor. Moreover, there is a state coupling between damage and internal sliding, which is physically motivated by the fact that the more damaged the material is, the higher the energy released by internal sliding will be. The rate at which energy is released by the damage mechanism, denoted by Y, is expressed by:

$$Y = -\frac{\partial\rho\Psi}{\partial d} = \frac{1}{2}\left\{(\underline{\underline{\epsilon}} - \underline{\underline{\epsilon}}^{p}) : \underline{\underline{\underline{\underline{C}}}} : (\underline{\underline{\epsilon}} - \underline{\underline{\epsilon}}^{p}) - (\underline{\underline{\epsilon}} - \eta\underline{\underline{\epsilon}}^{\pi} - \underline{\underline{\epsilon}}^{p}) : \underline{\underline{\underline{\underline{C}}}} : (\underline{\underline{\epsilon}} - \eta\underline{\underline{\epsilon}}^{\pi} - \underline{\underline{\epsilon}}^{p})\right\} \tag{2.34}$$

It can be noted that the rate of release of energy due to damage is also the sum of two contributions: the first one is related to the elasto-damage part of the energy and the second one is related to the sliding mechanism, which means there is an energy balance between the damage mechanism and the internal sliding, weighted by η. The thermodynamic forces associated with the isotropic hardenings are:

$$\begin{cases} Z = \dfrac{\partial \rho \Psi}{\partial z} = \dfrac{dH(z)}{dz} \\ R = \dfrac{\partial \rho \Psi}{\partial p} = \dfrac{dG(p)}{dp} \end{cases} \tag{2.35}$$

Finally, the back stress is a linear function of the kinematic hardening variable:

$$\underline{\underline{X}} = \frac{\partial \rho \Psi}{\partial \underline{\underline{\alpha}}} = \gamma \underline{\underline{\alpha}} \tag{2.36}$$

The potentials of dissipation

The damage mechanism and the isotropic hardening are managed in a coupled way. Moreover, an associative flow rule is assumed. The threshold surface is expressed as a function of the energy rate released by damage:

$$f_d = \bar{Y} - (Y_0 + Z) \geq 0 \tag{2.37}$$

where f_d is the threshold surface, $\bar{Y}$ is the rate of release of that part of the energy released by damage, which is defined next, Y_0 is an initial threshold that must be overcome, and Z is the thermodynamic force associated with isotropic hardening. Assuming that the damage is linked with positive extensions, $\bar{Y}$ can be defined as follows:

$$\bar{Y} = \frac{1}{2} < \underline{\underline{\epsilon}} - \underline{\underline{\epsilon}}^p >_+ \underline{\underline{\underline{\underline{C}}}} :< \underline{\underline{\epsilon}} - \underline{\underline{\epsilon}}^p >_+ \tag{2.38}$$

To improve the numerical robustness of the time-integration strategy used to compute the Cauchy stress from the proposed constitutive equations, it has been chosen to drive the damage variable by a function of the total strain (for extensions only). This quantity must be an increasing function of the total strain. If the thermodynamic force Y had been employed, the damage could not have been driven in a satisfactory way, since Y is not an increasing quantity in the total strain (due to the compression load step, for example). This is the main reason why the energy rate defined by Equation 2.38 has been employed. The internal sliding mechanism is assumed to be coupled with the kinematic hardening at the flow level. The threshold surface is expressed in terms of the sliding stress and the back stress. One can note that there is no initial threshold in the expression for the threshold surface, allowing this mechanism to be activated only when damage is activated. The threshold surface f_π is enhanced by an indicator that is a function of Cauchy's stress tensor:

$$f_\pi = J_2(\underline{\underline{\sigma}}^\pi - \underline{\underline{X}})\mathcal{H}(\mathbf{tr}\underline{\underline{\sigma}}) \tag{2.39}$$

The unilateral effect can be defined as an initial (undamaged) stiffness recovering when switching from tension to compression. This effect can be included in the model in various ways (changes of the signs of the strains, stresses, or an expression that couples the stresses with the strains). A closure function is used to gradually cancel the permanent strains created in tension (which no longer flow) when unloading. Following the proposal of LaBorderie (1991), a linear function is assumed:

$$\eta = 1 - \frac{\mathbf{tr}\underline{\underline{\sigma}}}{\sigma_f} \tag{2.40}$$

where σ_f is a material parameter which needs to be identified. If $\mathbf{tr}\underline{\underline{\sigma}} > 0$, cracks obviously remain opened ($\eta = 1$) and if $\mathbf{tr}\underline{\underline{\sigma}} < \sigma_f$, cracks are fully closed ($\eta = 0$). The last potential of dissipation which needs to be considered is related to the smeared cracking process considered

in compression. In order to take into account the triaxiality effects, especially when dealing with bi-compressive stress states, a Drucker–Prager threshold surface is considered. From Equation 2.32, we can note that when plasticity is activated, the term $d\underline{\underline{\epsilon}}^{\pi}$ has no effect since the closure function η is null.

$$f_p = \left(J_2(\underline{\underline{\sigma}}) + \alpha_{f_p} I_1(\underline{\underline{\sigma}})\right) \mathcal{H}(\sigma_f - \mathbf{tr}(\underline{\underline{\sigma}})) - (R + f_c) \geq 0 \tag{2.41}$$

where f_c is a material parameter which needs to be identified.

The flow rules

According to the previous presentation, the flow rules in connection with three dissipative mechanisms have to be considered: isotropic damage, frictional sliding, and plasticity. Regarding the continuum damage mechanism, an associative flow rule is assumed. Therefore, normality rules with respect to the potential of dissipation f_d are used:

$$\begin{cases} \dot{d} = \dot{\lambda}_d \dfrac{\partial f_d}{\partial \bar{Y}} = \dot{\lambda}_d \\ \dot{z} = \dot{\lambda}_d \dfrac{\partial f_d}{\partial Z} = -\dot{\lambda}_d \end{cases} \tag{2.42}$$

where $\dot{\lambda}_d$ is the Lagrange multiplier, which can be computed from the consistency conditions. Regarding the internal sliding variable $\underline{\underline{\epsilon}}^{\pi}$, a non-associative flow rule is postulated. Similarly to the case of the initial set of constitutive equations, this strategy ensures describing quite well nonlinearities related to the hysteretic effects. The related flow rules are expressed by Equations 2.27 and 2.28. The last variable whose flow should be determined is the plastic strain in compression $\underline{\underline{\epsilon}}^{p}$. In order to allow the possibility to describe the dilatancy phenomenon, which is characterized by an increase of the apparent Poisson ratio, a non-associative flow rule is assumed. The pseudo-potential of dissipation considered is

$$\phi_p = J_2(\underline{\underline{\sigma}}) + \alpha_{\phi_p} I_1(\underline{\underline{\sigma}}) - R \tag{2.43}$$

where α_{ϕ_p} is a material parameter that manages the dilatancy capacity. Under these assumptions, the flow rules are obtained using normality rules with respect to the pseudo-potential of dissipation presented above:

$$\begin{cases} \dot{\underline{\underline{\epsilon}}}^{p} = \dot{\lambda}_p \dfrac{\partial \phi_p}{\partial \underline{\underline{\sigma}}} \\ \dot{p} = -\dot{\lambda}_p \dfrac{\partial \phi_p}{\partial R} \end{cases} \tag{2.44}$$

where $\dot{\lambda}_p$ is a new Lagrange multiplier in connection with the plasticity-based mechanism in compression.

2.2.4 The regularized unilateral effect

Driving ideas

In particular, the feedback we got from the use of the constitutive law presented in Section 2.2.3 showed that the local time integration strategy had some convergence issues. It was noted that most of the numerical issues appeared when switching from tension to compression. This observation made us work on improving treatment of the crack closure effect. In particular, we worked on a strategy to take into account the unilateral effect in a smoother way than was used in the case of the constitutive law based on the coupled damage/plasticity. In order to reach

this objective, new physical assumptions were introduced. In particular, in accordance with Mihai et Jefferson (2013), we assumed that the stress state in an RVE could be split into two different contributions: one coming from the matrix and one coming from the cracks. Under these assumptions, the constitutive model is formulated using a typical decomposition of the Cauchy stress tensor characterizing the stress state in the RVE. It is assumed that the Cauchy stress $\underline{\underline{\sigma}}$ can be split into two independent parts:

$$\underline{\underline{\sigma}} = \underline{\underline{\sigma}}^m + \underline{\underline{\sigma}}^f \tag{2.45}$$

where $\underline{\underline{\sigma}}^m$ stands for the stress in the cracked continuum domain and $\underline{\underline{\sigma}}^f$ the stress transmitted by the cracks. In addition, it is assumed that no interaction occurs between the cracks. Within this framework, the Helmholtz free energies Ψ^m and Ψ^f associated with the two stress tensors can be defined. In accordance with the additive decomposition of the Cauchy stress tensor, the total free energy of the RVE, denoted by Ψ, is obtained by summing each of these energetic contributions:

$$\Psi = \Psi^m + \Psi^f \tag{2.46}$$

The free energy Ψ^m can be expressed in accordance with isotropic continuum damage mechanics theory. The way of constructing the free energy Ψ^f is detailed in the next section.

The state potential and the state equations

Fracture processes are modeled by means of isotropic continuum damage theory. In general, the simpler the damage variable is kept, the more robust the proposed macroscopic model will be. Therefore, in view of the structural applications of the proposed model, an isotropic damage mechanism is assumed, leading to a unique scalar damage variable ranging from 0 to 1. However, even though the numerical robustness of the local time integration algorithm should be ensured by this strategy, the description of the anisotropy related to the cracking process will not be achieved. The free energy associated to the cracked continuum medium is simply:

$$\Psi^m = \frac{1}{2}(1-d)\,\underline{\underline{\epsilon}} : \underline{\underline{\underline{\underline{C}}}} : \underline{\underline{\epsilon}} + H(z) \tag{2.47}$$

Equation 2.47 leads to the following expression for $\underline{\underline{\sigma}}^m$:

$$\underline{\underline{\sigma}}^m = (1-d)\,\underline{\underline{\underline{\underline{C}}}} : \underline{\underline{\epsilon}} \tag{2.48}$$

The energetic contribution related to the cracked areas is introduced by considering a new strain variable $\underline{\underline{\epsilon}}^f$. This variable is defined as a part of the total strain tensor, the proportionality constant is assumed to be equal to the damage variable. Furthermore, $\underline{\underline{\epsilon}}^f$ can be interpreted as the homogenized contribution of the crack openings to the total strain in the RVE. Under these assumptions, the homogenized contribution of the crack openings is defined as follows:

$$\underline{\underline{\epsilon}}^f = d\underline{\underline{\epsilon}}^f \tag{2.49}$$

The following assumption is made on the time-evolution of $\underline{\underline{\sigma}}^f$ with respect to $\underline{\underline{\epsilon}}^f$:

$$\dot{\underline{\underline{\sigma}}}^f = \vartheta\left(\underline{\underline{\epsilon}}^f\right)\underline{\underline{\underline{\underline{C}}}} : \dot{\underline{\underline{\epsilon}}}^f \tag{2.50}$$

The function ϑ is chosen to be a scalar. In other words, the tangent modulus of the cracks stress/strain relation is proportional to the undamaged Hooke elastic tensor and can be controlled by the ϑ function. Therefore, ϑ represents the part of the stiffness lost due to cracking that is recovered thanks to crack closure, and can only take values ranging from 0 (when the

cracks are fully opened) to 1 (when cracks are fully closed). Since ϑ flows according to the material's loading state, it is considered to be dependent on $\underline{\underline{\epsilon}}^f$. Setting aside its physical meaning, ϑ can be considered as a numerical regularization of the multiple Signorini contact problem induced by crack closure. ϑ should then be defined to flow from 0 to 1 in a sufficiently regular way to avoid spurious discontinuities of the constitutive laws or of their (first at least) derivatives. As a function of $\underline{\underline{\epsilon}}^f$, the scalar nature of ϑ is obtained by means of a scalar indicator of this strain tensor. A simple indicator dependent on the sign of the loading is required, so as to observe stiffness recovery when switching from tension to compression. Therefore, the first invariant is used. The elastic part of the free energy associated to crack behavior is then written as:

$$\Psi^{f,e} = \int_0^T \left(\int_0^T \vartheta \left(I_1 \left(\underline{\underline{\epsilon}}^f \right) \right) \underline{\underline{\underline{\underline{C}}}} : \frac{d\underline{\underline{\epsilon}}^f}{dt} dt \right) \frac{d\underline{\underline{\epsilon}}^f}{dt} dt \tag{2.51}$$

where T is the final pseudo-time of the loading. In order to ensure that the free energy $\Psi^{f,e}$ is $\mathcal{C}^2$, ϑ should remain integrable. The explanation of hysteretic effects relying on the occurrence of frictional sliding at the cracks' surfaces justifies the use of a plasticity based approach to describe them. Using a framework based on perfect plasticity, the free energy Ψ^f is reduced to an elastic part $\Psi^{f,e}$ and introduces a single internal variable, the plastic strain accumulated through the internal sliding mechanism between cracks $\underline{\underline{\epsilon}}^{f,p}$, defined as $\underline{\underline{\epsilon}}^f = \underline{\underline{\epsilon}}^{f,e} + \underline{\underline{\epsilon}}^{f,p}$:

$$\begin{aligned} \Psi^f &= \Psi^{f,e} \left(\underline{\underline{\epsilon}}^f - \underline{\underline{\epsilon}}^{f,p} \right) \\ &= \int_0^T \left(\int_0^T \vartheta \left(I_1 \left(\underline{\underline{\epsilon}}^f - \underline{\underline{\epsilon}}^{f,p} \right) \right) \underline{\underline{\underline{\underline{C}}}} : \frac{d\left(\underline{\underline{\epsilon}}^f - \underline{\underline{\epsilon}}^{f,p} \right)}{dt} dt \right) \frac{d\left(\underline{\underline{\epsilon}}^f - \underline{\underline{\epsilon}}^{f,p} \right)}{dt} dt \end{aligned}$$

Assuming $\underline{\underline{\epsilon}}^{f,p}$ is purely deviatoric ($\mathbf{tr}\underline{\underline{\epsilon}}^{f,p} = 0$), Equation 2.52 becomes:

$$\Psi^f = \int_0^T \left(\int_0^T \vartheta \left(I_1 \left(\underline{\underline{\epsilon}}^f \right) \right) \underline{\underline{\underline{\underline{C}}}} : \frac{d\underline{\underline{\epsilon}}^f}{dt} dt \right) \frac{d\underline{\underline{\epsilon}}^f}{dt} dt - \frac{1}{2} \vartheta \left(I_1 \left(\underline{\underline{\epsilon}}^f \right) \right) \underline{\underline{\epsilon}}^{f,p} : \underline{\underline{\underline{\underline{C}}}} : \underline{\underline{\epsilon}}^{f,p} \tag{2.52}$$

and finally:

$$\Psi^f = \Psi^{f,e} \left(\underline{\underline{\epsilon}}^f \right) - \frac{1}{2} \vartheta \left(I_1 \left(\underline{\underline{\epsilon}}^f \right) \right) \underline{\underline{\epsilon}}^{f,p} : \underline{\underline{\underline{\underline{C}}}} : \underline{\underline{\epsilon}}^{f,p} \tag{2.53}$$

We can note that the contribution coming from the cracked areas to the total Helmholtz free energy Ψ has been built a posteriori, assuming a given state law linking $\dot{\underline{\underline{\sigma}}}^f$ with $\dot{\underline{\underline{\epsilon}}}^f$ a priori. This is a major feature of the proposed constitutive model to introduce the crack closure effect in a smooth way. The idea behind this was to control the tangent modulus $\frac{\partial \underline{\underline{\sigma}}^f}{\partial \underline{\underline{\epsilon}}^f}$ in order to ensure that its variation preserves $\mathcal{C}^1$ property of the stress/strain relation.

The potential of dissipation and the flow rules

According to the previous presentation of the thermodynamic state potential and the associated state laws, the flow of the three internal variables needs to be defined. The damage variable d and the related isotropic hardening variable z) are flow coupled. The third variable is the plastic strain $\underline{\underline{\epsilon}}^{f,p}$. Consequently, two distinct potentials of dissipation should be introduced. The isotropic damage mechanism and the associated hardening is based upon a Mazars-like failure criterion which is expressed in terms of strain energy rates:

$$f_d = \bar{Y} - (Y_0 + Z) \geq 0 \tag{2.54}$$

where Z stands for the thermodynamic force associated to z, $\bar{Y}$ is the energy rate $\bar{Y} = \frac{1}{2}E\epsilon_0\epsilon^{eq}$, written as a function of the Mazars equivalent strain $\epsilon^{eq} = \sqrt{\langle \underline{\underline{\epsilon}} \rangle_+ : \langle \underline{\underline{\epsilon}} \rangle_+}$, ϵ_0 is the elastic limit strain, and Y_0 is the elastic limit energy rate written in a similar manner: $Y_0 = \frac{1}{2}E\epsilon_0^2$. The asymmetry between traction and compression loading is only taken into account through its consequence on the peak load and the softening behavior of the material, and is introduced into the flow rule for the damage variable derived from the consolidation function H. Under these assumptions, the following flow rules are introduced:

$$\begin{cases} \dot{d} = \dot{\lambda}_d \dfrac{\partial f_d}{\partial \bar{Y}} = \dot{\lambda}_d \\ \dot{z} = \dot{\lambda}_d \dfrac{\partial f_d}{\partial Z} = -\dot{\lambda}_d \end{cases} \tag{2.55}$$

The hysteretic effects are described by means of the plastic strain $\underline{\underline{\epsilon}}^f$. In order to treat the nonlinearities related to this mechanism, a non-associative flow rule is assumed. Furthermore, this strategy makes it possible to ensure that $\underline{\underline{\epsilon}}^f$ is purely deviatoric. A Drucker–Prager criterion is chosen as the potential of dissipation:

$$f_{f,p} = J_2\left(\underline{\underline{\sigma}}^f\right) + \mu_0 I_1\left(\underline{\underline{\sigma}}^f\right) \geq 0 \tag{2.56}$$

where μ_0 is a material parameter which needs to be identified and which can be interpreted as a fiction coefficient. The pseudo-potential of dissipation is simply a Von Mises criterion:

$$\phi_{f,p} = J_2\left(\underline{\underline{\sigma}}^f\right) \tag{2.57}$$

The flow rule is expressed by considering the normality of the rate of the plastic strain with respect to the pseudo potential. Under these considerations, the flow rule has the following expression:

$$\dot{\underline{\underline{\epsilon}}}^{f,p} = \dot{\lambda}_{f,p} \frac{\partial \phi_{f,p}}{\partial \underline{\underline{\sigma}}^f} \tag{2.58}$$

where $\dot{\lambda}_{f,p}$ is the Lagrange multiplier related to the plastic strain, which can be computed from the consistency condition.

2.3 Concrete behavior: Critical review

In the previous sections, three different strategies allowing for the description of the cyclic response quasi-brittle materials behavior have been summarized. In the following, a comparison of the proposed approaches is presented.

2.3.1 Softening description, asymmetry between tension and compression, and regularization

Softening is one of the major consequences of cracking development. Within the framework of the proposed modeling strategies, isotropic continuum damage mechanics has been used in order to describe this phenomenon. More precisely, a scalar damage variable has been introduced to represent the progressive decrease of the RVE's elastic properties. As a consequence, a consolidation function has been used in order to define the way the damage variable evolves in time. Furthermore, it has been mentioned that the consistency conditions related to the damage could be integrated in closed form. Hence the damage variable remains explicit and therefore no implicit time-integration strategies have to be used. Expressions for the first derivative of

each consolidation function and the resulting damage variable are given in Tables 2.1 and 2.2, respectively. The strategies # 1, # 2 and # 3 correspond to those presented in Sections 2.2.2, 2.2.3 and 2.2.4, respectively.

Let us first focus on Table 2.1. In modeling strategy # 1, the first derivative of the consolidation is built as the sum of two contributions, each of them being characterized by a specific material parameter. This decomposition has been employed in order to describe the asymmetry between the tension response and the compression response. This is quite similar to the idea introduced in Mazars (1984), even though the driving variables are not the same. Even though a robust decomposition between the tension and compression can be realized this way, the case of a pure shear stress state leads to some issues due to the fact that the first derivative does not exist close to the origin. In the second strategy, the previous expression has been drastically simplified. In particular, a single contribution is employed. Indeed, this is consistent with the basic assumptions that motivated the development of strategy # 2 and which lie in considering damage only in the case of tension-dominated stress states. The asymmetry between tension and compression was described by a consolidation function dedicated to compression. Last, we can note that this expression is continuously differentiable and is characterized by a single material parameter. In the last modeling strategy (# 3), the expression is no longer a rational function, but is composed of a logarithmic function. Furthermore, we can observe the presence of an additional function κ. This function has been built for two reasons: (i) taking into account the confinement effect when dealing with compression stress states and (ii) allowing for a split between tension and shear. We can also note the smoothness of this expression with respect to the hardening variable z, except at $z = -1$, which is not an issue because this case corresponds to the limit of the damage variable, i.e., when it goes to 1.

Strategy	First derivative of the consolidation function $\frac{dH(z)}{dz}$
# 1	$\left(\frac{\mathcal{H}(<\underline{\underline{\epsilon}}>_+:<\underline{\underline{\sigma}}>_+)}{A_{Dir}} + \frac{1-\mathcal{H}(<\underline{\underline{\epsilon}}>_+:<\underline{\underline{\sigma}}>_+)}{A_{Ind}}\right)\frac{-z}{1+z}$
# 2	$\frac{1}{A_d}\frac{-z}{1+z}$
# 3	$\begin{cases} -\dfrac{\kappa}{B_0}\mathbf{ln}\left(\dfrac{Y_0}{\bar{Y}}(1+z)\right) \\ \kappa = 1 + k_0\left(\dfrac{<\underline{\underline{\underline{\underline{C}}}}:\underline{\underline{\epsilon}}>_-:<\underline{\underline{\underline{\underline{C}}}}:\underline{\underline{\epsilon}}>_-}{(\underline{\underline{\underline{\underline{C}}}}:\underline{\underline{\epsilon}}):(\underline{\underline{\underline{\underline{C}}}}:\underline{\underline{\epsilon}})}\right)^{\frac{1}{2}} \end{cases}$

Table 2.1: Closed-form expressions of the consolidation functions' first derivatives — # 1 = strategy presented in Section 2.2.2, # 2 = strategy presented in Section 2.2.3, # 3 = strategy presented in Section 2.2.4.

Closed-form expressions for the resulting damage variables are presented in Table 2.2. In strategy # 1, the damage variables are composed of two terms, each of them aiming at describing the softening in tension and in compression. The difference between the flow rates can be handled by setting the material parameters A_{Dir} and A_{Ind} to different values. In strategy # 2, the damage variable is bounded by 1. However, a unique flow rate can be used since a single parameter A_d has been introduced for the reasons explained in the previous paragraph. An important feature of the expressions considered in the first two strategies is the fact that the fracture energy-like term $\int_{t_0}^{\infty} \underline{\underline{\sigma}} : \underline{\underline{\dot{\epsilon}}} dt$ (t_0 stands for the localization pseudo-time) does not converge towards a finite value. In other words, a fracture energy-based regularization Hillerborg *et al.* (1976) can not be used in the first two approaches in order to reduce the mesh-dependency effects. Averaging techniques, such as the non-local approach Pijaudier-Cabot et Bazant (1987) or the second-order gradient

Peerlings *et al.* (1996); De Borst *et al.* (1996), have to be used. Despite the fact that the use of these techniques is possible, they usually induce a drastic increase in the computational time when dealing with non-linear analysis, which limits the possiblities for large-scale computations. This is the main reason why slight modifications have been considered in strategy # 3. Indeed, the presence of the exponential functions makes the fracture energy-like term bounded, and so the generalized integral converges towards a finite value. An energy-based regularization can be used, by making the parameter B_0 dependent on a characteristic length of the finite elements.

Strategy	Damage variable d
# 1	$1 - \frac{1}{1+\left(A_{Dir}\mathcal{H}(<\underline{\underline{\epsilon}}>_+ : <\underline{\underline{\sigma}}>_+) + A_{Ind}(1-\mathcal{H}(<\underline{\underline{\epsilon}}>_+ : <\underline{\underline{\sigma}}>_+))\right)\left(\bar{Y}-Y_0\right)}$
# 2	$1 - \frac{1}{1+A_d(\bar{Y}-Y_0)}$
# 3	$1 - \frac{Y_0}{\bar{Y}}\mathbf{exp}\left(-\frac{B_0}{\kappa}(\bar{Y}-Y_0)\right)$

Table 2.2: Closed-form expressions for the damage variables — # 1 = strategy presented in Section 2.2.2, # 2 = strategy presented in Section 2.2.3, # 3 = strategy presented in Section 2.2.4.

2.3.2 Material parameters and identification

In this section, we focus on the sets of material parameters needed for each modeling strategy introduced in the previous sections. They are presented in Table 2.3 for each constitutive model. For all constitutive laws, two parameters are needed to describe the linear elasticity region, namely Young's modulus and the Poisson ratio. They can be identified by fitting the initial modulus of the experimental uniaxial response in compression. In addition, a single parameter is needed to define the initial threshold surface in tension. In the case of the first two strategies, this parameter is the initial energy rate Y_0, whereas in the case of the third one, it is expressed as a limit strain ε_0. However, both parameters can be linked with the tension strength, which can be identified from either characterization tests or empirical formulae in which the tension strength may be estimated from the compressive strength measured at 28 days. We can note that the second modeling strategy involves a threshold in compression f_c. This threshold does not correspond to the compressive strength (defined at the peak stress in compression) but should be understood as the initial threshold that has to be overcome in compression to activate damage. Its identification is not straightforward: a full uniaxial response is needed. However, it allows controlling the peak stress in compression, which may be an interesting feature.

The fracture energy can be controlled, in a more or less simple way, in all modeling strategies. The related parameters allow for defining the brittleness of the post-peak branch. For instance, in the case of the first two approaches, the parameters A_{Dir} and A_d play this role. Nevertheless, it is important to keep in mind that no direct relation can be found between these parameters and the fracture energy, based upon the considrations presented in Section 2.3.1. In the case of the third modeling approach, the parameter B_0 can be linked with the fracture energy through a closed form expression. Similar parameters are also introduced in the case of the first two strategies to control the dissipated energy in compression, namely A_{Ind} and (α_f, β_f). All these parameters can be identified thanks to the knowledge of the fracture energy, at least in tension. However, based on our experience, it is better to identify them by fitting the load/displacement curve of a bending test performed on a notched concrete beam. This strategy allows taking into account the finite element mesh size in the identification procedure, otherwise a regularization technique has to be used.

The last set of parameters is related to the control of the hysteretic dissipation. In the case of the first two approaches, two parameters are needed, (a, γ), whereas in the case of the third approach, a single parameter should be identified μ_0. Their identification procedure is not straightforward at all, due to the experimental difficulties when dealing with the cyclic test's being tension-dominated. A promising approach lies in downscaling the identification step by considering a refined numerical description of the RVE. In other words, assuming that an efficient and predictive model is available at a lower scale, the experimental tests can be carried out virtually. The outputs can then be used to complement the experimental results coming from the mechanical tests. This aspect is discussed and illustrated in Section 3.2.1. In addition, this approach can be used to identify the parameters controlling the biaxial response of the RVE.

Strategy	Symbol	Meaning
# 1	E	Young modulus
	ν	Poisson ratio
	Y_0	Energy rate threshold to activate damage
	A_{Dir}	Brittleness in tension
	A_{Ind}	Brittleness in compression
	β	Confinement effects
	a	Hysteretic effects
	γ	Hysteretic effects
# 2	E	Young modulus
	ν	Poisson ratio
	Y_0	Energy rate threshold to activate damage
	A_d	Brittleness in tension
	a	Hysteretic effects
	γ	Hysteretic effects
	f_c	Compressive strength
	α_f	Threshold surface in compression
	α_ϕ	Threshold surface in compression
	a_R	Brittleness in compression
	b_R	Brittleness in compression
# 3	E	Young modulus
	ν	Poisson ratio
	ε_0	Strain threshold to activate damage
	B_0	Brittleness in tension
	k_0	Confinement effects
	μ_0	Hysteretic effects

Table 2.3: Sets of material parameters — # 1 = strategy presented in Section 2.2.2, # 2 = strategy presented in Section 2.2.3, # 3 = strategy presented in Section 2.2.4.

2.3.3 Main features

In this section, some features of the three modeling strategies are presented. To illustrate them, some local tests have been carried out and the results are compared and discussed.

Unilateral effect

The first aspect highlighted is related to the ability of the constitutive laws to describe the crack closure effect. Cyclic tension/compression tests have been simulated at the integration point

level. The results are presented in Figure 2.1. In the case of the first approach, we can observe the inability of the constitutive law to capture this effect. Indeed, coming back to Equation 2.14, the stiffness recovery is ensured only in the bulk modulus. Indeed, the Coulomb modulus is not recovered at all. The results shown in Figure 2.1a allow concluding that this simple strategy is not sufficient to account for this effect. The results obtained by the second strategy are shown in Figure 2.1b. Both the hysteretic loops and the progressive crack closure effect are described when switching from tension to compression. However, the resulting stress/strain response is not smooth at all, leading to numerical issues in the local time-integration algorithm. These results confirm the necessity of including a closure function in order to properly control the crack closure effect, as proposed by LaBorderie (1991) within a uniaxial framework. The results obtained with the last strategies are shown in Figure 2.1c. We can observe the smoothness of the stress/strain response when the cracks are closing. In addition, the hysteretic loops are in better agreement with the experimental ones from a qualitative point of view.

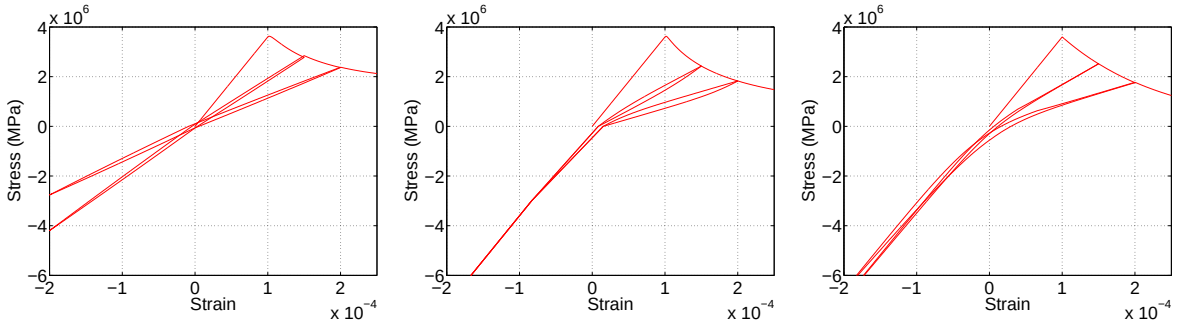

(a) Strategy # 1. (b) Strategy # 2. (c) Strategy # 3.

Figure 2.1: Control of the crack closure effect — uniaxial cyclic tension loading path.

Uniaxial complex loading path

The second aspect we focused on is the stress/strain response when dealing with a tension/compression loading path. Due to the limitations of strategy # 1 in describing the crack closure effect, the results coming from this constitutive law are not presented in what follows. However, we can mention that this type of loading path can be handled by this first strategy if the damage level remains low. The results obtained with the modeling approaches # 2 and # 3 are presented in Figures 2.2a and 2.2b respectively. The results are quite similar. However, the stress/strain relation is (i) smoother in the case of the third strategy than in the case of the second and (ii) the nonlinearities in compression observed in the case of the third modeling strategy are a consequence of the formulation. Indeed, no specific attention has been paid to describing nonlinearities in compression. The main experimental features of concrete-like materials subjected to cyclic loadings are quite well described by both approaches but the smoothness of the stress/strain relation observed in the case of strategy # 3 drastically improves the numerical robustness of the time-integration algorithm.

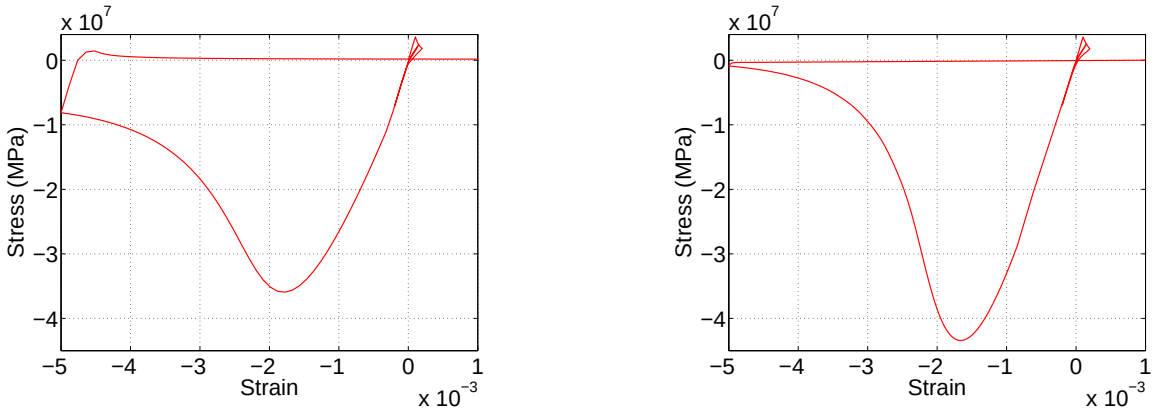

(a) Strategy # 2. (b) Strategy # 3.

Figure 2.2: Uniaxial tension/compression loading path.

Biaxial response

The last aspect discussed in this section is related to the ability of the constitutive laws to describe the biaxial response of a concrete-like material RVE. The results are presented in Figure 2.3. In the case of the first approach, the failure surface is quite smooth but the shear strength is overestimated. This can be explained by the fact the consolidation function associated with the isotropic hardening does not allow an accurate control of the shear response. In contrast, the consolidation function considered in the third strategy allows overcoming this drawback, as we can observe in Figure 2.3c. The biaxial response related to the second strategy is presented in Figure 2.3b. The overall shape is in quite good agreement with the experimental measurements but some singular points can be noted. This is due to the way of splitting the tension contribution from the compression one. This feature leads to convergence difficulties. In the case of the third modeling strategy, the failure surface fits well the experimental observations in the tension and shear regions ($k_0 = 3$). Nevertheless, the case of a pure compressive loading state is not well described. Indeed, we did not pay specific attention to taking it into account. In addition, trying to achieve such an objective by keeping the damage variable a scalar may not reasonable.

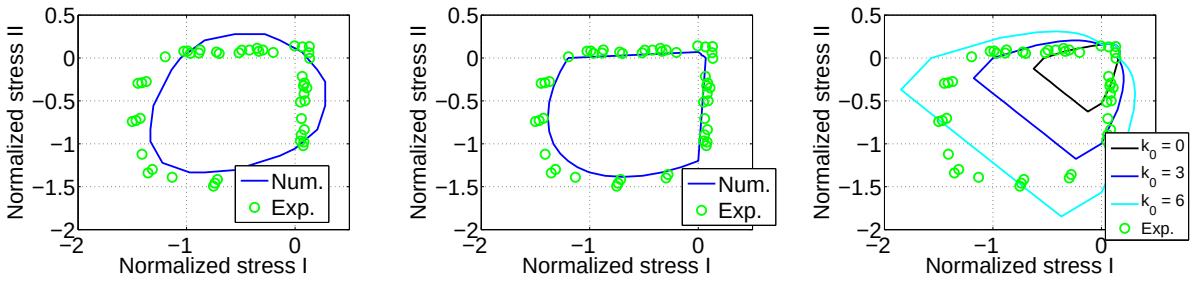

(a) Strategy # 1. (b) Strategy # 2. (c) Strategy # 3.

Figure 2.3: Biaxial response — experimental data from Kupfer et Gerstle (1973).

2.4 Steel/concrete interface behavior

2.4.1 Full 3D approach

Driving ideas

In the case of reinforced concrete structures, the interface between the steel and the concrete is a specific location where dissipative mechanisms may occur during a degradation process. Taking them into account when making a structural assessment is of primary importance because they influence the load transfer from the concrete to the steel. If the load transfer is full (perfect interaction) then all the internal loads which are in the concrete domain are balanced by the internal load which appears in the steel domain. But if the load transfer is only partial, then only a part of the internal loads which are in the concrete domain are balanced by those appearing in the steel domain Reinhardt et Balazs (1995). In this latter case, local cracking features such as crack spacing or openings will be influenced. It is therefore necessary to take into account the specific behavior of the steel/concrete interface when a refined structural assessment is aimed at. On the other hand, the steel/concrete interface may be the location where phenomena coming from the interaction between a reinforced concrete structure and the external environment develop. As an example, we can mention the case of corrosion of the steel reinforcing bars, which is one of the most critical pathologies faced by existing reinforced concrete structures. Among the dissipative mechanisms which appear when corrosion is developing, we can mention the creation of rust products that exhibit a trend to swell. Therefore, tensile stresses appear and increase over time, leading to the development of cracking from the steel to the concrete cover. Within such a framework, it is clear that appropriately modeling the steel/concrete interface is necessary.

Experimental evidence has shown that the steel/concrete interface could be damaged by means of two major mechanisms: mode I (local opening) and mode II (frictional sliding) Eligehausen *et al.* (1982). The first mechanism may appear when the reinforced concrete component works close to its failure state, i.e., macrocracks are opened. This mechanism also appears in the presence of corrosion, when the process has reached an advanced stage characterized by an important amount of rust products. The second mechanism appears as soon as the reinforcing bar is (at least locally) subjected to a tension stress state. Furthermore, these mechanisms may be considered as being coupled. Indeed, the mode II mechanism will be influenced by whether the steel is in contact with the surrounding concrete or not. This latter mechanism is also influenced by the radial stress state, which can either improve the peak stress or decrease it, depending on the nature of the radial stress (tension or compression) Nguyen *et al.* (2011).

From the aforementioned presentation, it appears that three mechanisms should be taken into account in order to reach a statisfactory description of the steel/concrete interface in the presence of corrosion. In addition, not only because these mechanisms have specific directions but also because the interface between the steel and concrete has no physical dimension, a dedicated numerical framework should be used. With the aim of proposing a refined steel/concrete interface constitutive model, we have made the choice to consider a degenerate kinematics that is compatible with zero-thickness finite elements technology. Within this framework, the constitutive law will be expressed in terms of a traction vector and relative displacements.

Constitutive equations

Uncorroded steel/concrete interface The formulation of the set of consitutive equations is inspired from both the framework presented in Section 2.2.2 and the earlier Ragueneau *et al.* (2006). In this paragraph, no corrosion is considered: we focus on the mechanical part of the

constitutive model. Equation 2.13 may be reformulated in terms of a traction vector and relative displacement vector as follows:

$$\begin{aligned}\rho\Psi =& \frac{K_n}{2}((1-d) < u_n >_+^2 + < u_n >_-^2) + \\ & (1-d)\boldsymbol{u_t}.\boldsymbol{K_t}.\boldsymbol{u_t} + d(\boldsymbol{u_t} - \boldsymbol{u_t^\pi}).\boldsymbol{K_t}.(\boldsymbol{u_t} - \boldsymbol{u_t^\pi}) + H(z) + \frac{\gamma}{2}\boldsymbol{\alpha}.\boldsymbol{\alpha}\end{aligned} \tag{2.59}$$

where K_n is the stiffness in the normal direction, u_n the relative displacement in the normal direction, $\boldsymbol{u_t}$ the relative displacement vector in the tangential direction, $\boldsymbol{u_t^\pi}$ the sliding displacement vector, $\boldsymbol{K_t}$ the stiffness matrix in the orthnormal directions, and $\boldsymbol{\alpha}$ the kinematic hardening variable. Some state laws can be derived from Equation 2.59 quite straightforwardly:

$$\begin{cases} t_n = \dfrac{\partial\rho\Psi}{\partial u_n} = K_n((1-d) < u_n >_+ + < u_t >_-) \\ \boldsymbol{t_t} = \dfrac{\partial\rho\Psi}{\partial \boldsymbol{u_t}} = 2(1-d)\boldsymbol{K_t}.\boldsymbol{u_t} + 2d\boldsymbol{K_t}.(\boldsymbol{u_t} - \boldsymbol{u_t^\pi}) \end{cases} \tag{2.60}$$

In addition, the thermodynamical forces in connection with both isotropic and kinematic hardening can be defined as follows:

$$\begin{cases} Z = \dfrac{\partial\rho\Psi}{\partial z} = \dfrac{dH(z)}{dz} \\ \boldsymbol{X} = \gamma\boldsymbol{\alpha} \end{cases} \tag{2.61}$$

The potentials of dissipation which allow handling the activation of both the damage and frictional sliding mechanisms can now be introduced. The first one is related to the damage and has been chosen as follows:

$$f_d = \alpha_0 Y_n^+ + Y_t - (Z_0 + Z) \geq 0 \tag{2.62}$$

where α_0 is a material parameter which allows for the definition of the relative importance of the damage in the normal direction compared to the damage in the orthonormal directions, Y_n^+ is the rate of energy released in mode I, and Y_t is that for mode II. Both rates are defined as follows:

$$\begin{cases} Y_n^+ = \dfrac{K_n}{2} < u_n >_+^2 \\ Y_t = 2\boldsymbol{u_t}.\boldsymbol{K_t}.\boldsymbol{u_t} \end{cases} \tag{2.63}$$

Consider the following expression for the consolidation function:

$$H(z) = \frac{1}{A_d}(-z + \mathbf{ln}(1+z)) \tag{2.64}$$

where A_d is a material parameter which allows setting up the post-peak brittleness (i.e., the softening branch). Summing the associative flow rules for damage and isotropic hardening, a closed form expression for the Lagrange multiplier related to the damage can be obtained. After some analytical computations, the damage can be expressed as follows:

$$d = 1 - \frac{1}{1 + A_d(\alpha_0 Y_n^+ + Y_t - Z_0)} \tag{2.65}$$

The frictional sliding mechanisms are treated according to the considerations presented in Section 2.2.2. The potential of dissipation takes the following form:

$$f_\pi = || \boldsymbol{t_t} - \boldsymbol{X} || + c < t_n >_- \geq 0 \tag{2.66}$$

where c is a material parameter allowing setting up the effect coming from the confinement. Assuming a non-associative flow in order to treat the nonlinearities related to the frictional sliding, the following pseudo-potential of dissipation is considered:

$$\phi_\pi = f_\pi + \frac{a}{2}\boldsymbol{X}.\boldsymbol{X} \tag{2.67}$$

Now the flow rules related to the frictional mechanism can be derived:

$$\begin{cases} \dot{\boldsymbol{u}_t^\pi} = \dot{\lambda}_\pi \dfrac{\partial \phi_\pi}{\partial \boldsymbol{t_t^\pi}} \\ \dot{\boldsymbol{\alpha}} = \dot{\lambda}_\pi \dfrac{\partial \phi_\pi}{\partial \boldsymbol{X}} \end{cases} \tag{2.68}$$

Corroded steel/concrete interface With the aim of including the effects related to corrosion, the constitutive framework presented previously has been enhanced. But first, it is necessary to frame the developments in order to clarify the additional set of variables to be introduced. Among the complex effects induced by corrosion, we focus only on those which take place at the steel/concrete interface. In other words, the influence of corrosion on the concrete and steel is not considered.

The quantification of the phenomenon of corrosion requires the definition of a macroscopic variable which characterizes the corrosion state for a given time t Fang *et al.* (2004). Therefore, the mapping $t \mapsto T_c(t)$ is assumed to be known. Among the possibilities offered in the literature to define the corrosion degree, the most used lies in considering the reduction of the steel cross section or the overall mass loss. Both possibilities may be found. Within the framework of our research, two mechanisms characterizing the phenomenon of corrosion are considered. First, it is necessary to describe the swelling related to the expansive nature of the rust products, which will lead to the development of cracking in the concrete around the reinforcing bar. To this end, a dedicated variable u_n^r is introduced. In addition, experimental obervations have pointed out that the rust products behave like a granular material, i.e., their normal stiffness increases when subjected to compression Zandi Hanjari *et al.* (2011). This aspect has also been taken into account by making the elastic parameters dependent on the void density through a modified Needlman–Tvergaard–Gurson criterion Needlemann (1988). Secondly, rust products lead to the modification of the frictional properties at the steel/concrete interface. In order to take these into account, a natural way lies in modifying the damage variable characterizing the degradation state at the steel/concrete interface according to the value of the macroscopic corrosion degree.

Based upon the aforementioned considerations, the state potential expressed by Equation 2.59 has been enhanced as follows:

$$\begin{aligned} \rho\Psi = &\frac{K_n}{2}((1-d) < u_n >_+^2 + \underbrace{< u_n - u_n^r >_-^2}_{Compacting\ character}) + 2(1-d)\boldsymbol{u_t}.\boldsymbol{K_t}.\boldsymbol{u_t} + \\ &2d(\boldsymbol{u_t} - \boldsymbol{u_t^\pi}).\boldsymbol{K_t}.(\boldsymbol{u_t} - \boldsymbol{u_t^\pi}) + H(z) + \frac{\gamma}{2}\boldsymbol{\alpha}.\boldsymbol{\alpha} + \underbrace{K_n u_n < u_n^r(t_0) >_+}_{Swelling} \end{aligned} \tag{2.69}$$

where t_0 is the duration of the corrosion, which is linked with the macroscopic corrosion degree. It is important to note that two time-scales are considered: one related to the corrosion

phenomenon and another related to the mechanical effects (degradation process). The corresponding state laws can be derived as follows:

$$\left\{\begin{array}{rl} t_n = \dfrac{\partial \rho \Psi}{\partial u_n} = K_n((1-d) < u_n >_+ + < u_n - u_n^r >_-) \\ \boldsymbol{t_t} = \dfrac{\partial \rho \Psi}{\partial \boldsymbol{u_t}} = (1-d)\boldsymbol{K_t}.\boldsymbol{u_t} + d\boldsymbol{K_t}.(\boldsymbol{u_t} - \boldsymbol{u_t^\pi}) \\ t_n^r = -\dfrac{\partial \rho \Psi}{\partial u_n^r} = K_n < u_n - u_n^r >_- \end{array}\right. \tag{2.70}$$

The way to treat the displacement related to the rust products has been determined in order to describe the fact that they become stiffer when subjected to a compressive stess state. To reach this objective, a modified Needlman–Tvergaard–Gurson criterion is introduced. Taking into account the fact that u_n^r acts in the normal direction, the following expression is obtained:

$$f_r = 2q_1 f^\star \mathbf{ch}(q_2 \frac{t_n^r}{2t_M}) - (1 + (q_3 f^\star)^2) \tag{2.71}$$

where q_1, q_2 and q_3 are material parameters, t_M a hardening variable, and $f^\star$ an internal variable which may be interpreted as the void density. Three complementary equations should now be introduced in order to treat the flow of the void density, the hardening variable, and the normal displacement of the rust products:

$$\left\{\begin{array}{r} \dot{u}_n^r = \dot{\lambda}_r \dfrac{\partial f_r}{\partial t_n^r} \\ \dot{u}_M = \dot{\lambda}_r \dfrac{\partial f_r}{\partial t_M} \\ \dot{f}^\star = k(1-f^\star) < \dot{u}_n^r >_- \end{array}\right. \tag{2.72}$$

The hardening law is defined as follows:

$$\left\{\begin{array}{ll} t_M = K_n u_M & \text{if} \quad t_M \leq t_M^0 \\ t_M = t_M^0 \left(\dfrac{K_n u_M}{t_M^0}\right)^{\frac{1}{n}} & \text{if} \quad t_M > t_M^0 \end{array}\right. \tag{2.73}$$

where t_M^0 is an initial threshold. The elastic properties K_n and $\boldsymbol{K_t}$ are made dependent on the void density in order to describe the fact they increase with the intensity of the loading in compression. Assuming a Poisson ratio equal to 0.2, The Mori–Tanaka homogenization scheme provides a closed form expression for the homogenized elastic parameters:

$$\left\{\begin{array}{r} K_n(f^\star) = \dfrac{1-f^\star}{a_1 + a_2 f^\star} \\ \boldsymbol{K_t}(f^\star) = \boldsymbol{K_t} \dfrac{1-f^\star}{a_3 + a_4 f^\star} \end{array}\right. \tag{2.74}$$

where $(a_i)_{i=1,\cdots,4}$ are material paremeters which allow setting up the range of variation of the elastic parameters.

The second effect taken into account is related to the fact that rust production lead to the modification of the properties of the steel/concrete interface and therefore of the degradation state of the steel/concrete variable. To take this into account, the potential of dissipation related to the damage has been enhanced as follows:

$$f_d = \alpha_0 Y_n^+ + Y_t - (Z_0 + Z + W) \geq 0 \tag{2.75}$$

where W is a function of the macroscopic corrosion degree, to be identified. Based upon similar considerations as those presented previously, the damage variable becomes

$$d = 1 - \frac{1}{1 + A_d(\alpha_0 Y_n^+ + Y_t - (Z_0 + W))} \tag{2.76}$$

Numerical examples

Local considerations In Figure 2.8a, the response of the proposed constitutive model with respect to the tangential direction is presented. Various simulations at the Gauss point level, for several lateral pressures, have been performed. An increase of the peak value of the shear stress can be noted. This feature has been widely observed experimentally Eligehausen *et al.* (1983); Lundgren (2001). Figure 2.8b highlights the response when mode I occurs at the steel/concrete interface. It can be noted that the peak value is almost 50% lower than that in the tangential direction (without any lateral pressure), which is in accordance with the results obtained by Dominguez (2005). This property is important when swelling occurs at the interface. It is possible to exhibit it because the asymmetrical Drucker–Prager criterion is used. Moreover, it is not rare that local opening happens when pull-out tests are performed. As a consequence, the way of controlling the asymmetry between the mechanical responses in modes I and II is crucial in order to ensure the accuracy of the underlying structural analysis. To move forward, some features of the proposed steel/concrete interface constitutive model in a corroded condition are shown in Figures 2.4c and 2.4d. Figure 2.4c depicts the response in the normal direction when an imposed pressure at the steel/concrete interface is applied. This analysis focused on the normal direction response and not on the tangential direction. It can be observed that the stiffness increases, as was to be expected. Some experimental data have been reported in order to show the relevancy of the approach. The local mechanisms occuring at the interface, which explain the non-monotonic evolution of the residual bond capacity with respect to the the corrosion degree, are still not fully understood in a clear way. A comparison between simulations at the Gauss point level and local measurements from Sulaimani *et al.* (1990) is presented in Figure 2.4d and a good agreement can be highlighted. However, it must be said that this latter result should not be understood as a demonstration of the predictive capability of the proposed steel/concrete interface model but as a demonstration of the possibility of describing the refined mechanisms occuring at the steel/concrete interface with corrosion. Indeed, the predictive ability of the constitutive model greatly depends on the availability of experimentaml data to properly identify the material parameters.

Structural case study In order to illustrate the capabilities of the proposed steel/concrete interface constitutive model, a structural case study at the member scale is shown in the following. The experimental campaign carried out by Nguyen *et al.* (2007) has been considered. This experimental campaign was chosen because the specific effects related to the corrosion phenomenon have been studied separately. On the one hand, the consequences of the reduction in the steel cross section have been analyzed and, on the other hand, the influence of the modification of the bond properties in connection with cracking have been studied. To reach this objective, the corrosion was created artificially by prescribing a current density considering two conditions: (i) before and (ii) after the concrete casting. This strategy allows avoiding accounting for the effect associated with the swelling of the corrosion products and therefore, getting rid of the cracking. Once the reinforced concrete specimens were corroded, they were subjected to a four-point bending loading in order to assess their bearing capacity. As a consequence, we can state that the full loading sequence had two different stages: (i) corrosion followed by (ii) a four-point bending loading. In addition, several reinforced concrete beams were tested, allowing the assessment of the evolution of the bearing capacity with respect to the corrosion degree.

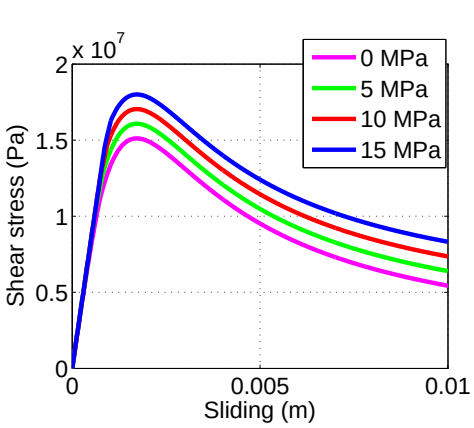

(a) Confinement sensitivity.

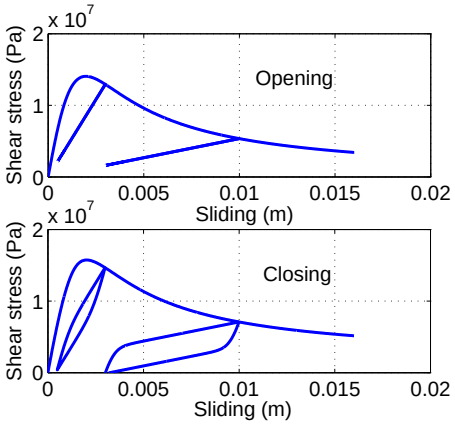

(b) Asymmetry between modes I and II.

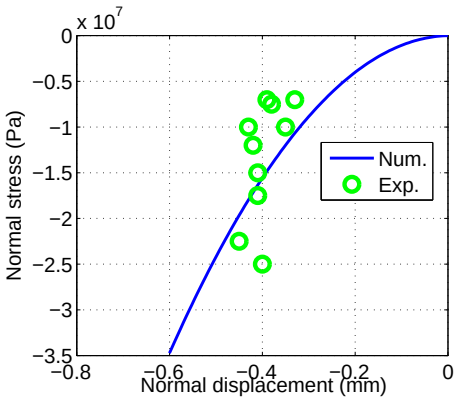

(c) Stiffness increase of the rust products.

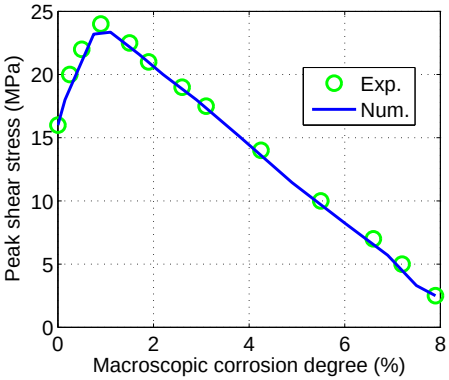

(d) Peak shear stress evolution due to corrosion.

Figure 2.4: Steel/concrete interface constitutive law — local results.

The finite element mesh is shown in Figure 2.5. Due to the employment of a zero-thickness finite element technology to implement the steel/concrete interface constitutive model, both the concrete and steel had to be discretized three-dimensionally. Both the stirrups and longitudinal reinforcing bars have been meshed because corrosion developed around them. Zero-thickness finite elements have been put between the steel bars and the surrounding concrete. In addition, elastic platens have been included in the finite element model in order to avoid spurious effects close to the boundaries. In the central part of the beam, we can note that the sturrups were cut off. Despite the fact that this choice does not represent any civil engineering design practices, it has been made in order to ensure a uniform corrosion distribution on the lower longitudinal steel bars. This way, no interaction with the stirrups can occur. The mechanical behavior of the concrete has been described by the constitutive model presented in Section 2.2.4, and that for the steel by the well-known Menegotto–Pinto constitutve model Menegotto (1973). Among the available experimental results, we have focused on the case where the corrosion is created after the concrete casting.

The nonlinear analysis was performed with the finite element software Cast3M CEA-Cast3M (2016). The damage patterns after corrosion and after applying the four-point bending test are shown in Figures 2.6 and 2.7 respectively. In accordance with the experimental setup, only the lower reinforcing bars were artificially corroded. We can note a progressive development of the damage around the bars with the increase of the macroscpic corrosion degree. In addition, it is interesting to note that cracking appears close to the steel anchorages. Despite the fact that

this effect was expected, it helps in understanding why corrosion leads to a loss of ductility. The damage patterns obtained after applying the mechanical loading are consistent with the experimental observations. The cracking is rather uniform in the constant bending moment area, and becomes directional in the shear dominated areas, close to the supports.

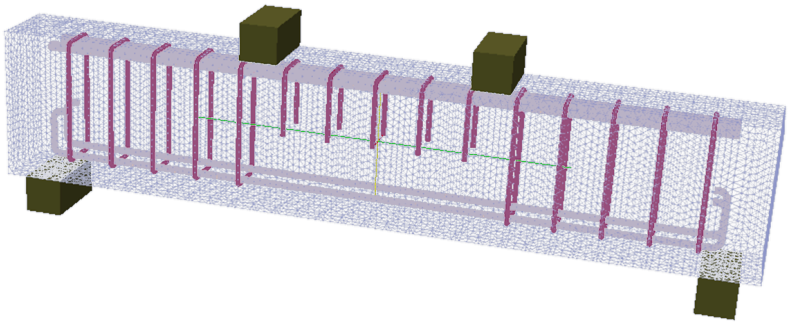

Figure 2.5: Finite element mesh — reinforced concrete beam.

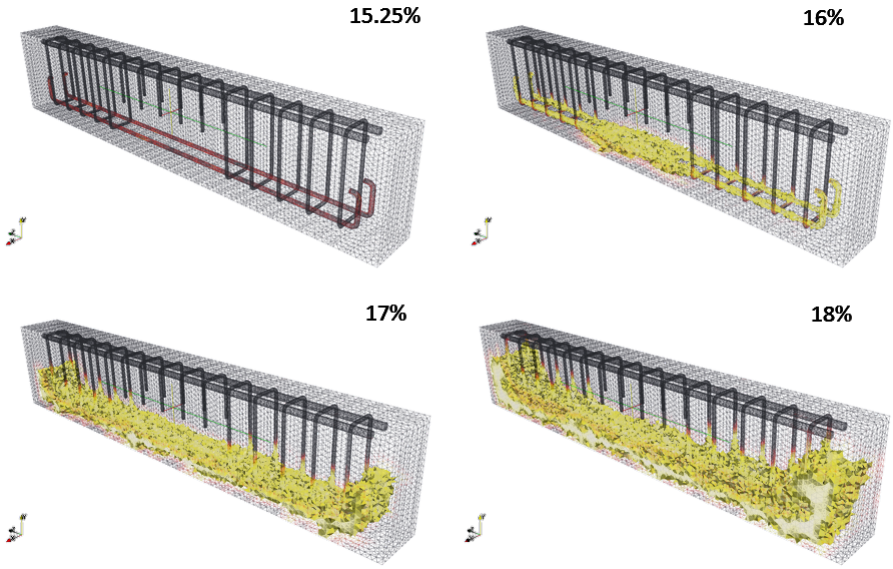

Figure 2.6: Damage pattern — after corrosion and before the mechanical loading for different corrosion degrees.

In order to analyze the consequences of corrosion on both (i) the load transfer between the concrete and steel and (ii) the evolution of the bearing capacity, more quantitative results were looked for. Especially, the variations of the load/midspan displacement curve with respect to the macroscpic corrosion degree are prsented in Figure 2.8a. On the one hand, we can observe the progressive decrease of the elastic stiffness and the decrease of the bearing capacity. Both effects were in accordance with the experimental observations. However, as shown in Figure 2.8a, a local steel failure appeared during the experiment. This effect could not be reproduced because the steel constitutive model used did not include a local failure criterion. The load transfer has been analyzed by observing the stress distributions along both the upper and lower reinforcing bars. As shown in Figure 2.8b, we can note that the stress in the upper steel bars is rather constant in the central part of the specimen whereas the maximum stress decreases drastically in the lower steel bars. This effect may be explained by the fact that corrosion decreases the bond properties at the steel/concrete interface, leading naturally to the unloading of the corroded rebars.

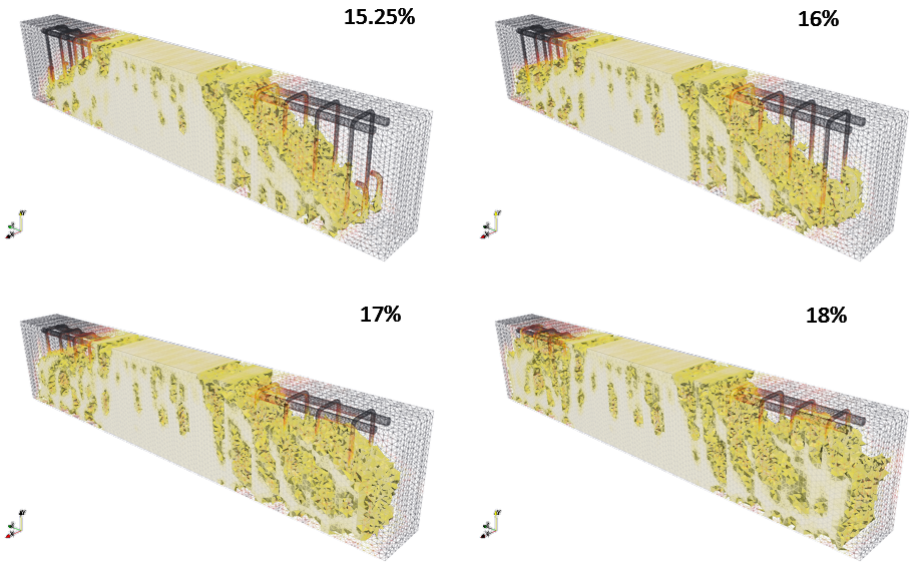

Figure 2.7: Damage pattern — after corrosion and after the mechanical loading for different corrosion degrees.

2.4.2 Simplified approach

Driving ideas

In Section 2.4.1, a set of constitutive equations allowing the description of the mechanical behavior of the steel/concrete interface with or without corrosion has been presented. The aim of this research was to build a constitutive model allowing refined and accurate structural assessments of reinforced concrete structures. To reach this goal, a dedicated finite element technology has been used, consisting in zero-thickness finite elements. Despite the fact that this strategy allows the explicit definition of a steel/concrete interface domain, it may lead to difficulties when meshing. Indeed, this strategy requires meshing the steel reinforcing bars in an explicit way, and generally leads to time consuming analyses. In order to overcome the aforementioned drawbacks, we explored the possibility of studying the steel/concrete interface in a way compatible with the use of simplified finite element technologies, such as the multifiber approach Taucer *et al.* (1991); Spacone *et al.* (1996); Neuenhofer et Filippou (1997).

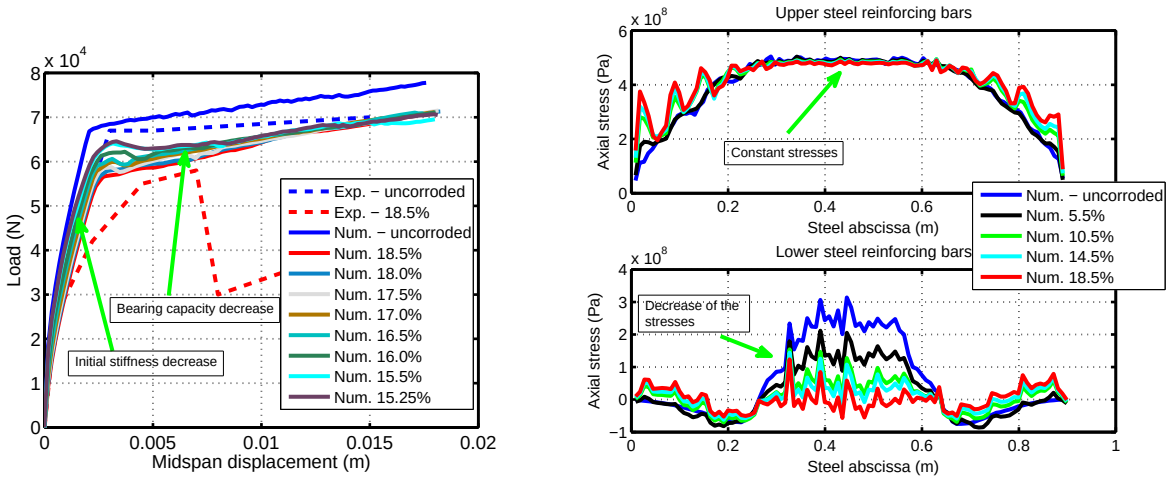

(a) Load/midspan displacement curve

(b) Axial stresses in the rebars

Figure 2.8: Local and structural responses after the four-point bending tests.

In addition, we made the choice to keep the strategy light in terms of numerical implementation. As a consequence, we decided not to go to kinematic enhancement based approaches although they might lead to satisfactory results.

The multifiber approach is based upon Timoshenko kinematics. Two discretization levels are introduced: the first one lies in describing the beam itself whereas the second lies in describing the cross section. The link between both levels is ensured thanks to load/stress relations coming from the well-known beam theory. At the cross section level, nonlinear constitutive laws can be taken into account. However, constitutve operators have to be projected in specific directions in order to be compatible with the Timoshenko kinematics. Within the framework of reinforced concrete structures modeling, two types of constitutive laws are generally considered at the cross section level: one related to the concrete and one related to the steel. As we made the choice not to go to kinematic enhancement based approaches for the sake of computational efficiency, the only degrees of freedom we have to take into account for the steel/concrete interface lies in modifying the aforementioned constitutive laws. Modifying the concrete constitutive law does not seem meaningful because the location of the steel/concrete interface remains somehow fuzzy. Hence, we introduced a strategy to take it into account in the steel constitutive law.

The essence of our proposal lies in its assumptions on the load transfer mechanism between the concrete and the steel reinforcing bars. Considering a given loading, we assume that the load in the rebar is balanced by frictional stresses at the steel/concrete interface. In the numerical description of the steel/concrete interface with corrosion, due to the kinematic assumptions related to the multifiber approach, the swelling that has been taken into account in the full three-dimensional constitutive model is not in the proposed simplified strategy.

Numerical strategy

Describing the partial interaction between the concrete and the steel means the existence of a frictional sliding. In other words, the strain in the steel ε_S may be expressed as follows:

$$\varepsilon_S = \underbrace{\eta\varepsilon_S}_{Steel\ contribution} + \underbrace{(1-\eta)\varepsilon_S}_{Interface\ contribution} = \varepsilon_S^A + \varepsilon_S^I \tag{2.77}$$

where η is a partition factor, $\varepsilon_S^A = \eta\varepsilon_S$ is the steel contribution, and $\varepsilon_S^I = (1-\eta)\varepsilon_S$ is the steel/concrete interface contribution. As a new unknown has been introduced, it is necessary to use an additional equation to determine it. This equation should express the load balance between the steel and concrete. It can be expressed as follows:

$$\int_{S(x)} \sigma^A dS - l_c \int_{\partial S(x)} \tau^I d\Gamma = 0 \tag{2.78}$$

where $S(x)$ is the cross section of the beam element at the abscissa x, l_c the anchorage length (allowing setting the relative weight of the contributions of the steel and the concrete), τ the frictional stress at the steel/concrete interface, and $\partial S(x)$ the boundary of the steel bar. Denoting by $\mathcal{L}^A$ and $\mathcal{L}^I$ the constitutive operators allowing the computation of the stress in the steel σ^A and in the steel/concrete interface τ^I, Equation 2.78 becomes:

$$\int_{S(x)} \mathcal{L}^A(\varepsilon_S, \eta) dS - l_c \int_{\partial S(x)} \mathcal{L}^I(\varepsilon_S, \eta) d\Gamma = 0 \tag{2.79}$$

Assuming a constant strain ε_S and a constant partition factor over the finite element, Equation 2.79 can be analytically integrated:

$$\mathcal{L}^A(\varepsilon_S, \eta) S(x) - l_c \mathcal{L}^I(\varepsilon_S, \eta) P(x) = 0 \tag{2.80}$$

where $S(x)$ and $P(x)$ are, respectively, its cross-sectional area and its perimeter. Equation 2.80 may be nonlinear because of the nature of the constitutive operators. However, it can be solved by a fixed-point based method, leading to the value of the partition coefficient. The constitutive operators defining the stress contributions related to both the steel and the steel/concrete interface can be chosen according to the desired accuracy of the assessment.

The constitutive operator related to the steel $\mathcal{L}^A$ has been chosen according to the proposal made by Ouglova (2004), known as Ouglova's law. Indeed, Ouglova (2004) has developed a steel constitutive law which may account for some features related to the phenomenon of corrosion, such as the reduction in the cross section of the steel or the decrease in the ultimate strain. We restricted the three-dimensional formulation to a coupling between the damage and plasticity not only in terms of the state but in terms of the flow. On the other hand, the constitutive operator related to the steel/concrete interface $\mathcal{L}^I$ has been constructed according to the research presented in Section 2.4.1 in the case of corrosion. As mentioned previously, the only feature which could not be taken into account in a straightforward way is the swelling. However, the consequences of its effect on the degradation state of the steel/concrete interface could be taken into accoun by means of the additional energy rate W (see Equation 2.75), which is a function of the macroscopic corrosion degree. The full set of constitutive equations allowing the definition of both operators $\mathcal{L}^A$ and $\mathcal{L}^I$ are presented in detail in Richard *et al.* (2011).

The proposed steel/concrete interface model has two main limitations and we would like to point them out. The first one is related with the identification of the material parameters. The proposed model is able to represent the bond–slip relation as soon as the material parameters have been satisfactorily calibrated. Especially the parameter related to the corrosion may be difficult to be identified. However, a framed process to identify material parameters is proposed in Richard *et al.* (2011). The second limitation is related to the change of failure mode. Indeed, it is well known that the growth of corrosion leads to switching from a pull-out failure to a

splitting failure. This can be modeled by switching the bond–slip relation from a brittle one to a ductile one. The proposed steel/concrete interface model can be calibrated to obtain this effect. Nevertheless, the concrete model used in the analysis plays an important role when such failure modes occur, since concrete cracking is responsible for the global failure of the structure. As the multifiber approach does not aim at accurately representing cracking patterns (through damage patterns), the change of failure mode is only taken into account at a structural level (no significant differences in the damage pattern will be observed).

Numerical examples

Local considerations The main features of the proposed approach are analyzed in the present section. To perform this analysis, the proposed model has been implemented in the finite element software Cast3M. One single steel fiber is considered in order to obtain local results at the Gauss point level. Consequently, the anchorage length l_c has been chosen equal to 1.0 m and the other material parameters have been identified according to the process presented in Richard *et al.* (2011). Three local tests have been performed: first, the coupling effect between the constitutive laws driving the behaviors of the steel and the steel/concrete interface is studied; second the effect of an increase of the corrosion degree is analyzed; last, the possibility of describing the effects of reverse loading is discussed.

Figure 2.9 illustrates the local response of the steel/concrete interface in terms of the shear stress versus the sliding strain. The three different degradation stages are taken into account and are in good agreement with the observations published by Lutz et Gergely (1967). The pre-peak and the post-peak behaviors are well exhibited, making possible analyses up to failure. The local response of the steel rebar in terms of the normal stress versus the total strain is also shown. An elastoplastic response is obtained. An unloading step can be seen, although the loading is increasing during the computations. This is due to the fact that from a specific loading state, the steel/concrete interface becomes too damaged and therefore cannot ensure equilibrium with the steel rebar. The equilibrium state is therefore obtained by the unloading of the steel fiber. The evolution of the partition factor versus the number of load steps is presented in Figure 2.9. It first decreases, reflecting the predominance of the steel/concrete interface. It then increases up to 0.85, reflecting the predominance of the steel behavior. Finally, it decreases drastically, highlighting the unloading of the steel rebar. All these evolutions clearly show that the behavior of the steel is coupled with the behavior of the steel/concrete interface.

Numerical results for the corroded condition are shown in Figure 2.10a. The shear stress peak associated with the steel/concrete interface clearly decreases. Therefore, the steel rebar cannot be loaded at the same level as in the case of no corrosion. The steel does not reach the plastic stage because the steel/concrete interface is too damaged to provide a suitable stress transfer. The partition factor evolution highlights a strong predominance of the steel/concrete interface. Indeed, the latter is decreasing to zero, sliding being the main mechanism. A simple tension test under repeated loading has been simulated. For the sake of simplicity, the corrosion degree is set to zero. The results are presented in Figure 2.10b. The nonlinearities due to hysteretic effects are clearly taken into account in the proposed model. Moreover, the dissipated energy within a cycle is influenced by the damage level; this is represented by a variation of the hysteretic loops areas. The steel response is influenced by the behavior of the steel/concrete interface. Although the hysteretic effects are not explicitly taken into account in the steel constitutive law, since the coupling equilibrium equation is satisfied they appear in the steel response. The evolution of the partition factor shows the different patterns of behavior along the simulation.

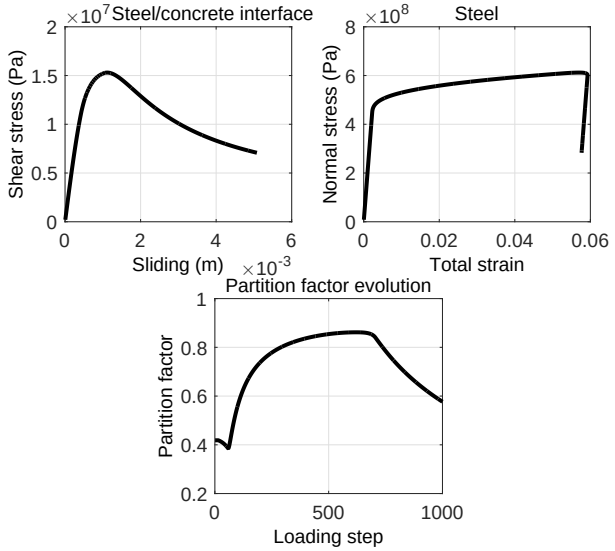

Figure 2.9: Local results — monotonic loading — uncorroded.

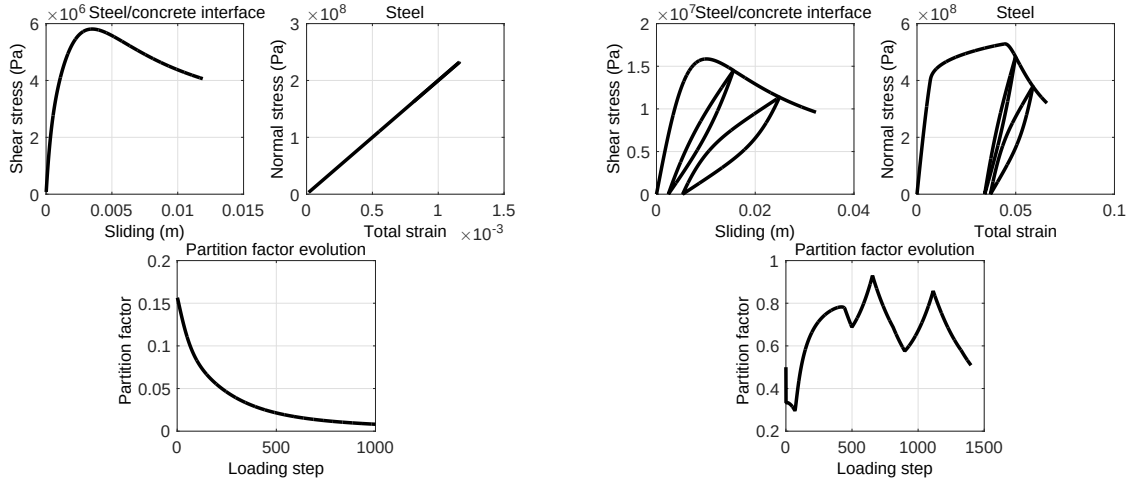

(a) Monotonic loading — corroded.

(b) cyclic loading — uncorroded.

Figure 2.10: Local results.

Structural case study The possibilities offered by the simplified approach we proposed have been explored at the member scale. To this end, several structural case studies have been carried out. Especially, we assessed the relevancy of the approach to reinforced concrete beams by considering several loading cases: (i) monotonic loading without corrosion effects, (ii) cyclic loading without corrosion effects, and (iii) monotonic loading with corrosion effects. These three structural case studies are presented in Richard *et al.* (2011). In the following, we aim at comparing the influence of a full interaction between steel and concrete with a partial interaction. Furthermore, no corosion is assumed.

The reinforced concrete beam analyzed has been experimentally studied by Ragueneau (1999). The three point bending test was realized by controlling the loading in five different steps: 10 kN, 30 kN, 50 kN, 70 kN and 90 kN (failure). To avoid fatigue effects, only ten cycles were performed at the loading step. Two structural cases have been simulated. The first one uses

a perfect steel/concrete interface and the second one uses an imperfect interface. The results are expressed in terms of load/midspan displacement curves and are presented in Figure 2.11. The experimental results are bounded by those obtained numerically. First, with a perfect steel/concrete interface, the initial elastic stiffness is well described. Nevertheless, both the tension stiffening stage and the yielding stage are overestimated. The load/displacement curve appears to be smooth, meaning that redistribution phenomena do not seem to be of primary importance. Moreover, since the steel/concrete interface is considered as being perfect, the steel rebar can yield more easily than if the interface is imperfect. Indeed, the stress transfer between concrete and steel is complete and not degraded whatever the load level. The numerical failure mode is a flexural one, which does not accurately match with experiments, since a combination between a flexural failure and a bond failure has been reported experimentally. Second, with an imperfect steel/concrete interface, the elastic stiffness and the concrete cracking stages are better captured compared to the previous case. Nevertheless, the yielding stage is underestimated but remains well described. This is due to the absence of accurate experimental data related to the properties of the bond. The load/displacement curve appears less smooth than the previous one; the stress redistribution phenomena seem to be better characterized than in the previous case. The strength is lower since the steel/concrete interface is starting to be damaged. Therefore, as soon as the interface has reached a critical level of degradation, the stress transfer between the concrete and steel cannot be maintained, resulting in a lower strength. The numerical failure mode is a bond failure.

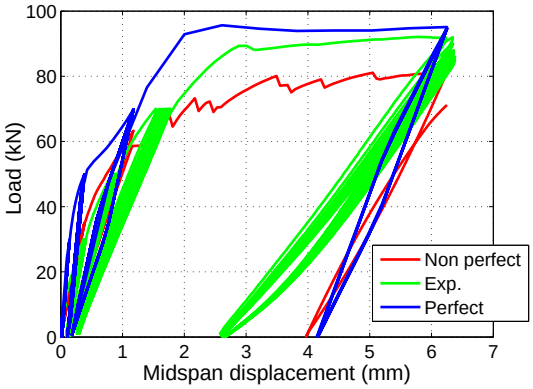

Figure 2.11: Structural results — load/midspan displacement.

The damage patterns obtained are shown in Figures 2.12a and 2.12b for, respectively, a full interaction and a partial interaction between the steel and concrete. The results are in agreement with the load/midspan displacement curve presented in Figure 2.11. Two distinct failure mechanisms can be observed. In the case of a full interaction, the reinforced concrete specimen reaches failure by compression. In contrast, in the case of a partial interaction, the compressive area does not have the same pattern as the one observed in the previous case. Cracks start from the bottom part of the beam and propagate towards the upper part. These different failure mechanisms are driven by the load transfer, which is conditioned by the degradation state of the steel/concrete interface.

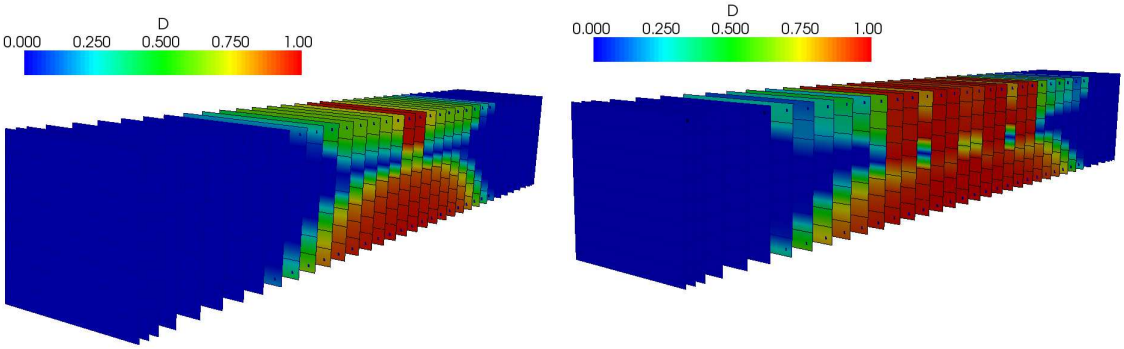

(a) Perfect steel/concrete interface. (b) Non perfect steel/concrete interface.

Figure 2.12: Damage pattern.

2.5 Summary

In this section, a summary of contributions aiming at improving the numerical description of some dissipative mechanisms occuring during the degradation process of quasi-brittle materials, such as concrete-like materials or a steel/concrete interface. In the first part, three different modeling strategies were presented. The physical assumptions as well as the constitutive equations were presented and discussed. The capabilities of each set of constitutive equations were illustrated and discussed in the second part. Especially, we focused on some important features, such as the way of describing the softening and how the material parameters can be interpreted and identified. Results coming from some local uniaxial tests carried out at the integration point level were also presented and discussed in order to emphasize the pros and cons related to each constitutive model. The main contributions are in *proposing constitutive equations coupling a unilateral effect with hysteretic loops to handle the complex case of cyclic loadings*. The third part aimed at presenting more or less simplified strategies to include the specific behavior of the steel/concrete interface in the structural analysis, when dealing with reinforced concrete structures. After explaining a fully three-dimensional approach based on the use of zero-thickness finite elements, the developments we made to formulate a simplified strategy were highlighted. The main contributions related to this last part are: (i) *formulating a fully three-dimensional steel/concrete interface consitutive model accounting for the effects related to corrosion* and (ii) *proposing a simplified strategy aiming at reducing the computational cost of the nonlinear analysis and which could be used within a probabilistic context.*

Publications in peer reviewed journals

A1 **Richard, B.**, Ragueneau, F., Crémona, C., Adélaïde, L. (2010). Isotropic continuum damage mechanics for concrete under cyclic loading: Stiffness recovery, inelastic strains and frictional sliding. *Engineering Fracture Mechanics* 77(8):1203–1223.

A2 **Richard, B.**, Ragueneau, F., Crémona, C., Adélaïde, L., Tailhan, J.-L. (2010). A three dimensional steel–concrete interface model including corrosion effects. *Engineering Fracture Mechanics* 77(6): 951–973.

A3 Adélaïde, L., **Richard, B.**, Ragueneau, F., Crémona, C. (2010). Thermodynamical admissibility of a set of constitutive equations coupling elasticity, isotropic damage and internal

sliding. *Comptes Rendus Mécanique* 338:158–163.

A4 Ragueneau, F., **Richard, B.**, Crémona, C., Berthaud, Y. (2010). Damage mechanics applied to the modelling of corroded reinforced concrete structures: Steel, concrete and steel/concrete interface. *European Journal of Environmental and Civil Engineering* 14(6–7):869–890.

A5 **Richard, B.**, Ragueneau, F., Adélaïde, L., Crémona, C. (2011). A multifiber approach for modeling corroded reinforced concrete structures. *European Journal of Mechanics A/Solids* 30(6):950–961.

A6 Adélaïde, L., **Richard, B.**, Ragueneau, F., Crémona, C. (2012). A simplified numerical approach of global behaviour of RC beams degraded by corrosion. *European Journal of Environmental and Civil Engineering* 16(3–4).

A7 **Richard, B.**, Quiertant, M., Bouteiller, V., Adélaïde, L., Tailhan, J.-L., Crémona, C. (2012). Influence of accelerated corrosion on the reinforced cover concrete cracking behavior: Experimental and numerical study. *European Journal of Environmental and Civil Engineering* 16(3–4).

A8 **Richard, B.**, Ragueneau, F. (2013). Continuum damage mechanics based model for quasi-brittle materials subjected to cyclic loadings: Formulation, numerical implementation and applications. *Engineering Fracture Mechanics* 98:383–406.

A9 Vassaux, M., **Richard, B.**, Ragueneau, F., Millard, A. (2015). Regularized cracks behaviour effects on continuum modelling of quasi-brittle materials under cyclic loading. *Engineering Fracture Mechanics* 149:18–36.

3 Quantification of the vulnerability of reinforced concrete structures

3.1 Introduction

Nowadays, most structures are made of reinforced concrete. Following the second world war, many reinforced concrete structures were erected in a short period due to the necessity to rebuild. Within this context, buildings devoted to housing, public infrastructure, and energy production facilities were constructed. Because of the necessity to bring some answers as quickly as possible and to face the tremendous demand, the issues related to the performance of the new reinforced concrete structures were not fully addressed. Today, many reinforced concrete structures can not be considered as being new since they are nearly 40 years old. As a consequence, it is necessary to quantify their performance level in order to check whether they can still achieve the objectives for which they were built. In other words, it is important to be able to quantify not their vulnerability but also the design provisions in the case of extreme loading scenario.

Quantifying the vulnerability of a reinforced concrete sructure requires describing the dissipative mechanisms related to the constitutive materials. In the previous chapter, several constitutive laws have been presented. Especially, we have shown their ability to represent several features which should be taken into account for an accurate description of the material behavior. Among these features, cracking has been identified as being a key point. However, because cracking is a complex phenomenon, its description may be undertaken by several indicators, such as crack openings, crack spacing, or crack tortuosity. These indicators must be determined because the limit states may depend on them. To reach this objective, it is necessary (i) to identify the set of material parameters in a robust way and (ii) to use approaches allowing the definition of such indicators. Furthermore, in the case of dynamic loadings, a new variable appears: the damping. Damping is a phenomenon that is still not clearly understood. It is usually decomposed into two contributions: one coming from the material dissipation (related to the material nonlinearities) and that coming from all other sources of dissipation. Therefore, it seems necessary to identify both contributions in order to make robust the model considered in the context of a structural assessment study. From the aforementioned presentation, it appears that methodological tools are needed in order to quantify the structural vulnerability.

However, the predictive ability of a given model is highly dependent on the way of identifying the set of material parameters. Uncertainties related to the material parameters should be taken into account. Based upon the definition of a satisfactory structural model, the responses corresponding to a set of realizations of the material parameters should be computed by using a satisfactory structural model. Due to the large number of responses needed to computed statistical estimators, the issue of computational efficiency becomes salient. In addition, the probabilistic model should be able to be updated based upon new pieces of information.

The formulation of advanced approaches to predict the beyond-design behavior of either new or existing reinforced concrete structures is not sufficient. It is also necessary to validate these approaches intrinsically and to frame the way to use them. The issue of the validation of methods should also be addressed in a regulatory context. A natural practice for validating structural assessment methods is in benchmarking the approaches, based upon reference data coming from experiment. Within the framework of our research, we have focused on two issues coming from two different fields, both issues addressing the case of torsion-sensitive reinforced concrete structures. The first one is related to the quantification of the design provisions when dealing with an extreme seismic scenario. Broad experimental studies, including shaking table tests, were carried out to produce reference experimental data which have fed an international benchmark to assess the predictive capabilities of advanced assessment approaches. The second one addresses the issue of the seismic behavior of innovative structural components, called thermal breakers, which have been designed to provide the shear wall–slab connection with improved thermal insulation properties. Within this context, we contributed in providing some answers by defining an experimental program and carrying out the related numerical analysis in order to quantify the influence of thermal breakers on the structural response of a torsion-sensitive reinforced concrete structure subjected to a seismic scenario.

In this chapter, we sum up the contributions of our work aiming at improving the way of quantifying cracking, idenfifying the dissipative capabilities of reinforced concrete components, improving the computational efficiency of probabilistic approaches, and validating structural assessment approaches.

3.2 Quantification of cracking features

3.2.1 Discrete element strategy

Background

When dealing with structural assessments, the quantification of cracking features has become of primary importance, mainly because of sustainability requirements. However, civil engineering reinforced concrete structures are often complex and the description of their mechanical behavior is generally achieved by means of continuous constitutive laws. Despite the fact that this strategy allows estimating both structural and local responses, the major drawbacks lie in (i) their inability to represent kinematic discontinuities and (ii) the need to have sufficiently many pieces of information to identify the material parameters in the case of complex loading paths. Within this framework, we focused on the use of particle models, also called lattice models, in order to provide some answers to the aforementioned issues. The particle model we focused on was initially proposed by D'addetta *et al.* (2002) and modified by Delaplace (2008) and Vassaux *et al.* (2015). The concrete domain is spatially represented through polygonal particles linked together by brittle Euler–Bernouilli beams. The cohesive forces between two particles' centroids are expressed by the following set of equations:

$$\boldsymbol{F}_{coh,ij} = \begin{cases} F_{N,ij} = \dfrac{EA_{b,ij}}{I_{b,ij}} \left(\boldsymbol{u}_i - \boldsymbol{u}_j\right).\boldsymbol{n}_{b,ij} \\ F_{T,ij} = \dfrac{12EI_{b,ij}}{l_{b,ij}^3} \left(\boldsymbol{u}_i - \boldsymbol{u}_j\right).\boldsymbol{t}_{b,ij} - \dfrac{6EI_{b,ij}}{l_{b,ij}^2} \left(\theta_i - \theta_j\right) \\ M_{Z,ij} = \dfrac{6EI_{b,ij}}{l_{b,ij}^2} \left(\boldsymbol{u}_i - \boldsymbol{u}_j\right).\boldsymbol{t}_{b,ij} + \dfrac{4EI_{b,ij}}{l_{b,ij}} \left(\theta_i - \dfrac{\theta_j}{2}\right) \end{cases} \tag{3.1}$$

where E stands for the Young's modulus of the beams, $A_{b,ij}$ the cross section of the beam, $l_{b,ij}$

the length of the beam, $I_{b,ij}$ the moment of inertia, $\boldsymbol{u}_i$ and $\boldsymbol{u}_j$ the displacement of the particles i and j respectively, θ_i and θ_j the rotations of the particles i and j respectively, $\boldsymbol{n}_{b,ij}$ and $\boldsymbol{t}_{b,ij}$ are the normal and tangential vectors associated with the beam ij. The beams' behavior is assumed to be brittle in order to treat the fracture process that characterizes quasi-brittle materials. Therefore, a local breaking criterion is used:

$$P_{ij}\left(\frac{\varepsilon_{ij}}{\varepsilon_{ij}^{cr}}, \frac{\mid \theta_i - \theta_j \mid}{\theta_{ij}^{cr}}\right) > 1 \tag{3.2}$$

where P_{ij} is a threshold to be overcome in order to break the beam ij, ε_{ij}^{cr} is a critical strain, and θ_{ij}^{cr} a critical rotation. As soon as the failure criterion is reached, the beam is removed from the particle mesh and a local crack opening can be computed.

Handling cyclic loading through contact and friction

Implicit time integration strategy Based upon the aforementioned considerations, it appears the particle model can describe fracture. This feature makes it capable of dealing with monotonic loadings but does not allow dealing with cyclic ones. To overcome this limitation, we added two mechanisms: *contact* and *frictional sliding* between the particles. Contact is introduced only when two particles are overlapping, i.e., when the failure criterion has already been reached. To manage contact, an intersection area S_r has been introduced as the overlapping area of two intersecting polygons. Once the area is identified, the contact band width can be defined as the longest segment inside the area S_r. Furthermore, a local basis (normal and tangental vectors) is defined by assuming the normal vector $\boldsymbol{n}_c$ is perpendicular to the contact band width. The tangential vector $\boldsymbol{t}_c$ is then deduced. Finally, the point at which the contact forces will be applied is defined as the center of inertia of the intersection area S_r. Figure 3.1 depicts the assumptions related to the contact mechanism.

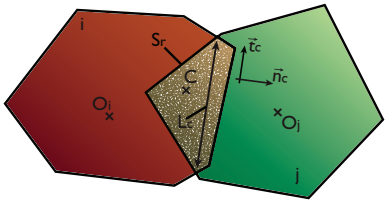

Figure 3.1: Description of the setup for the contact mechanism.

In the normal direction $\boldsymbol{n}_c$, the contact force is computed with respect to geometrical indicators $S_{r,ij}$ and $l_{c,ij}$ as follows:

$$\boldsymbol{F}_{cont,ij} = -\frac{ES_{r,ij}}{l_{c,ij}}\boldsymbol{n}_{c,ij} \tag{3.3}$$

where $l_{c,ij}$ stands for a characteristic length defined as the harmonic mean of the diameters of two contacted particles. On the other hand, a Coulomb-based law is employed in the tangential direction $\boldsymbol{t}_c$. Therefore, a friction coefficient μ is introduced:

$$\boldsymbol{F}_{fric,ij} = \mathbf{min}\left(\frac{EI_{c,ij}}{l_{c,ij}^3}\left[\left(\boldsymbol{u}_{c,ij} - \boldsymbol{u}_{c,ji}\right).\boldsymbol{t}_{c,ij} - \Delta u_{s,ij}\right], \mu \mid\mid \boldsymbol{F}_{cont,ij} \mid\mid\right).\boldsymbol{t}_{c,ij} \tag{3.4}$$

where $I_{c,ij} = \frac{l_c^3}{12}$ and $\Delta u_{s,ij}$ stands for the sliding displacement (or relative displacement) in the tangential direction in between two particles. Indeed, the behavior remains elastic before

reaching a perfectly plastic friction. Considering two particles, only the fraction of displacements accumulated since the the contact has been initiated is taken into account:

$$\boldsymbol{u}_{c,ij}^{t+1} = \begin{cases} \boldsymbol{u}_{c,ij}^{t} + \delta \boldsymbol{u}_{c,i}^{t} & \text{if } i \text{ and } j \text{ are overlapping} \\ \mathbf{0} & \text{if } i \text{ and } j \text{ are not overlapping} \end{cases} \tag{3.5}$$

Most of the beam-particle models are based upon the use of an explicit time integration strategy. This class of solver algorithms is not suitable to handle quasi-static problems. Indeed, the dynamic effects (velocity-proportional resisting force field and inertia force field) are naturally neglected due to the quasi-static nature of the problem to solve. Under these assumptions, the neglect of dynamic effects leads to an interesting reduction in the computational costs and consequently permits implicit integration. Therefore, we made the solver algorithm implicit, avoiding the introduction of a local kinematic displacement field assumption and allowing a reduction of the computational cost at the RVE scale. The integration strategy we proposed is based upon a combination of (i) the well known saw-tooth algoritm Rots *et al.* (2008), (ii) a predictor–corrector algorithm, and (iii) a numerical relaxation scheme. To clarify, the saw-tooth algoritm consists in solving the balance equation, removing the first beam that leads to exceeding the failure criterion, and solving again the balance equation. In this way, the stress redistribution is taken into account in a natural way. Between two consecutive saw-tooth iterations, an iterative process is used, due to the nonlinearities related to contact and frictional sliding. Numerical experience has shown that the convergence issues could be mitigated by considering a secant stiffness matrix for the prediction step. Numerical relaxation is applied to the correction step of the aforementioned predictor–corrector strategy. The relaxation coefficient is chosen according to the convergence rate. More advanced strategies based upon the convergence radius extension/contraction might have been used, such as the well known line search method.

Numerical example In order to illustrate the capabilities of the particle model for handling cyclic loadings, the experiment realized by Nouailletas (2013) has been simulated. It consists in a cyclic direct tension test carried out on a plain concrete notched specimen under a fixed boundary condition. The loading was displacement-controlled and several loading/unloading cycles were considered. During the experiment, some rotations were monitored on the edge that was subjected to the prescribed displacement. Simulations were carried out by including this feature, an additional loading has therefore been considered (see Figure 3.2a). The results are shown in Figure 3.2. We can note a satisfactory agreement between the experimental and the numerical results. This would not have happened if both contact and frictional sliding had not been treated in a robust way.

Coupling discrete element/finite element strategy for a refined cracking analysis

Despite the fact that continuous constitutive models allow for large-scale structural computations, a major drawback lies in their inability to provide quantitative results related to local quantities, such as cracking features (crack spacing, openings, etc.). In order to overcome this drawback, the particle model presented above can be advantageously used in order to post-process the results coming from continuous computations Oliver-Leblond (2013); Giry *et al.* (2014).

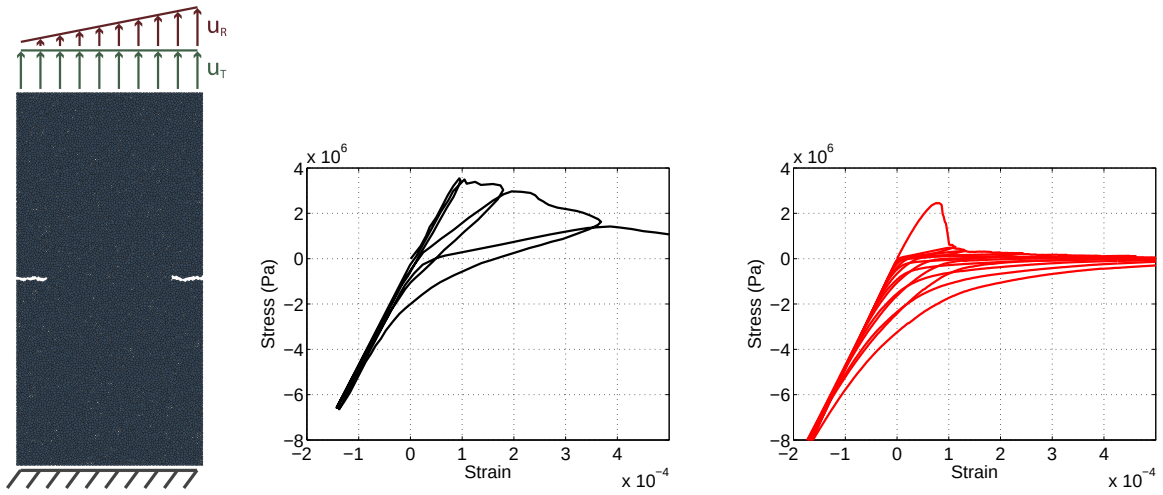

(a) Numerical setting. (b) Experimental results. (c) Numerical results.

Figure 3.2: Numerical comparison of the cyclic direct tension test performed by Nouailletas (2013).

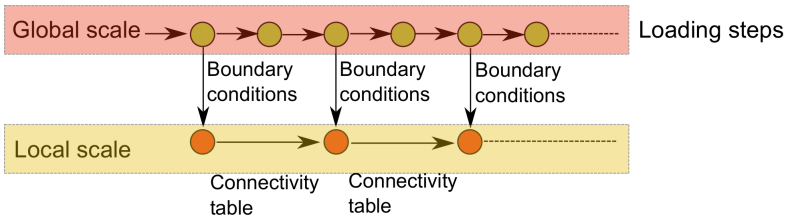

Figure 3.3: Sequential description of the global/local analysis strategy.

General concept The post-processing strategy is inspired by submodeling techniques often used within the framework of industrial problems, due to their simplicity. These methods have two major steps: in the first step, the whole domain under study is analyzed; in the second step, specific areas, also called regions of interest (ROI), are accurately studied. The ROIs are extracted from the domain under study and therefore should be subjected to dedicated boundary conditions. In the proposed approach, Dirichlet boundary conditions are used. More precisely, the displacement field computed at the global level is projected onto the boundaries of the ROI. This choice has been made in order to ensure that the post-processing strategy does not depend on the constitutive model chosen at the global level. The method is non-intrusive because because it only uses the available input and output (nodal displacement field). A flowchart of the post-processing strategy is presented in Figure 3.3.

Four main steps are performed during the global/local analysis:

1. global analysis of the whole domain by means of a continuous constitutive model,
2. extraction of the ROI, which is generally the area where a strain localization occurs,
3. projection of the displacement field coming from the the global level onto the boundaries of the ROI,
4. local analysis of the ROI thanks to the particle model presented in Section 3.2.1.

It is important to note that no interaction between the local and the global levels is considered. For instance, no force-based correction at the boundaries is carried out. Indeed, the aim of the post-processing strategy is to provide refined information on the local kinematic and cracking features. The two models complete each other by describing, each in its own different way, the same phenomenon, namely cracking. In addition, as shown in Figure 3.3, the post-processing strategy is sequential. In other words, for several damage levels, a local analysis is performed. An important feature lies in the fact that it is not necessary to perform a local analysis at each global loading step. In practice, the number of local analysis steps is chosen according to the rate of evolution of the damage pattern.

The boundary conditions of the local computations are obtained from the global analysis performed on the whole domain. Those boundary conditions are Dirichlet boundary conditions, which is often the case for submodeling techniques. A natural way to transfer the displacement field from a higher scale to a lower one is to use the finite element shape functions. In this way, the displacement field at each particle centroid can be expressed as follows:

$$\boldsymbol{u}(\boldsymbol{x}_D) = \sum_{i=1}^{nn} \boldsymbol{N}_i(\boldsymbol{x}_D)\boldsymbol{u}_i \tag{3.6}$$

where $\boldsymbol{u}$ stands for the interpolated displacement field, $\boldsymbol{x}_D$ for the coordinates of the centroid, nn for the number of nodes, $\boldsymbol{N}_i$ for the shape functions associated with the node i, and $\boldsymbol{u}_i$ for the nodal displacements at the node i. Focusing on Equation 3.6, we can observe that the continuity of the rotations is not ensured. Indeed, numerical experience has shown that the kinematic errors are not preponderant and therefore may lead to not considering this additional kinematic constraint. Another aspect which has been studied is related to the equilibrium of the ROI. Indeed, the momentum balance equation is naturally fulfilled as soon as the same model is considered at the global scale. If two different constitutive models are considered, unbalanced forces may appear at the boundary but equilibrium is ensured for both models independently.

In order to ensure consistency between the models used at each scale, it is necessary to identify the corresponding material parameters in an appropriate manner. In the case of the continuous constitutive model, the set of material parameters can be identified thanks to experimental characterization tests. If necessary, the experimental data can be complemented by using a virtual testing based approach. This latter aspect is presented and discussed in the next section. In the case of the particle model, the corresponding material parameters are identified from both the strain/stress uniaxial response in tension given by the continuous model and the dissipated energy (also in tension).

Numerical example In order to illustrate the possibilities of the global/local computational strategy, a numerical example is presented in this section. The three-dimensional test carried out by Feist et Hofstetter (2007b) has been chosen. Indeed, this test allows studying the validity of the global/local approach in the case of a three-dimensional crack propagation problem. The specimen is a plain concrete beam with a prismatic notch. A sketch of the experimental setup is shown in Figure 3.4. Two steel reinforcing bars have been cast in the concrete specimen in order to support it. The load is displacement-controlled in order to capture the post-peak region. From a mechanical point of view, the loading can be considered as a quasi-static coupling between bending and torsion.

The spatial discretizations at the global and local levels are shown in Figures 3.5a and 3.5b, respectively. The continuous constitutive model used at the global scale is the one presented in Section 2.2.2. The local mesh corresponds to an ROI located at the left side of the notch, where the crack plane is expected to start and to propagate.

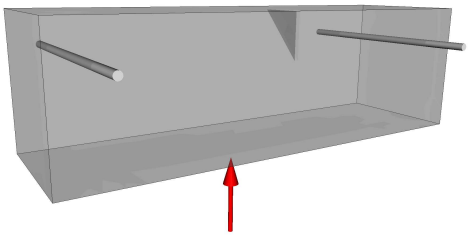

Figure 3.4: Experimental setup of the PCT3D test as in Feist et Hofstetter (2007b).

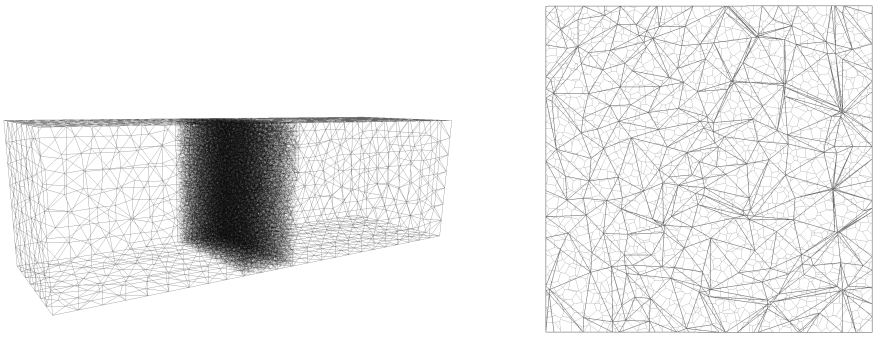

(a) Mesh at the global level. (b) Mesh at the local level.

Figure 3.5: Spatial discretizations considered for the refined re-analysis of the PCT3D.

Three damage states, at the global scale, have been considered for the refined local analysis. These states are shown in Figures 3.6a to 3.6c and the corresponding cracking patterns in Figures 3.6d to 3.6f. On the one hand, we can see a pretty good agreement between both patterns (cracking and damage), and on the other hand, a good accordance with the experimental measurements reported by Feist et Hofstetter (2007b). Despite the fact that the experimental values of the crack openings are not known all along the crack plane, we observed a satisfactory accordance between the maximum crack openings: 6.8×10^{-4} mm for the numerical value versus 8.0×10^{-4} mm for the experimental one.

Virtual testing for the identification of the material parameters

Another possibility offered by the particle model lies in using it as a virtual testing machine in order to complement the experimental information available at the RVE scale or to simulate experimental tests which may be complex to realize from a practical point of view due to the quasi-brittle nature of concrete. Especially for such materials, experimental data related to both the tension and tension/compression loading cases at the RVE scale is rare. However, this data is of primary importance when a refined description of these mechanisms is aimed at. In order to illustrate the capabilities of the developed particle model to be used as a virtual testing

machine Willans et Harrison (2001), we focused on the case of the constitutive model presented in Section 2.2.4, for which this strategy was used.

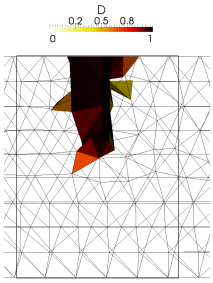

(a) Damage pattern — state # 1.

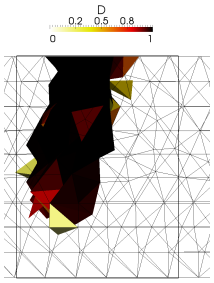

(b) Damage pattern — state # 2.

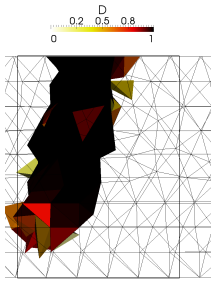

(c) Damage pattern — state # 3.

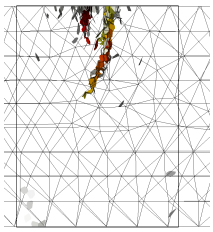

(d) Cracking pattern — state # 1.

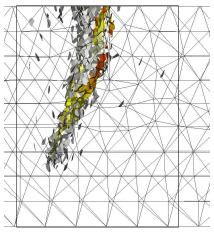

(e) Cracking pattern — state # 2.

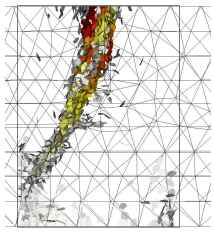

(f) Cracking pattern — state # 3.

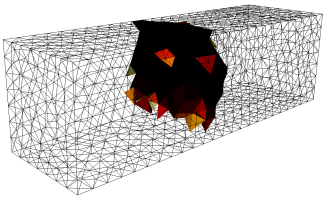

(g) Damage pattern — 3D view — state # 3.

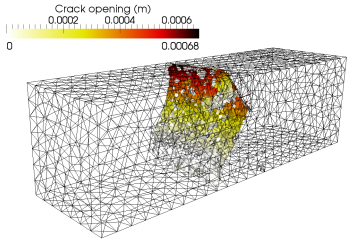

(h) Cracking pattern — 3D view — state # 3.

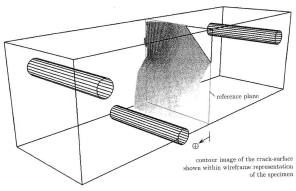

(i) Cracking pattern — 3D view — state # 3 — exp. observations according to Feist et Hofstetter (2007b).

Figure 3.6: Results obtained after the re-analysis of the PCT3D test by means of the global/local post-processing strategy.

Local considerations Among the set of constitutive equations presented in Section 2.2.4, Equation 2.50 expresses the fact that a fraction of the elastic modulus is continuously recovered when switching from tension to compression. In other words, the ϑ function describes the fraction of closed cracks in the RVE and therefore, should vary from 0 (no crack closed) to 1 (all the cracks closed). Furthermore, we assume a priori that the crack closure function can be expressed as a Gaussian cumulative probability function centered at 0:

$$\vartheta = 1 - \frac{1}{1 + \mathbf{exp}\left(-f(\underline{\underline{\epsilon}}^f)\right)} \tag{3.7}$$

where f is a function to be determined. Expression 3.7 will be a posteriori verified thanks to the results coming from the virtual testing process. On the other hand, the damage level reached in the RVE seems to have an influence on the crack closure function. In order to take into account these features, various tension/compression tests have been carried out considering different damage levels, characterized by the maximum crack strain over the pseudo-time, or a scalar indicator in the three-dimensional case. The results of such an identification process are shown in Figure 3.10.

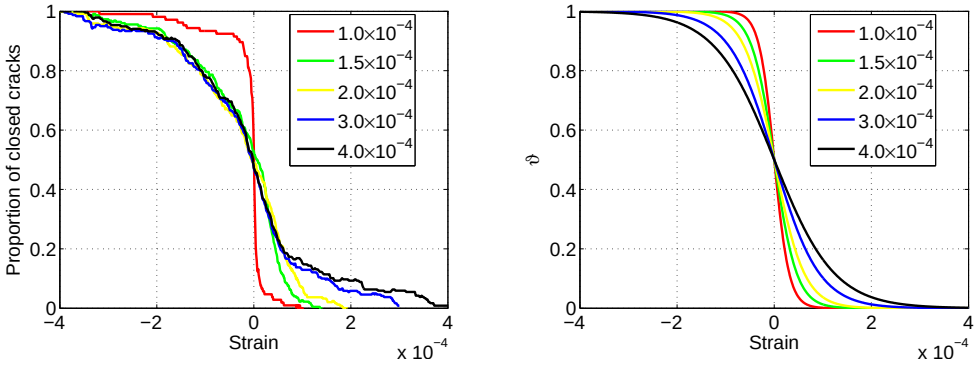

(a) Reference data. (b) Fitted data.

Figure 3.7: Fraction of closed cracks versus the maximum crack strain.

More precisely, Figure 3.7a depicts the fraction of closed cracks for different damage levels obtained by using the particle model. We can note that the curves seem to be close to a sigmoid. Our initial assumption seems to be suitable. On the other hand, Figure 3.7b shows fitted curves based on the following expression:

$$\vartheta = 1 - \frac{1}{1 + \mathbf{exp}\left(-\alpha_0 \dfrac{I_1\left(\underline{\underline{\epsilon}}^f\right)}{\underset{0\leq\tau\leq t}{\mathbf{max}}\, I_1\left(\underline{\underline{\epsilon}}^f(\tau)\right)}\right)} \tag{3.8}$$

where α_0 is a material parameter set to 6.5 in the case of the present identification, and t is the current pseudo-time. The latter value of the α_0 coefficient has been found as being the one which leads to the most satisfactory results. For the sake of concision, this aspect is not presented in the present memoir. The term $\underset{0\leq\tau\leq t}{\mathbf{max}} I_1\left(\underline{\underline{\epsilon}}^f(\tau)\right)$ allows taking into account the influence of the level of damage on the way the cracks close.

Another material parameter which is not straightforward to identify is the friction coefficient μ_0, introduced in Equation 2.56. The main difficulty in the identification process is due to the fact that the local cyclic responses at the RVE scale have to be known. The identification process of the μ_0 coefficient consists in quantifying, for a given damage level, the energy dissipation when the RVE is subjected to a loading/unloading/re-loading path. In the case of the particle model, the dissipated energy is estimated by accumulating the incremental contributions coming from the set of contacted particles:

$$E_\mu^{d,t+1} = E_\mu^{d,t} + \frac{1}{2}\sum_{i=1}^{n_p}\sum_{j=1}^{n_c^i}\left(^t\left(\boldsymbol{F}_{fric,ij}^{t+1} + \boldsymbol{F}_{fric,ij}^{t}\right).\left(\Delta u_{s,ij}\boldsymbol{t}_{c,ij}\right)^{t+1}\right) \tag{3.9}$$

where n_p is the number of contacted particles, n_c^i the number of contacts for particle i, and $E_\mu^{d,t}$

is the energy dissipated at the pseudo-time t. On the other hand, in the case of the continuous model, the dissipated energy is computed in a similar manner:

$$E_{\mu}^{c,t+1} = E_{\mu}^{c,t} + \frac{1}{2}\int_{\Omega}\left(\underline{\underline{\sigma}}^{f,t+1} + \underline{\underline{\sigma}}^{f,t}\right) : \Delta\underline{\underline{\epsilon}}^{f,p,t+1} d\Omega \tag{3.10}$$

where $E_{\mu}^{c,t}$ stands for the energy dissipated at the pseudo-time t. Finally, the μ_0 coefficient is calibrated by minimizing the gap between E_{μ}^{d} and E_{μ}^{c}. As depicted in Figure 3.8, we end up with $\mu_0 = 2.89$.

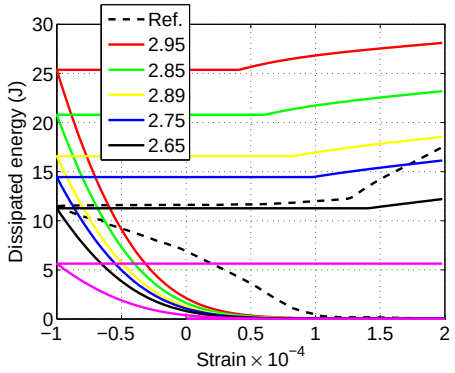

Figure 3.8: Fraction of closed cracks versus the maximum crack strain.

Structural example In order to assess the validity of the material parameter identification approach presented in the previous section, a structural case study at the member scale has been analyzed. The experimental study realized within the framework of the French research project CEOS.fr has been chosen Rospars et Chauvel (2014). Among the reinforced concrete specimens studied, two low-aspect ratio reinforced concrete shear walls were tested up to failure. The drawings of the shear wall considered are shown in Figure 3.9. The reinforced concrete shear walls were subjected to cyclic loadings (non-reverse and reverse), which are described in Figures 3.10a and 3.10b, respectively. The loading is force-controlled. The loading is applied in the horizontal direction by means of one or two actuators which have been fixed on a dedicated steel plate located on the edges of the upper reinforced concrete beam.

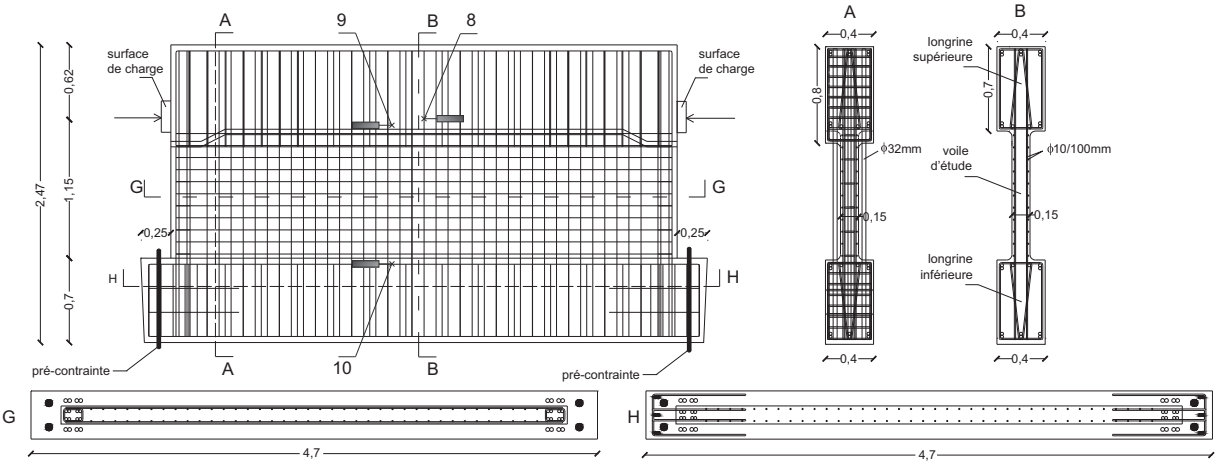

Figure 3.9: Drawings of the CEOS.fr shear wall.

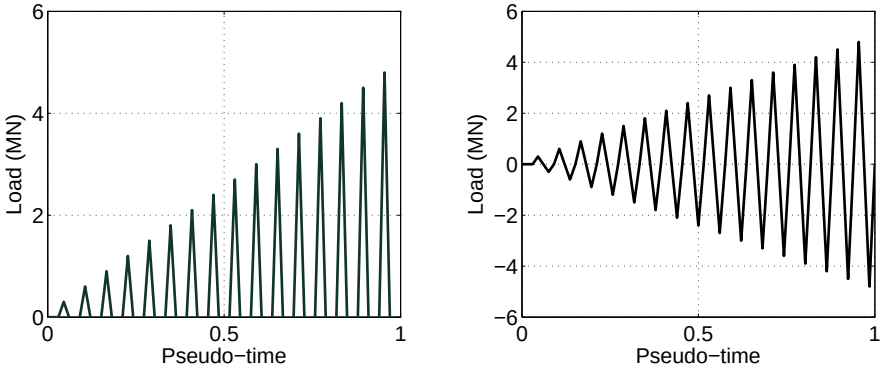

(a) Non-reverse loading. (b) Reverse loading.

Figure 3.10: Description of the loading histories.

A fully three-dimensional strategy has been retained to simulate the mechanical response of the shear wall. The finite element mesh is shown in Figure 3.11. The concrete domain has been discretized by means of 8-node finite elements and steel reinforcing bars by means of 2-node elements. Timoshenko beam elements have been used in the case of the reinforcing bars located on the edges whereas simple bar elements have been chosen in the other parts of the wall. Both the upper and lower reinforced concrete beams have been considered to be linear elastic whereas the central part has been described by means of the constitutive model presented in Section 2.2.4. The simulations have been carried out with the finite element software Cast3M.

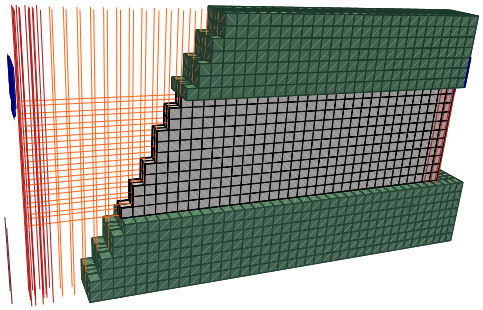

Figure 3.11: Finite element mesh used for the reinforced concrete shear wall.

It is crucial to note that the material parameters have been identified, on the one hand, from the experimental characterization tests and, on the other hand, from the virtual tests carried out to complement the aforementioned set of data. Experimental–numerical comparisons are shown in Figure 3.12. In the case of the non-reverse cyclic loading, the results presented in Figures 3.12a and 3.12b show a satisfactory agreement in terms of the ultimate load and relative displacement. The residual displacements when unloading and the energy dissipated by friction during the loading/unloading cycles seem to be underestimated. However, we can note that the hysteretic dissipation increases with the number of cycles, which is in accordance with the experimental obsevations. Furthermore, looking at the experimental results when the load is equal to zero, we can observe a sliding displacement, which allows thinking that the experimental loops are overestimated. Even if the sliding displacement had been substracted, the simulated hysteretic loops would have underestimated the experimental ones. The results obtained in the case of the reverse cyclic loading are shown in Figures 3.12c and 3.12d. To complement the

remarks made previously, which remain applicable, we can note that the mechanical response is symmetric with respect to the origin. This shows that the unilateral effect is captured not only in a satisfactory way but also in such a manner the continuity of the stress/strain relation is preserved. The qualitative results related to the cracking pattern have also been analyzed, and are shown in Figure 3.13. In order to compare the numerical results with the experimental measurements obtained from the digital image correlation technique, the principal strains have been computed. In the case of the non-reverse cyclic loading, the results are shown in Figures 3.13a and 3.13b. We can note a pretty good agreement. In such a case, the failure mechanism seems to be satisfactorily reproduced. In contrast, the case of the reverse cyclic loading has been much more complex to handle. The results obtained for load values equal to 3.9 MN and -3.9 MN are shown in Figures 3.13c and 3.13d, respectively. At first sight, two groups of cracks with different orientations are captured, which is in accordance with the experimental observations. However, when looking at the pattern for both load values, we note that some cracks do not close. Indeed, the existence of some strain localization areas seems to show that the unilateral effect is not full. In addition, neither is the pinching effect, when switching from positive loads to negative ones, is not accurately reproduced. This observation may be explained by the fact the local sliding between the steel reinforcing bars and the surrounding concrete is not taken into account.

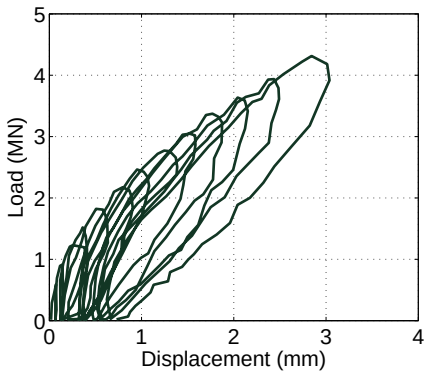

(a) Exp. — non-reverse response.

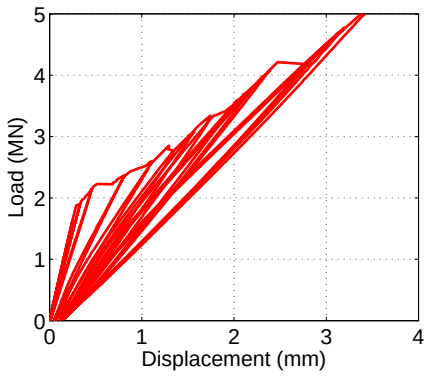

(b) Num. — non-reverse response.

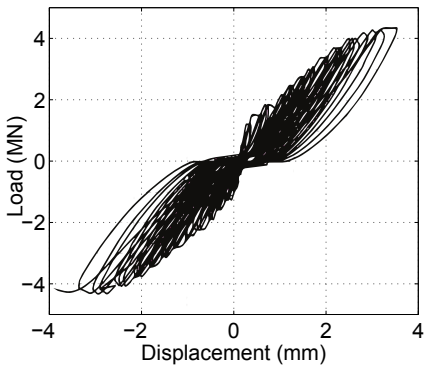

(c) Exp. — reverse response.

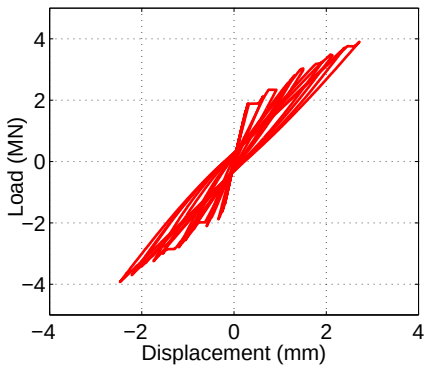

(d) Num. — reverse response.

Figure 3.12: Experimental–numerical comparaison of the load/relative displacement of the shear wall under cyclic loading.

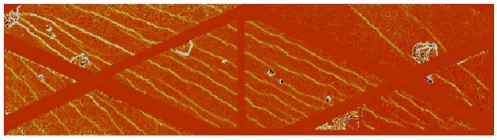

(a) Exp. — non-reverse response — 4.2 MN.

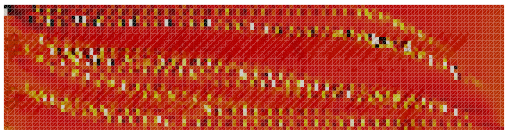

(b) Num. — non-reverse response — 4.2 MN.

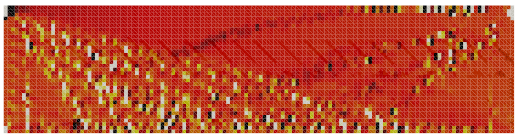

(c) Num. — reverse response — 3.9 MN.

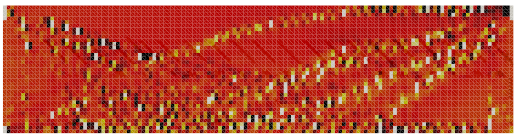

(d) Num. — reverse response — -3.9 MN.

Figure 3.13: Numerical and experimental principal strains — experimental–numerical comparisons.

3.2.2 Enhanced kinematics approach

Background

Cracking features can not be quantified in a natural way when dealing with a continuous description of the media. Indeed, it is necessary to use post-processing techniques such as the one presented in Section 3.2.1 in order to extract specific quantities. Despite the fact that these approaches lead to accurate results, specific attention should be paid to the way of calibrating them and an additional computational effort is required.

Alternative approaches based on a kinematic enhancement of the displacement field came up. We can distinguish two groups of techniques, according to the type of kinematic enhancement considered. Some of them assume a local[1] enhancement Simo *et al.* (1993); Alfaiate *et al.* (2003); Feist et Hofstetter (2006); Dias-da Costa *et al.* (2009a,b); Radulovic *et al.* (2011); Linder et Zhang (2013) whereas others postulate a global[2] enhancement Belytschko *et al.* (2001); Moës et Belytschko (2002). Among the approaches based upon a local kinematic enhancement, the strong discontinuity method (SDM) is one of the most used Oliver (1996a,b) because of (i) its low-intrusiveness in computational software and (ii) the absence of additional degrees of freedom, keeping unchanged the structure of the algebraic system of equations to be solved. Within this framework, it has been shown that the kinematic enhancement of the displacement field allows defining a discrete constitutive law (expressed in terms of a traction vector and a displacement jump), from specific classes of continuous constitutive laws (expressed in terms of stress and strain) Oliver *et al.* (2002a); Simone *et al.* (2003); Cazes *et al.* (2010). Especially, this result has been established in the case of isotropic continuum damage mechanics and J_2-plasticity based models.

However, from a physical point of view, the development of microcracks is a directional degradation process. The information related to the directional character of the damage can be taken into account by representing the damage tensorially. In this way, the description of the physical mechanisms in given directions can be accurately carried out. Based on these considerations, the

[1]The term *local* refers to the fact that the additional degrees of freedom related to the kinematic enhancement can be condensed at the finite element level. The size of the algebraic system of equations to be solved is not modified with respect to the case of a classical kinematics.

[2]The term *global* refers to the fact that the additional degrees of freedom are considered at the node. Therefore, the size of the algebraic system of equations to be solved increases.

first objective of our research was to show that a strong discontinuity kinematic enhancement leads naturally to the definition of a discrete constitutive model when a family of anisotropic continuum damage based constitutive models is considered instead of an isotropic continuum damage mechanics or J_2-plasticity based models. From this result, an original tension/separation constitutive law has been proposed to allow for an anisotropic description of cracking.

As an inherent drawback of SDM, the local nature of the kinematic enhancement induces a loss of the $\mathcal{C}^0$-continuity of the displacement discontinuity field. This feature may lead to spurious crack orientations and stress locking phenomenon. As a direct consequence, the numerical results may become mesh-dependent Feist et Hofstetter (2006). In order to overcome this limitation of SDM, tracking algorithms have been developed over the past decades to ensure the continuity of the displacement discontinuity field on the domain under study. Tracking algorithms may be sorted into two categories. The first one gathers the so-called local strategies, which ensure the continuity of the crack paths by means of geometrical considerations for each finite element. When such local tracking algorithms are used, SDM somehow loses its local character and becomes non-local in the sense that the quantities have to be estimated on neighborhoods for all finite elements. With the aim of pr eserving the local character of the SDM, a second category of tracking algorithms has been developed. These strategies are called global tracking algorithms and determin the envelopes of all the possible crack paths by solving a heat-conduction-like boundary value problem Oliver *et al.* (2004). Potential crack paths correspond to the isovalues of a temperature-like field. This strategy allows preserving the local nature of the SDM because quantities defined on neighborhoods of the finite elements are no longer needed: the potential crack paths are determined once on the whole domain. Despite this interesting feature, the global tracking step is generally performed at the beginning of the analysis and therefore the isolines do not change once they have been determined. This strategy leads to accurate results in the case of quasi-static loadings but is not appropriate in the case of cyclic loadings, when the local stress states may be subjected to strong variations. Furth ermore, local redistribution phenomena at the crack tip may not be described properly if the crack path can not change during the computational analysis. According to the aforementioned discussion, the second objective of our research was to improve the global tracking algorithm originally proposed by Oliver *et al.* (2002b) in order to make it able to deal with cyclic loadings.

Consequences from a strong discontinuity kinematics in an anisotropic damage setting

Anisotropic continuum damage framework The class of anisotropic continuum damage models under study is inspired by the Bargellini *et al.* (2006) and can be classified among the so-called micro-mechanics-based approaches. They are based on a tensorial decomposition of the stress/strain relation. This feature allows giving a physical meaning to each component of the damage-like variables. A summary of the constitutive equations is given in Table 3.1. We can note the presence of a famility of functions $(g_i)_{i=1,\cdots,n} : \mathcal{E} \rightarrow \mathbb{R}^+$, with $\mathcal{E}$ being the space of compatible strain tensors. The $(g_i)_{i=1,\cdots,n}$ are assumed to be combinations of quadratic strain-based terms in order to ensure (i) the convexity and (ii) the continuity of the second order derivative of the state potential. The functions g_i may be chosen according to tensorial representation theories in order to particularize the way of taking into account the damage anisotropy Boehler (1978); Walpole (1984); Bargellini *et al.* (2006). Furthermore, the thermodynamic forces associated to the isotropic hardening are naturally bounded $Z_i \in [0, Z_0]$ since the loading/unloading conditions are assumed to be fulfilled.

Description	Equation
Total state potential	$\Psi(\underline{\underline{\varepsilon}}, (\rho_i)_{i=1,\cdots,n}) = \Psi_0(\underline{\underline{\varepsilon}}) - \Psi_a(\underline{\underline{\varepsilon}}, (\rho_i)_{i=1,\cdots,n})$
Elastic potential	$\Psi_0(\underline{\underline{\varepsilon}}) = \frac{1}{2}\underline{\underline{\varepsilon}} : \underline{\underline{\underline{\underline{C}}}} : \underline{\underline{\varepsilon}}$
Inelastic potential	$\Psi_a(\underline{\underline{\varepsilon}}, (\rho_i)_{i=1,\cdots,n}) = \sum_{i=1}^{n} \rho_i g_i(\underline{\underline{\varepsilon}})$
Stress/strain relation	$\underline{\underline{\sigma}}(\underline{\underline{\varepsilon}}) = \frac{\partial \Psi}{\partial \underline{\underline{\varepsilon}}}(\underline{\underline{\varepsilon}}, (\rho_i)_{i=1,\cdots,n}) = \underline{\underline{\sigma}}_0(\underline{\underline{\varepsilon}}) - \sum_{i=1}^{n} \rho_i \frac{dg_i}{d\underline{\underline{\varepsilon}}}(\underline{\underline{\varepsilon}})$
Thermodynamic force — damage variable ρ_i	$F_{\rho_i}(\underline{\underline{\varepsilon}}) = -\frac{\partial \Psi}{\partial \rho_i}(\underline{\underline{\varepsilon}}) = g_i(\underline{\underline{\varepsilon}})$
Thermodynamic force — hardening	$Z_i = \frac{dH_i(z_i)}{dz_i}$
Threshold surface	$\phi_{\rho_i}(F_{\rho_i}, Z_i) = F_{\rho_i} - Z_i$
Flow rules — damage variable ρ_i	$\dot{\rho}_i = \dot{\lambda}_i \frac{\partial \phi_{\rho_i}}{\partial F_{\rho_i}} = \dot{\lambda}_i$
Flow rules — hardening variable z_i	$\dot{z}_i = \dot{\lambda}_i \frac{\partial \phi_{\rho_i}}{\partial Z_i} = -\dot{\lambda}_i$
Loading/unloading conditions	$\dot{\lambda}_i \geq 0; \quad \phi_{\rho_i} \leq 0; \quad \dot{\lambda}_i \phi_{\rho_i} = 0$

Table 3.1: Summary of the constitutive equations characterizing the anisotropic continuum damage model.

Strong discontinuity kinematics Let us denote by Ω a body in $\mathbb{R}^3$. Let us also assume that a strong discontinuity occurs at a certain location Γ in Ω, such that Ω is split into two sub-bodies Ω^+ and Ω^-. These two sub-bodies can be identified in a consistent manner according to the normal $\boldsymbol{n}$ to the discontinuity Γ. The discontinuous displacement field can be expressed as follows:

$$\boldsymbol{u}(\boldsymbol{x}, t) = \overline{\boldsymbol{u}}(\boldsymbol{x}, t) + \mathcal{H}_\Gamma(\boldsymbol{x})[\boldsymbol{u}](\boldsymbol{x}, t) \tag{3.11}$$

where $\overline{\boldsymbol{u}} : \Omega \times [t_i, t_f] \to \mathbb{R}^3$, $[\boldsymbol{u}] : \Omega \times [t_i, t_f] \to \mathbb{R}^3$ and $\mathcal{H}_\Gamma : \Omega \to \{0, 1\}$ is the Heaviside function centered on Γ. $[t_i, t_f]$ stands for the pseudo-time interval in which the loading process takes place. The corresponding strain field can be deduced from Equation 3.11 as follows:

$$\underline{\underline{\varepsilon}}(\boldsymbol{x}, t) = \underline{\underline{\nabla}}^s \boldsymbol{u}(\boldsymbol{x}, t) = \overline{\underline{\underline{\varepsilon}}}(\boldsymbol{x}, t) + \delta_\Gamma(\boldsymbol{x})([\boldsymbol{u}] \otimes \boldsymbol{n})^s(\boldsymbol{x}, t) \tag{3.12}$$

where $\underline{\underline{\nabla}}(.)$ stands for the the gradient of $(.)$, $(.)^s$ stands for the symmetric part of $(.)$, $\overline{\underline{\underline{\varepsilon}}}$ is the regular (bounded) part of the strain tensor $\underline{\underline{\varepsilon}}$, and $\delta_\Gamma(\boldsymbol{x})$ is the Dirac function (the derivative of the Heaviside function $\mathcal{H}_\Gamma$ in the distributional sense) centered on Γ. It can be seen that $\overline{\underline{\underline{\varepsilon}}}$ is the sum of two contributions, which are not given in detail since the important feature is that the sum is bounded. Furthermore, let us note that $\delta_\Gamma(\boldsymbol{x})[\boldsymbol{u}]$ constitutes the irregular (unbounded) part of the strain tensor $\underline{\underline{\varepsilon}}$. Considering the kinematics defined by Equation 3.12, it is necessary to introduce mathematical conditions which make it compatible with the class of continuum c onstitutive models summarized in Table 3.1

Furthermore, because the equilibrium equations should be fulfilled in both Γ and $\Omega \setminus \Gamma$, the continuity of the traction vector through the discontinuity must be ensured. On the other hand, since the stress (and the corresponding rates) must be bounded on $\Omega \setminus \Gamma$, we can deduce that they should also be bounded in Γ Oliver *et al.* (2002a). Therefore, the continuity of the traction vector implies that the following condition must be fulfilled:

$$\boldsymbol{t}_{|\Gamma} = \underline{\underline{\sigma}}_{|\Omega \setminus \Gamma} . \boldsymbol{n} \tag{3.13}$$

The condition expressed by Equation 3.13 is known as the traction continuity condition.

Compatibility conditions The Dirac function is regularized by the following sequence Oliver (1996b):

$$\delta_\Gamma(\underline{x}) \approx \delta_\Gamma^k(\underline{x}) = \frac{1}{k}\mu_\Gamma(\underline{x}) \tag{3.14}$$

where μ_Γ is a collocation function centered on Γ, i.e., $\mu_\Gamma(\boldsymbol{x}) = 1$ if $\boldsymbol{x} \in \Gamma$, but $\mu_\Gamma(\boldsymbol{x}) = 0$ otherwise. Hence, the strong discontinuity kinematics can be expressed in a regularized way as follows:

$$\underline{\underline{\varepsilon}}(\boldsymbol{x},t) \approx \underline{\underline{\varepsilon}}^k(\boldsymbol{x},t) = \underline{\underline{\overline{\varepsilon}}}(\boldsymbol{x},t) + \frac{1}{k}([\boldsymbol{u}] \otimes \boldsymbol{n})^s(\boldsymbol{x},t) \tag{3.15}$$

For the sake of clarity, the dependance on the position vector $\boldsymbol{x}$ and on the pseudo-time t are omitted when no confusion is possible. Combining the stress/strain relation shown in Table 3.1 with Equation 3.15, the Cauchy stress on the discontinuity Γ is expressed as follows:

$$\underline{\underline{\sigma}}^k = \frac{1}{k}\underline{\underline{\underline{\underline{C}}}} : (k\underline{\underline{\overline{\varepsilon}}} + ([\boldsymbol{u}] \otimes \boldsymbol{n})^s) - \sum_{i=1}^{n} \frac{\rho_i}{k}\frac{dg_i}{d\underline{\underline{\varepsilon}}}(k\underline{\underline{\overline{\varepsilon}}} + ([\boldsymbol{u}] \otimes \boldsymbol{n})^s) \tag{3.16}$$

The Cauchy stress tensor $\underline{\underline{\sigma}}$ can be obtained by taking the limit of Equation 3.16 when k tends to 0:

$$\underline{\underline{\sigma}} = \lim_{k\to 0} \underline{\underline{\sigma}}^k = \lim_{k\to 0}\left(\frac{1}{k}\underline{\underline{\underline{\underline{C}}}} : ([\boldsymbol{u}] \otimes \boldsymbol{n})^s\right) - \sum_{i=1}^{n} \lim_{k\to 0}\left(\frac{\rho_i}{k}\right)\frac{dg_i}{d\underline{\underline{\varepsilon}}}([\boldsymbol{u}] \otimes \boldsymbol{n})^s \tag{3.17}$$

Finally, the traction vector $\boldsymbol{t}$ can be deduced. After some algebraic manipulations, one ends up with the following expression:

$$\boldsymbol{t} = \underline{\underline{\sigma}}.\boldsymbol{n} = \lim_{k\to 0}\left(\frac{1}{k}\underline{\underline{Q}}\right).[\boldsymbol{u}] - \sum_{i=1}^{n} \lim_{k\to 0}\left(\frac{\rho_i}{k}\right)\frac{dg_i([\boldsymbol{u}\otimes\boldsymbol{n}])^s}{d\underline{\underline{\varepsilon}}}.\boldsymbol{n} \tag{3.18}$$

where $\underline{\underline{Q}} = \boldsymbol{n}.\underline{\underline{\underline{\underline{C}}}}.\boldsymbol{n}$ stands for the acoustic tensor.

Analysis The expression of the traction vector on the discontinuity Γ shows that two terms must be analyzed. The first one is related to the micro-cracking density variables $\lim_{k\to 0}\left(\frac{\rho_i}{k}\right)$ and the second one can be interpreted as an initial stiffness $\lim_{k\to 0}\left(\frac{1}{k}\underline{\underline{Q}}\right)$. In order to study the first term, let us introduce the discrete hardening variable $\bar{z}_i$ which will be required to be bounded, such as:

$$\bar{z}_i = \frac{z_i}{k} \tag{3.19}$$

The micro-cracking damage variable ρ_i can be linked with its time derivative as follows:

$$\rho_i = \int_{t_i}^{t_f} \dot{\rho}_i dt \tag{3.20}$$

Furthermore, considering the continuous flow rules, we end up with:

$$\rho_i = -\int_{t_i}^{t_f} \dot{z}_i dt = -\int_{t_i}^{t_f} k\dot{\bar{z}}_i dt \implies \frac{\rho_i}{k} = -\int_{t_i}^{t_f} \dot{\bar{z}}_i dt = -\bar{z} \tag{3.21}$$

Finally, we show the bounded character of the first term:

$$\lim_{k\to 0}\left(\frac{\rho_i}{k}\right) = -\bar{z} < \infty \tag{3.22}$$

Furthermore, it seems interesting to study what are the consequences of the introduction of a bounded discrete hardening variable on the tangent modulus when the strong kinematics is considered. The hardening modulus can be expressed as follows:

$$\dot{Z} = \frac{dZ}{dz}\dot{z} = \underbrace{\frac{dZ}{dz}}_{=\frac{d\bar{Z}}{d\bar{z}}} k\dot{\bar{z}} \tag{3.23}$$

In Equation 3.23, we note that both terms $\dot{Z}$ and $\dot{\bar{z}}$ are bounded in an intrinsic way (because Z and z are also bounded). Therefore, the term $\frac{dZ}{dz}k$ also has to be bounded. This result can be interpreted as the fact that the discrete tangent modulus is bounded on the discontinuity. A second implication of this result is the fact that a discrete flow rule can be derived from the continuous one in order to manage the discrete hardening variable, and therefore the discrete micro-cracking variable (since they are flow-coupled).

Now, let us consider the second term $\lim_{k\to 0}\left(\frac{1}{k}\underline{\underline{Q}}\right)$. This term is related to an initial elasticity exhibited by the traction vector when the displacement jump flows. Indeed, by differentiating Equation 3.18, we end up with:

$$\left.\frac{\partial \boldsymbol{t}}{\partial [\boldsymbol{u}]}\right|_{t=t_i} = \lim_{k\to 0}\left(\frac{1}{k}\underline{\underline{Q}}\right) \tag{3.24}$$

However, if we consider a displacement jump introduced (or in other words, the introduction of a discontinuity Γ) at the pseudo-time t_i, we can note that on the one hand $\lim_{k\to 0}\left(\frac{1}{k}\underline{\underline{Q}}\right) = +\infty$, and on the other hand $[\boldsymbol{u}] = 0$. Therefore, the product $\lim_{k\to 0}\left(\frac{1}{k}\underline{\underline{Q}}\right).[\boldsymbol{u}]$ is an undetermined form. To move forward, it is necessary to invoke the continuity conditions of the traction vector Oliver *et al.* (2002a). Indeed, since they should vanish for all pseudo-times, they are especially fulfilled at the pseudo-time $t = t_i$. In this way, we can see that this product is bounded. The bound can be determined by the continuity of the traction vector (see Equation 3.13). Therefore, we can see that $\lim_{k\to 0}\left(\frac{1}{k}\underline{\underline{Q}}\right).[\boldsymbol{u}] = \boldsymbol{t}_0$. The bound $\boldsymbol{t}_0$ depends on the lo calization criterion to introduce the discontinuity Γ. Equation 3.18 can be re-written consistently as follows:

$$\boldsymbol{t} = \boldsymbol{t}_0 - \sum_{i=1}^{n} \bar{\rho}_i \frac{dg_i([\boldsymbol{u}]\otimes\boldsymbol{n})^s}{d\underline{\underline{\varepsilon}}}.\boldsymbol{n} \tag{3.25}$$

Anisotropic discrete damage framework From the aforementioned presentation, we can conclude that there can be defined a set of discrete variables which remain bounded although the strain field is unbounded. This feature is of primary importance because it leads to the possibility of building bounded flow rules. This set of discrete variables needs to be complemented by a discrete state potential. To reach this objective, the k-regularization of the Dirac function is combined with the expression of the continuous state potential presented in Table 3.1:

$$\Psi^k = \Psi_0^k(\underline{\underline{\bar{\varepsilon}}} + \frac{1}{k}([\boldsymbol{u}]\otimes\boldsymbol{n})^s) - \bar{\Psi}_a^k((\bar{\rho}_i)_{i=1,\cdots,n}, \underline{\underline{\bar{\varepsilon}}} + \frac{1}{k}([\boldsymbol{u}]\otimes\boldsymbol{n})^s) \tag{3.26}$$

After factoring the term $\frac{1}{2k^2}$, the first term $\Psi_0^k(\underline{\underline{\bar{\varepsilon}}} + \frac{1}{k}([\boldsymbol{u}]\otimes\boldsymbol{n})^s)$ can be expressed as follows:

$$\Psi_0^k(\underline{\underline{\bar{\varepsilon}}} + \frac{1}{k}([\boldsymbol{u}]\otimes\boldsymbol{n})^s) = \frac{1}{2k^2}\left(k\underline{\underline{\bar{\varepsilon}}} + ([\boldsymbol{u}]\otimes\boldsymbol{n})^s\right) : \underline{\underline{\underline{\underline{C}}}} : \left(k\underline{\underline{\bar{\varepsilon}}} + ([\boldsymbol{u}]\otimes\boldsymbol{n})^s\right) \tag{3.27}$$

Considering the limit of Ψ_0^k when k tends to 0, one ends up with:

$$\Psi_0^k(\underline{\underline{\varepsilon}} + \frac{1}{k}([\boldsymbol{u}] \otimes \boldsymbol{n})^s) \underset{k\to 0}{\sim} \frac{1}{2k^2}([\boldsymbol{u}] \otimes \boldsymbol{n})^s : \underline{\underline{\underline{\underline{C}}}} : ([\boldsymbol{u}] \otimes \boldsymbol{n})^s = \frac{1}{2k}[\boldsymbol{u}].\left(\frac{1}{k}\boldsymbol{n}.\underline{\underline{\underline{\underline{C}}}}.\boldsymbol{n}\right).[\boldsymbol{u}] \tag{3.28}$$

Now the elastic contribution of the discrete state potential can be expressed as follows:

$$\bar{\Psi}_0 = \lim_{k\to 0} k\Psi_0^k = \frac{1}{2}[\boldsymbol{u}].\underbrace{\lim_{k\to 0}\left(\frac{1}{k}\underline{\underline{Q}}\right)}_{=\boldsymbol{t}_0}.[\boldsymbol{u}] \tag{3.29}$$

Let us consider now the second term in Equation 3.26. Keeping in mind that the set of functions $(g_i)_{i=1,\cdots,n}$ are combinations of quadratic strain-based terms, we can obtain from Equation 3.26 the following expression:

$$\Psi_a^k((\bar{\rho}_i)_{i=1,\cdots,n}, \underline{\underline{\varepsilon}} + \frac{1}{k}([\boldsymbol{u}] \otimes \boldsymbol{n})^s) = \frac{1}{k^2}\sum_{i=1}^{n} \rho_i g_i(k\underline{\underline{\varepsilon}} + ([\boldsymbol{u}] \otimes \boldsymbol{n})^s) = \frac{1}{k}\sum_{i=1}^{n} \frac{\rho_i}{k} g_i(k\underline{\underline{\varepsilon}} + ([\boldsymbol{u}] \otimes \boldsymbol{n})^s) \tag{3.30}$$

Taking the limit of Equation 3.30, the inelastic contribution of the discrete state potential takes the following form:

$$\bar{\Psi}_a = \lim_{k\to 0} k\Psi_a^k = \sum_{i=1}^{n} \bar{\rho}_i g_i(([\boldsymbol{u}] \otimes \boldsymbol{n})^s) \tag{3.31}$$

The discrete state potential can be expressed by subtracting the inelastic contribution from the elastic one:

$$\bar{\Psi} = \frac{1}{2}\boldsymbol{t}_0.[\boldsymbol{u}] - \sum_{i=1}^{n} \bar{\rho}_i g_i(([\boldsymbol{u}] \otimes \boldsymbol{n})^s) \tag{3.32}$$

The full set of discrete constitutive equation can now be defined. It is summarized in Table 3.2.

Description	Equation
Total state potential	$\bar{\Psi} = \frac{1}{2}\boldsymbol{t}_0.[\boldsymbol{u}] - \sum_{i=1}^{n} \bar{\rho}_i g_i(([\boldsymbol{u}] \otimes \boldsymbol{n})^s)$
Elastic potential	$\frac{1}{2}\boldsymbol{t}_0.[\boldsymbol{u}]$
Inelastic potential	$\sum_{i=1}^{n} \bar{\rho}_i g_i(([\boldsymbol{u}] \otimes \boldsymbol{n})^s)$
Traction — separation relation	$\boldsymbol{t} = \boldsymbol{t}_0 - \sum_{i=1}^{n} \bar{\rho}_i \frac{dg_i([\boldsymbol{u}] \otimes \boldsymbol{n})^s}{d\underline{\underline{\varepsilon}}}.\boldsymbol{n}$
Thermodynamic force — damage variable $\bar{\rho}_i$	$\bar{F}_{\bar{\rho}_i} = -\frac{\partial \bar{\Psi}}{\partial \bar{\rho}_i} = g_i(([\underline{u}] \otimes \underline{n})^s)$
Thermodynamic force — hardening	$\bar{Z}_i = \frac{d\bar{H}_i(\bar{z}_i)}{d\bar{z}_i}$
Threshold surface	$\bar{\phi}_{\rho_i}(\bar{F}_{\rho_i}, \bar{Z}_i) = \bar{F}_{\rho_i} - \bar{Z}_i$
Flow rules — damage variable $\bar{\rho}_i$	$\dot{\bar{\rho}}_i = \dot{\bar{\lambda}}_i \frac{\partial \bar{\phi}_{\rho_i}}{\partial \bar{F}_{\bar{\rho}_i}} = \dot{\bar{\lambda}}_i$
Flow rules — hardening variable $\bar{z}_i$	$\dot{\bar{z}}_i = \dot{\bar{\lambda}}_i \frac{\partial \bar{\phi}_{\rho_i}}{\partial \bar{Z}_i} = -\dot{\bar{\lambda}}_i$
Loading/unloading conditions	$\dot{\bar{\lambda}}_i \geq 0; \quad \bar{\phi}_{\bar{\rho}_i} \leq 0; \quad \dot{\bar{\lambda}}_i \bar{\phi}_{\bar{\rho}_i} = 0$

Table 3.2: Summary of the constitutive equations characterizing the anisotropic discrete damage model.

Application to the description of mixed-mode cracking The set of constitutive equations presented in Table 3.2 characterizes a class of tension/separation laws induced by a strong discontinuity kinematics. With the aim of describing mixed-mode cracking in a refined way, this set of discrete constitutive equations has been particularized. For the sake of clarifty, a two-dimensional framework has been considered. Especially, specific choices for both the functions $(g_i)_{i=1,2,4,7}$ and the discrete hardening variables $\left(\bar{Z}\right)_{i=1,2,4,7}$ have been made. Based on Bargellini *et al.* (2006), the following set of functions has been chosen:

$$\left\{\begin{array}{l} g_i : \mathcal{E} \to \mathbb{R}^+ \\ \quad \underline{\underline{\varepsilon}} \mapsto g_i(\underline{\underline{\varepsilon}}) \quad = \alpha \left[\mathbf{tr}(\underline{\underline{\varepsilon}}.\underline{\underline{\varepsilon}}) - \frac{1}{2}\mathbf{tr}^2(\underline{\underline{\varepsilon}}) + \mathbf{tr}(\underline{\underline{\varepsilon}})\mathbf{tr}(\underline{\underline{\varepsilon}}.\underline{\underline{\underline{\underline{N}}}}_i) \right] + 2\beta \mathbf{tr}(\underline{\underline{\varepsilon}}.\underline{\underline{\varepsilon}}.\underline{\underline{\underline{\underline{N}}}}_i) \end{array}\right. \tag{3.33}$$

where $(\underline{\underline{\underline{\underline{N}}}}_i)_{i=1,2,4,7}$ are directional second order tensors which can be determined according to the normal and the tangent vectors to the discontinuity, α and β are positive constants that can be identified from the elastic properties, and $\mathcal{E}$ is the space of admissible strains. The directional tensors aim at considering micro-cracking density variables in specific directions. For each direction, a specific mechanism (tension, shear, compression, etc.) can be considered with respect to the orientation of the discontinuity. More precisely, the directional tensors can be expressed as follows:

$$\left\{\begin{array}{r} \underline{\underline{\underline{\underline{N}}}}_1 = \boldsymbol{n} \otimes \boldsymbol{n} \\ \underline{\underline{\underline{\underline{N}}}}_2 = \boldsymbol{t} \otimes \boldsymbol{t} \\ \underline{\underline{\underline{\underline{N}}}}_4 = \dfrac{1}{2}\left(\boldsymbol{n} + \boldsymbol{t}\right) \otimes \left(\boldsymbol{n} + \boldsymbol{t}\right) \\ \underline{\underline{\underline{\underline{N}}}}_7 = \dfrac{1}{2}\left(\boldsymbol{n} - \boldsymbol{t}\right) \otimes \left(\boldsymbol{n} - \boldsymbol{t}\right) \end{array}\right. \tag{3.34}$$

where $\boldsymbol{n}$ and $\boldsymbol{t}$ stand for the normal and tangential vectors to the displacement discontinuity. Both the discrete damage variables and the isotropic hardening thermodynamic forces are defined through a consolidation function $\bar{H}_i$. We make use of the proposal made by Bargellini *et al.* (2006), which consists in the following expression:

$$\left\{\begin{array}{l} \bar{H}_i : \mathbb{R} \to \mathbb{R} \\ \quad x \mapsto \bar{H}_i(x) = \quad -Z_0 C_i \mathbf{exp}\left(-\dfrac{x}{C_i}\right) \end{array}\right. \tag{3.35}$$

where Z_0 and C_i are the elastic energy rate stored at the localization time and material parameters to be identified for each damage variable and **exp** stands for the exponental function. To take into account mixed-mode cracking, let us project the displacement discontinuity onto the local basis $(\boldsymbol{n}, \boldsymbol{t})$. Furthermore, taking advantage of the tensorial representation defined by the set of equations 3.35, the strain-like term in the traction/separation law (see Equation 3.2) can be reformulated as follows:

$$\left([\boldsymbol{u}] \otimes \boldsymbol{n}\right)^s = \left([u]_n \boldsymbol{n} + [u]_t \boldsymbol{t}\right) \otimes \boldsymbol{n})^s = [u]_n \underline{\underline{\underline{\underline{N}}}}_1 + \frac{1}{2}[u]_t \left(\underline{\underline{\underline{\underline{N}}}}_4 - \underline{\underline{\underline{\underline{N}}}}_7\right) \tag{3.36}$$

where $[u]_n = [\boldsymbol{u}].\boldsymbol{n}$ and $[u]_t = [\boldsymbol{u}].\boldsymbol{t}$. Equation 3.36 shows the usefulness of the tensorial decomposition introduced through the choice of the $(g_i)_{i=1,2,4,7}$. Indeed, the first term allows driving the crack opening/closing effect whereas the second one describes the shear/sliding effects. It is interesting to note that the strain-like term does not depend on the directional tensor $\underline{\underline{\underline{\underline{N}}}}_2$, which is interpreted according to Bargellini *et al.* (2006) as the contribution of purely compressive loadings. After some analytical developments and considering the strain-like term expression, the traction/separation law becomes:

$$\boldsymbol{t} = \boldsymbol{t}_0 - \begin{pmatrix} (3\alpha + 4\beta)\bar{\rho}_1 + 2(\alpha + \beta)(\bar{\rho}_4 + \bar{\rho}_7) & (0.5\alpha + \beta)(\bar{\rho}_4 - \bar{\rho}_7) \\ (0.5\alpha + \beta)(\bar{\rho}_4 - \bar{\rho}_7) & (\alpha + \beta)(\bar{\rho}_1 + \bar{\rho}_4 + \bar{\rho}_7) \end{pmatrix} \cdot \begin{pmatrix} [u]_n \\ [u]_t \end{pmatrix} \tag{3.37}$$

We can note that a symmetric stiffness-like matrix which depends on the damage variables comes out. Assuming the damage variables $\bar{\rho}_4$ and $\bar{\rho}_7$ flow in a similar way, the out-of-diagonal terms of the stiffness matrix becomes equal to zero and therefore, the normal component of the traction vector is only driven by the normal component of the displacement discontinuity. However, cracking modes I and II remain coupled through the damage variables $\bar{\rho}_4$ and $\bar{\rho}_7$.

Local considerations In order to illustrate the main features of the constitutive law presented in the previous sections, some local tests have been simulated. However, within the framework of the SDM, local simulations are performed at the finite element level since the displacement discontinuity field is spatially discretized. The corresponding shape functions are generally taken to be a linear combination of classical shape functions, but this is not mandatory. The only condition to be fulfilled in order to make possible the static condensation of the additional unknowns characterizing the displacement discontinuity is to ensure that their spatial mean is null over a given finite element. The results coming from a cyclic tension test are shown in Figure 3.14. In particular, the stress/strain relation and the tension/separation law are depicted in Figures 3.14a and 3.14b, respectively. On the one hand, we can observe that the unloading modulus is equal to the secant modulus. In addition, we note that the crack closure effect is also taken into account. Indeed, SDM provides a very convenient framework to handle this effect, mainly because it is sufficient to remove the contribution of the displacement discontinuty to recover Hooke's law without violating any thermodynamical principles. Indeed, this is made possible because the crack features (such as the crack opening) are quantified. The use of closure functions is no longer necessary.

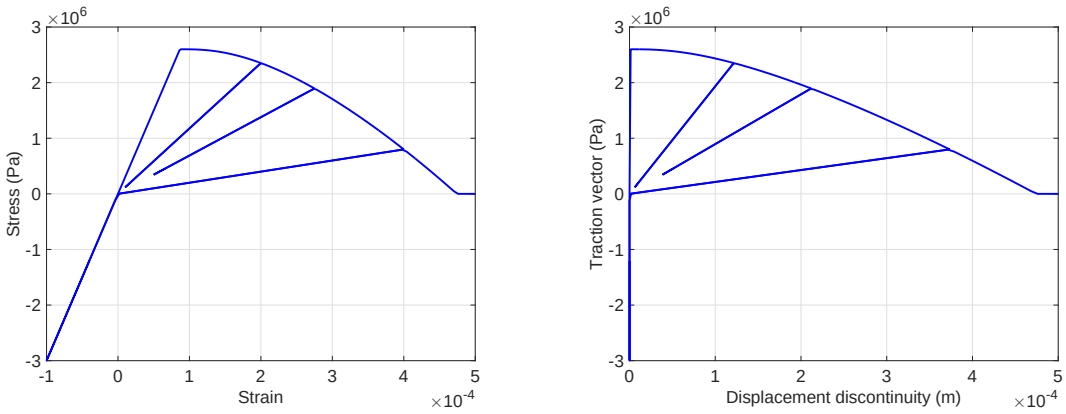

(a) Stress/strain relation.

(b) Tension/separation law.

Figure 3.14: Numerical results — cyclic tension test.

To move forward, a cyclic tension/shear test has also been simulated. It consists in applying a tension loading path in the first step (at a pseudo time t such that $0 \leq t \leq 1$). Then, the RVE is unloaded in the second step (at a pseudo time t such that $1 \leq t \leq 2$). The last step consists in applying a shear loading path (at a pseudo time t such that $2 \leq t \leq 3$). The results are shown in Figure 3.15. In Figure 3.15a, we note that, during the first step (tension), the damage variable $\bar{\rho}_1$ flows from 0 upwards, to reach a constant value. The damage variables $\bar{\rho}_4$ and $\bar{\rho}_7$ flow at the same time but at a slower rate. During the same step, the results shown in Figure 3.15b show an increase of the normal component of the displacement discontinuity and no flow

of the tangential component, which is meaningful in the case of a tension loading. In the second step (unloading), the damage variables remain constant and the normal component of the crack opening decreases. In the last step (shear), Figure 3.15a shows that only the damage variable $\bar{\rho}_4$ and $\bar{\rho}_7$ flow: the damage variable $\bar{\rho}_1$ remains constant, which is consistent with the fact that the loading is shear dominated. Regarding the components of the displacement discontinuity, only the tangential one increases.

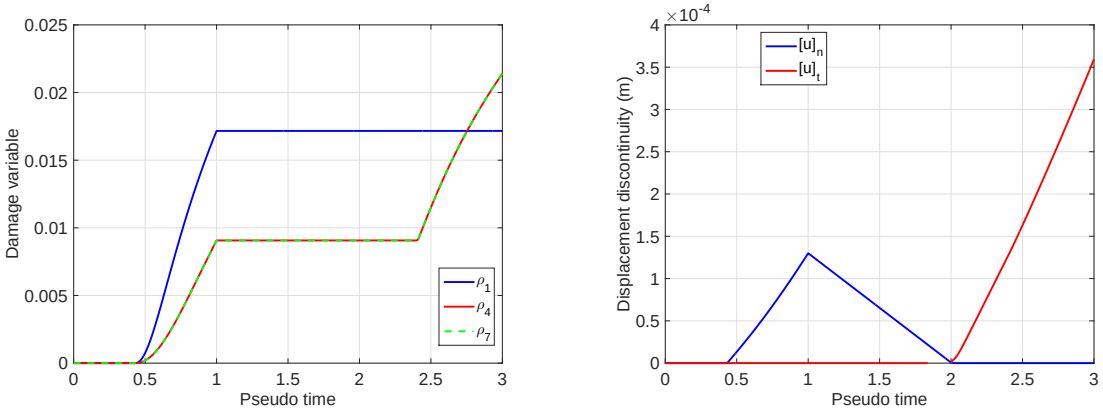

(a) Stress/strain relation.

(b) Tension/separation law.

Figure 3.15: Numerical results — cyclic tension test.

Alternative cracking path continuity strategy

Background The objective of the global tracking algorithm is to determine the envelopes S_i, defined as $S_i = \{\boldsymbol{x} \in \Omega \mid \theta(\boldsymbol{x}) = \theta_{S_i}\}$. The constants θ_{S_i} can be determined by assuming a localization criterion that should be fulfilled in order to locally introduce the strong discontinuity kinematic. For the sake of clarity, the theoretical background of the global tracking algorithm is presented within a two-dimensional framework. However, the extension to three dimensions does not lead to any specific difficulties. According to the proposal made by Oliver *et al.* (2002b), the starting point of the approach lies in introducing a unitary vector field $\boldsymbol{T}(\boldsymbol{x})$ defined for all points $\boldsymbol{x} \in \Omega$, Ω being the domain under study. The vector field $\boldsymbol{T}(\boldsymbol{x})$ is an input: it can be computed according to the principal stresses for instance, in the case of a Rankine-based localization criterion. The problem consists in finding a scalar field $\theta(\boldsymbol{x})$ such that:

$$\boldsymbol{T}(\boldsymbol{x}).\nabla\theta(\boldsymbol{x}) = 0 \quad \forall \boldsymbol{x} \in \Omega \tag{3.38}$$

Equation 3.38 expresses the fact that a $\theta(\boldsymbol{x})$ is sought such that its directional derivative in the direction prescribed by $\boldsymbol{T}(\boldsymbol{x})$ should be null. Omitting some analytical computations, it can be shown that the aforementioned problem can be reformulated as a boundary value problem:

$$\begin{cases} \nabla \boldsymbol{q}(\boldsymbol{x}) = 0 & \forall \boldsymbol{x} \in \Omega \\ \boldsymbol{q}(\boldsymbol{x}) = -\left(\boldsymbol{T}(\boldsymbol{x}) \otimes \boldsymbol{T}(\boldsymbol{x})\right).\nabla\theta(\boldsymbol{x}) & \forall \boldsymbol{x} \in \Omega \\ \boldsymbol{q}(\boldsymbol{x})|_{\boldsymbol{x}\in\partial\Omega_q}.\boldsymbol{\nu} = 0 & \forall \boldsymbol{x} \in \partial\Omega_q \\ \theta(\boldsymbol{x})|_{\boldsymbol{x}\in\partial\Omega_\theta} = \theta^\star(\boldsymbol{x}) & \forall \boldsymbol{x} \in \partial\Omega_\theta \end{cases} \tag{3.39}$$

Looking at the formulation 3.39, it can be noted that the Neumann boundary condition on $\partial\Omega_q$ is automatically fulfilled. On the other hand, the Dirichlet boundary condition on $\partial\Omega_\theta$ should be prescribed with care. Indeed, it can be shown that the solution does not depend on the choice of the Dirichlet boundary conditions as soon as the values of the scalar temperature-like field

are prescribed at two different nodes belonging to different isovalues Oliver *et al.* (2002b). Last, the second-order tensor $\underline{\underline{Q}} = \boldsymbol{T}(\boldsymbol{x}) \otimes \boldsymbol{T}(\boldsymbol{x})$ can be interpreted as a conductivity-like tensor when coming back to the analogy with a heat conduction-like problem.

Furthermore, it is interesting to analyze the second-order conductivity tensor $\underline{\underline{Q}}$. Assuming this tensor is projected on the two-dimensional canonical basis, it is represented by the following 2×2 matrix:

$$[\boldsymbol{T}(\boldsymbol{x}) \otimes \boldsymbol{T}(\boldsymbol{x})] = \begin{pmatrix} T_X^2 & T_X T_Y \\ T_X T_Y & T_Y^2 \end{pmatrix} \tag{3.40}$$

where $\boldsymbol{T}(\boldsymbol{x}) = [T_X(\boldsymbol{x})\ T_Y(\boldsymbol{x})]^t$. Looking at Equation 3.40, it is obvious that the conductivity matrix can not be inverted, due to the nullity of its determinant. In other words, the rank of the conductivity matrix is not equal to 2. This feature may be the source of an ill-posed problem. In order to overcome this drawback, Oliver *et al.* (2002b) proposes to add a so-called algorithmic conductivity as follows:

$$[\boldsymbol{T}(\boldsymbol{x}) \otimes \boldsymbol{T}(\boldsymbol{x})]_{\varepsilon} = \begin{pmatrix} T_X^2 & T_X T_Y \\ T_X T_Y & T_Y^2 \end{pmatrix} + \varepsilon \begin{pmatrix} 1 & 0 \\ 0 & 1 \end{pmatrix} \tag{3.41}$$

where ε is a user-defined numerical parameter. The way to choose this numerical parameter is not clear at all. The only recommendation provided in the cited paper is to set this parameter to a small value. However, it is easy to show that the results obtained when solving the boundary value problem defined by Equations 3.39 are highly dependent on this numerical parameter. In addition, the fact of adding a diffusivity term, as shown in Equation 3.41, leads to the non-fulfillment of the governing equations 3.39. This last comment can be interpreted as a limitation of the global tracking strategy expressed in its initial form and has already been pointed out in the recent studies Feist et Hofstetter (2007a); Zhang *et al.* (2015).

For our first illustration of the use of the global tracking algorithm, the well-known experiment performed by Schlangen (1993) has been simulated. The specimen is a single edge notched (SEN) plain concrete beam subjected to asymmetric bending. The concrete cracking has been described by means of the tension/separation law derived from the class of anisotropic continuum damage models analyzed in the previous sections. Some of the results are shown in Figures 3.16 and 3.17 in terms of the crack path and the isovalues of the normal component of the displacement discontinuity, respectively. The heat conduction-like problem is solved only once, at the beginning of the nonlinear analysis. Three cases have been considered: (i) no tracking at all (see Figures 3.16a and 3.17a), (ii) tracking without considering previously intersecting finite elements during the crack propagation (see Figures 3.16b and 3.17b), and (iii) tracking considering previously intersecting finite elements during the crack propagation (see Figures 3.16c and 3.17c). In the first case, we noted many convergence issues, mainly due to the poor prediction of the crack orientations during the propagation leading to stress locking. This assumption is corroborated by the fact that sometimes no softening could be obtained. In the second case, we noted fewer numerical issues, but the stress states were not well described. In particular, we observed some residual stresses at some integration points. However, a softening branch at the beam scale could be described. In the last case, the information related to the intersecting finite element was exploited in order to take into account the position of the displacement discontinuity in the current finite element. No specific convergence issues were reported. In addition, we saw that the analysis was almost fully mesh-independent.

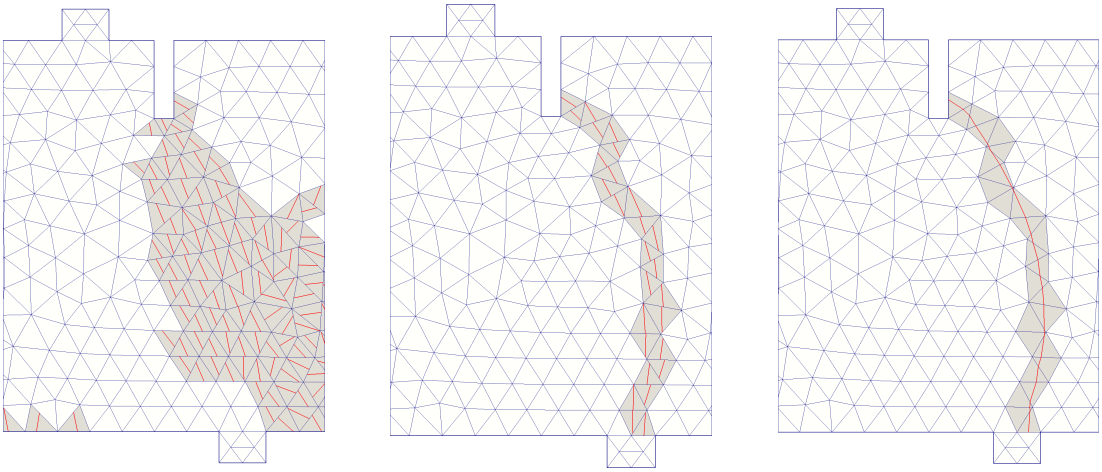

(a) No tracking.

(b) Tracking without considering intersecting finite element edges.

(c) Tracking considering intersecting finite element edges.

Figure 3.16: Crack path around the notch — gray finite elements having enhanced kinematics are highlighted in gray.

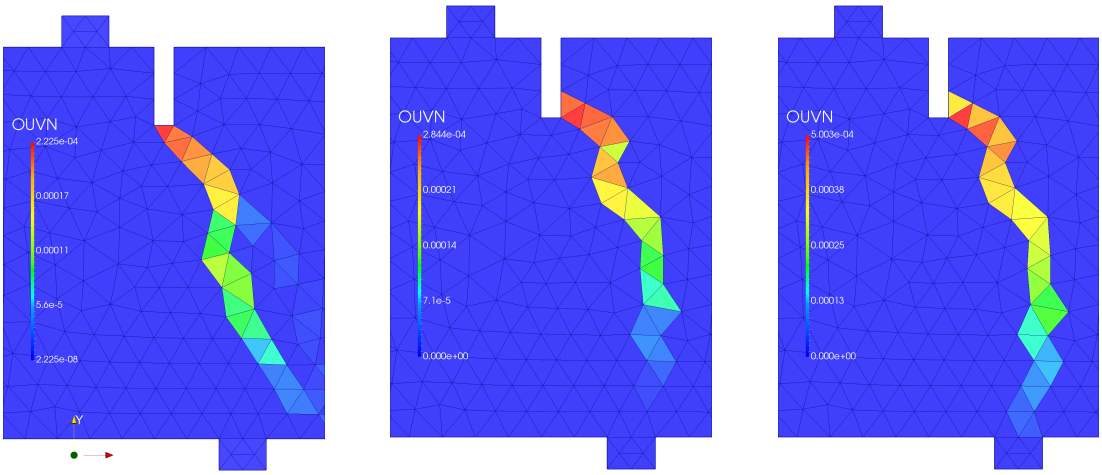

(a) No tracking.

(b) Tracking without considering intersecting finite element edges.

(c) Tracking considering intersecting finite element edges.

Figure 3.17: Normal component of the displacement discontinuity around the notch — gray finite elements having enhanced kinematics are highlighted in gray.

Towards a new interpretation of the boundary value problem to enforce the $\mathcal{C}^0$-geometrical continuity of the crack path With the aim of overcoming the aforementioned limitation, we have proposed a new interpretation of the initial boundary problem defined by Equations 3.39. To start with, let us consider a convection–diffusion problem that consists

in finding a scalar temperature-like field $\theta(\boldsymbol{x})$ such that:

$$\begin{cases} \underbrace{\boldsymbol{T}(\boldsymbol{x}).\nabla\theta(\boldsymbol{x})}_{Convective\ term} - \underbrace{\mathbf{div}\left(\alpha\nabla\theta(\boldsymbol{x})\right)}_{Diffusive\ term} & \forall \boldsymbol{x} \in \Omega \\ \theta(\boldsymbol{x})|_{\boldsymbol{x}\in\partial\Omega_\theta} = \theta^\star(\boldsymbol{x}) & \forall \boldsymbol{x} \in \partial\Omega_\theta \end{cases} \tag{3.42}$$

where α is a diffusion coefficient. Equation 3.42 is pretty close to the initial problem defined by the set of equations 3.39. Indeed, an additional term which can be interpreted as a diffusive contribution has been included. Let us focus on the one-dimensional case. Assuming a constant diffusion coefficient and considering on the one hand a first order upward scheme for the convective term and, on the other hand, a second order centered scheme for the diffusive term, the problem 3.42 gives the following set of equations:

$$\begin{cases} T\dfrac{\theta_i - \theta_{i-1}}{\Delta x} - \alpha\dfrac{\theta_{i+1} - 2\theta_i + \theta_{i-1}}{\Delta x^2} = 0 & i \in \{1, \cdots, n\} \\ \theta_0 = \theta^\star & i = 0 \end{cases} \tag{3.43}$$

where Δx is the one-dimensional spatial discretization step. To move forward, let us analyze the discretized expression of the convective term. After some analytical computations, it can be shown that:

$$\underbrace{T\frac{\theta_i - \theta_{i-1}}{\Delta x}}_{Upward\ scheme} = T\ \underbrace{\frac{\theta_{i+1} - \theta_{i-1}}{2\Delta x}}_{Centered\ scheme} - \underbrace{\frac{T\Delta x}{2}}_{Diffusion\ coefficient}\ \underbrace{\frac{\theta_{i+1} - 2\theta_i + \theta_{i-1}}{\Delta x^2}}_{Centered\ scheme} \quad i \in \{1, \cdots, n\} \tag{3.44}$$

Equation 3.44 shows that the discretized expression of the convective term by means by the first order upward scheme is equal to the discretized expression of this same term by using a first order centered scheme plus an additional contribution which is equal to the discretized expression of the diffusive term, considering a second order centered scheme. Comparing Equations 3.43 and 3.44, we note that a numerical diffusive term comes out naturally and is characterized by a diffusion coefficient $\frac{T\Delta x}{2}$, which is a function of a mesh characteristic length: Δx in the case of one-dimensional problems. This term is similar to the diffusion coefficient ε introduced in Equation 3.41 but is no longer user defined. This observation constitutes the fundamentals of upward discretization methods classically used in fluid mechanics Hughes (1987). Within the framework of our research, this feature is crucial since it allows recovering, in a rigorous and consistent manner, the initial heat-conduction-like problem arbitrarily enhanced with an additional term (see Equation 3.41). Higher-dimensional extensions of the numerical diffusion concept have been well established in the literature of fluid mechanics but have never been applied to enforce the $\mathcal{C}^0$-geometrical continuity of the crack path in the case of a strong discontinuity kinematics. More precisely, we focused on the case of two formulations. Given a vector field $\boldsymbol{T}(\boldsymbol{x})$, a straightforward multi-dimensional extension of the concept of numerical diffusion, the following formulation has been proposed Hughes (1987):

$$\begin{cases} \boldsymbol{T}(\boldsymbol{x}).\nabla\theta(\boldsymbol{x}) - \mathbf{div}\left(\dfrac{h_T\ ||\ \boldsymbol{T}(\boldsymbol{x})\ ||}{2}\nabla\theta(\boldsymbol{x})\right) & \forall \boldsymbol{x} \in \Omega \\ \theta(\boldsymbol{x})|_{\boldsymbol{x}\in\partial\Omega_\theta} = \theta^\star(\boldsymbol{x}) & \forall \boldsymbol{x} \in \partial\Omega_\theta \end{cases} \tag{3.45}$$

where h_T is a mesh characteristic length. Equation 3.45 describes the numerical diffusion as an isotropic process, which may not be appropriate for all situations. Another formulation, which assumes the numerical diffusion is only in the direction of the vector field $\boldsymbol{T}(\boldsymbol{x})$, has also been proposed:

$$\begin{cases} \boldsymbol{T}(\boldsymbol{x}).\nabla\theta(\boldsymbol{x}) - \mathbf{div}\left(\dfrac{h_T \mid\mid \boldsymbol{T}(\boldsymbol{x}) \mid\mid}{2}\dfrac{\boldsymbol{T}(\boldsymbol{x})\otimes\boldsymbol{T}(\boldsymbol{x})}{\mid\mid \boldsymbol{T}(\boldsymbol{x}) \mid\mid^2}\nabla\theta(\boldsymbol{x})\right) & \forall \boldsymbol{x}\in\Omega \\ \theta(\boldsymbol{x})_{\mid \boldsymbol{x}\in\partial\Omega_\theta} = \theta^\star(\boldsymbol{x}) & \forall \boldsymbol{x}\in\partial\Omega_\theta \end{cases} \tag{3.46}$$

Weak formulations associated with problems described by Equations 3.45 and 3.46 have been built and implemented in the finite element software Cast3M. In order to illustrate their capabilities, the SEN plain concrete beam has been considered once again. Figures 3.18a and 3.18b depict the isovalues of the temperature-like field. In the case of isotropic diffusion, the isovalues are much more stable: no oscillation appears. In contrast, in the case of directional diffusion, the isovalues seem to be less stable. Therefore, in the case of our problem, considering a direction diffusion does not seem to be sufficient.

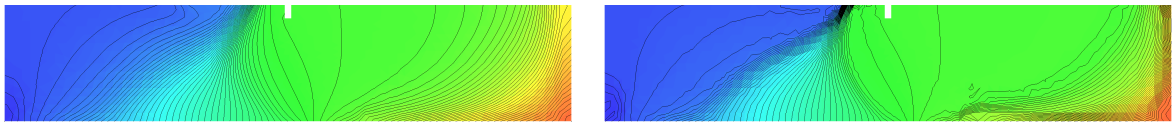

(a) Isotropic diffusion.

(b) Directional diffusion.

Figure 3.18: Isovalues of the temperature-like field.

As a consequence of the above considerations, the most appropriate strong formulation of the global tracking algorithm is given by Equation 3.18a. Another interesting feature of this method is related to the fact that the diffusion coefficient is not user-defined but is a function of a mesh characteristic length h_T. A sensivity analysis has been performed with different meshes. The results are presented in Figure 3.19. We can note that the isovalue starting from the notch changes. Indeed, the more refined the finite element mesh, the less intense the numerical diffusion. This feature is due to the fact that the diffusion coefficient decreases with the mesh size. In the case of an infinitely fine mesh, the diffusion coefficient becomes also infinitely small. The method is therefore consistent with the initial (ill-posed) problem (see Equation 3.40). In addition, the isovalue changes in a stable way with the mesh refinement, which is a very nice property when coupling this tracking approach with SDM.

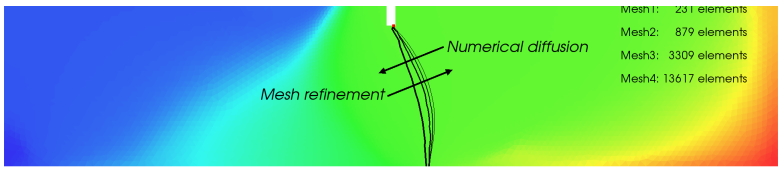

Figure 3.19: Isovalues of the temperature-like field for different meshes — root element plotted in red.

Online tracking strategy to handle cyclic loadings Usually, in the context of a nonlinear analysis, the boundary value problem related to the tracking strategy is solved only once, at the first pseudo-time. This gives satisfactory results in the case of quasi-static loading, in which the stress state flows continuously smoothly. The main reason for this choice is related to the fact the isovalues of the temperature-like field may change during the analysis Feist et Hofstetter (2007b), which leads to unstable crack propagation and stress locking issues. One

of the possibilities for overcoming this drawback lies in applying Dirichlet boundary conditions in Ω in order to make the isolines more stable. This strategy is not appropriate because the initial boundary value problem is drastically modified. Another solution lies in mixing the global algorithm with local strategies, requiring specific information related to the vicinity of the finite elements. A knowledge of the connectivity table becomes necessary, which makes this approach nonlocal Zhang *et al.* (2015). Despite the fact that good results may be obtained, the globality of the tracking strategy becomes lost.

In order to preserve the global nature of the tracking strategy, in the sense that the connectivity table does not need to be known, we introduced an alternative strategy based upon a modification of the former definition of the potential crack paths. More precisely, the former definition of the i^{th} crack path, denoted S_i, is expressed as follows at the localization pseudo-time t_0:

$$S_i(t_0) = \left\{ \begin{array}{r} \boldsymbol{x} \in \Omega \mid \theta(\boldsymbol{x}) = \theta_{S_i}(t_0) \\ \theta_{S_i}(t_0) = \theta(\boldsymbol{x}_r, t_0);\ \boldsymbol{x}_r \in \Omega \mid \mid\mid \underline{\underline{\sigma}}(\boldsymbol{x}_r, t_0) \mid\mid \geq f_t \end{array} \right. \tag{3.47}$$

where f_t is an initial threshold to be overcome in order to induce the strong discontinuity kinematics and $\mid\mid . \mid\mid$ is a tensorial norm. The previous definition implicitly assumes that the portion of the isovalue associated with the active part of the crack (i.e., points characterized by $[\boldsymbol{u}] \neq \boldsymbol{0}$) does not change any more. However, due to the approximate nature of a finite element solution, this feature is not generally ensured. As a consequence, stress locking effects may take place, mainly due to changes of the decomposition of a finite element. In order to overcome this drawback, the root element should be updated $\forall t \geq t_0$. This ensures taking into account both the active part S_{i_a} and the potential part S_{i_p} of the crack. In order to allow for online tracking and ensure a stable and consistent evolution of the isovalues, Definition 3.47 has been complemented by the following one:

$$\left\{ \begin{array}{r} S_i(t) = S_{i_a}(t) \cup S_{i_p}(t) = \bigcup_{k=0}^{n-1} \tilde{S}_{i_a}(t_k) \cup \tilde{S}_{i_p}(t_n) \\ \tilde{S}_i(t_k) = \{\boldsymbol{x} \in \Omega \mid \theta(\boldsymbol{x}, t_k) = \theta(\boldsymbol{x}_r, t_k),\ [\boldsymbol{u}](\boldsymbol{x}_r, t_k) \neq \boldsymbol{0}\} \\ \tilde{S}_i(t_n) = \{\boldsymbol{x} \in \Omega \mid \theta(\boldsymbol{x}, t_n) = \theta(\boldsymbol{x}_r, t_n),\ [\boldsymbol{u}](\boldsymbol{x}_r, t_n) = \boldsymbol{0}\} \\ \boldsymbol{x}_r \in \Omega \mid \mid\mid \underline{\underline{\sigma}}(\boldsymbol{x}_r, t_k) \mid\mid \geq f_t \end{array} \right. \tag{3.48}$$

where n is the total number of pseudo-time steps. The definition expressed by Equation 3.48 simply expresses the fact that the root element $\boldsymbol{x}_r$ is updated at each converging time step. In other words, the crack is tracked sequentially all along its propagation. The potential crack path is then defined sequentially, ensuring its stable evolution during the crack propagation. An illustration of the proposed online strategy is given in Figure 3.20. In particular, when no root element updating is used (see Figure 3.20a), we observe that the evolution of the isovalue leads to additional finite elements in which the strong discontinuity kinematics is activated. This is not consistent, because the strong discontinuity regime appears far from the crack tip. In contrast, when the root element is updated during the nonlinear analysis, complemented by a sequential building of the crack path, the latter effect is no longer observed, as shown in Figure 3.20b. The fact that the isovalues change in a stable way when employing online tracking opens the way to handling the complex case of cyclic loadings.

Numerical example

In the following, a structural case study is presented in order to illustrate not only the discrete traction/separation law accounting for mixed mode cracking but also the alternative tracking strategy discussed above. The specimen tested by Schlangen (1993) is considered once more.

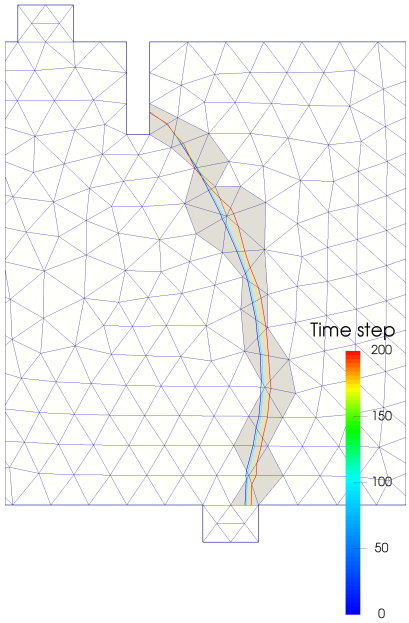

(a) Online tracking — without root element updating.

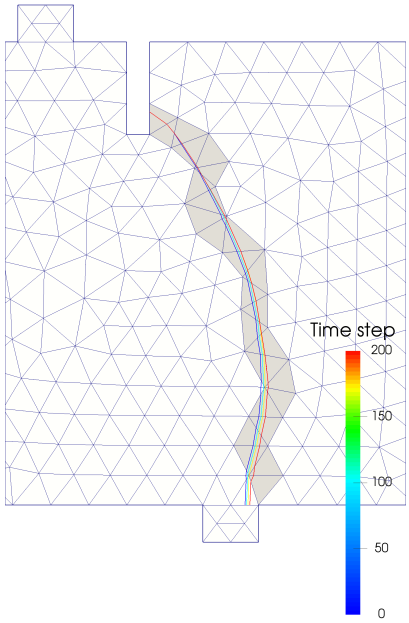

(b) Online tracking — with root element updating and sequential building of the crack path.

Figure 3.20: Comparison between online tracking strategies — gray area = strong discontinuity kinematics activated.

The loading setup is shown in Figure 3.21. The thickness of the beam is 50 mm and the rigid platens have a width of 20 mm. The asymmetry of the load is obtained by mounting a trimmer on the beam. Numerically, a rigid trimmer has been modeled in order to represent a controlled asymmetry of the load. The platens have been modeled by perfect rigid bodies. Nevertheless, in order to make the post critical analysis more robust, the loading was controlled in terms of vertical displacement. The online tracking strategy presented in the previous paragraph has been used. The concrete is described by the traction/separation law presented, derived from the class of anisotropic continuum damage models discussed above. Two cases have been considered: (i) only mode I is taken into account, and (ii) the mixed mode is included in the traction/separation law. In other words, in the first case, the tangential component of the displacement discontinuity vector is set to zero.

The results are presented in Figure 3.22. The quantitative experimental–numerical comparison highlights the preponderant role played by the tangential component of the displacement discontinuity vector. Indeed, when it is not taken into account, we note the inability of the computational model to exhibit softening. In addition, the deformed shape of the SEN beam shown in Figure 3.22c allows discerning the continuity of the crack path. Research aimed at handling the case of multicracking is ongoing.

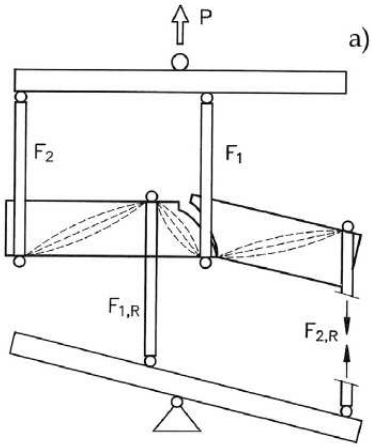

Figure 3.21: Loading setup according to Schlangen (1993) — SEN plain concrete beam.

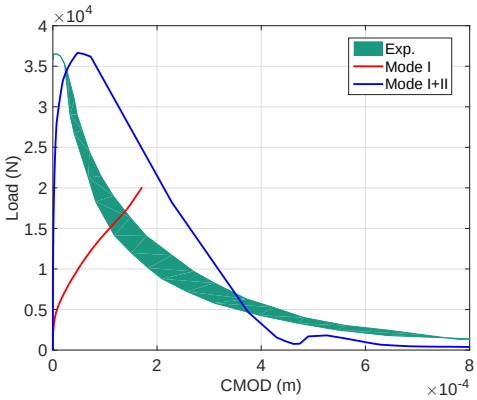

(a) Crack mouth opening displacement (CMOD).

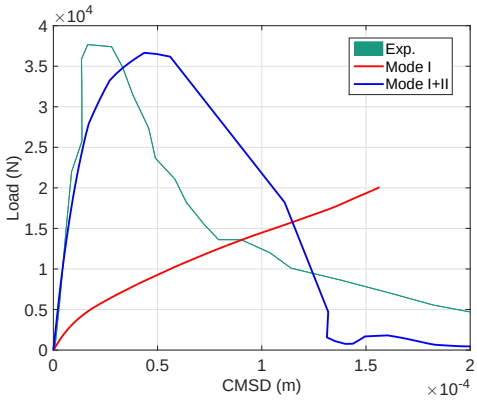

(b) Crack mouth sliding displacement (CMSD).

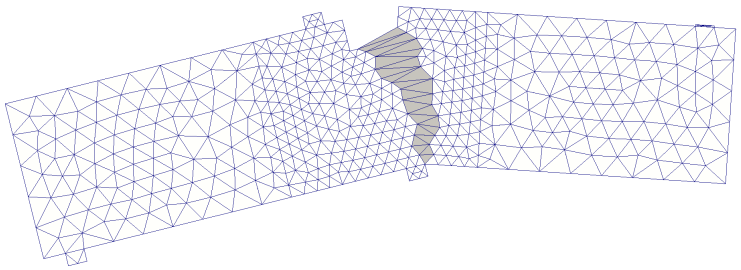

(c) Deformed shape.

Figure 3.22: Experimental–numerical comparisons — SEN plain concrete beam.

3.3 Structural dissipation capability

3.3.1 Effect of cracking on damping

Driving ideas

Nowadays, several sources of damping have been identified and related phenomena are recognized as contributing factors to the overall damping phenomenon. In the case of concrete or reinforced

concrete, one can point to (i) the frictional sliding between the surfaces of the crack, (ii) the bond at the steel/concrete interface that may induce residual displacements, (iii) radiation damping, and (iv) the energy dissipation at connections or the dissipation due to non-structural components Semblat *et al.* (2001). The most common way of modeling damping in structural analysis consists in including a velocity proportional force field in the balance equation. This field is characterized by a viscous damping matrix which can be computed according to several proposals made in the literature. In particular, the most common linear viscous damping model is Rayleigh's damping model Rayleigh (1877). In this case, the viscous damping matrix is expressed by the following equation:

$$\boldsymbol{C} = \alpha \boldsymbol{M} + \beta \tilde{\boldsymbol{K}} \tag{3.49}$$

where (α, β) are scalar coefficients chosen by the user, $\boldsymbol{M}$ is the mass matrix of the system, and $\tilde{\boldsymbol{K}}$ is a stiffness matrix. Much research has been carried out in order to give a physical meaning to the use of viscous damping. Most lies in considering the specific stiffness in Equation 3.49. For instance, $\tilde{\boldsymbol{K}}$ may be chosen as the secant matrix or as the tangent matrix Priestley *et al.* (1996); Priestley et Grant (2005); Petrini *et al.* (2008). However, recent studies Demarie et Sabia (2011); Jehel *et al.* (2014) have demonstrated that such strategies lead to inaccurate estimates of the displacement and internal forces in the structure when dealing with nonlinear time history analysis.

From the aforementioned discussion, it is clear that properly modeling the damping phenomenon is not an easy task. Coming back to physical considerations, damping can be seen as the result of local dissipative mechanisms. As a consequence, a natural way to reduce the contribution of the viscous damping matrix lies in better identifying the local constitutive models. A key issue is how to account for hysteretic phenomena. In the case of steel, effective constitutive models have been proposed in the literature. However, things are not so clear in the case of concrete, for which the hysteretic scheme needs to be properly identified. To do so, an experimental study has been carried out in order to acquire the appropriate experimental data related to the energy dissipation in reinforced concrete structural elements. This study was based on a reverse cyclic three-point bending loading applied to reinforced concrete beams. After post-processing the experimental results, the data has been used to analyze different hysteretic schemes for constitutive models of concrete. In this way, recommendations for the key mechanisms to be included in the constitutive model can be made, both to naturally represent the damping and to drastically reduce the contribution of the viscous damping matrix.

Experimental and numerical setups

Reinforced concrete specimen and loading Six rectangular reinforced concrete beams have been tested with different ratios of the longitudinal steel reinforcement, as presented in Table 3.3. They were subjected to cyclic loading, following two different loading paths. The specimens are 1.65 m in length, 0.22 m high, and 0.15 m wide.

In order to manifest the dissipative capability of the reinforced concrete specimen, two types of loadings have been considered, denoted by $L1$ and $L2$, respectively. The $L1$ loading is composed of several blocks. The first block creates a limited damage level. Then, the subsequent blocks create intermediate damage, and finally, the last ones create high levels of damage. Each block is divided into five cycles: cycle #1 creates a given damage level, cycles #2, #3, and #4 have an increasing intensity (1/3 of cycle#1, 2/3 of cycle #1 and 100% of cycle) and make the reinforced concrete specimens exhibit hysteretic effects. Cycle #5 aims at stabilizing the dissipated energy. The loading path $L1$ is presented in Figure 3.24a. The aim of such a loading is to evaluate the damping for different levels of progressive cracking. The $L2$ loading is composed of two blocks

of cycles. The first block creates a damage level and stabilizes the behavior of the beam. This block has an intensity of 80% of the predicted maximum load. Then, several blocks of three cycles are applied and each block has an increasing intensity. The loading path $L2$ is presented in Figure 3.24c. In comparison with the $L1$ loading, the $L2$ history tends to generate dissipation for a pre-cracked specimen, generating progressive erosion of the cracked surfaces.

Series	Beam	$E_c(MPa)$	$f_{cm}(MPa)$	$f_{tm}(MPa)$	Steel ratio (%)	Loading case
1	HA8-L1	26,500 (0.9)	32 (0.6)	2.6 (0.1)	0.67	Uncracked
	HA8-L2					Pre-cracked
2	HA10-L1	28,500 (3.5)	34 (2.5)	2.7 (10)	1.05	Uncracked
	HA10-L2					Pre-cracked
3	HA12-L1	29,000 (5.2)	38 (12.3)	2.7 (1.6)	1.51	Uncracked
	HA12-L2					Pre-cracked

Table 3.3: Specimen specifications and loading characteristics — E_c = Young's modulus for the concrete — f_{cm} = Compressive strength of the concrete — f_{tm} = Tensile strength of the concrete — Values in brackets stands for the coefficients of variation.

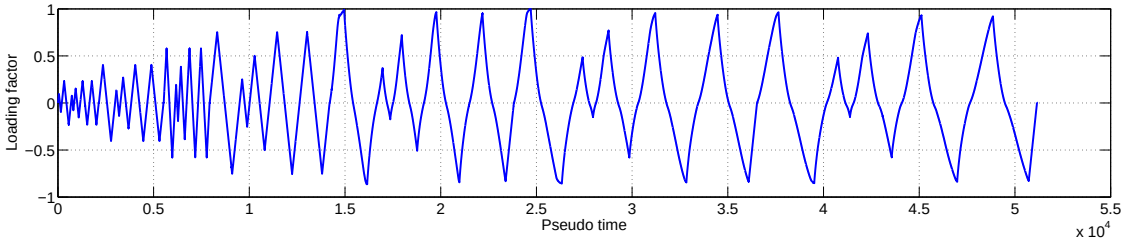

(a) $L1$ loading.

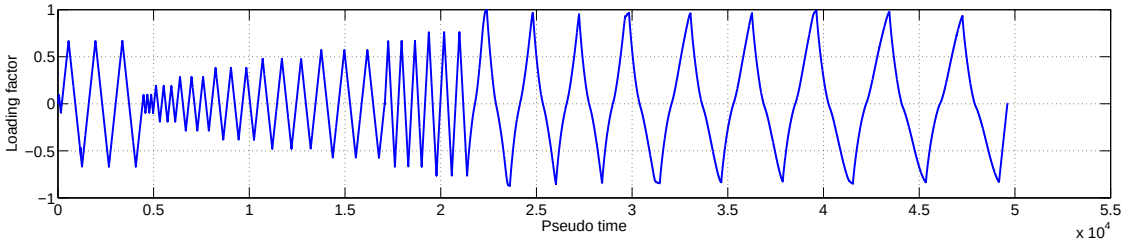

(b) $L2$ loading.

Figure 3.23: Description of the loadings — loading factor = percentage of maximum force.

Equivalent damping ratio In order to quantify the energy dissipation related to hysteretic phenomenon, in particular the part due to cracking, the damping of the structure has been quantified by mean of the equivalent viscous damping ratio. For the case of a symmetric hysteretic response, the equivalent viscous damping ratio ξ_{eq} can be expressed by Equation 3.50, as proposed by Jacobsen (1960).

$$\xi_{eq} = \frac{A_h}{4\pi A_e} = \frac{A_h}{2\pi V_m D_m} \tag{3.50}$$

where A_h stands for the dissipated energy within a given cycle, V_m and D_m are the mean values of the peak force and displacement, V_{max}, V_{min} and D_{max}, D_{min} are respectively the maximum and minimum values of the peak force and displacement, and A_e is the elastic strain energy stored

in the equivalent linear elastic system having an effective stiffness equal to $k_{eff} = V_m/D_m$. However, reverse cyclic responses are rarely perfectly symmetric. This can be explained by the fact that concrete cracking induces anisotropy. Consequently, Equation 3.50 can not be used straightforwardly. According to Varum (2003), the equivalent viscous damping can be evaluated for each half-cycle of the load/displacement curves. The principle lies in defining a half-cycle by two successive zero load points. Then, for each half-cycle, the maximum generalized displacement D_{max} and the corresponding generalized load V_{max} are determined. Finally, the strain energy can be determined by computing the area $A_{half\ loop}$ and the equivalent damping ratio is computed according to Equation 3.51 for each half-cycle:

$$\xi_{eq} = \frac{1}{\pi} \frac{A_{half\ loop}}{V_{max} D_{max}} \tag{3.51}$$

Constitutive models In order to analyze the influence at the member scale of the way the local hysteretic effects are taken into account, several constitutive laws have been considered. The first one was proposed by LaBorderie (1991) and can be considered as a reference law since it has been used for a large range of applications. Nevertheless, it is known that this law does not account for hysteretic effects, and therefore it is interesting to compare its results with those from more refined models accounting for this effect. In the following, the reference model is referred to as the "No Hysteretic Dissipation" (NHD) model. The second and third constitutive models considered are derived from that presented in Section 2.2.3. Both models account for the unilateral effect with different unilateral criteria accounting for crack closure. In the case of the second model, the unilateral effect criterion is expressed in terms of stresses, whereas in the case of the third model, it is expressed in terms of strains. The main consequence of these two assumptions is the size of the hysteretic loops and therefore, the capability of dissipating energy that will contribute to the structural damping. In the following, the second model is referred to as the "Low Hysteretic Dissipation" (LHD) model and the third one as the "High Hysteretic Dissipation" (HHD) model. The steel reinforcing steel bars are modeled by the well known constitutive law of Menegotto Pinto, as modified by Filippou *et al.* (1983). This constitutive model accounts for both isotropic and kinematic nonlinear hardenings. In particular, Bauschinger's effect can be described. The material parameters of all the constitutive models considered have been identified according the mechanical tests carried out within the framework of the experimental program. The uniaxial reverse cyclic responses of the three constitutive models which have been considered are shown in Figure 3.24.

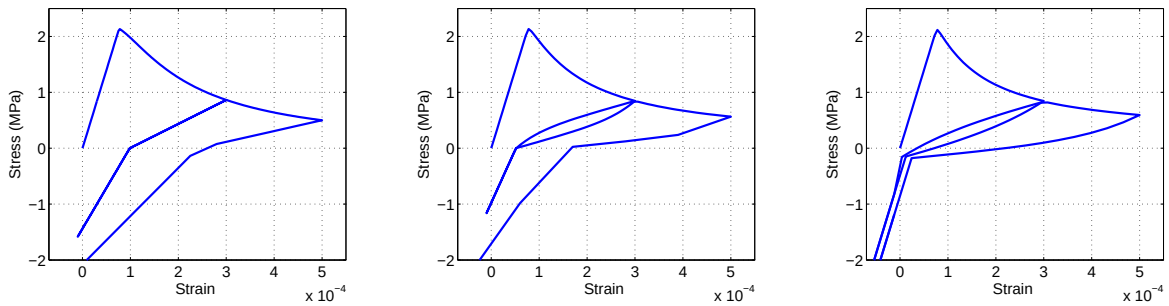

(a) NHD model. (b) LHD model. (c) HHD model.

Figure 3.24: Uniaxial reverse cyclic responses.

Representative results

The numerical and the experimental equivalent viscous damping ratios have been compared with each other. The results are shown in Figure 3.25 for all the reinforced concrete beams. Noticeable differences between all the models can be observed. The experimental results exhibit an equivalent viscous damping ratio at least equal to 1% for every cycle. The NHD model is not able to damp for most of the cycles that are lower than 60% of the maximum load. The HHD model allows obtaining the best results in the case of the $L1$ loading, as one can see in 3.25. In the case of the $L2$ loading, the LHD model allows obtaining results that are close to the ones obtained by the NHD model. The HHD model leads to the best results even if the damping is overestimated when the reinforcing bars yield. This is not surprising because the local dissipation due to hysteretic effects is higher than in the case of the other models. In the case of the low level of loading, the dissipation may come from the hinge device and some compression near the loading system. The study of the equivalent damping ratio has clearly revealed the influence of the hysteretic loop scheme on the ability of the model to dissipate energy. These results are of primary importance since they allow understanding the ability of the models to describe the damping in a physical way. Based on these results, one can conclude that the HHD model seems to be able to describe the energy dissipation contributing to damping.

Nevertheless, the simulations performed with the HHD constitutive law lead to satisfactory results as long as the steel reinforcements do not yield. In the yielding region, the damping is overestimated. When plasticity is activated, phenomena such as steel/concrete interface sliding, local shear degradation, and pinching also appear at the same time. These mechanisms are not included in the model. This result seems helpful for practical applications, since it gives some guidelines for realistically taking into account not only the hysteretic effect but also the crack closure effect. Considering the main features of this constitutive law, it can be stated that the unilateral effect should be treated in terms of strains, meaning that the stiffness recovery is activated as soon as the total strain becomes negative. Furthermore, the hysteretic effect should be allowed even though the Cauchy stress (or related indicator) becomes negative. All in all, if the major sources of dissipation are included in the constitutive models at the material scale, a physical explanation for damping can be given and the contribution of the viscous damping matrix can be drastically reduced. As a consequence, the damping may no longer be seen as a tuning parameter.

3.3.2 Effect of corrosion on the ductility

Driving ideas

Nowadays, stakeholders are reporting a loss of performance of existing structures due to the presence of aggressive agents. This usually starts with a decrease of the durability of the constituent materials, and is followed by a decrease in the serviceability. If no specific maintenance action is undertaken, the structural safety of the existing structures can be affected. Then, the key question lies in finding a way to preserve or even improve existing structures by mean of economical solutions. In such a context, it is becoming necessary to carry out in situ strength assessments in order to estimate the safe load-carrying capacity of existing reinforced concrete structures. Within the framework of the European project *Sustainable Bridges* Olofsson *et al.* (2005), in situ tests of existing bridges were carried out. One of them was a two-span reinforced concrete bridge located in Sweden, in the city of Ornskoldsvik. Benefitting from the availability of the experimental data, we focus on this large-scale case study in order to assess the utility of both (for the concrete and and for the steel/concrete interface) constitutive models we developed. In particular, the research we conducted aimed at quantifying the effects of local degradation on the overall dissipative ability of the reinforced concrete bridge.

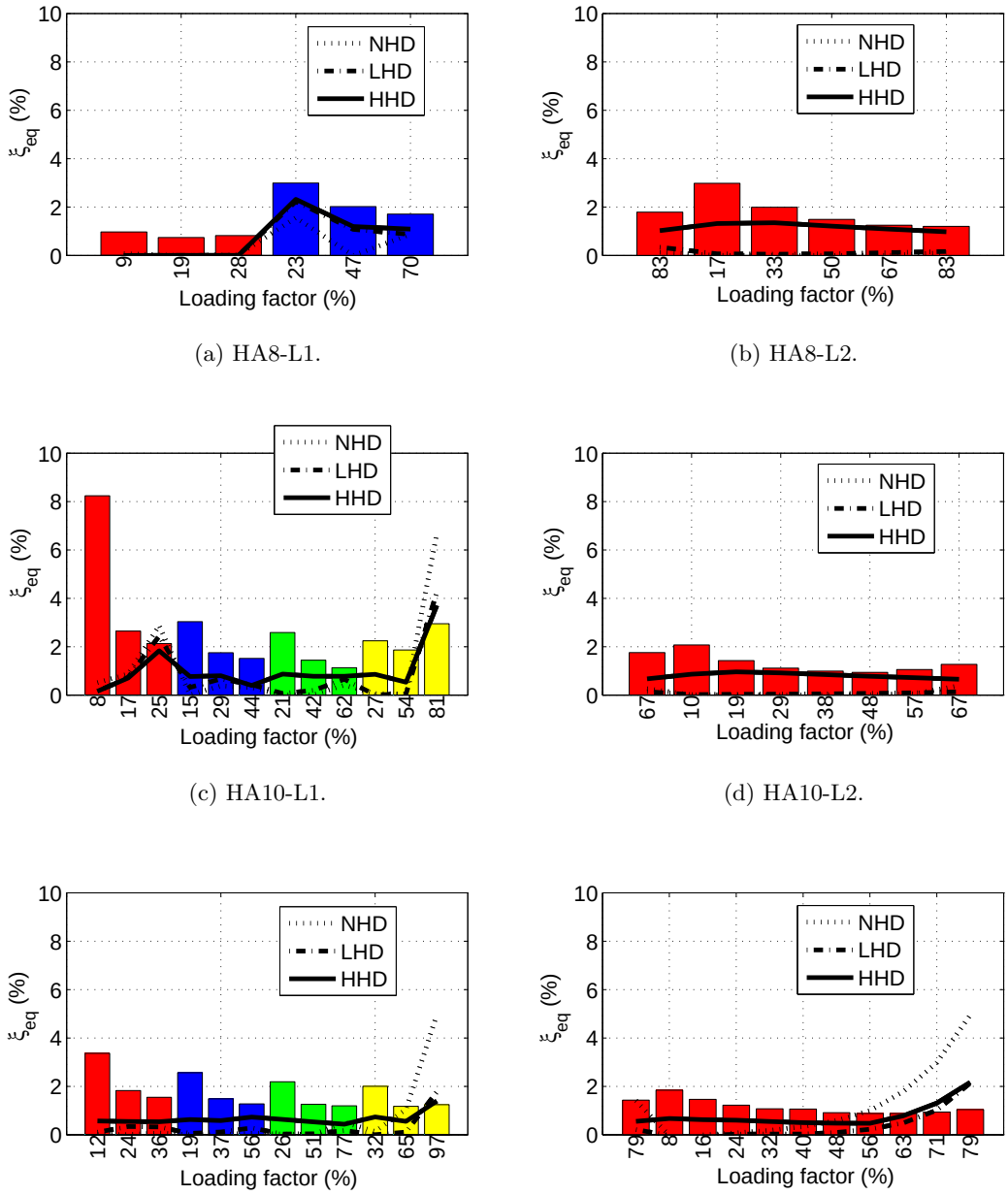

(a) HA8-L1.

(b) HA8-L2.

(c) HA10-L1.

(d) HA10-L2.

(e) HA12-L1.

(f) HA12-L2.

Figure 3.25: Equivalent viscous damping ratio versus loading factor.

To reach this objective, a two-dimensional finite element model has been developed and calibrated in order to describe the overall mechanical response of the reinforced concrete bridge when subjected to a coupling shear/bending loading. Then, local effects, such as a decrease in the cross section of the steel and the loss of the bond at the steel/concrete interface, were assumed. The consequences of such local degradations on the structural response of the reinforced concrete bridge have been analyzed in order to discern some trends helping to understand how it would have behaved if it had been corroded.

Large-scale in situ tests

The bridge was built in 1955 and was taken out of service in 2005 due to the construction of a new high-speed railway, the Bothnia Line. The bridge was planned to be demolished in 2006 and was loaded to failure after its decommissioning in order to assess its ultimate load carrying capacity after a 50-year service period. A picture of the reinforced concrete bridge and part of the formwork drawings are shown in Figures 3.26a and 3.26b, respectively.

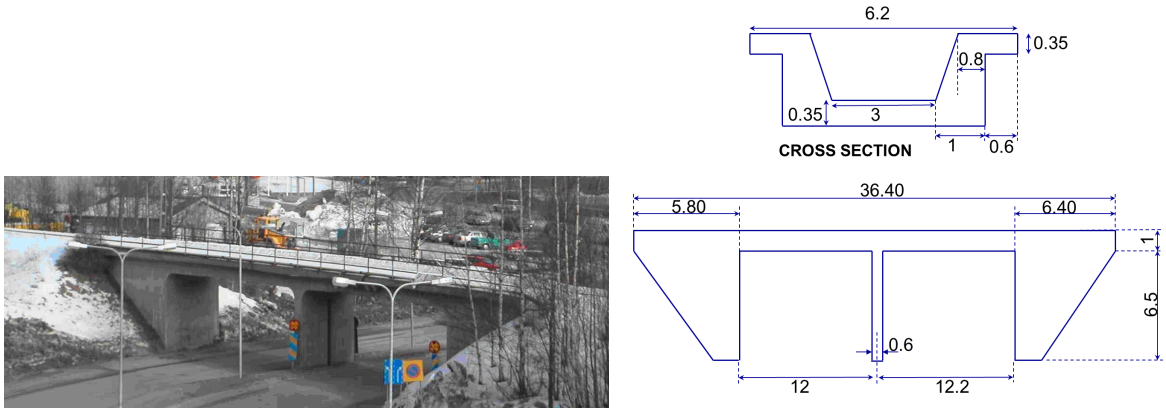

(a) Side view.

(b) Geometry — dimensions in meters.

Figure 3.26: Description of the Ornskoldsvik bridge.

The railway bridge was tested with a vertical point load at midspan, as shown in Figure 3.27. The experimental testing setup was designed to ensure that the bridge failure would be the result from a combination of shear and bending. The instrumentation included measurements of the actual material properties of the steel in the reinforcement bars and of the concrete. The deflections and strains in reinforcement bars were monitored during the loading process in order to check the deformations and sectional forces. In order to prevent an unwanted bending failure (without shear), the bridge slab was strengthened with rectangular bars of carbon fiber-reinforced polymers (CFRP), which were mounted as near-surface mounted reinforcement by drilling out grooves in the slab. The loading was displacement-controlled in order to make sure the post-peak region could be captured.

Figure 3.27: Loading setup of the Ornskoldsvik bridge.

Structural model

The proposed finite element analysis was performed under the plane stress state assumptions. The steel reinforcement bars were meshed explicitly. The bridge's strengthening by the addition of the CFRP bars was also taken into account. In order to improve the numerical robustness of the nonlinear analysis, small linear elastic areas were considered close to the boundary conditions. The finite element mesh is depicted in Figure 3.28.

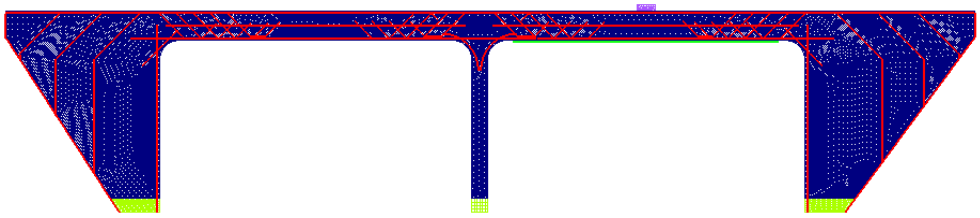

Figure 3.28: Finite element mesh of the Ornskoldsvik bridge — concrete in blue; reinforcing bars in red; elastic platen in purple; elastic areas and CFRP bars in geen.

The mechanical behavior of the concrete has been described by the constitutive model presented in Section 2.2.2. The steel/concrete interface has been taken into account by inserting two-dimensional zero-thickness finite elements between the reinforcing bars and the surrounding concrete. The constitutive model which has been presented in Section 2.4.1 was used. The steel bars were modeled by the law of Menegotto–Pinto. The CFRP bars were assumed to be linear elastic. The material parameters related to both the concrete and steel constitutive models were identified thanks to the mechanical characterization tests carried out within the framework of the experimental study. In contrast, the mechanical response of the steel/concrete interface was poorly documented. It was decided to simulate classical pull-out tests up to failure based upon the experimental study reported in Dominguez (2005). That data was employed because of the similarity of the mechanical properties related to concrete and steel. The material parameters were then identified by performing an inverse analysis. Due to the lack of local experimental data, no better option was available at the time this work was carried out.

The numerical analysis was carried out with the finite element software Cast3M. The numerical–experimental comparison in terms of load–midspan displacement is shown in Figure 3.29. The proposed finite element model gives results in pretty good agreement with those coming from experiment. The experimental data allows discerning three main degradation stages: first a brief linear stage, which shows that all the constitutive materials remain fully elastic (from a midspan displacement equal to 0.0 mm up to 2.89 mm), then a nonlinear stage, which highlights the cracking of the concrete (from a midspan displacement equal to 2.89 mm up to 8.25 mm), and lastly, a stage in which the steel reinforcements are yielding (from a midspan displacement equal to 8.25 mm up to failure). The numerical results obtained by the proposed finite element model and by the *Sustainable Bridges* project are both in accordance with the experiment. However, the numerical simulation performed in the *Sustainable Bridges* project tends to underestimate the load carrying capacity of the bridge. Several hypotheses can be made to explain this difference. In particular, no frictional effect is included in the constitutive model used in the *Sustainable Bridges* project. This key mechanism seems rather preponderant when shear occurs. The fact that CFRP bars were added to the bridge before testing decreases the effects of bending cracks and improves the probability of obtaining a shear failure, and this is what happened, as shown in Figure 3.30a. The principal strain pattern computed at the failure is shown in Figure 3.30b. A pretty good agreement can be observed between the numerical failure mechanism and the experimental one.

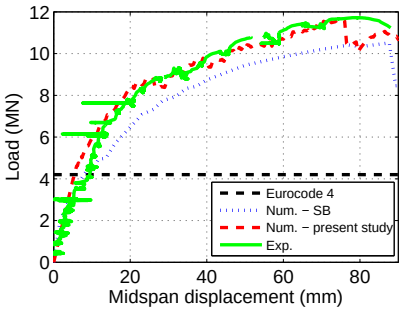

Figure 3.29: Experimental–numerical comparison of load–midspan displacement response.

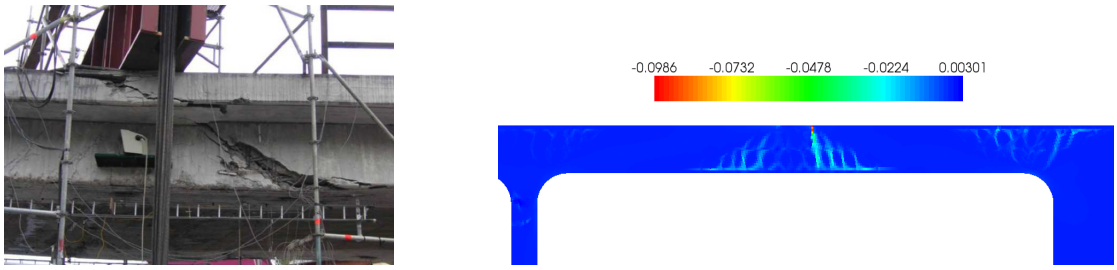

(a) Cracking pattern at failure.

(b) Principal strain localization area.

Figure 3.30: Experimental–numerical comparison of the failure mechanism.

Corrosion and dissipative capability

Known as one of the major effects related to the phenomenon of corrosion, the reinforcement cross section tends to decrease because of the electrochemical process involved. In order to study the evolution of the load carrying capacity due to the reduction in the cross section of the steel, the finite element analysis presented previously has been performed considering four different steel distributions in the tested span of the bridge. The cross sections of steel reinforcement bars have been considered as Gaussian random variables. The mean was chosen equal to 100%, 85%, 65% and 50% of the initial cross section. The coefficients of variation were all chosen equal to 1%. The coherence function is an exponential function, which required the identification of an internal length. In order to ensure a certain continuity level between the reinforcement, it was chosen equal to the mean bar element length. It is interesting to note that the iterative incremental procedure converged more and more slowly as the cross section was reduced. The numerical results are given in Figure 3.31.

As expected, the load carrying capacity of the bridge decreases with the reduction of the reinforcement cross sections. However, two specific features can be pointed out. The decrease of the cross section acts almost in proportionally on the load carrying capacity of the bridge. Although no experimental result is available at such a scale, as far as the authors' knowledge extends, similar observations were made in Jason *et al.* (2010), who performed direct tensile mechanical tests on steel bars in order to study the effect of the reduction of the cross section on the stress/strain response. A bi-linear relation linking the reduction in the cross section to the steel's critical stress was found. The simulation presented in Figure 3.31 clearly shows that one could expect a similar result for a large-scale reinforced concrete structure. One can also observe that a local reduction in the reinforcement's cross section clearly acts on the whole behavior of the structure. Although these results seem to be interesting because they give some direction

for further research, the present authors insist on the fact that they are only qualitative, due to the lack of experimental data at such a scale.

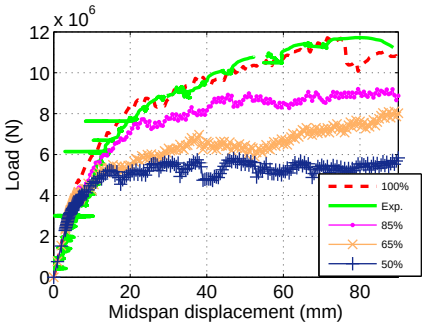

Figure 3.31: Sensitivity of the load–midspan displacement with respect to steel cross section reduction.

Another major effect due to the phenomenon of corrosion is the change in the bond strength at the steel/concrete interface. In order to analyze the influence of this effect on the structural response of the bridge, four degrees of corrosion (expressed in terms of steel mass loss) were chosen: 0.0%, 4.0%, 5.0% and 7.0%. The results are shown in Figure 3.32. As expected, one can see that the carrying capacity decreases with an increase in the degree of corrosion. Nevertheless, regarding the results previously discussed, one can conclude that the change in the bond strength is less damaging than the reduction in the cross section. This result goes in the same direction as those presented in Jason *et al.* (2010). When a structure is corroded, the bond strength at the steel/concrete interface reaches an asymptotic value before the steel cross section is totally consumed by the electrochemical process. In other words, even though the bond strength has reached a critical value, the carrying capacity of the structure keeps on decreasing due to the reductionin the cross section of the steel. These results also corroborate those obtained in Ouglova (2004).

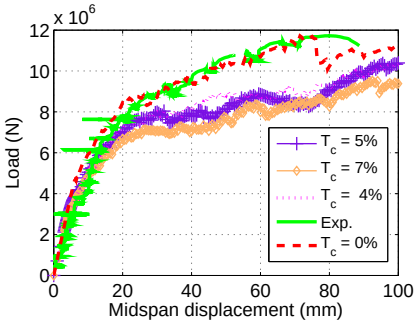

Figure 3.32: Sensitivity of the load–midspan displacement to the bond properties.

3.4 Probabilistic analysis

3.4.1 Driving ideas

Meaningful structural assessments require accurate and efficient modeling strategies, which are often nonlinear, as shown in the previous sections. The computational labor required by a single deterministic analysis is often great. The input parameters of a finite element model

are identified from experience and therefore have an uncertain nature. Taking into account uncertainties is an important feature that can improve the decision-making process in various fields of activities. Structural reliability is a theoretical framework able to take into account parameter uncertainties Cremona (1995). The reliability assessments of a mechanical system requires the computation of several quantities of interest, among them, the probability of failure P_f. Its determination depends on the probability distribution functions (PDF) of the input variables that have been identified as preponderant. These random variables can be related to many aspects, such as the geometry, material parameters (tension strength, Young's modulus, etc.), and boundary conditions (stiffness, reaction, wave heights, wind pressures, etc.). The probability of failure can be seen as the probability of exceeding a given threshold. To be more specific, the random variables $\boldsymbol{X} = (X_1, \cdots, X_d)$ are gathered into a random vector $\boldsymbol{X}$ and are called the basic variables. They are defined by a multivariate PDF $p_{\boldsymbol{X}}(\boldsymbol{x})$. The aforementioned threshold is classically expressed by a performance function $g_{\boldsymbol{X}}(\boldsymbol{x})$. Then, the basic space can be split up into three regions: the safety domain $\mathcal{S} = \{\boldsymbol{x} \in \mathbb{R}^d : g_{\boldsymbol{X}}(\boldsymbol{x}) > 0\}$, the failure domain $\mathcal{F} = \{\boldsymbol{x} \in \mathbb{R}^d : g_{\boldsymbol{X}}(\boldsymbol{x}) < 0\}$, and the limit state $\mathcal{L} = \{\boldsymbol{x} \in \mathbb{R}^d : g_{\boldsymbol{X}}(\boldsymbol{x}) = 0\}$. The probability of failure of a mechanical system can be defined by

$$P_f = \int_{\mathcal{F}} p_{\boldsymbol{X}}(\boldsymbol{x}) d\boldsymbol{x} \tag{3.52}$$

Several methods have been developed to estimate the results of the integration of the PDF over the failure domain. However, in the case of complex structural models, the limit state function is only rarely defined in a closed form and may be highly nonlinear. Therefore, it is necessary to evaluate the structural response through a given model. If the model is complex (which is often the case when refined structural assessment are the goal), the number calls to the structural model will control the time consumption related to the failure probability estimation. An way to reduce the number of performance function calls is to build an analytical approximation of the performance function. Among the techniques that have been recently developed, one can find the classical response surface method Bucher et Bourgund (1990) as well as statistical learning methods such as neural networks and support vector machines (SVMs) Papadrakakis *et al.* (1996); Hurtado et Alvarez (2001); Hurtado (2002, 2004). In addition, the number of structural model calls may further decrease if an appropriate structural design of the input parameters is employed to build an analytical approximation of the limit state function. Based upon these considerations, we proposed a strategy benefitting from both the SVM approach and experimental design theory in order to compute a limit state approximation allowing a reduction of the structural model calls.

According to the aforementioned considerations, it appears that a set of material parameters may be represented by a random vector $\boldsymbol{X}$, defined by a joint PDF $p_{\boldsymbol{X}}$ on an appropriate probability space. This PDF is generally defined according to the current state of knowledge, characterized by a set of realizations $\boldsymbol{x}$. In particular, a closed form expression of the PDF may be naturally determined by the maximum entropy principle. However, when additional experimental data are acquired from either expert judjements or from measurements, the PDF should be updated. In other words, a robust updating strategy should be used in order to allow including additional pieces of knowledge in the probabilistic description of the set of material parameters considered as uncertain.

In the following, we present a summary of the work we carried out in order to (i) improve the efficiency of probabilistic methods by minimizing the number of the structural model calls and (ii) to update a priori joint PDFs based upon new pieces of knowledge.

3.4.2 Equational framework

An improved response surface method

SVM is a technique which aims at building a relation between two sets: the first one is called the input data $(\boldsymbol{x}_i)_{i=1,\cdots,n}$ and the second one is called the response data $(y_i)_{i=1,\cdots,n}$. Both sets can be gathered and lead to the definition of the training set $\{(\boldsymbol{x}_1, y_1), \cdots, (\boldsymbol{x}_n, y_n) \in \overset{n}{\underset{i=1}{\times}} (\mathbb{R}^d \times \mathbb{R})\}$. Within the framework of our research, we defined the input set $(x_i)_{i=1,\cdots,n}$ to be a realization of the vector of material parameters. The output set $(y_i)_{i=1,\cdots,n}$ was defined as the values of the limit state function. The SVM provides a closed form expression $\tilde{g}_{\boldsymbol{X}}$ linking both these sets. In the nonlinear case, it is expressed as follows:

$$\tilde{g}_{\boldsymbol{X}}(\boldsymbol{x}) = \sum_{i=1}^{n} (\alpha_i - \alpha_i^\star) K(\boldsymbol{x}, \boldsymbol{x}_i) - b \tag{3.53}$$

where α and $\alpha_i^\star$ are Lagrange multipliers, K is a kernel function, and b is a scalar called the bias. $(\alpha_i, \alpha_i^\star)_{i=1,\cdots,n}$ and b can be computed by solving a quadratic optimization problem with the appropriate constraints. A detailed presentation of the solving strategy can be found in Cortes et Vapnik (1995).

In addition to building an analytical approximation of the limit state function through an SVM, it is possible to appropriately choose the samples to be evaluated by the structural model in order to make the SVM approximation as close as possible to the limit state. With this aim, experimental designs can be used. An experimental design consists in a specific arrangement of the samples to be evaluated. To make this clearer, two examples of well-known experimental designs are presented in Figure 3.33.

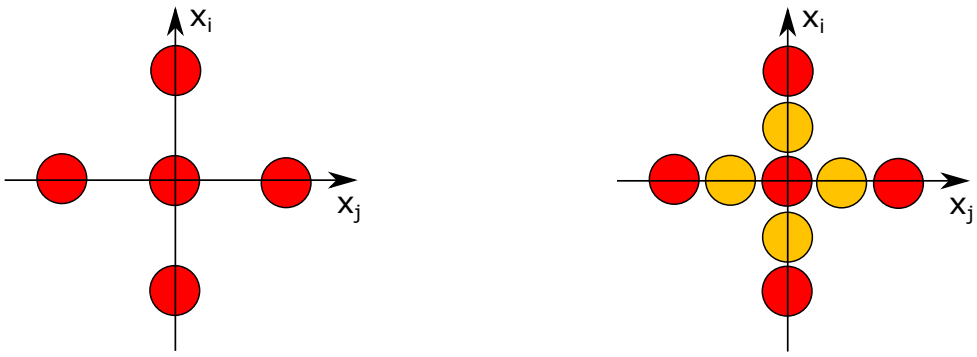

(a) Star (b) Modified star

Figure 3.33: Classic experimental designs in a two-dimensional physical space.

Each sample, in a given experimental design, can be subjected to a rotation using the rotation matrix P. Figure 3.34 shows both the initial and final positions of a star experimental design. The objective of this rotation is to place the training samples in an orthogonal plane to the gradient of the limit state. This way, one expects to obtain a better local approximation of the limit state function. Indeed, the quality of the response surface is highly dependent on the knowledge of the implicit (but unknown) limit state. The closer the samples are to the implicit limit state, the more accurate the approximation will be. Therefore, considering the case of a symmetric experimental design (with distinct branches, such as the star experimental design, for instance), the geometrically organized samples can become very close to the implicit limit state if the design is rotated as proposed in the present approach. One can note that the rotation

is performed with respect to the center of the experimental design and not with respect to the design point of the space.

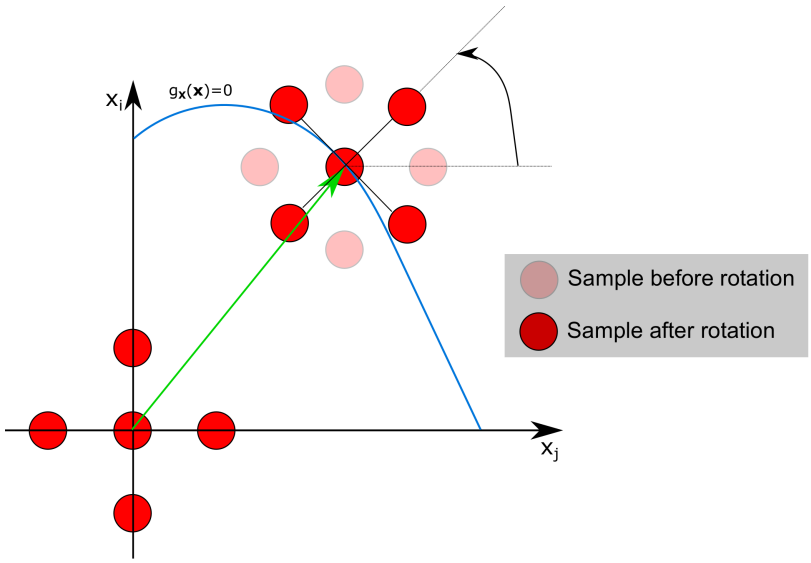

Figure 3.34: Initial and final positions of the proposed adaptive experimental design — application to the star configuration.

Benefitting from the appropriate experimental design leads to choosing the samples to be evaluated in an optimal way. Furthermore, because the SVM provides a closed form expression of the limit state approximation, it possible to derive not only the gradient but also the Hessian matrix. The gradient vector can be expressed as follows:

$$\nabla \tilde{h}_{\boldsymbol{U}}(\boldsymbol{u}) = \left(\frac{\partial \tilde{h}_{\boldsymbol{U}}(\boldsymbol{u})}{\partial u_1}, \cdots, \frac{\partial \tilde{h}_{\boldsymbol{U}}(\boldsymbol{u})}{\partial u_d} \right)^t \tag{3.54}$$

where $\tilde{h}_{\boldsymbol{U}}$ stands for the limit state approximation with normally standard distributed random variables. After some analytical computations and considering a radial basis function as a kernel function, we end up with the following expression:

$$\frac{\partial \tilde{h}_{\boldsymbol{U}}(\boldsymbol{u})}{\partial u_k} = -\frac{1}{\sigma^2} \sum_{i=1}^{n} (\alpha_i - \alpha_i^\star)(u^{(k)} - u_i^{(k)}) K(\boldsymbol{u}, \boldsymbol{u}_i) \tag{3.55}$$

where σ is a scalar parameter. From the above expression of the gradient, one can easily deduce the Hessian matrix H:

$$H_{jk} = \begin{cases} \dfrac{1}{\sigma^4} \displaystyle\sum_{i=1}^{n} (\alpha_i - \alpha_i^\star) K(\boldsymbol{u}, \boldsymbol{u}_i)(u^{(k)} - u_i^{(k)})(u^{(j)} - u_i^{(j)}) & \text{if } j \neq k \\ -\dfrac{1}{\sigma^2} \displaystyle\sum_{i=1}^{n} (\alpha_i - \alpha_i^\star) K(\boldsymbol{u}, \boldsymbol{u}_i)(1 + \dfrac{u^{(j)} - u_i^{(j)}}{2})(1 - \dfrac{u^{(j)} - u_i^{(j)}}{2}) & \text{if } j = k \end{cases} \tag{3.56}$$

Once the Hessian matrix has been obtained, the curvatures can be deduced and well known approximations of the probability of failure, such as Breitung's, Tvedt's, or Hohenbichler's, can be used Adhikari (2004).

Bayesian updating strategy for structural applications

A Bayesian network (BN) associated with a set of variables $\boldsymbol{X} = (X_1, \cdots, X_n),\ n \in \mathbb{N}^\star$, is a way of representing a joint PDF between those variables. The network consists of two components: a network structure G and a set P of conditional probabilities Friedman *et al.* (1997); Pearl (2014). G encodes the conditional dependencies between the variables. It is an n-node directed acyclic graph (DAG) in which the nodes correspond to the random variables identified. For all $(i, j) \in \mathbb{N}^\star \times \mathbb{N}^\star$ such that $1 \leq i, j \leq n$, there exists an arc in G from X_i to X_j if and only if X_j is conditionally dependent on X_i. The set P describes the conditional dependencies between the set of variables that are directly connected to arcs in the structure G. If a node X_i has arcs coming in from the set of nodes $(X_{i_1}, \cdots, X_{i_k})$, then P contains the PDF of X_i conditioned on the variables $(X_{i_1}, \cdots, X_{i_k})$. The set of conditional probabilities is usually represented by a conditional probability table (CPT), whose determination involves a computational cost.

Since the BN structure G is acyclic, the nodes of G can be topologically sorted in such a way that if there is an arc from a node X_i to another node X_j, then X_i must precede X_j in the ordering. The acyclicity of G also induces ancestral relations. If there is an arc from X_i to X_j, then X_j is called a child of X_i and X_i is called a parent of X_j. For each j, $\pi(i)$ denotes the set of all parents of X_i and $\kappa(i)$ denotes the set of children of X_i. The joint PDF related to the set of variables $(X_1, \cdots, X_n)$ can then be represented in the following factored form:

$$P(X) = \prod_{i=1}^{n} p(X_i \mid X_{\pi(i)}) \tag{3.57}$$

where $P(X)$ stands for the probabilty that X is realized, $p(X_i \mid X_{\pi(i)})$ is the conditional probability of X_i given the assignment to $X_{\pi(i)}$. From a practical point of view, the use of BNs is particularly interesting due to their property of inference. Let us consider a random variable X_i with its related set of parents $\boldsymbol{X}_{\pi(i)} = (X_{i_1}, \cdots, X_{i_k})$ (assume that X_i has k parents). The marginal distribution of the variable X_i can be computed as follows:

$$P(X_{i_h} \mid X_i) = \frac{P(X_i \mid X_{i_h})}{P(X_i)} \tag{3.58}$$

Since the updated PDFs related to all the parents of the variable X_i are determined, the updated PDF of X_i can be computed. The gap between the initial PDF of the variable X_i and the PDF of the observations is reduced. Moreover, it can be seen that the updating acts on the parents of the variable X_i, which, in turn, induces the updating of X_i, but does not act on X_i straightforwardly. This key point justifies the use of BNs instead of other classical Bayesian updating methods Deby *et al.* (2009). In the updating method we proposed, structural reliability methods are used to (i) identify the most influent variables, and (ii) compute the updated structural model response. The theory of BNs is used to perform the updating of the statistical parameters of the PDFs associated with the random variables. This powerful tool has been chosen for two reasons: first, it can be used when several random variables are considered; second, it allows updating the PDFs of the random variables, which is not possible when using the well known Bayesian updating methods Melchers (1999), which only update the structural model response. To use the proposed updating method, the considered mean structural model is assumed to be satisfactory but not optimal. The objective of the proposed method is to reduce the gap between a set of observations and the structural model's predictions, thanks to the updating of the PDF of the considered random variables.

The proposed updating approach has three different steps. The first step aims at choosing from among the input variables of the structural model those which should be considered as

random. In theory, all the input variables can be considered as random since they are subjected to uncertainties. Nevertheless, the sensitivity of the structural model response to different random variables may not be the same. Since the number of random variables influences the whole computational cost of the updating process, it is of primary importance to consider as random only the most influential ones. The second step aims at defining the BN used to carry out the updating of the PDF of the random variables. Both the graph structure G and the set of conditional dependencies P have to be defined. The DAG structure is chosen as a V-structure. The corresponding set of conditional probabilities is computed by means of the Monte Carlo simulation method. It can be seen that building the V-structure is a time-consuming process. The reason is that the size of the CPT required for the children nodes is equal to the size of the full joint sample outcome space of the random variables. Nevertheless, the computational cost is also linked with the structural model solving process. Therefore, the whole computational cost of the updating analysis can also be restrained by simplifying the structural model. This is why simplified modeling strategies such as the one presented in Section 2.4.2 should be considered. The last step of the proposed updating framework aims at both updating the random variables' PDF and computing the updated mean response of the structural model. When considering a set of random variables $(X_1, \cdots, X_p),\ p < n$ that are the parent variables of a structural model response Y, and a set of observations coming from experts' judgements or in-situ measurements, the updated PDF associated with the random variables X_k can be computed as

$$P(X_k \mid Y) = \frac{P(Y \mid X_k)}{P(Y)} \quad \forall k \in \{1, \cdots, p\} \tag{3.59}$$

where $P(X_k \mid Y)$ stands for the probability of X_k given the assignment of the observation Y, $P(Y \mid X_k)$ is the a priori probability of Y given the assignment X_k, and $P(Y)$ is the probability of Y coming from the structural model. Considering the updated PDFs of the random variables allows computing the updated mean structural model response. One can note that the confidence intervals related to the structural model can also be updated if needed.

3.4.3 Numerical examples

Reliability analysis in a high dimensional space

This case study has been treated by Liu et Der Kiureghian (1986) and Bucher et Bourgund (1990) and more recently by Nguyen *et al.* (2009). Four analyses were carried out, denoted by 1, 2, 3 and 4. The analysis 1 means that neither the adaptive experimental design nor the explicit computation of the probability of failure has been used. The analysis 2 differs from the previous one by the fact that the probability of failure has been computed using the closed-form expression of the Hessian matrix. In the analysis 3, the adaptive experimental design is used and the probability of failure is computed from a first order reliability method. Last, in the analysis 4, both the adaptive experimental design and the closed-form expression of the Hessian matrix are used. The considered structure is a three-bay five-story rigid frame, as depicted in Figure 3.35. Twenty-one random variables have been defined. This problem illustrates clearly the fact that the number of limit state function calls drives the whole computational cost of the analysis. The statistical parameters and the distributions of the random variables are presented in Table 3.4 and have been chosen according to the data given by Bucher et Bourgund (1990). The variables F_i are the loads, E_i is the Young's modulus, A_i is the cross-sectional area, and I_i is the inertia. All loads are correlated by a coefficient of correlation $\rho = 0.95$. All properties of the cross-sectional areas are also correlated by a factor $\rho_{A_i A_j} = 0.13$. The two different moduli of elasticity E_1 and E_2 are correlated by $\rho = 0.9$. All other variables are assumed to be uncorrelated. The performance function is expressed in terms of a safety margin:

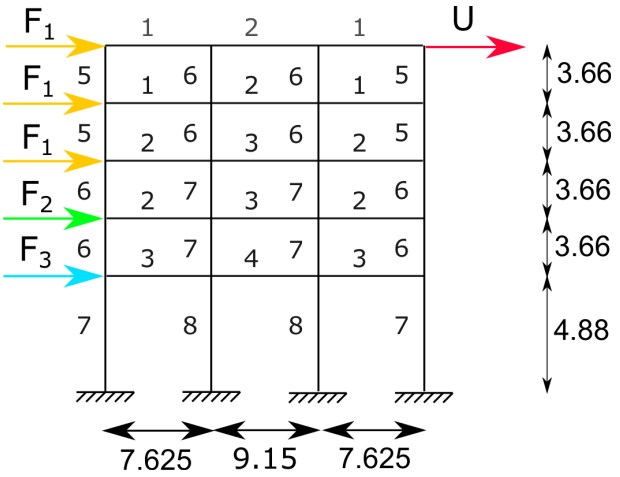

Figure 3.35: Structural system — the dimensions are in meters.

$$g_X(x) = 0.061 - U \tag{3.60}$$

where U is a vertical displacement on the top-right corner of the structure (see Figure 3.35). One can note that the limit state function is implicitly defined. A comparison between the results coming from the published literature and those obtained by means of the proposed approach is presented in Table 3.5.

The value of the reliability index computed by the proposed approach is fairly close to that obtained by the other authors. Furthermore, one can note that the use of an adaptive experimental design allows drastically decreasing the computational cost. When it is employed, only two iterations are needed (132 limit state function calls) although when it is not, five iterations are needed (220 limit state function calls). Another point of interest is the value of the performance function $g_X(x_d)$. The magnitudes are equal to 10^{-5}, which means that the computed design point reaches the limit state surface fairly well. Moreover, it appears that the use of the adaptive experimental design helps decrease this quantity. The rotation of the initial experimental design according to the gradient of the SVM approximation naturally makes the evaluation samples closer to the implicit limit state function.

Bayesian robust updating applied to a reinforced concrete beam subjected to cyclic loading

The objective of this structural example is to show that the proposed updating approach can be applied when dealing with reinforced concrete structure which behaves close to its failure state. The reinforced concrete beam considered is the same as the one presented in Section 2.4.2. Therefore, the structural model is built within the framework of the multifiber beam finite element method. The concrete is described by means of the constitutive law presented in Section 2.2.2, and a perfectly plastic constitutive law with kinematic hardening has been used for the steel. The steel/concrete interface is considered as being perfect in order to reduce the computational cost associated with each structural model call. As shown in Figure 2.11, the initial structural model is satisfactory but not optimal.

Variable	Distribution	Unit	Mean deviation	Standard deviation
F_1	Gumbel max	kN	133.454	40.04
F_2	Gumbel max	kN	88.97	35.59
F_3	Gumbel max	kN	71.175	28.47
E_1	Normal	kN/m^2	2.173752×10^7	1.9152×10^6
E_2	Normal	kN/m^2	2.379636×10^7	1.9152×10^6
I_1	Normal	m^4	0.813443×10^{-2}	1.08344×10^{-3}
I_2	Normal	m^4	1.150936×10^{-2}	1.298048×10^{-3}
I_3	Normal	m^4	2.137452×10^{-2}	2.59609×10^{-3}
I_4	Normal	m^4	2.596095×10^{-2}	3.028778×10^{-3}
I_5	Normal	m^4	1.081076×10^{-2}	2.596095×10^{-3}
I_6	Normal	m^4	1.410554×10^{-2}	3.46146×10^{-3}
I_7	Normal	m^4	2.327853×10^{-2}	5.624873×10^{-3}
I_8	Normal	m^4	2.596065×10^{-2}	6.490238×10^{-3}
A_1	Normal	m^2	0.312564	0.055815
A_2	Normal	m^2	0.3721	0.07442
A_3	Normal	m^2	0.50606	0.093025
A_4	Normal	m^2	0.55815	0.11163
A_5	Normal	m^2	0.253028	0.093025
A_6	Normal	m^2	0.29116825	0.10232275
A_7	Normal	m^2	0.37303	0.1209325
A_8	Normal	m^2	0.4186	0.195375

Table 3.4: Statistical parameters and distributions of the random variables.

Type of analysis	β	Number of calls	P_f	$g_X(x_d)$
1	3.41	220	3.24×10^{-4}	-9.98×10^{-5}
2	3.41	220	4.02×10^{-4}	-9.98×10^{-5}
3	3.25	132	5.77×10^{-4}	-7.01×10^{-5}
4	3.25	132	7.64×10^{-4}	-7.01×10^{-5}
Bucher et Bourgund (1990)	2.29	87	5.01×10^{-4} (FORM)	Not available
Nguyen *et al.* (2009)	3.22	259	6.41×10^{-4} (FORM)	-6.76×10^{-5}
			8.05×10^{-4} (SORM)	

Table 3.5: Results.

To reduce the gap between the experimental data and the numerical results, the updating method described previously has been employed for the reinforced concrete beam. The first step is to identify the most preponderant variables in the structural analysis. From engineering assessments (assuming that the structure behaves close to its failure state), the total number of potential input variables has been reduced to three: the concrete tensile strength, the concrete cover thickness, and the lower steel rebar yield stress. From these considerations, the elasticity indicators have been computed and the results are presented in Table 3.6. One can note that the lower steel rebar yield stress is clearly predominant, which was to be expected since the steel yields. Nevertheless, all three variables have been considered as random. The PDFs related to the random variables are also given in Table 3.6. The corresponding CPT has been computed by means of BN (15,000 samples) and all the samples are shown in Figure 3.36.

Random variable	Distribution	Mean	COV	Sensitivity vs mean	Sensitivity vs std
Concrete tensile strength (MPa)	LN	3.15	0.15	-0.3146	-0.0036
Concrete cover thickness (m)	LN	0.010	0.15	-0.6571	-0.0056
Yield stress (MPa)	LN	450	0.07	-9.5567	-0.2705

Table 3.6: Identification of the probabilistic model — LN = Lognormal; COV = Coefficient Of Variation; std = Standard Deviation.

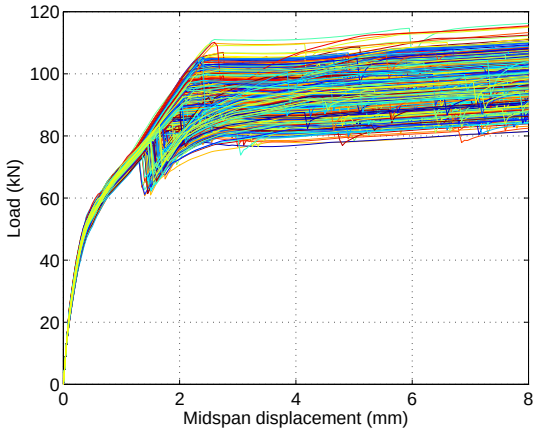

Figure 3.36: 15,000 samples computed by the Monte Carlo simulation method.

The experimental information used to update the PDF of each input variable is based on the midspan displacement. The results of the updating analysis are presented in Figures 3.37a and 3.37b. From such an analysis, one can note that the material properties are decreased with respect to their initial values. This is consistent with the fact that the measured mid-span displacement is larger than the mid-span displacement predicted by the numerical model. The relative gap between the prediction and the experience is reduced by almost 15%. Moreover, the updated material parameters can be seen as the true parameters related to the reinforced concrete beam. This structural example shows that the proposed updating process allows not only reducing the gap between a numerical prediction but also estimating the true material parameters related to a given structure when behaving close to its failure state.

3.5 Structural assessment of torsion-sensitive structures subjected to extreme loading

3.5.1 Seismic margins assessment

Context

Identified as having the potential to withstand severe damage, reinforced concrete shear walls been extensively studied worldwide since the 1970s. Many research programs aimed at studying the structural behavior of isolated shear walls under static loading have been carried out Hidalgo *et al.* (2002). The experimental data obtained reveal that shear walls have a high bearing capacity when subjected to static loadings. Shear walls are generally not used as isolated components but rather are included and connected with other components: this is an important fact that has not yet been fully analyzed. The specific structural effects of such a use must be understood.

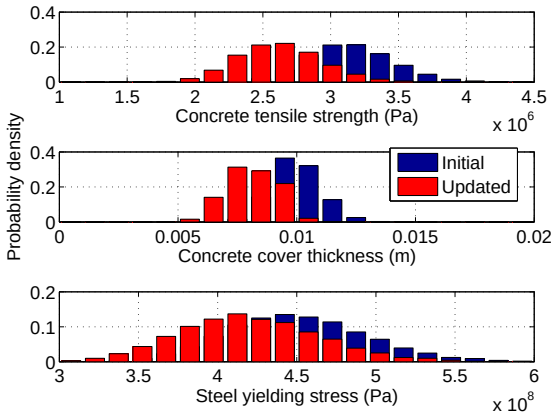

(a) Initial and updated PDF of the input parameters.

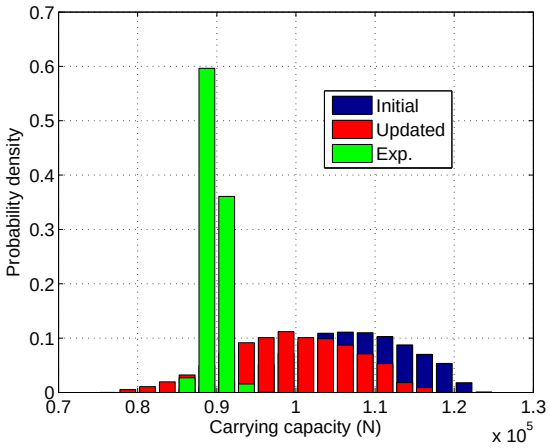

(b) Initial and updated PDF of the output response.

Figure 3.37: Results from the updating strategy.

Additional experimental investigations have focused on shear walls with end walls Lefas *et al.* (1990) or walls framed with beams and columns under static loadings Farrar *et al.* (1991). The structural effects due to the assembly between each component appear to be significant. Subsequently, experimental investigations were carried out on a three-dimensional shear wall assembly, mainly with a symmetrical geometry not only in-plane but also in elevation, and tested under static conditions. In order to assess the ability of a structure based on shear walls to withstand seismic loadings, experimental studies with a dynamic loading factor have been carried out. Nevertheless, the difficulties of applying a dynamic loading where the inertia force field is reproduced to a reinforced concrete specimen make experimental data rare in the scientific literature, especially when such a loading condition is applied to a three-dimensional model of a structure based on shear walls. Experiments where an impulsive loading was considered to analyze the fundamental dynamic properties of a structure are available in the literature Ogata et Kabeyasawa (1984). A few scientific works where a fully three-dimensional structural model was subjected to a dynamic load Mahin et Bertero (1976) are also reported in the literature. In 2010, an extensive experimental study was carried out at the University of California at San Diego.

A symmetric seven-story reinforced concrete structure based on shear walls was subjected to uniaxial shaking table tests of increasing intensity Moaveni *et al.* (2010); Martinelli et Filippou (2009). These tests were carried out within the framework of an international benchmark aiming at comparing various modeling strategies and identifying the benefits and limitations under a blind condition. This experimental program led to fruitful conclusions regarding the identification of model uncertainties and the determination of the need for further large-scale testing. In 2006, the French Atomic Energy and Sustainable Energies Commission (CEA) and Electricité De France (EDF) began a wide research program entitled "Seismic Design and Best-Estimate Methods Assessment for Reinforced Concrete Buildings Subjected to Torsion and Nonlinear Effect" (SMART). In 2008, a large experimental program was launched to carry out seismic tests on an asymmetric reduced scale model of a reinforced concrete wall based structure by means of the AZALEE shaking table operated by the Nuclear Energy Division (DEN) at the CEA center located in Saclay (France). It was called SMART 2008. Synthetic seismic loadings with increasing intensities were applied to the reinforced concrete specimen: the main aim was to

quantify the seismic margin with respect to the design level. It has been clearly shown that there are seismic margins. A well-documented experimental database was set up for the aim of validating numerical simulation methods for engineering purposes and for setting a basis for a benchmark exercise in that field.

Despite the improvements made, several questions were still unanswered. Hence, CEA and EDF began a new experimental program in 2011, called SMART 2013, which is partially supported by the International Atomic Energy Agency (IAEA); in this program, the same type of wall-based asymmetrical structure as that part of the SMART 2008 program is being tested. The aims of this new experimental program are to improve the representativeness of the seismic loading regarding real seismic scenarios and to better quantify the effects of nonlinearities and torsion on the dynamic response of the equipment and secondary structures. In addition, in order to supply inputs to the numerical models, the monitoring of the boundary conditions during shaking table tests was given special attention. The reference data created within the framework of the SMART 2013 experimental program were used to make up an international benchmark.

Test specimen

The reinforced concrete specimen is a scaled model of a simplified half-part of a nuclear electrical building. It was prepared to reproduce the geometrical, physical and dynamical characteristics of a part of the real building. Due to the inherent limitations related to a laboratory's capacity, regardless of the laboratory in question, some simplifying assumptions have to be employed. In particular, considering the size or the mass of the real building and the load capacity of the AZALEE shaking table, the model had to be geometrically reduced to a scale of 1:4. The well-known Cauchy–Froude similitude law was chosen in this experiment. This choice ensures that both the acceleration and the stress fields remain unchanged throughout the scale change if the following conditions are met: the frequencies are multiplied by a factor of two, the mass is multiplied by a factor of four, and the time is divided by a factor of two. The reinforced concrete specimen was designed according to the current French design rules to be followed when dealing with a nuclear building. The design spectrum considered is shown in Figure 3.38.

This corresponds to an earthquake magnitude equal to 5.5 at a distance of 10 km from the failure plane. The peak ground acceleration (PGA) is 0.2 g. Synthetic accelerograms were generated from the design spectrum and the corresponding acceleration response spectra are compared to the design spectra in Figure 3.38. A satisfactory agreement between the design spectra and the response spectra derived from synthetic signals can be seen.

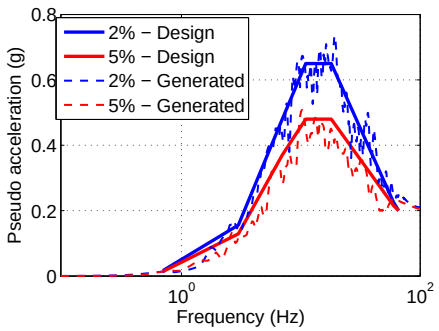

Figure 3.38: Comparison between design and response spectra — 2% and 5% damping — magnitude equal to 5.5.

The geometry of the reinforced concrete specimen was defined in order to satisfy the following conditions: (i) the specimen should have an asymmetric shape to ensure significant torsional effects during the loading and (ii) the first eigenfrequencies should be in the range 4–10 Hz to ensure that significant damage appears and that the specimen is representative of existing nuclear buildings currently operating in France. A picture of the test specimen is presented in Figure 3.39.

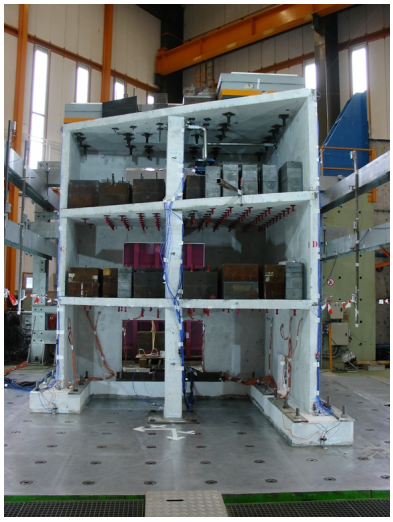

Figure 3.39: Picture of SMART 2013 specimen fixed on the AZALEE shaking table, ready to be tested.

It is composed of nine structural elements: one foundation, three shear walls (referred to as shear walls #1 to #4 in the in-plane view of the formwork drawings presented in Figure 3.40), three slabs, three beams, and one column. In order to avoid any potential differential displacements, a new anchorage and foundation design was considered with respect to the former SMART 2008 specimen. The continuous reinforced concrete footing is 650 mm wide and 250 mm high; it is bolted at 34 anchoring points in a 20-mm thick steel plate; planarity defaults are mitigated by means of a mortar layer against the steel plate, which is fastened to the shaking table. Uniformly distributed additional masses are clamped on the mock-up slabs (apart from on the reinforced concrete beams) to ensure the condition related to the similitude rule; the total mass of the reinforced concrete specimen is then equal to 45.69 tons.

Instrumentation arrangement

The instrumentation arrangement defined within the framework of the SMART 2013 joint project is similar to the one defined within the framework of the SMART 2008 joint project regarding the measurement channels dedicated to the reinforced concrete specimen. However, the feedback from the SMART 2008 experimental program has clearly pointed out the importance of accurately monitoring the boundary conditions of the whole structural system (the reinforced concrete specimen and the shaking table). Therefore, the main improvements were to employ additional sensors at junctions between the shaking table and the actuators. Eight actuators (four in the horizontal directions and four in the vertical direction) were monitored in order to record the displacement and acceleration time histories over the whole experimental program. The knowledge of this data means that it is possible to accurately control the boundary conditions which are of primary importance when dealing with a numerical simulation of the dynamic behavior of such a complex structural system. The pipe has also been monitored so that this component can be studied separately from the rest of the reinforced concrete specimen.

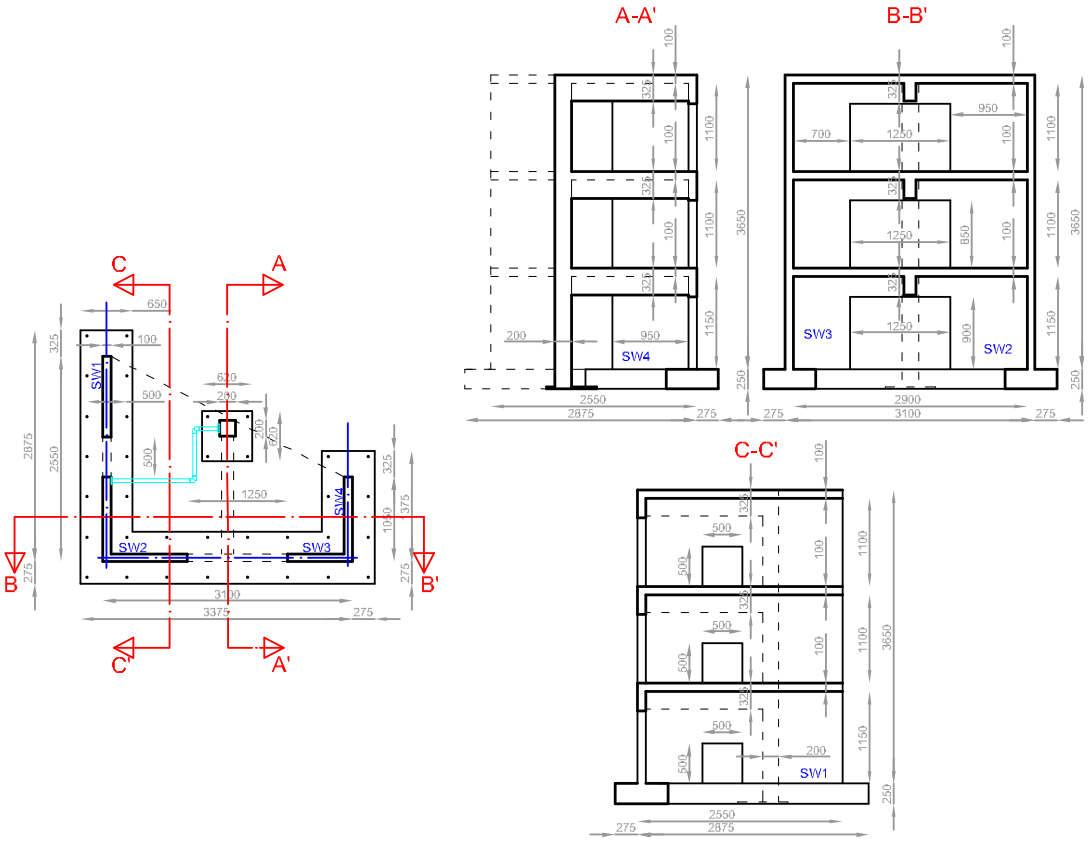

Figure 3.40: Formwork drawing of the SMART 2013 test specimen — dimensions in millimeters.

Accelerometers in the three directions were put at the pipe-ends to monitor the seismic loading and also on the central valve to capture its global dynamic response. Approximately 200 measurement channels were devoted to monitoring the structural system, including the boundary conditions, and several steel strain gauges. The measurement channels were apportioned as follows: 75 accelerometers dedicated to the structure, 55 low-velocity-displacement transducers, 35 strain gauges, 15 specific low-velocity-displacement transducers to monitor the interface between the foundation and the shaking table's upper plate, 10 diagonal sensors fixed on the little shear wall, and 10 accelerometers dedicated to the pipeline. Both the acceleration and displacement were monitored at the corners of each slab. In addition, the acceleration was monitored at the center of each half of the slabs and at the centers of the beams. A sketch of a part of the instrumentation arrangement is shown in Figure 3.41. Moreover, a digital image stereo-correlation technique was set up to monitor the evolution of the crack pattern of shear wall #4 at the first story during the tests, using two high frequency cameras.

Seismic loading procedure

Specific attention has been given to the definition of the seismic loading procedure. The driving idea was to choose a set of highly damaging bi-axial seismic input ground motions considered to be representative of a real seismic scenario. Mainly natural input ground motions were applied to the reinforced concrete specimen. Considering the feedback from the SMART 2008 project, the seismic signals were chosen so that their frequency contents are in accordance with the eigenfrequencies of the reinforced concrete specimen, so as to ensure their damaging character.

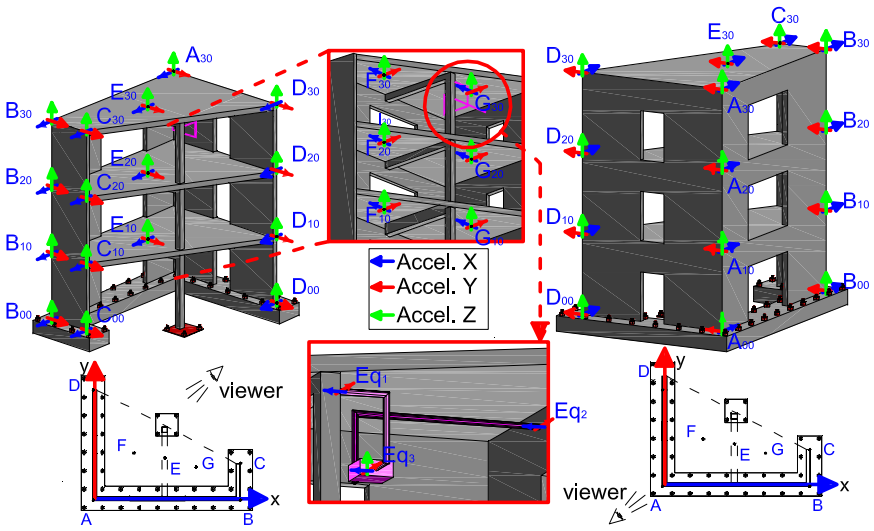

Figure 3.41: Summary of the measurement points.

In addition, to avoid the unwanted effects of cumulative damage, a consensus was reached to reduce the number of intermediate seismic tests. The seismic loading is composed of three seismic test sequences. In test sequence #1, a synthetic seismic signal corresponding to the seismic demand at the design stage was employed. In test sequence #2, the main shock of the Northridge earthquake that occurred in California, USA, in 1994 was employed (Magnitude 6.7) and, in test sequence #3, the first aftershock of the same earthquake was considered (Magnitude 5.2). In test sequences #2 and #3, the natural seismic signals extracted from the PEER NGA database Chiou *et al.* (2008) at the same monitoring station, Tarzana Cedar Hill (7 km from the epicenter), were selected. The eigenfrequency shifts measured during SMART 2008 were taken into account in the choice of these input ground motions. In this way, the input ground motions were chosen so that their frequency content is in accordance with the resonance frequencies of the reinforced concrete specimen, in order to ensure their damaging character. To ensure a satisfactory realization of the seismic input ground motion by means of the shaking table, each test sequence was split into several seismic runs. Each run aimed to apply a given percentage of the nominal seismic signal to the reinforced concrete specimen. In order to avoid unwanted effects due to cumulative damage from one run to another, a limited number of intermediate runs was carried out. The full seismic test procedure is described in Table 3.7. Low level random signals with a PGA in both horizontal directions between 0.05 and 0.1 g were also applied between each seismic run in order to monitor the evolution of the modal properties of the reinforced concrete specimen. In addition, similar signals were applied to the specimen from runs #1 to #6 in order to get the shaking table properly set up.

Overall damage pattern

From run #7 to run #11, no significant cracking was observed on the reinforced concrete specimen, only diffuse cracking close to the geometric singularities was observed. The main localized cracks began during run #13. The main areas that cracked were shear wall #4, the first slab and the junction between the foundation and shear wall #4. From run #17 to run #19, the aforementioned parts of the reinforced concrete specimen become more and more cracked. In particular, shear cracking pattern could be observed in shear wall #4, as shown in Figures 3.42a and 3.42b.

Test sequence number	Run number	Target PGA in X direction (g)	Target PGA in Y direction (g)	Realized PGA in X direction (g)	Realized PGA in Y direction (g)	Brief description
#1	#7	0.10	0.10	0.13	0.14	DL - 50%
#1	#9	0.20	0.20	0.22	0.23	DL - 100%
#2	#11	0.20	0.11	0.21	0.16	Northridge MS - 11%
#2	#13	0.40	0.21	0.40	0.25	Northridge MS - 22%
#2	#17	0.80	0.42	0.60	0.40	Northridge MS - 44%
#2	#19	1.78	0.99	1.10	0.94	Northridge MS - 100%
#3	#21	0.12	0.07	0.14	0.14	Northridge AS - 33%
#3	#23	0.37	0.31	0.70	0.40	Northridge AS - 100%

Table 3.7: Seismic loading procedure — DL = design level; MS = Main Shock; AS = After Shock — percentages are computed, for a given test sequence, as the ratio between the PGA of a run and the nominal PGA.

The failure of the reinforced concrete specimen occurs during run #19 with the propagation of a crack at the junction between the foundation and shear wall #4. Due to the presence of this crack, an important uplift of shear wall #4 was observed during run #19. During this uplift, the steel reinforcing bars yielded. It is also believed that sliding at the steel/concrete interface occurred. When the reinforced concrete specimen went down, the concrete crushed suddenly, as shown in Figure 3.42c.

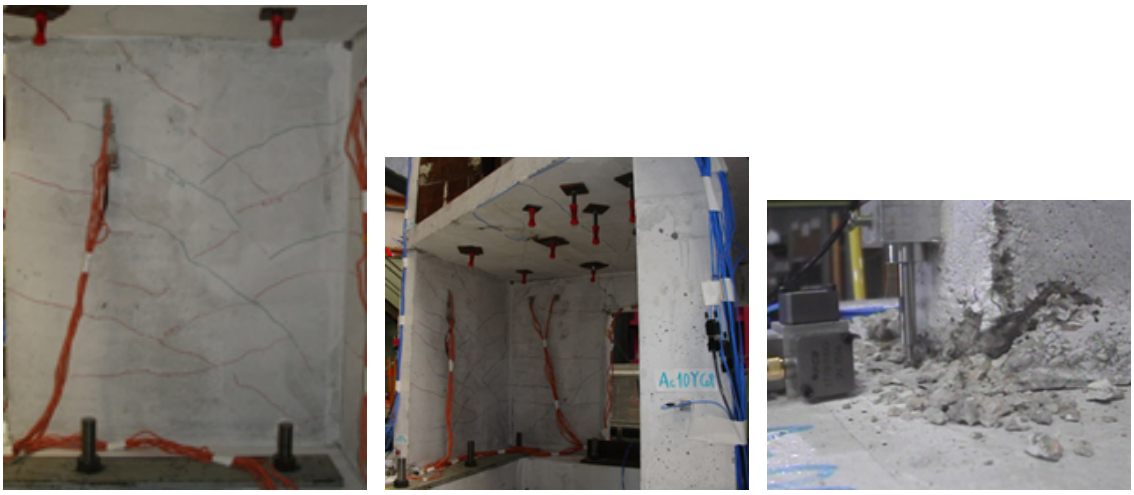

(a) Cracking in shear wall #4 after run #17.

(b) Cracking at the 1^{st} level after run #19.

(c) Concrete crushing at the junction between shear wall #4 and the foundation during run #19.

Figure 3.42: Experimental observations of the degradation process of the SMART 2013 specimen.

Description of SMART 2013 international benchmark

The SMART 2013 international benchmark was organized between February 2012 and September 2014 and was concluded by an international workshop which took place in Saclay, France, 25–27 November 2014. Forty-two participating teams from all over the world were registered. A list of the participants is provided in Tables 3.8 and 3.9, including the parts of the benchmark they were involved in.

The objectives of the benchmark were (i) to assess the capabilities of advanced best-estimate methods in predicting the seismic response of a complex reinforced concrete specimen, subjected to overdesign dynamic loadings that may occur in the case of extreme seismic events; in particular, the capabilities of nonlinear numerical models to satisfactorily capture the structural damage from a natural seismic scenario consisting of a main shock and an aftershock for a given magnitude/distance pair, (ii) to improve the use of probabilistic methods addressing random and epistemic uncertainties to estimate the fragility curves, and (iii) to share seismic assessment methods and build a consensus in the international seismic engineering community. To reach these objectives, the experimental measurements coming from the SMART 2013 experimental program were considered as reference data to make up a benchmark.

The SMART 2013 international benchmark was composed of four stages. Stage 1 was devoted to the characterization of the numerical model used by all the participating teams. Several data regarding the spatial/time discretization, the time integration algorithms used and the ways of taking the boundary conditions into account were asked for from the participants. A description of the structural model was also required. In order to assess the relevancy of the assumptions used in the formulation of the constitutive laws (concrete, steel and steel/concrete interface), a description of the effects taken into account was required. Therefore, each participant was asked to carry out basic static tests considering more or less complex (both monotonic and cyclic) loading paths on an RVE of concrete, steel, and reinforced concrete. No dynamic loading was considered in stage #1. Stage #2 aimed at calibrating the numerical finite element structural models in the elastic range. In order to reach this objective, modal analyses considering various boundary conditions and transient analysis were required. Only two low-intensity seismic loadings, with PGA equal to 0.1 g, were considered: a random signal (run #6) and a synthetic seismic signal (run #7) corresponding to 50% of the design seismic loading in terms of PGA. Both measured seismic inputs and outputs were provided to the participants. In order to leave them the choice of how to accurately control the boundary conditions, the time histories of the displacements and accelerations measured at the shaking table actuators were provided to the participants. In addition, CEA provided a numerical model of the AZALEE shaking table taking into account the exact position of the actuators to allow an accurate description of the whole dynamic system. In stage #3, blind nonlinear dynamic computations for medium- to high-intensity seismic loading sequences (PGA ranging from 0.2 to 1.78 g) were asked for from the participants.

Institution	Country	Stage #1	Stage #2	Stage #3	Stage #4
National University of Cuyo	Argentina	X	X	X	
Phimeca	France	X	X		X
ENSI Team 2 (Stangenberg & Partner Ingenieur-GmbH)	Germany	X	X	X	X
University of Parma	Italy	X	X	X	X
CKTI-Vibroseism	Russian Federation	X		X	
Korea Institute of Nuclear Safety	South Korea	X	X	X	X
Scanscot Technology	Sweden	X	X		
Ecole Normale Supèrieure de Cachan	France	X	X	X	
Pakistan Atomic Energy Commission	Pakistan	X	X	X	
Woelfel Beratende Ingenieure	Germany	X	X	X	
Institut Nationale des Sciences Appliquées de Lyon	France	X	X	X	
AREVA GmbH	Germany	X	X		
Laboratoire 3SR	France	X	X	X	
EDF-SEPTEN 3SR	France	X	X	X	X
IDOM	Spain	X	X		
Cervenka Consulting	Czech Republic	X	X	X	
Technical University of Civil engineering	Romania		X	X	
ENSI Team 1 (Basler-Hofmann & AG Consulting Engineers)	Switzerland	X	X	X	X
EGIS Industries	France	X	X	X	
Faculty of Civil Engineering	Macedonia		X	X	
China Guangdong Nuclear Power Design Company	China	X	X	X	
Nagoya University	Japan	X	X	X	
Middle-East Technical University	Turkey	X			
University of Houston	USA	X			
State Nuclear Electric Power Planning	China	X			

Table 3.8: Teams involved in the SMART 2013 international benchmark—Part 1.

The nonlinear analysis of seven seismic loadings, two being optional, was required. Only the seismic inputs were provided to the participants. The measured outputs were not available when stage #3 was ongoing, this strategy enabled analyzing the predictive capabilities of the assessment methods used by the participants. Lastly, stage #4 was devoted to a numerical vulnerability analysis of the reinforced concrete specimen within a probabilistic framework addressing random and epistemic uncertainties. The purpose of this stage was to assess the effect of the type of uncertainties on the fragility curves considering various failure criteria. Two substages were considered. In the first, the numerical model was assumed to be linear elastic.

Participants were free to use their own method to compute the fragility curves. In the second substage, participants had to consider nonlinear constitutive laws to describe the energy dissipation. The method to compute the fragility curves was imposed, assuming a lognormal distribution of the random variables. For all substages, the set of input ground motions was provided.

Institution	Country	Stage #1	Stage #2	Stage #3	Stage #4
Computational Engineering and Structures	France	X	X	X	
Alyotech Technologies	France	X			
Technical University Gheorghe Asachi	Romania	X			
Swissnuclear	Switzerland	X	X	X	X
Rene Lagos Engineers SAC	Chile	X			
Ecole Polytechnique Fédérale de Lausanne	Switzerland	X	X	X	
PRINCIPIA	Spain	X	X	X	
Autodesk	France	X	X	X	
Laboratório Nacional de Engenharia Civil	Portugal	X	X		
TNO DIANA BV	The Netherlands	X	X	X	
ATR Ingenierie	France	X	X	X	
Géodynamique et Structure	France	X	X		
SDA-engineering GmbH	Germany		X		
Fortum Power and Heat Oy	Finland	X	X	X	
Numerical Engineering and Consulting Services	France	X	X	X	
University of California Berkeley	USA	X			

Table 3.9: Teams involved in the SMART 2013 international benchmark—Part 2.

Lessons learned

Modeling assumptions SMART 2013 has been an opportunity to draw up a collection of engineering practices to assess the beyond-design behavior of a complex reinforced concrete specimen subjected to seismic loadings. The modeling assumptions and feedback from all the participating teams were shared during the final international workshop and several key points appeared as being crucial: (i) the type of laws to consider in order to describe the mechanical behavior of the constitutive material (in particular, concrete), (ii) the choice of the damping model, and (iii) the way of applying the seismic loading. First, regarding the modeling assumptions related to the constitutive laws, most of the participants agreed with the importance of taking into account the nonlinear mechanisms responsible for the material dissipation in their structural model. A consensus was reached on the fact that equivalent linear approaches are inappropriate when dealing with the assessment of seismic margins, and therefore with beyond-design behavior. Most of the participants used constitutive laws based on either continuum damage theory (including smeared crack models, which are a particular type of damage model) or coupled damage–plasticity theory. The results show that recent techniques allowing the prop-

agation of displacement discontinuities in the continuum are not mature enough to be used in the case of such complex analyses. Second, the question of the choice of the damping model remains an important issue and no specific consensus has been reached. However, in the case of the use of constitutive laws including hysteretic effects, no specific reduction of the viscous damping contribution was noted. This observation highlights the fact that the quantification of the material dissipation contributing to the structural damping is an issue that still needs to be studied. In addition, the use of damage-driven damping models remains rare, which confirms the aforementioned need. Last, as one of the main lessons from the SMART 2008 project, the sensitivity of the numerical results to the way of applying the seismic loading to the structural system has been confirmed. A consensus on the best practice to follow was reached. More specifically, most of the participants agreed with the necessity of including the shaking table in the structural model. In this way, the initial dynamic properties of the system can be captured well and the seismic loading can be input at the actuator level. Most of the participants made the choice to input the actuator displacement time histories, which allowed the full kinematics of the system to be taken into account. However, this practice requires checking the consistency of the frequency contents of the numerical and the experimental acceleration responses at the upper plate of the shaking table.

Predictive capabilities of nonlinear seismic assessment methods of the beyond-design behavior of the SMART 2013 specimen The assessment of the predictive capabilities of nonlinear structural models when dealing with beyond-design behavior makes it necessary to control their initial state, that is, to ensure they are well calibrated in the elastic range. This aspect has been addressed in a specific stage of the benchmark and one ended up with the fact that the initial modal properties of the dynamic system were well captured, the acceleration based responses were also satisfactorily described, but the displacement-based quantities were underestimated. However, the maximum value of the displacement being lower than 1 mm, the weight of the experimental uncertainties become important, and so no definite conclusions could be drawn from this observation. It appeared that most of the participants succeeded in calibrating their structural models when dealing with low-level seismic loadings. The quantitative analysis of the mechanical indicators computed from the results provided by the participants was then carried out under a blind condition. Among the indicators studied, it appeared that the stiffness degradation, occurring mainly during the Northridge main shock seismic sequence, was satisfactorily captured by most of the participants. In other words, the structural dissipation is well described thanks to the use of nonlinear constitutive laws. Subsequently, the peak frequency shifts (PFS) appeared to be particularly well captured in this experimental program. However, as with the case of the low-level seismic loadings, the inter-story drifts (ISDs) were, on average, underestimated. No specific consensus on the key factors explaining this observation came about during the international workshop. However, the nonlinear approaches seem to exhibit different capabilities, depending on the nature of the quantity to be described. Indeed, member scale dissipation-related quantities seem to be captured more easily than those related to local dissipation. Another point of interest is related to the validity of the prediction of the seismic behavior of the SMART 2013 specimen during the Northridge aftershock sequence. The displacement based quantities were badly predicted, due to the fact that only some constitutive laws accounted for residual strains, which were important to be considered since an important increase in the damage occurred during the previous seismic sequence. However, satisfactory results were obtained regarding the acceleration based quantities.

Assessment of the structural robustness of the SMART 2013 reinforced concrete specimen The specimen was subjected to several transient seismic signals and was therefore gradually damaged. These transient signals were sorted according to three sequences introduced

in Table 3.7 in order to quantify the damaging power of each seismic sequence. Each sequence was composed of several scaled transient signals, based on a nominal signal. In a given sequence, the loading factor, defined as the ratio between the PGA of the scaled signal and the PGA of the nominal signal, was increased by up to 100%. In order to assess the robustness of the structure, two indicators (or engineering demand parameters) were defined and analyzed: the maximal ISD between the second and the third floors (the ISD is calculated from the absolute displacements; those for the other stories follow the same trend), and the frequency shift related to the first peak identified from the floor response spectra (FRS) computed at point D, located on the third floor. The ISD is a local indicator that can be associated with the ductility capacity of the reinforced concrete structure, and represents the capability of the numerical models to reproduce the differential displacements between two stories by comparison with experimental measurements. The PFS is a structural indicator that represents the capabilities of the numerical models to capture the overall behavior of the specimen while the stiffness degradation and dissipation are increasing. Three damage thresholds, allowing the definition of three engineering damage states (light, controlled, and extended damage) have been introduced for each mechanical indicator. These damage indicators can correspond to the values of the ISD or to the PFSs exhibited by the structural system. For each participant, the first peak frequency was identified from the first transient signal of each seismic sequence (i.e., runs #7, #11 and #21), allowing the definition of the *reference peak frequency*. This reference peak frequency is compared with the first peak frequency of the following transient signals in a given seismic sequence to estimate the PFS. The experimental values of these two mechanical indicators are compared with the numerical ones considering the damage thresholds to assess the robustness of the structure subjected to the different seismic sequences. The quite arbitrary three values chosen as the thresholds are expected to be relevant for distinguishing damaged structural states. In particular, the PFS thresholds can not only be justified regarding the floor response spectra frequency content demand for equipment seismic assessment, but also by an engineering practice of reducing the Young's modulus by 50% in cracked zones of bended reinforced concrete sections in linear elastic calculations. Regarding the design level, the ISD led to concluding that no damage appeared (see Figure 3.43a), whereas the PFS led to concluding that some small damage appeared (see Figure 3.43b).

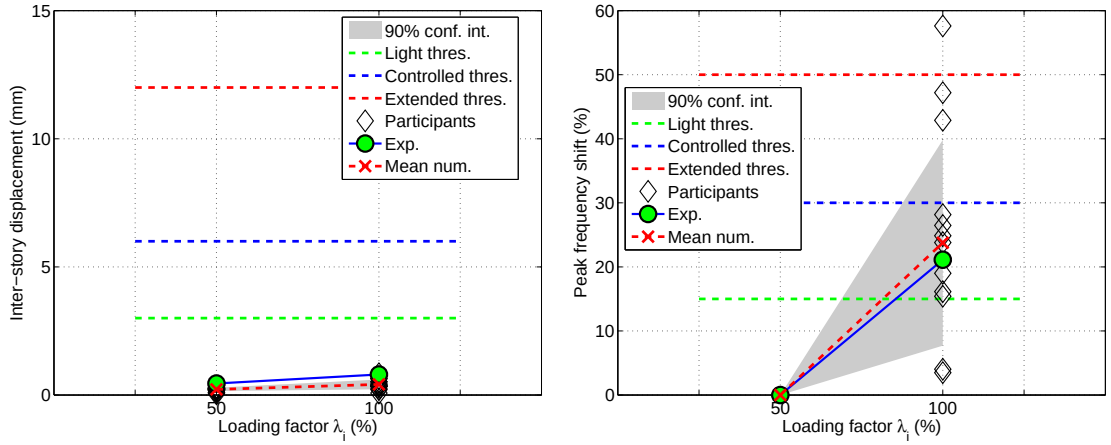

(a) Displacement based indicator.

(b) Peak frequency based indicator.

Figure 3.43: Robustness indicators — design level — numerical–experimental comparisons.

The experimental observations were in agreement with the last conclusion: even in the case of the design level, small nonlinearities, mainly related to concrete cracking, appeared, and it is crucial to use nonlinear approaches to capture this effect. Regarding the Northridge main shock, the analysis of the ISD led to concluding that the specimen is highly damaged since the extended damage threshold was surpassed by almost a factor of two. However, the results expressed in terms of PFS revealed that the extended damage threshold was not surpassed at all. Again, the experimental observations were in agreement with the conclusions that could be drawn from the PFS. Indeed, besides localized cracks observed on the shear walls and on the slabs, a main crack appeared at the interface between the foundation and the shortest shear wall, leading to concrete crushing due to compressive failure. However, it is worth mentioning that the concrete crushing remained confined to a limited area, as can be observed in Figure 3.42c. Therefore, the description of the damage state given by the PFS at the end of the Northridge main shock seems to be in better agreement with the experimental observations than the one given by the ISD. Regarding the Northridge aftershock sequence, both indicators led to similar conclusions, even though the ISD captured an increase in the damage, since the light damage threshold expressed in terms of the ISD was exceeded, as shown in Figure 3.44.

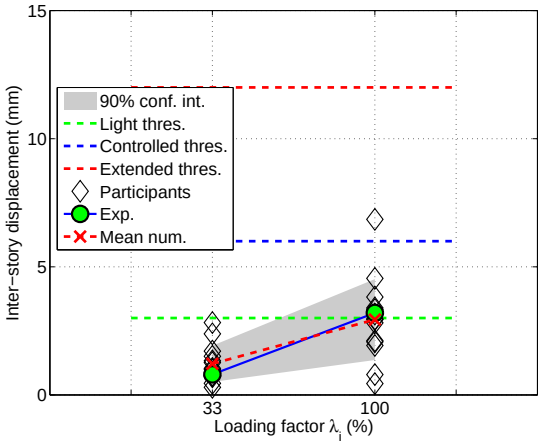

Figure 3.44: Robustness indicator — displacement based indicator — Northridge after shock.

However, as mentioned previously, the experimental observations confirmed the fact that the Northridge aftershock did not lead to a significant increase in damage. Consequently, the physics of the structural response seems to be described more realistically when using the PFS. From the aforementioned discussion, it appears that the choice of the structural indicator to describe the structural damage is a crucial question, since the quantification of the structural robustness is a consequence of it. Within the framework of the SMART 2013 project, the PFS indicator appeared to be more appropriate than the ISD, based on the experimental observations. In addition, defining the robustness as *the ability of a structure to withstand extreme events without being damaged to an extent disproportionate to the original cause*, the SMART 2013 specimen can be qualified as robust, since only moderate cracks were observed after the Northridge main shock, which had a PGA greater than four or five times the design PGA. This trend was confirmed by the results expressed in terms of the PFS.

Probabilistic vulnerability analysis Stage #4 of the benchmark was dedicated to calculations of the fragility curves from time-history analyses. The participants were invited to make their calculations with the structural model developed for the previous stages and validated on the experimental results. In order to have a more realistic exercise, the shaking table finite element model was replaced by the simplified equivalent foundation impedances—having been fitted

to the reduced scale—at the bottom of the mock-up model. The first step aimed at comparing methods for evaluating fragility curves with the linear structural model, using the participants' practice. However, the linear regression method was the only one used, although the maximum likelihood principle method was also allowed. In addition, the Latin hypercube sampling approach based on a set of time-history analyses was used. The parameters of the equivalent lognormal distribution of the fragility curves were fitted from their results. The second step focused on calculating the fragility curves in the nonlinear range by means of the regression method. Both steps allowed determining the median capacity and the log-standard deviation, depicting the aleatory and epistemic uncertainties. The following structural properties were considered as random variables, first: the overall foundation stiffness and damping coefficients; and during the second step of stage #4, in the nonlinear range, there were added: the tensile concrete strength and structural damping ratio. Lognormal probabilistic distributions were assumed for all these random variables. The same two damage indicators were considered: the ISD at point D in the X direction, and the PFS, with the same three levels as those presented in the previous sections. Three seismic intensity measures were proposed: the PGA, the cumulative absolute velocity (CAV), and the structure-specific average spectral acceleration (ASA) De Biasio *et al.* (2014), which is the area obtained by integrating the ground motion response spectrum between half and one times the first eigenfrequency of the structure. A database of 100 pairs of synthetic non-stationary accelerograms (X and Y directions), compatible with median (plus and minus one standard deviation) spectra, for a specific relevant seismic event, was provided. This database was expected to be sufficient to cover the whole range of damage indicators to be analyzed in the computation of the fragility curves. A reduced pool of seven participants took part in stage #4. Huge computational resources were needed for these calculations. From the comparison of the log-standard deviations obtained for the computed fragility curves, in the case of both the ISD and PFS damage indicators, it appears that the discrepancy is higher using the CAV intensity measure. It seems that this measure is less valid for such reinforced concrete structure, leading to the highest log-standard deviation. This observation may be linked with the fact that its definition is more appropriate for cumulative dissipation processes, such as yielding. The ASA indicator led to the results with the lowest log-standard deviations. This may be explained by the fact it is more appropriate for structures whose evolving eigenfrequencies are associated with material damage processes. Furthermore, for the three levels of the two damage indicators, computations of the fragility curves based on nonlinear simulations always gave higher values of the mean capacity and lower values of the probability of failure than those obtained using linear structural calculations. This confirms the ability of nonlinear structural transient analyses to assess the existence of seismic margins. Finally, it has been observed from the responses provided by the participants that there is a large scatter in the method (calculation and practice) to establish the fragility curves for engineering office purposes.

3.5.2 Influence of thermal breakers on the seismic response of an asymmetric reinforced concrete structure

Context

The thermal performance of such structures is becoming a requirement in European countries. Consequently, much research has been carried out to limit, ideally to erase, the sources of thermal dissipation between the building and the external environment Ge *et al.* (2013). Successful insulation techniques and dedicated components have been developed, leading to a drastic reduction of the thermal energy loss. Indeed, new structural components called *thermal break components* have been designed to improve the in-building thermal insulation. Despite the fact that such a technique of insulation appears promising regarding the results coming from the thermal analysis, their effects on the overall mechanical response of the equipped structure have

still to be addressed, especially when considering seismic loadings.

The issue of thermal and seismic compatibility arose in the case of conventional buildings. Nevertheless, the research carried out so far to address this issue has been mainly related to beam-column type structures. Although this structural configuration is recommended, for instance, by the design rules for conventional building, it is not forbidden to consider wall-based structures (even irregular) for conventional applications. One of the originalities of the research presented in this memoir resides in this key point. In addition, assessing the seismic response of a reinforced concrete structure equipped with thermal break components that exhibits torsional effects is also a key point since the thermal break components were not initially designed to withstand torsion. Within the framework of the European research project *Seismic Engineering Research Infrastructures for European Synergies* (SERIES), financially supported by the 7^{th} frame research program, experimental and numerical studies of the seismic behavior of an asymmetric half-scaled mock-up equipped with thermal break components have been carried out Fardis (2012). The objectives of this research project were (i) to assess the overall seismic behavior of such structures to provide some quantitative knowledge, and (ii) to analyze the local behavior of thermal break components under seismic conditions.

Seismic tests have been carried out with the AZALEE shaking table of the TAMARIS experimental facility Payen *et al.* (2006). The main advantage of shaking table tests is their ability to represent inertial forces on a physical time scale. A mock-up of a reinforced concrete specimen designed according to Eurocodes 2 (EC2) and 8 (EC8) was built and then equipped with thermal break components. Bi-directional seismic loadings, all gathered in a seismic testing sequence, with increasing PGAs were applied to the specimen to assess its seismic behavior up to a severe damage state. The input signals were synthetic: they were generated using the design spectra defined in EC8. Local data acquisition systems were used to monitor the behavior of the thermal break components. In addition to the experimental investigations, a numerical study was also carried out.

Test specimen

The specimen represents a typical three-story conventional building. The shape of the specimen was inspired by the one considered within the framework of SMART 2008. However, it is important to highlight that the specimen considered in this study is not devoted to nuclear applications, as was the case of the SMART research project. Therefore, the design practices followed are not the ones considered in the French nuclear industry but are the ones considered in the case of civil engineering buildings.

Due to the dimensions of the shaking table, a full scale structure could not be tested. A reduced scale mock-up at the 1:2 scale had to be built for this reason. In order to ensure, as best as could be done, the representativeness of the measurements carried out on the reduced scale mock-up, a similitude rule had to be employed. The similitude rule employed in this study is Froude's rule, which was developed with the aim of keeping unchanged the stress and the acceleration field through the scale change. To keep these quantities constant, the requirements consist in using both (i) a time contraction and (ii) an increase of the mass density of the constitutive materials (both the steel and the concrete). In addition, the design spectrum of the reinforced concrete mock-up is obtained by dividing the period of the design spectrum related to the full scale structure by the square root of the scale factor (equal to 2). The full scale structure should have its first three eigenfrequencies in the range 4–14 Hz (or 0.071–0.250 s if it is expressed in periods). Due to the scale change, the reduced scale mock-up should have its first three eigenfrequencies in the range 5.65–19.79 Hz (or 0.050–0.176 s if it is expressed in

periods). This requirement was posed to make the frequency content of the loading compatible with the natural frequencies of the tested system.

Condition (ii) could not be precisely fulfilled, since it was not possible to act on the mass density from a practical point of view. Therefore, additional masses were put on the slabs, assuming most of the mass is concentrated on them. For this purpose, 6.45 tons were put down on each floor, leading to a total amount of additional mass equal to 19.35 tons. The total mass of the mock-up loaded with the additional masses was about 40.2 tons. This strategy was followed to make the reduced scale structure as representative of the full scale one as possible. If it is assumed that the similitude rule is fulfilled, neither the stress and the acceleration field are modified. This strategy allows conserving the original materials for the construction of the specimen and using classical constitutive laws for the numerical modeling. A picture of the ENISTAT mock-up is shown in Figure 3.45.

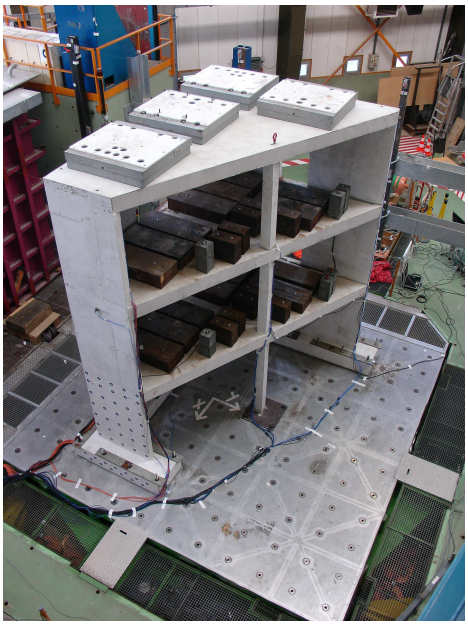

Figure 3.45: Picture of ENISTAT mock-up.

The structural frame is composed of various components: three shear walls, one column, three beams, three slabs, and one footing. The main dimensions of the formwork are given in Figure 3.46.

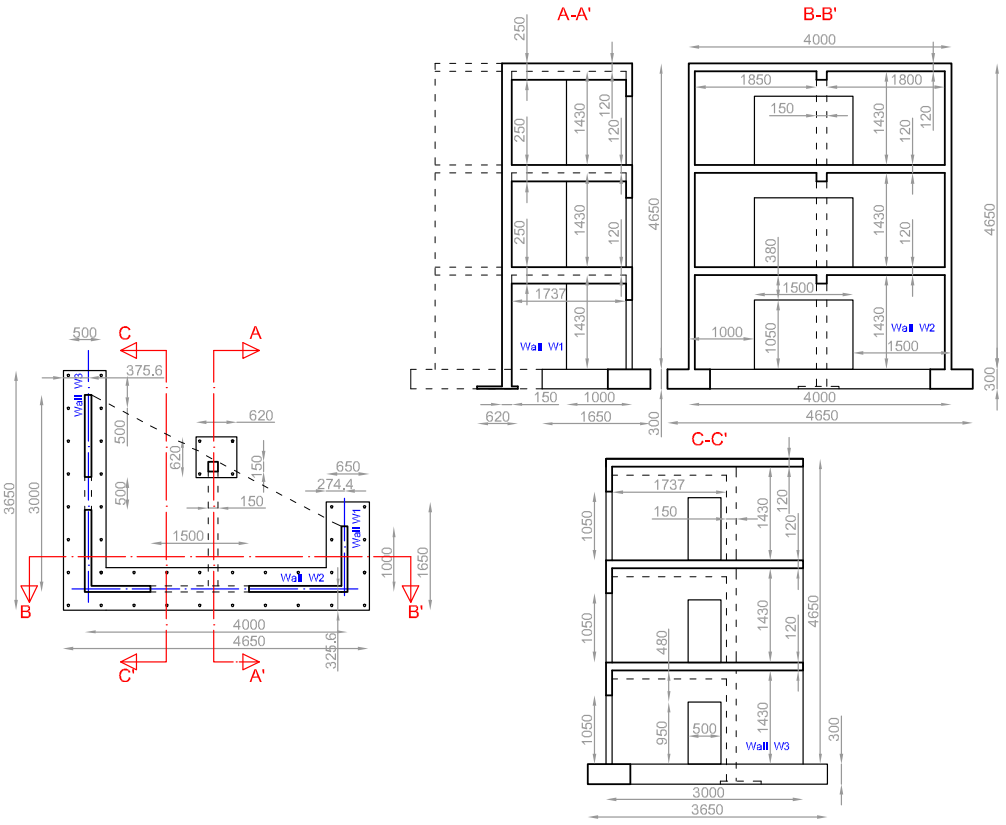

Figure 3.46: Sketch of the specimen geometry — dimensions in millimeters.

Recent construction technology aims at developing and producing energy efficient buildings. An efficient way to reduce energy loss is to reduce thermal bridges from forming, especially at wall–slab connections. Thermal break components are innovative technological components developed in Europe. If their thermal benefits have already been proved, the dynamic behavior of such a wall–slab connection in a building under a seismic loading has not yet been assessed at the member scale. Nevertheless, experimental and numerical investigations have been conducted at the component scale for identification purposes. To assess the modification of the seismic vulnerability due to these thermal break components, the connections at the 2^{nd} floor level of the mock-up were made through these structural elements. Thermal break components were only put on the 2^{nd} floor for two main reasons. First, this structural configuration represents a real situation. Indeed, in the design stages, the task consisting in installing thermal break components in the building leads to a financial overhead (civil engineering work stopped, qualified technicians required, etc.). Therefore, it may appear that such components are only put at a given floor and not on the other ones. Second, if the thermal break components were put in an area located too close to the shaking table upper plate, they would not have been subjected to any significant dynamic amplification and therefore they would have been less loaded than they were in the experiment. Considering both reasons, it appeared best to put the thermal break components at the 2^{nd} floor.

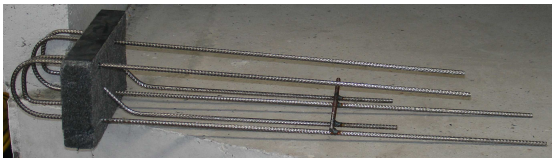

Figure 3.47: Picture of a thermal break component.

Three types of thermal break components were considered: DF (Dalle-Façade in French and Wall-Front in English) type 1, DF type 2, and ESI (Élement Sismique in French and seismic component in English). The two first modules are designed to take care of bending moments that appear at the wall–slab connection and the last one, to handle shear forces. All components were specifically designed by Schöck company for the ENISTAT mock-up. Drawings of the thermal break components are given in Figures 3.48, 3.49 and 3.50 according to their type. The mechanical characteristics of each type of thermal break component were characterized by Schöck company and are presented in Table 3.10. Only the constitutive steel bars of the thermal break components contribute to their bearing capacity, whereas the surrounding polystyrene does not.

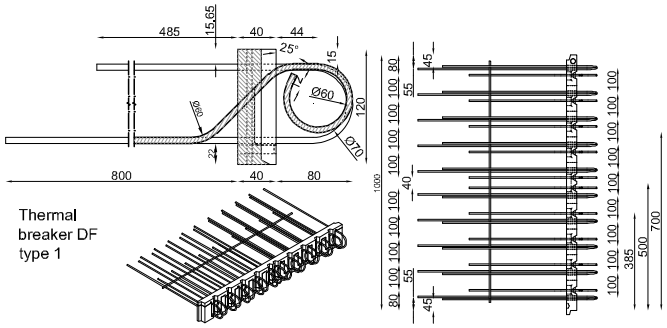

Figure 3.48: Drawing of the DF type 1 thermal break component.

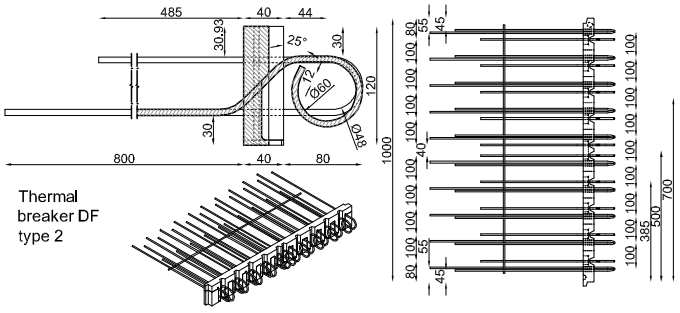

Figure 3.49: Drawing of the DF type 2 thermal break component.

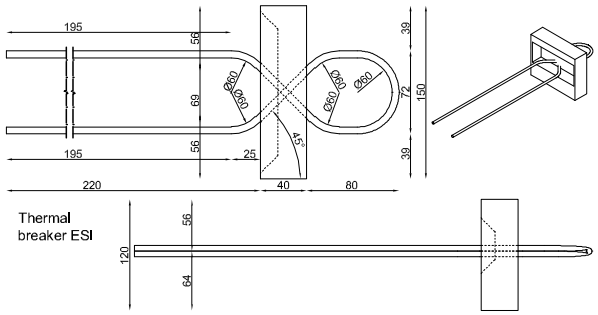

Figure 3.50: Drawing of the ESI thermal break component.

Strength parameter	DF Type 1	DF Type 2	ESI
Ultimate bending moment (kNm/m)	-	10.47	7.34
Ultimate shear strength (kN/m)	-	119.96	119.96
Ultimate tensile strength (kN)	-	169.65	169.65
Ultimate horizontal strength (kN)	12	-	-
Ultimate compressive strength (kN)	-	136	136

Table 3.10: Mechanical parameters of the thermal break components.

Instrumentation arrangement

The location of the measurement points is shown in Figure 3.51. Both linear variable displacement transducers (LVDTs) and accelerometers were attached to the reinforced concrete mock-up to monitor its overall behavior during the seismic tests. In addition, dedicated measurement points allowing monitoring the relative displacement between the 2^{nd} floor and the surrounding shear walls were also employed. The observation points were determined in order to capture the overall torsional response of the specimen and to accurately monitor the behavior of the slab located at the 2^{nd} floor. The most excited points were monitored with several accelerometers in the three directions. In particular, this explains why points A, D and H were equipped with accelerometers at each floor and why more than 15 strain gauges were put on the thermal break components.

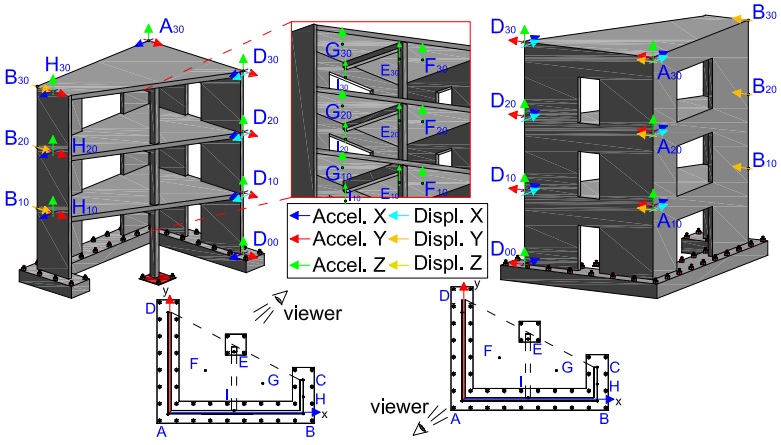

Figure 3.51: Measurement points.

Seismic loading procedure

The dynamic loading was applied to the mock-up by the AZALEE shaking table CEA-Tamaris (2016). The whole seismic sequence included two types of dynamic loading: low level random loadings and bi-directional seismic loadings in the horizontal plane (X, Y). The first type of loading aimed at identifying the variations of the modal properties of the dynamic system composed of the shaking table and the reinforced concrete mock-up, whereas the second type aimed at assessing its dynamic behavior. The objective of the shaking table experiment presented in this memoir was to quantify the dynamic behavior of an asymmetric reinforced concrete building equipped with thermal break components that were not initially designed to withstand induced dynamic loadings. Therefore, the seismic loading was defined in connection with the design spectrum recommended by EC8, taking into account the conditions from the similitude rule that was assumed and that was presented previously. Consequently, synthetic earthquakes were generated according to the method implemented in the software Cast3M. This strategy consists in assuming that the generated signal can be expressed as a sum of sinusoidal functions with random phases. The sum is weighted by an exponential function including parameters that are identified by the least-squares method to match the target frequency content and PGA prescribed by the user.

A reference bi-directional seismic loading was artificially generated from the design spectrum given by EC8 (taking into account the constraints coming from the similitude rule assumed) for a PGA scaled at 0.1 g. The comparison between the 5% damping response spectra computed from the target and the generated signals are shown in Figures 3.52b and 3.53b in the X and Y directions, respectively. It is worth mentioning that a single pair of seismic signals were generated. Other bi-directional signals with higher PGAs were deduced from this single pair by scaling it in such a way that the desired PGA was reached. The PGA of the seismic loading was progressively increased in order to exceed the design level. The main bi-directional seismic loadings are presented in Table 3.11. One can note that the PGAs in both horizontal directions range from 0.2 to 0.8 g. Random noise or hammer shocks are not included in Table 3.11, this explains why the run numbers are not strictly increasing.

Run number	PGA (g) X-direction	PGA (g) Y-direction
19	0.1	0.1
20	0.2	0.2
25	0.4	0.4
28	0.6	0.6
31	0.8	0.8

Table 3.11: Target PGAs of all the bi-directional seismic runs.

Overall damage pattern

The reinforced concrete mock-up was progressively degraded along the bi-directional seismic runs. The degradation process can be split into three different parts according to the PGA of the input ground motion that was applied to the reinforced concrete specimen: The first stage, in which the PGA is lower than 0.2 g; the second stage, in which the PGA is higher than 0.2 g and lower than 0.6 g; and the last stage, in which the PGA is higher than 0.6 g.

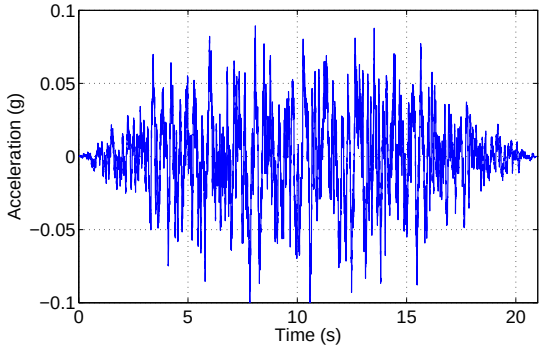

(a) Acceleration time history.

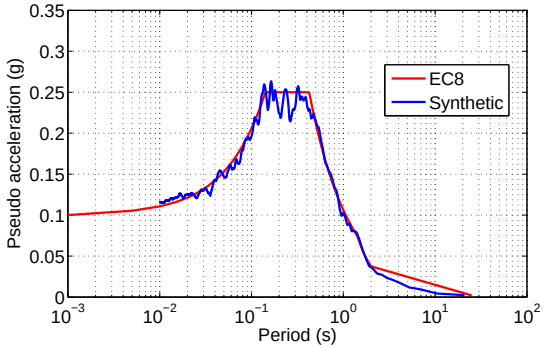

(b) Response spectra — 5% damping.

Figure 3.52: Seismic loading in the X direction — comparison between the target response spectrum with the synthetic one — PGA scaled at 0.1 g.

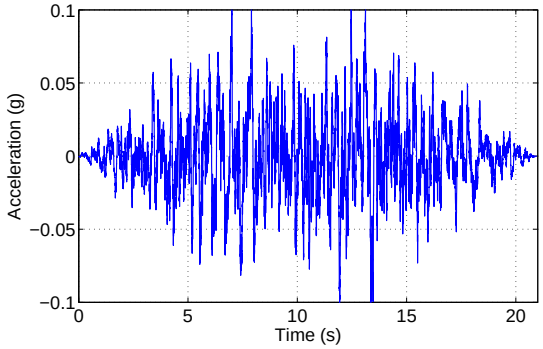

(a) Acceleration time history.

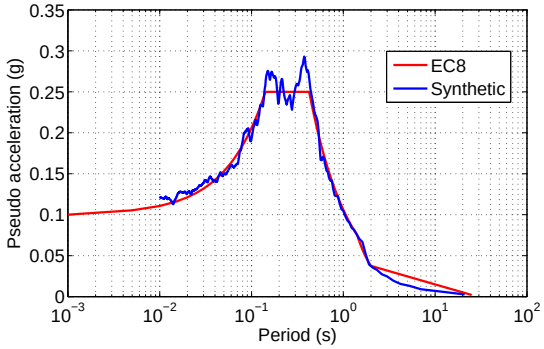

(b) Response spectra — 5% damping.

Figure 3.53: Seismic loading in the Y direction — comparison between the target response spectrum with the synthetic one — PGA scaled at 0.1 g.

Regarding the development of the overall cracking pattern, the first cracks appeared at the corners of the opening located at the 1^{st} floor and in the corresponding lintels. The opening located at shear wall #3 at the 1^{st} floor was monitored with the digital image correlation technique in order to capture the development of cracking during the seismic test. The strain component ε_{xx} is shown in Figure 3.55. It is interesting to observe that the cracking starts from the corner and propagates outside of the area monitored by the digital image correlation technique, following a diagonal path. In the second stage, diagonal cracks started in shear wall #1. Cracks appeared close to the openings and kept on propagating. It is worth mentioning that a major crack started at the shear wall–foundation interface. The shear cracks in shear wall #1 became more and more numerous. In the last stage, some new cracks appeared in the slabs and also in shearwall #1 due to shear, as shown in Figure 3.54a. The crack that appears at the shear wall–foundation interface kept on propagating up to the middle of shear wall #2, as can be observed in Figures 3.54b and 3.54c.

Regarding the strain level in the steel reinforcing bars, this quantity was monitored by classical strain gauges that were stuck on the steel bars before the concrete was cast in. A preliminary numerical analysis of the mock-up allowed identifying the position of the most stressed area,

and therefore strain gauges were put at this location. Whatever the stage considered, no yielding in the steel reinforcing bars was monitored. However, the properties of the steel–concrete interface became more and more weakened during the seismic tests, leading to thinking that a bond failure occurred at the interface between shear wall #1 and the foundation.

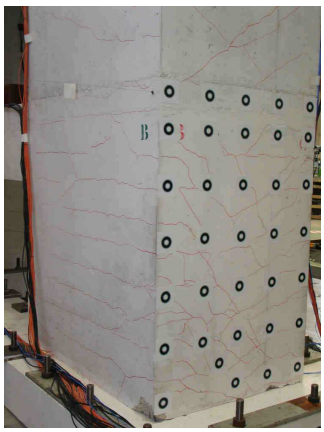

(a) Walls #1 and #2 — shear cracking.

(b) Walls #1 and #2 — concrete crushing.

(c) Wall #1 — transversal crack.

Figure 3.54: Cracking pattern — input signal with a PGA = 0.8 g.

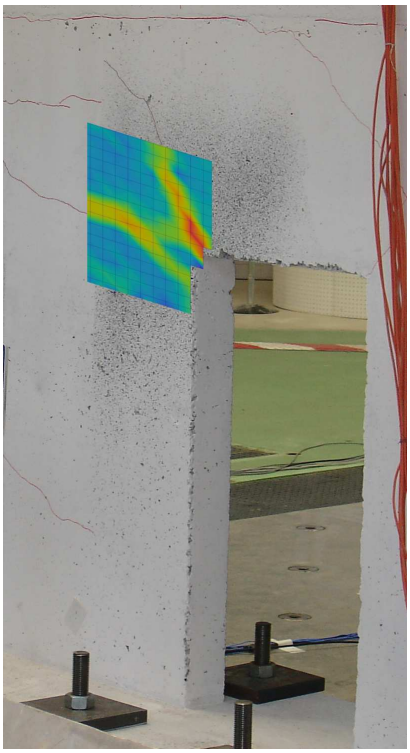

Figure 3.55: DIC results — input signal with a PGA = 0.2 g — opening at the 1^{st} floor — shear wall #3.

Influence of thermal breakers on the structural behavior

The 2^{nd} floor was monitored carefully in order to capture the effect of the thermal break components on the overall behavior. Two types of quantities were monitored: (i) the relative displacements in the X and Y directions between the 2^{nd} floor and the surrounding shear walls using eight LVDTs and (ii) the strains in the steel of the thermal break components using 34 dedicated gauges. The evolution of the relative displacement vs. the input ground motion level are plotted in Figure 3.56. The maximum amplitude is reached at point M in the X direction with a relative displacement equal to 1.2 mm. The 2^{nd} floor is subjected to an internal rigid body motion that is driven by torsional effects. The low maximum amplitude demonstrates that the thermal break components can be seen as highly rigid connections.

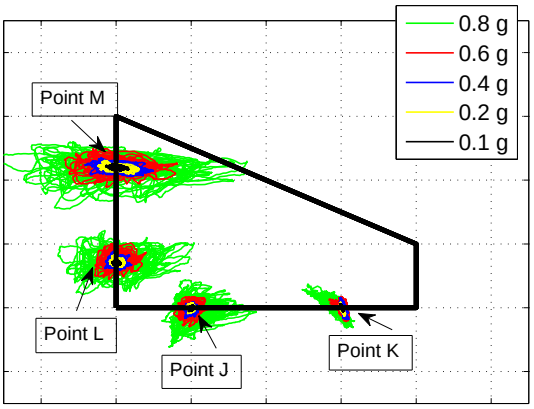

Figure 3.56: Qualitative representation of the overall relative displacement of the 2^{nd} floor — amplification factor equal to 1500.

The strain distribution in the thermal break components was analyzed in order to study the load transfer from the shear walls to the 2^{nd} floor. The *engineering stress*, denoted P, was computed as the product between the strain and the Young's modulus of the reinforcing bar $P = E\epsilon$. For each shear wall, the maximum engineering stress distribution was plotted as a function of the PGA of the seismic input ground motion. For shear wall #1, the results are shown in Figures 3.57a and 3.57b for the thermal break components DF type 1 and ESI, respectively. One can note that the most stressed thermal break components are located close to point M, defined in Figure 3.56. This is fully in accordance with the relative displacement measurements. In addition, for the seismic level with a PGA equal to 0.8 g, the engineering stress ranges from almost 90 MPa to 400 MPa, which is lower than the yield stress (516 MPa). The load transfer is clearly ensured, not only in terms of bending moments but also in terms of shear forces. This is confirmed by the results shown in Figure 3.57b. The maximum engineering stress in the ESI thermal break components ranges from 150 MPa to almost 250 MPa, showing an efficient shear force transfer. This is confirmed by the fact that no significant slip between the steel bars of thermal break components and the surrounding concrete appeared. Indeed, the maximum relative displacement between the slab located on the 2^{nd} floor and the surrounding shear walls was very small.

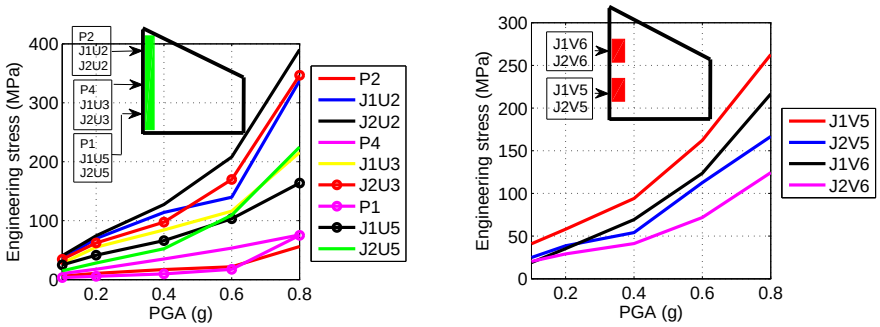

(a) Thermal breaks DF type 1. (b) Thermal breaks ESI.

Figure 3.57: Maximum engineering stress versus seismic ground motion level — shear wall #1.

For shear wall #2, three types of thermal break components were installed. The maximum engineering stress is shown in Figures 3.58a, 3.58b and 3.58c for each type of thermal break component. As previously, one can observe that no yielding occurs. The fact that the maximum engineering stress is lower than in the case of shear wall #1 is consistent with the fact that lower relative displacements were monitored at points J and K, as presented in Figure 3.56. Figure 3.58b shows that the DF type 2 thermal break components monitored by the strain gauges P8, J1U6 and J2U6 have approximately the same stress level as the ESI ones monitored by the strain gauges J1V1 and J2V1. The low stress level is in accordance with the fact that no significant relative displacement was monitored in this part of the structure. Finally, one can observe that all the thermal break components behave in their elastic domain. For shear wall #3, only DF type 1 thermal break components were used. The maximum engineering stress is shown in Figure 3.59 and no yielding is observed.

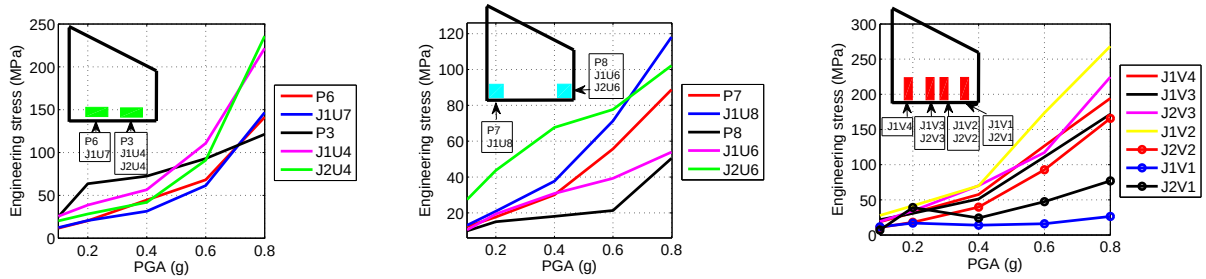

(a) Thermal breaks DF type 1. (b) Thermal breaks DF type 2. (c) Thermal breaks ESI.

Figure 3.58: Maximum engineering stress versus seismic ground motion level — shear wall #2.

For all the shear walls, the maximum engineering stresses in the thermal break components increase faster than the PGA. Furthermore, the results in terms of relative displacements between the slab at the 2^{nd} floor and the surrounding shear walls show a trend that is in agreement with the fact that the maximum engineering stresses in the thermal break components increase faster than the PGA. The maximum amplitude of the relative displacements seems proportional to the PGA in the range 0.2–0.4 g and increases faster for higher PGAs.

From the results presented above, we can note the satisfactory dynamic properties of the thermal break components under seismic loading. Indeed, the thermal break components do not significantly modify the load transfer between the shear walls and the related floor. One can add that structure failure has not been reached because of a local failure of such a component, as mentioned in Section 3.5.2.

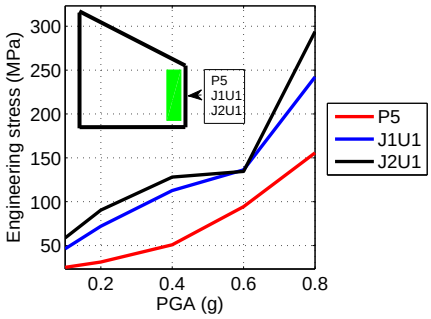

Figure 3.59: Maximum engineering stress versus seismic ground motion level — thermal breaks DF type 1 — shear wall #3.

Nonlinear time history analysis

Description The numerical investigations that were carried out by using the finite element software Cast3M are presented in this section. It is important to mention that the numerical investigations were realized after the experimental study. The validity of the numerical model was assessed through post-test comparisons of the numerical results with experiment. The ability of advanced modeling techniques to handle such a complex structure is investigated and analyzed.

The numerical model includes the reinforced concrete mock-up as well as the shaking table. This choice has been made in order to ensure an accurate description of the boundary conditions. Each structural component has been represented by appropriate finite elements in order to reduce the computational time required as much as possible, without reducing the accuracy of the whole analysis. The overall mesh is shown in Figure 3.60. Considering the results coming from the experiments, the thermal break components have been included in the finite element model using a linear elastic constitutive law. Indeed, since the experimental observations have shown that a full load transfer is ensured as well as the continuity of the displacements at the shear wall–slab connections, the same assumptions have been kept in the modeling strategy.

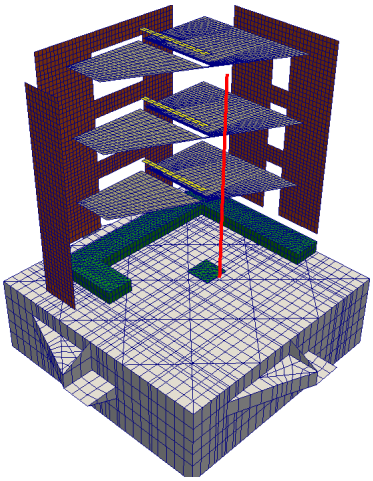

Figure 3.60: Finite element mesh of the shaking table and the mock-up — red: shear walls; white: plates; yellow: beams; red: column; green: foundation; gray: shaking table.

Except for the reinforced concrete column that was modeled by the uniaxial version of the constitutive law introduced in Section 2.2.3, a single constitutive law was used in order to describe the dynamic behavior of an RVE of a reinforced concrete component Markovic *et al.*

(2007). It is expressed within the framework of the thermodynamics of irreversible processes. This strategy ensures not only consistency with the principles of physics but also numerical robustness. It is based upon the following assumptions:

- the reinforcing bars are orthotropically distributed;
- the loading does not lead to an extended damage state.

Under these assumptions, the mechanical behavior of a reinforced concrete RVE can be split into two parts with two different modulus: a linear elastic stage and a cracking stage. It is worth noting that the *extended damage state* refers to the part of the behavior in which the steel bars yield. In other words, yielding of the steel reinforcement can not be described. A detailed description of the constitutive equation as well as a well established procedure to identify the material parameters can be found in Markovic *et al.* (2007).

The nonlinear time history analyses were carried out in the relative basis. The time/acceleration signals (X and Y directions) recorded at the center of gravity of the shaking table were prescribed to the system as an equivalent inertial force field distributed proportionally to the mass. In addition, kinematic relations between the lower surface of the mock-up foundation model and the shaking table upper plate model were employed in order to link them to each other.

The damping was represented by the well-known Rayleigh viscous damping model, meaning that a viscous damping matrix was introduced into the balance equations. The parameters of the damping model were selected according to the first eigenfrequency and to the frequency for which 90% of the total mass of the dynamic system was taken into account. An equivalent damping ratio was assumed equal to 4% and was kept unchanged for all the seismic loadings analyzed. The nonlinear dynamic problem was solved using the well-known Newmark ($\alpha = \frac{1}{2}$ and $\beta = \frac{1}{4}$) time integration algorithm, available in Cast3M. The computational parameters were selected so as to make the algorithm unconditionally stable. The average acceleration was kept constant within the time interval $[t, t + \Delta t]$, in order to avoid time step dependency issues. The time step selected was equal to 10^{-3} s. The duration of each seismic loading was 40 s. The computations were carried out on a 20-core computer with 32 Gb of RAM. The equivalent of four cores was used at their maximum capability during the nonlinear dynamic computations. The computational time of one seismic run was about five days.

Post-run modal properties The evolution of the first eigenfrequencies of the reinforced concrete specimen were numerically investigated using the nonlinear model presented previously. From among the possibilities for determining the eigenfrequencies, the choice was made to carry out a modal analysis after each computed seismic loading. Assuming that the mass matrix remained constant, the damage stiffness matrix was computed numerically from the secant Hooke matrix as follows:

$$K = \sum_{e=1}^{n} \int_{\Omega_e} B_e^t \tilde{C}_e B_e d\Omega \tag{3.61}$$

where $\sum(.)$ stands for the assembly operator, n for the number of finite elements Ω_e, B_e for the gradient matrix of the shape functions, and $\tilde{C}_e$ for the secant Hooke local matrix.

Mode number	Experimental eigenfrequency (Hz)	Numerical eigenfrequency (Hz)	Error $\varepsilon_i = \frac{\lvert f_i^{exp} - f_i^{num} \rvert}{f_i^{exp}}$ (%)
After 0.2 g			
1	4.3	4.5	4.6
2	7.7	8.2	6.5
3	15	16.1	7.3
4	24	27	12.5
After 0.4 g			
1	4	4.1	2.5
2	6.9	7.2	4.3
3	15	15.5	3.3
4	23	25.5	10.8
After 0.6 g			
1	3	3.3	9.1
2	6	6.5	8.3
3	12.5	13.7	9.6
4	22	24	9.1

Table 3.12: Experimental–numerical comparison of the eigenfrequencies — damaged structural state.

This strategy allows taking into account the damage when computing the eigenfrequencies and the modeshapes. A comparison between the numerical and the experimental results is presented in Table 3.12. It is worth noting that the error between the experimental data and the numerical results never exceeds 13%. After the seismic loadings with PGA equal to 0.2 and 0.4 g, the lower the eigenfrequencies are, the better they are estimated. This trend is different after the seismic loadings with PGA equal to 0.6 g: the error seems almost the same whatever the mode considered. In addition, the values of the error emphasize the fact that the numerical model is too stiff and the energy dissipation is not enough. This is in accordance with the observations presented in Combescure *et al.* (2013), in which an updated version of the constitutive law is suggested.

Floor response spectra in the case of a beyond-design seismic loading The nonlinear finite element model presented in the previous sections was used to simulate three bi-directional runs. The comparisons of the numerical results with experiment are based on acceleration response spectra that were computed with a 5% damping ratio. Three seismic runs have been considered, with a PGA ranging from 0.2 g to 0.6 g. Indeed, the results presented in the previous sections show that the reinforced concrete mock-up reached a severe damage state after run #31, with a PGA equal to 0.8 g. Since yielding is not taken into account by the constitutive law, this run was not simulated. Nevertheless, the relevancy of the finite element model has been assessed through comparisons of experiment with the numerical results, made at point H (see Figure 3.51), located on the 3^{rd} floor, and for the three directions X, Y and Z. In the following, only the results obtained in the case of the ground motion with the highest intensity are shown. The results are presented in Figure 3.61 in terms of the acceleration time histories, and in Figure 3.62 in terms of the FRS computed for 5% damping. A satisfactory agreement between the experimental and the numerical results has been obtained. This result allows supporting the assumptions made to model the thermal break components, such as the full load transfer

and the continuity of the displacements at the wall–slab connection.

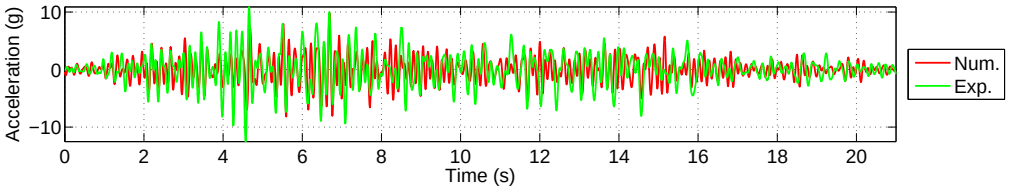

(a) X direction.

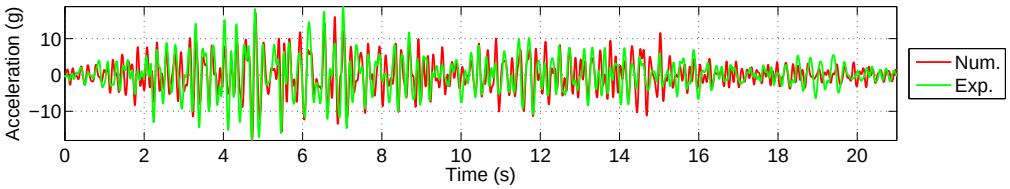

(b) Y direction.

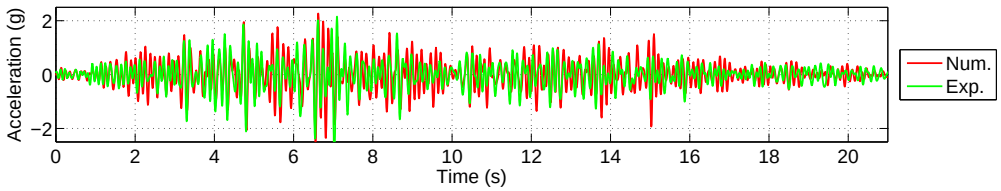

(c) Z direction.

Figure 3.61: Acceleration time histories — experimental–numerical comparison — run #28.

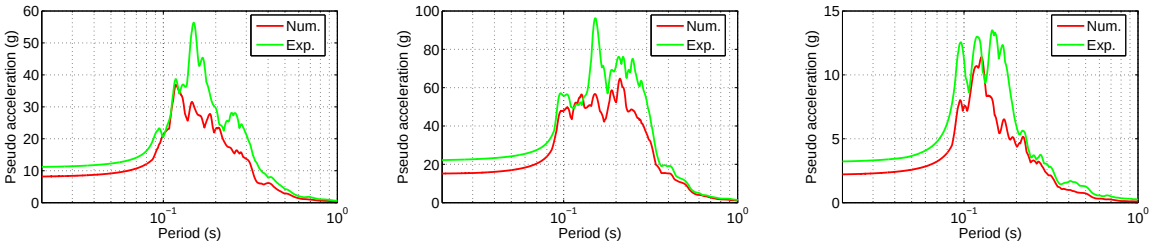

(a) X direction. (b) Y direction. (c) Z direction.

Figure 3.62: Floor response spectra — experimental–numerical comparison — run #28.

Lessons learned

Regarding the analysis of the experimental results presented in previous section, the following conclusions can be drawn:

- a severe damage state is reached at the end of the whole seismic sequence;
- a bond failure occurred at the steel–concrete interface close to the connection between the foundation and shear wall #1;
- the presence of thermal break components does not modify the structural response of the mock-up, since an almost-perfect full load transfer between the slab and the surrounding shear walls is ensured by the thermal break components.

In order to support the experimental data, an advanced modeling approach was used to analyze its capability to describe the structural behavior of the dynamic system subjected to seismic loadings. The constitutive law, expressed within the framework of continuum damage mechanics, aims at describing the behavior of a reinforced concrete RVE. Yielding of the steel reinforcing bars is not taken into account, therefore the seismic loading with a PGA equal to 0.8 g was not analyzed in this study. The relevancy of the modeling approach was assessed by analyzing several quantities, such as (i) the modal properties of the reinforced concrete mock-up after each seismic loading and (ii) the FRS computed for 5% damping. From these comparisons, it appeared that the evolution of the first eigenfrequencies along the seismic loadings is slightly underestimated. This may be related to a lack of dissipation capability of the constitutive law used.

According to the results presented above, the thermal break components do not seem to influence the dynamic behavior of the reinforced concrete mock-up when subjected to seismic loadings. Indeed, the stiffness as well as the deformability at the wall–slab connection seem to be satisfactory, at least in the case of the designs considered in this study. It can be concluded that the inclusion of such new thermal insulation components does not lead to significant structural modifications. In other words, the provisions made by EC8 remain justified even though these additional components are included in a complex structure.

3.6 Summary

This section was devoted to the presentation of our contributions aiming at (i) quantifying in a refined way the cracking features, (ii) estimating the dissipative capabilities of reinforced concrete structures under cracked conditions, (iii) improving the computational efficiency of probabilistic approaches, and (iv) better understanding not only the complex behavior of torsion-sensitive reinforced concrete structures but also the applicability of structural assessment methods.

In the first part, a particle model was presented. The improvements made in order to make it capable of handling cyclic loadings were presented. Especially the time-integration algorithm and the additional dissipative mechanisms that have been included were presented. The ability of the resulting model to be used as a virtual testing machine to complement the set of experimental results when dealing with the identification of the material parameters for continuous constitutive laws have been pointed out. Because the analysis carried out with the aforementioned discrete approach is highly time-consuming, the case of a large-scale structure is not straightforward to handle. As a consequence, the developments to improve the traction/separation law considered in the kinematic enhancement based approach have been presented. In particular, we formulated, within a consistent framework, a mixed-mode traction/separation law based

on micromechanical assumptions. Despite the fact this approach is low intrusive in computational software and does not lead to additional computational costs due to the extra degrees of freedom describing the crack opening, the $\mathcal{C}^0$-geometrical continuity of the crack path is not ensured. Therefore, by reformulating the boundary value problem to be solved, we improved the well-known global tracking strategies in order to make the results less user-sensitive and allow online tracking during the incremental/iterative integration scheme. Representative case studies have also been shown and discussed. The main contributions consist in: (i) *improving the particle model in order to make it capable of handling cyclic loading path*, (ii) *showing the pros of an implicit time integration strategy*, (iii) *expressing in a consistent way an anisotropic damage based traction/separation law* and (iv) *improving the existing global tracking strategy to ensure the continuity of the crack path.*

In the second part, the dissipative capability of reinforced concrete structures was studied. In particular, we focused on the quantification of the effects of cracking on the damping, based on an experimental study that we had defined. In addition, some recommendations have been made aiming at identifying a hysteretic scheme allowing for a natural description of damping. Another research topic consists in estimating the effects of corrosion on the bearing capacity of a large-scale reinforced concrete bridge that had been experimentally tested. The objective was reached with the help of the constitutive models we developed. Some conclusions already reached in the literature, but at a lower structural scale, have been confirmed.

In the third part, light was shed on some developments aiming at (i) taking into account uncertainties related to the material parameters of a structural model with a reduced computational demand, and (ii) updating an a priori probabilistic model. The possibilities offered by the proposed techniques have been emphasized by a structural case study.

In the last part, some contributions aiming at better understanding the behavior of torsion-sensitive reinforced concrete structures subjected to an extreme loading were presented. In particular, two large-scale experimental studies including shaking table tests were presented. On the one hand, the experimental results have allowed for some assessments on the local effects of thermal break components on the structural behavior, and on the other hand, the seismic margins available on a reinforced concrete structure designed according to the French nuclear practices have been estimated. In addition, these last results have served as input to an international benchmark we organized in order to share approaches to the best design and assessment methods to employ when dealing with strongly asymmetric reinforced concrete structures. The main contributions are: (i) *creating and making available data coming from shaking table tests performed on large-scale reinforced concrete structures*, (ii) *assessing the capabilities of best-estimate approaches to provide meaningful information when dealing with beyond-design behavior* and (iii) *creating an international event to encourage the international earthquake engineering community to share.*

Publications in peer reviewed journals

A10 **Richard, B.**, Adélaïde, L., Crémona, C. (2012). A Bayesian approach to estimate material properties from global statistical data. *European Journal of Environmental and Civil Engineering* 16(3–4).

A11 **Richard, B.**, Adélaïde, L., Crémona, C., Orcési, A. (2012). A methodology for robust updating of nonlinear structural models. *Engineering Structures* 41:356–372.

A12 **Richard, B.**, Crémona, C., Adélaïde, L. (2012). A response surface method based on support vector machines trained with an adaptive experimental design. *Structural Safety*

39:14–21.

A13 **Richard, B.**, Epaillard, S., Crémona, C., Elfgren, L., Adélaïde, L. (2010). Nonlinear finite element analysis of a 50-year old reinforced concrete trough bridge. *Engineering Structures* 32:3899–3910.

A14 Oliver, C., Delaplace, A., Ragueneau, F., **Richard, B.** (2013). Non-intrusive global/local analysis for the study of fine cracking. *International Journal for Numerical and Analytical Methods in Geomechanics* 37:973–992.

A15 Crambuer, R., **Richard, B.**, Ile, N., Ragueneau, F. (2013). Experimental characterization and modeling of energy dissipation in reinforced concrete beams subjected to cyclic loading. *Engineering Structures* 56:919–934.

A16 Vassaux, M., **Richard, B.**, Ragueneau, F., Millard, A., Delaplace, A. (2015). Lattice models applied to cyclic behavior description of quasi-brittle materials: Advantages of implicit integration. *International Journal for Numerical and Analytical Methods in Geomechanics* 39(7), 775–798.

A17 **Richard, B.**, Ile, N., Frau, A., Ma, A., Loiseau, O., Giry, C., Ragueneau, F. (2015). Experimental and numerical study of a half-scaled reinforced concrete building equipped with thermal break components subjected to seismic loading up to severe damage state. *Engineering Structures* 92:29–45.

A18 Vassaux, M., Oliver-Leblond, C., **Richard, B.**, Ragueneau, F. (2016). Beam-particle approach to model cracking and energy dissipation in concrete: Identification strategy and validation. *Cement and Concrete Composites* 70:1–14.

A19 **Richard, B.**, Martinelli, P., Voldoire, F., Corus, M., Chaudat, T., Abouri, S., Bonfils, N. (2015). SMART 2008: Shaking table tests on an asymmetrical reinforced concrete structure. *Engineering Structures* 105:48–61.

A20 **Richard, B.**, Martinelli, P., Voldoire, F., Chaudat, T., Abouri, S., Bonfils, N. (2016). SMART 2008: Overview, synthesis and lessons learned from the International Benchmark. *Engineering Structures* 106:166–178.

A21 **Richard, B.**, Cherubini, S., Voldoire, F., Charbonnel, P. E., Chaudat, T., Abouri, S., Bonfils, N. (2016). SMART 2013: Experimental and numerical assessment of the dynamic behavior by shaking table tests of an asymmetrical reinforced concrete structure subjected to high intensity ground motions. *Engineering Structures* 109:99–116.

A22 **Richard, B.**, Voldoire, F., Fontan, M., Mazars, J., Chaudat, T., Abouri, S., Bonfils, N. (2016). SMART 2013: Lessons learned from the International Benchmark about the seismic margin assessment of nuclear RC buildings. *Engineering Structures*. Submitted.

A23 **Richard, B.**, Kishta, E., Giry, C., Ragueneau, F. (2016). Strong discontinuity analysis of a class of continuum anisotropic damage constitutive models. Part I: Fundamentals. *Mechanics Research Communication*. Submitted.

A24 **Richard, B.**, Kishta, E., Giry, C., Ragueneau, F. (2016). Strong discontinuity analysis of a class of continuum anisotropic damage constitutive models. Part II: Numerical case studies. *Mechanics Research Communication*. Submitted.

4 Conclusions and outlook

The main objectives of the research summarized in this memoir are to improve the numerical description of the behavior of a quasi-brittle material subjected to cyclic loadings, and to better understand the way complex reinforced concrete structures behave under extreme loading conditions. On the one hand, my work has been focused on the improvement of the continuous descriptions of the cyclic behavior of the RVEs, allowing the formulation of simplified numerical strategies to serve probabilistic approaches. On the other hand, we contributed to improving the way of analyzing and quantifying the vulnerability of reinforced concrete structures. To reach these goals, we explored advanced modeling techniques to allow a refined description of cracking and we contributed in the definition of shaking table experimental campaigns to create reference data in order to assess of the efficiency of best-estimate approaches.

In the first part, several constitutive models were presented. We first focused on the case of concrete-like materials, presenting three modeling strategies. The progressive improvements we made have been explained by discussing the pros and cons of each strategy. Special attention was paid to the description of the crack closure effect and its coupling with the hysteretic response when switching from tension to compression. Regarding this aspect, we can conclude that: (i) a spherical/deviatoric split is not sufficient, (ii) a regular closure function is needed, and (iii) an incremental formulation (in terms of stress and strain rates) reduces the convergence issues in the local time-integration algorithm. Next, the case of the steel–concrete interface was addressed. The developments of a set of constitutive equations aiming at describing the behavior of the steel–concrete interface in the presence of corrosion show that accurate results could be obtained at the structural component scale. However, dealing with large-scale structures remains complex due to the computational burden. This is the reason why a simplified strategy has been proposed, within the framework of the multifiber approach. Despite the fact that not all the mechanisms included in the three-dimensional model could be considered in the simplified model, the main characteristics of the behavior at the structural component scale could be reproduced.

The last part of this memoir was devoted to the presentation of some contributions aiming at assessing the vulnerability of reinforced concrete structures by means of different numerical and experimental techniques. Our contributions have been gathered under four complementary topics, which are summarized in the following.

To begin with, we focused on the complex issue of the quantification of the cracking features. To reach this objective, we explored two strategies: on the one hand, a particle model and on the other hand, an approach based on kinematic enhancement, explicitly taking into account the discontinuity of the displacement. Regarding the development related to the particle model, our developments allowed making it applicable to the case of cyclic loadings, by both improving the time-integration strategy and enhancing the dissipative mechanisms included, namely the contact and the frictional sliding. The capabilities of the beam model were illustrated through two examples. First, the crack features can be quantified a posteriori, following a continuous

analysis of the structure under study. Second, we benefitted from the predictive capabilities of the model to carry out virtual tests in order to complement the experimental data available to serve as inputs into the identification process of the material parameters of a continuous model. According to the results obtained so far, the particle model has now reached a sufficient degree of maturity to make us confident in it. However, because the computational time required by such an analysis is quite important, the analysis of a whole structure remains difficult. Next, we focused on a kinematic enhancement based approach. The advantageous role of the strain singularity on a class of anisotropic damage constitutive models based on micro-mechanical assumptions has been shown, which extends the well-known result achieved in the case of constitutive models of isotropic damage. In this way, a traction/separation law taking into account refined mechanisms such as mode I and mixed mode cracking could be formulated. As a major drawback of this numerical framework, the continuity of the crack is not ensured. We improved the well-known global tracking strategy in order to ensure a well-posed boundary value problem and to allow online tracking to handle cyclic loadings involving complex stress states.

Then we focused on the estimation of the dissipative capability of reinforced concrete components subjected to complex loadings. Indeed, estimating the ductility level is a key point when dealing with either design studies or the reassessment of existing structures. The relation between cracking and damping was investigated by means of quasistatic tests. The experimental results were analyzed in order to quantify the internal damping or, in other words, the damping contribution coming from the energy dissipation at the material scale. Based upon these results, we could assess the efficiency of some hysteretic schemes to describe the energy dissipation due to frictional sliding. If the hysteretic scheme is well chosen, the contribution from the viscous damping matrix can be drastically decreased, and so one can avoid using it as a tuning parameter within the framework of a nonlinear transient analysis. The case of existing structures has also been addressed. A 40-year old reinforced concrete bridge was analyzed in order to estimate the influence of corrosion on the bearing capacity. Despite the fact that this study was purely numerical, we could observe trends which confirmed the results published in the literature but obtained at a lower scale.

Because it is necessary not only to take into account the uncertainties related to the material parameters of a mechanical model, but also to update an a priori probabilistic model based upon new available information, we contributed to the improvement of statistical techniques. In particular, we proposed an alternative strategy allowing an accurate estimation of the probability of exceeding a given limit state and we applied the concept of Bayesian updating within the framework of beyond-design analysis to adjust, in a consistent way, the statistical parameters of a probabilistic model.

In sum, the research we carried out to better understand the behavior of strongly asymmetric reinforced concrete structures subjected to dynamic loading has been presented. The main issue lies in being able to comprehend the torsional effects coming from the existence of an in-plane geometrical eccentricity. Experimental studies involving shaking table tests performed on large-scale reinforced concrete structures were defined. The first one was devoted to understanding the influence of thermal break components on the dynamic response of an asymmetric structure. The experimental results, corroborated by a numerical nonlinear analysis, show only slight modifications of the overall behavior due to the presence of these additional components. The second experimental study aimed at confirming the existence of seismic margins exhibited by a reinforced concrete structure designed according to the French practices applicable in the nuclear industry, and quantifying them. To provide some answers to this issue, an extreme seismic scenario was considered, including natural ground motion signals. The experimental data

were used within the framework of an international benchmark, the objective being to assess the capabilities of best-estimate approaches to predict the dynamic response of such a complex structure. The analysis of the benchmark outputs and the discussions that took place during an international workshop have allowed reaching a consensus about identifying not only the best practices but also paths to improvement when dealing with structural beyond-design assessment issues.

Following on from the results and conclusions presented above, we plan to work on several topics. ***In the short term***, we envisage focusing on three main aspects, which are enumerated below:

1. application of the concept of regularized unilateral effect in the case of constitutive models formulated within an anisotropic framework,
2. identification and quantification of the dissipative capability of reinforced concrete components,
3. comprehension of the consequences of structural pathologies, such as the corrosion of the steel reinforcing bars, on the dynamic response of reinforced concrete structures.

Regarding the first topic, the conclusions reached in the second part of this dissertation have shown the necessity of considering both a continuous approach and more local techniques to be able to estimate in a refined way the cracking features. As a consequence, we think it would be interesting to study the possibility of extending the concept of a regularized unilateral effect within two frameworks: the first would be an anisotropic continuum damage constitutive setup in which the damage variable is described in a tensorial form to allow a robust split between the tension, compression and shear. To reach this objective, the recent work carried out by Desmorat (2015) could be advantageously considered. The second framework we plan to focus on is the microplane theory Bazant et Oh (1985). Indeed, based upon a local variational principle allowing linking two different scales, uniaxial relations can be included within this framework. Due to the energetic principle, a uniaxial response can be upscaled in order to describe the mechanical response of an RVE. This theoretical context could be used in connection with a kinematic enhancement based technique, including displacement discontinuities. This may contribute, at least in part, to tackling the challenge that lies in dealing with several discontinuities in a single finite element. In addition, because the microplane approach requires uniaxial relations, the concept of a regularized unilateral effect could be introduced quite easily in a specific traction/separation law. The principle of the approach we plan to focus on is illustrated in Figure 4.1.

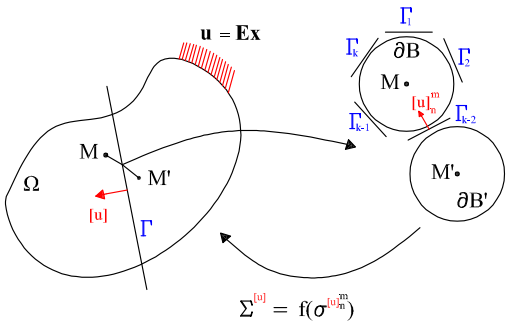

Figure 4.1: Principle of the enhanced microplane approach.

Regarding the second aspect, the work we carried out to improve the understanding of the relation between damping and damage has two major limitations. Indeed, the absence of experimental data obtained under a dynamic loading led to the necessity to extrapolate, somehow, the quasistatic results in order to be able to estimate the damping. In addition, the fact that three-point bending tests were carried out has led to some difficulties due to the heterogeneous distribution of the damage. Learning from these lessons, a new experimental program, named IDEFIX[1], has been designed within the framework of the French national research project SINAPS@. The experimental setup is represented in Figure 4.2. Both quasistatic and dynamic tests are planned. The specimen will be subjected to dynamic loading having a frequency content that matches the first eigenfrequencies. In this way, the modification of the modal properties (mainly the modal damping and eigenfrequencies) with respect to the growth of the damage will be estimated. The experimental results should supply a model identification approach in order to estimate, in a consistent way, the relations between the damage and the modal properties. This research has already begun, and the initial results are encouraging. To move forward, the next step we envisage lies in considering reinforced concrete plates instead of beams. In this way, the relations between the damage and the modal properties may be included in plate or shell finite elements, which are the those most used when dealing with a nonlinear transient analysis.

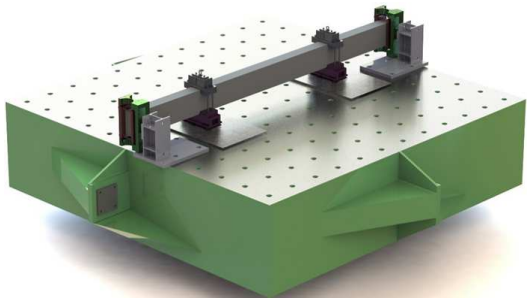

Figure 4.2: Experimental setup of the IDEFIX experiments.

Regarding the last aspect, we plan to focus on the effects of structural pathologies on the dynamic response of reinforced concrete structures. This issue represents, as far as our knowledge extends, a nearly unexplored field of research with many scientific challenges to tackle. Nowadays, we see that most operators are working on the life-extension of their energy production facilities. It is well known that reinforced concrete is a composite material that can be subject to several pathologies. Therefore, understanding their effects on the dissipative capability of such a building should be clarified. The literature shows a clear lack of research aiming at answering this complex issue. When focusing on the case of corrosion, its mechanical consequences for the quasistatic response of reinforced concrete structures has been explored. This is not the case for the extreme loading scenario, such as earthquake loading. Among the scientific challenges related to this aspect, we first should think about the definition of an experimental study involving shaking table tests in order to understand the physical mechanisms which take place during the degradation process. Then and only then, will we be able to start thinking about the formulation of numerical strategies to describe the mechanical consequences in connection with this coupled loading, involving not only different time scales but also different dissipative mechanisms.

[1]IDEFIX: French acronym for *damping identification of reinforced concrete components under cracked condition.*

In the long term, we plan to develop topics which are more application oriented:

1. clarification of failure criteria to consider in the case of strongly asymmetric reinforced concrete structures,

2. integration of simplified modeling strategies aiming at describing the performance loss with respect to the time into the framework of uncertain system analysis.

The first aspect is motivated by the fact that design engineers often have to face the complex issue of defining a damage indicator when dealing with the structural assessment of a reinforced concrete structure. Indeed, linear analysis is very popular in engineering practice and therefore the type of damage indicator is naturally restricted. For instance, the use of the well known inter-story drift may not be the most appropriate indicator in the case of wall-based structures. More accurate structural assessments might be obtained if nonlinear methods became more used in design offices. Indeed, the nonlinear nature of the common assessment methodology leads to the ability to consider new indicators that could help engineers to design complex structures, such as asymmetric ones, in a less conservative way that still remains safe. However, the use of nonlinear assessment methods to derive new damage indicators at the member scale leads to two scientific/technical issues: (i) new thresholds should also be introduced in order to define the concept of *failure*, and (ii) the way to use nonlinear assessment approaches should be framed in order to become usual in engineering practice. The definition of new thresholds can not be thought of from a purely numerical point of view (even though nonlinear modeling approaches have reached a certain degree of maturity over the past decades) but new pieces of knowledge should also come from experimental investigations. The second challenge may be addressed, at least partially, only thanks to fruitful exchanges among the international scientific community. Indeed, best practices always come from consensus and the sharing of knowledge.

Stakeholders are in charge of the maintenance policy of a building network. The definition of the planning of maintenance actions should serve two main objectives: (i) a sufficient performance level must be ensured and (ii) the maintenance costs should be optimized. The second aspect we plan to work on is motivated by the latter observation. Indeed, maintenance cost optimization strategies generally include performance loss models, which are generally empirical, mainly because this topic is located at the frontier between two research communities. We seriously think we could derive great benefits from advanced nonlinear modeling strategies to develop simplified laws allowing the description of structural performance loss. In this way, system-based approaches might be enhanced. Furthermore, extreme loading scenarios are generally not considered, only long-term loadings, such as the effects of reinforced concrete pathologies, are included. Based on this observation, the new pieces of knowledge which could arise from ongoing projects we are working on could be used. Hence, coupled effects (pathologies and extreme loading) may be included within the framework of a system-based modeling to improve the management of maintenance policy.

The long term research topics presented above are not exhaustive, they will depend on the future collaborative frameworks we have and the financial support available in the next years.

Bibliography

S. Adhikari : Reliability analysis using parabolic failure surface approximation. *Journal of engineering mechanics*, 130:1407, 2004.

J. Alfaiate, A. Simone et L.J. Sluys : Non-homogeneous displacement jumps in strong embedded discontinuities. *International Journal of Solids and Structures*, 40(21):5799–5817, 2003.

P.J. Armstrong et C.O. Frederick : A mathematical representation of the multiaxial bauschinger effect. Rapport technique, Chalmers University of Technology Göteborg Sweden, 1996. G.E.G.B., Report RD/B/N.

R. Bargellini, D. Halm et A. Dragon : Modelling of anisotropic damage by microcracks: towards a discrete approach. *Archives of Mechanics*, 58(2):93–123, 2006.

Z.P. Bazant et B.H. Oh : Microplane model for progressive fracture of concrete and rock. *Journal of Engineering Mechanics*, 111(4):559–582, 1985.

T Belytschko, N Moës, S Usui et C Parimi : Arbitrary discontinuities in finite elements. *International Journal for Numerical Methods in Engineering*, 50(4):993–1013, 2001.

J.P. Boehler : Lois de comportement anisotrope des milieux continus. *Journal de Mécanique*, 17(2):153–190, 1978.

U. Bucher et U. Bourgund : A fast and efficient response surface approach for structural reliability problems. *Structural Safety*, 7(1):57–66, 1990.

F. Cazes, A. Simatos, M. Coret et A. Combescure : A cohesive zone model which is energetically equivalent to a gradient-enhanced coupled damage-plasticity model. *European Journal of Mechanics-A/Solids*, 29(6):976–989, 2010.

CEA-Cast3M : Cast3M, 2016. URL `http://www-cast3m.cea.fr/`.

CEA-Tamaris : Tamaris, 2016. URL `http://www-tamaris.cea.fr/`.

B. Chiou, R. Darragh, N. Gregor et W. Silva : Nga project strong-motion database. *Earthquake Spectra*, 24(1):23–44, 2008.

C. Combescure, H. Dumontet et F. Voldoire : Homogenised constitutive model coupling damage and debonding for reinforced concrete structures under cyclic solicitations. *International Journal of Solids and Structures*, 50(24):3861–3874, 2013.

C. Cortes et V. Vapnik : Support-vector networks. *Machine learning*, 20(3):273–297, 1995.

Ch. Cremona : *Application de la théorie de la fiabilité à la sécurité d'éléments structuraux d'ouvrages d'art*. Numéro OA17. Ecole Nationale des Ponts et Chaussées, 1995.

G.A. D'addetta, F. Kun et E. Ramm : On the application of a discrete model to the fracture process of cohesive granular materials. *Granular matter*, 4(2):77–90, 2002.

M. De Biasio, S. Grange, F. Dufour, F. Allain et I. Petre-Lazar : A simple and efficient intensity measure to account for nonlinear structural behavior. *Earthquake Spectra*, 30(4):1403–1426, 2014.

R. De Borst, A. Benallal et O.M. Heeres : A gradient-enhanced damage approach to fracture. *Le Journal de Physique IV*, 6(C6):C6–491, 1996.

F. Deby, M. Carcasses et A. Sellier : Probabilistic approach for durability design of reinforced concrete in marine environment. *Cement and Concrete Research*, 39(5):466–471, 2009.

A. Delaplace : Modélisation discrète appliquée au comportement des matériaux et des structures. *Mémoire d?Habilitation à Diriger des Recherches. Cachan*, 2008.

G.V. Demarie et D. Sabia : Non-linear damping and frequency identification in a progressively damaged rc element. *Experimental mechanics*, 51(2):229–245, 2011.

R. Desmorat : Anisotropic damage modeling of concrete materials. *International Journal of Damage Mechanics*, page 1056789515606509, 2015.

D. Dias-da Costa, J. Alfaiate, L.J. Sluys et E. Júlio : A discrete strong discontinuity approach. *Engineering Fracture Mechanics*, 76(9):1176–1201, 2009a.

D. Dias-da Costa, J. Alfaiate, L.J. Sluys et E. Júlio : Towards a generalization of a discrete strong discontinuity approach. *Computer Methods in Applied Mechanics and Engineering*, 198 (47):3670–3681, 2009b.

N. Dominguez : *Etude de la liaison acier-béton : De la modélisation du Phénomène à la Formulation d'un Elément Finis enrichi Béton Armé*. Thèse de doctorat, Ecole Normale Supérieure de Cachan, Cachan, France, 2005.

C. Eckart : The thermodynamics of irreversible processes. iv. the theory of elasticity and anelasticity. *Physical Review*, 73(4):373, 1948.

R. Eligehausen, E.P. Popov et V.V. Bertero : Local bond stress-slip relationships of deformed bars under generalized excitations. *Internal Report - Stuttgart University*, 1982.

R. Eligehausen, E.P. Popov et V.V. Bertero : Local bond stress-slip relationships of deformed bars under generalized excitations. Rapport technique, National Science Foundation, 1983.

C. Fang, K. Lundgren, L. Chen et C. Zhu : Corrosion influence on bond in reinforced concrete. *Cement and concrete research*, 34(11):2159–2167, 2004.

M.N. Fardis : Seismic engineering research infrastructures for european synergies (series). *In Proceedings, 15th world conference on earthquake engineering, Lisbon (Paper 3001)*, 2012.

C.R. Farrar, W.E. Baker et R.C. Dove : Static and simulated seismic testing of the trg-7 through-16 shear wall structures. Rapport technique, Nuclear Regulatory Commission, Washington, DC (United States). Div. of Engineering; Los Alamos National Lab., NM (United States), 1991.

C. Feist et G. Hofstetter : An embedded strong discontinuity model for cracking of plain concrete. *Computer Methods in Applied Mechanics and Engineering*, 195(52):7115–7138, 2006.

C Feist et G Hofstetter : Three-dimensional fracture simulations based on the sda. *International journal for numerical and analytical methods in geomechanics*, 31(2):189–212, 2007a.

C. Feist et G. Hofstetter : Validation of 3d crack propagation in plain concrete-part i: Experimental investigation-the pct3d test. *Computers and concrete*, 4(1):49–66, 2007b.

F.C. Filippou, E.P. Popov et V.V. Bertero : Modeling of r/c joints under cyclic excitations. *Journal of Structural Engineering*, 109(11):2666–2684, 1983.

N. Friedman, D. Geiger et M. Goldszmidt : Bayesian network classifiers. *Machine learning*, 29(2-3):131–163, 1997.

T. Gabet, Y. Malécot et L. Daudeville : Triaxial behaviour of concrete under high stresses: Influence of the loading path on compaction and limit states. *Cement and Concrete Research*, 38(3):403–412, 2008.

H. Ge, V.R. McClung et S. Zhang : Impact of balcony thermal bridges on the overall thermal performance of multi-unit residential buildings: a case study. *Energy and Buildings*, 60:163–173, 2013.

C. Giry, C. Oliver-Leblond, F. Dufour et F. Ragueneau : Cracking analysis of reinforced concrete structures. *European Journal of Environmental and Civil Engineering*, 18(7):724–737, 2014.

B. Halphen et N. Quoc Son : Plastic and visco-plastic materials with generalized potential. *Mechanics Research Communications*, 1(1):43–47, 1974.

P.A. Hidalgo, C.A. Ledezma et R.M. Jordan : Seismic behavior of squat reinforced concrete shear walls. *Earthquake Spectra*, 18(2):287–308, 2002.

A. Hillerborg, M. Modéer et P.E. Petersson : Analysis of crack formation and crack growth in concrete by means of fracture mechanics and finite elements. *Cement and concrete research*, 6(6):773–781, 1976.

T.J.R. Hughes : Recent progress in the development and understanding of supg methods with special reference to the compressible euler and navier-stokes equations. *International journal for numerical methods in fluids*, 7(11):1261–1275, 1987.

J.E. Hurtado : Analysis of one-dimensional stochastic finite elements using neural networks. *Probabilistic Engineering Mechanics*, 17(1):35–44, 2002.

J.E. Hurtado : *Structural reliability: statistical learning perspectives*. Springer Verlag, 2004.

J.E. Hurtado et D.A. Alvarez : Neural-network-based reliability analysis: a comparative study. *Computer methods in applied mechanics and engineering*, 191(1-2):113–132, 2001.

S. Ide, A. Baltay et G.C. Beroza : Shallow dynamic overshoot and energetic deep rupture in the 2011 mw 9.0 tohoku-oki earthquake. *Science*, 332(6036):1426–1429, 2011.

L.S. Jacobsen : Damping in composite structures. *In Proceedings of the 2nd world conference on earthquake engineering*, volume 2, pages 1029–1044, 1960.

L. Jason, A. Huerta, G. Pijaudier-Cabot et S. Ghavamian : An elastic plastic damage formulation for concrete: Application to elementary tests and comparison with an isotropic damage model. *Computer methods in applied mechanics and engineering*, 195(52):7077–7092, 2006.

L. Jason, C. La Borderie, C. Giry, B. Richard, M. Chambart et G. Thillard : Benchmark on the cracking simulation of reinforced concrete ties. *In Proceedings of FRAMCOS*, volume 7, 2010.

P. Jehel, P. Léger et A. Ibrahimbegovic : Initial versus tangent stiffness-based rayleigh damping in inelastic time history seismic analyses. *Earthquake Engineering & Structural Dynamics*, 43(3):467–484, 2014.

H.B. Kupfer et K.H. Gerstle : Behaviour of concrete under biaxial stresses. *ASCE Engineering Mechanics*, 99:853–856, 1973.

C. LaBorderie : *Phénomènes Unilatéraux dans un Matériau Endommageable : Modélisation et Application à l'Analyse de Structures en Béton.* Thèse de doctorat, Ecole Normale Supérieure de Cachan, Cachan, France, 1991.

I.D. Lefas, M.D. Kotsovos et N.N. Ambraseys : Behavior of reinforced concrete structural walls: strength, deformation characteristics, and failure mechanism. *Structural Journal*, 87 (1):23–31, 1990.

J. Lemaitre, J.L. Chaboche, A. Benallal et R. Desmorat : *Mechanics of solid materials.* Dunod, 2009.

C. Linder et X. Zhang : A marching cubes based failure surface propagation concept for three-dimensional finite elements with non-planar embedded strong discontinuities of higher-order kinematics. *International Journal for Numerical Methods in Engineering*, 96(6):339–372, 2013.

P.L. Liu et A. Der Kiureghian : Optimization algorithms for structural reliability analysis. *Dept. of Civil Engineering, University of California at Berkeley, Report No. UCB/SESM-86/09*, 1986.

K. Lundgren : Bond between corroded reinforcement and concrete. Rapport technique, Chalmers University of Technology Göteborg Sweden, 2001.

L.A. Lutz et P. Gergely : Mechanics of bond and slip of deformed bars in concrete. *ACI Journal*, 64(11):711–721, 1967.

S.A. Mahin et V.V. Bertero : Nonlinear seismic response of a coupled wall system. *Journal of the Structural Division*, 102(9):1759–1780, 1976.

J.J. Marigo : Modelling of brittle and fatigue damage for elastic material by growth of microvoids. *Engineering Fracture Mechanics*, 21(4):861–874, 1985.

D. Markovic, P. Koechlin et F. Voldoire : Reinforced concrete structures under extreme loading: Stress resultant global reinforced concrete models (glrc). *In ECCOMAS thematic conference on computational methods in structural dynamics and earthquake engineering (COMPDYN)*, 2007.

P. Martinelli et F.C. Filippou : Simulation of the shaking table test of a seven-story shear wall building. *Earthquake Engineering & Structural Dynamics*, 38(5):587–607, 2009.

J. Mazars : *Application de la mécanique de l'endommagement au comportement non-linéaire et à la rupture du béton de structure.* Thèse de doctorat, Université Pierre et Marie Curie (Paris VI), 1984.

J. Mazars, Y. Berthaud et S. Ramtani : The unilateral behaviour of damaged concrete. *Engineering Fracture Mechanics*, 35(4):629–635, 1990.

R.E. Melchers : *Structural reliability, Analysis and Prediction*. Wiley, 1999.

M. Menegotto : Method of analysis for cyclically loaded rc plane frames including changes in geometry and non-elastic behavior of elements under combined normal force and bending. *In Proc. of IABSE symposium on resistance and ultimate deformability of structures acted on by well defined repeated loads*, pages 15–22, 1973.

I.C. Mihai et A.D. Jefferson : A multi-asperity plastic-contact crack plane model for geomaterials. *International Journal for Numerical and Analytical Methods in Geomechanics*, 37 (11):1492–1509, 2013.

B. Moaveni, X. He, J.P. Conte et J.I. Restrepo : Damage identification study of a seven-story full-scale building slice tested on the ucsd-nees shake table. *Structural Safety*, 32(5):347–356, 2010.

N. Moës et T. Belytschko : Extended finite element method for cohesive crack growth. *Engineering fracture mechanics*, 69(7):813–833, 2002.

A. Needlemann : Material rate dependence and mesh sensitivity in localization problems. *Computer Methods in Applied Mechanics and Engineering*, 63:69–85, 1988.

A. Neuenhofer et F.C. Filippou : Evaluation of nonlinear frame finite-element models. *Journal of structural engineering*, 123(7):958–966, 1997.

Q.T. Nguyen, S. Caré, Y. Berthaud, A. Millard et F. Ragueneau : Experimental and numerical behaviour of reinforced mortar plates subjected to accelerated corrosion. *International Journal for Numerical and Analytical Methods in Geomechanics*, 35(10):1141–1159, 2011.

Q.T. Nguyen, S. Care, A. Millard et Y. Berthaud : Analyse de la fissuration du béton armé en corrosion accélérée. *Comptes Rendus Mecanique*, 335(2):99–104, 2007.

X.S. Nguyen, A. Sellier, F. Duprat et G. Pons : Adaptive response surface method based on a double weighted regression technique. *Probabilistic Engineering Mechanics*, 24(2):135–143, 2009.

O. Nouailletas : *Comportement d'une discontinuité dans un géomatériau sous sollicitations chemo-mécanique-expérimentations et modélisations*. Thèse de doctorat, Université de Pau et des Pays de l'Adour, 2013.

K. Ogata et T. Kabeyasawa : Experimental study on the hysteretic behavior of reinforced concrete shear walls under the loading of different moment-to-shear ratios. *Transactions, Japan Concrete Institute*, 6:274–283, 1984.

J. Oliver : Modelling strong discontinuities in solid mechanics via strain softening constitutive equations. part 1: Fundamentals. *International journal for numerical methods in engineering*, 39(21):3575–3600, 1996a.

J. Oliver : Modelling strong discontinuities in solid mechanics via strain softening constitutive equations. part 2: Numerical simulation. *International journal for numerical methods in engineering*, 39(21):3601–3623, 1996b.

J. Oliver, A.E. Huespe, M.D.G. Pulido et E. Chaves : From continuum mechanics to fracture mechanics: the strong discontinuity approach. *Engineering Fracture Mechanics*, 69 (2):113–136, 2002a.

J Oliver, AE Huespe, E Samaniego et EWV Chaves : On strategies for tracking strong discontinuities in computational failure mechanics. *In Fifth World Congress on Computational Mechanics*, 2002b.

J Oliver, AE Huespe, E Samaniego et EWV Chaves : Continuum approach to the numerical simulation of material failure in concrete. *International Journal for Numerical and Analytical Methods in Geomechanics*, 28(7-8):609–632, 2004.

C. Oliver-Leblond : *Comportement à rupture des structures: description à deux échelles des mécanismes locaux appliquée aux matériaux fragiles renforcés.* Thèse de doctorat, École normale supérieure de Cachan-ENS Cachan, 2013.

I. Olofsson, L. Elfgren, B. Bell, B. Paulsson, E. Niederleithinger, J. Sandager Jensen, G. Feltrin, B. Täljsten, Ch. Cremona et R. Kiviluoma : Assessment of european railway bridges for future traffic demands and longer lives–ec project ?sustainable bridges? *Structure and Infrastructure Engineering*, 1(2):93–100, 2005.

A. Ouglova : *Etude du comportement mécanique des structures en béton armé atteintes part la corrosion.* Thèse de doctorat, Ecole Normale Supérieure de Cachan, Cachan, France, 2004.

M. Papadrakakis, V. Papadopoulos et N.D. Lagaros : Structural reliability analyis of elastic-plastic structures using neural networks and monte carlo simulation. *Computer methods in applied mechanics and engineering*, 136(1-2):145–163, 1996.

T. Payen, J.C. Queval et P. Sollogoub : Large scale earthquake testing facility for vulnerability assessment. *In First European Conference on Earthquake Engineering and Seismology, Geneva, Switzerland*, pages 3–8, 2006.

J. Pearl : *Probabilistic reasoning in intelligent systems: networks of plausible inference.* Morgan Kaufmann, 2014.

R.H.J. Peerlings, R. de Borst, W.A.M. Brekelmans et J.H.P. de Vree : Gradient-enhanced damage for quasi-brittle materials. *International Journal of Numerical Methods in Engineering*, 39:3391–3403, 1996.

L. Petrini, C. Maggi, M.J.N. Priestley et G.M. Calvi : Experimental verification of viscous damping modeling for inelastic time history analyzes. *Journal of Earthquake Engineering*, 12 (S1):125–145, 2008.

G. Pijaudier-Cabot et Z.P. Bazant : Non-local damage theory. *Journal of Engineering Mechanics ASCE*, 113:1512–1533, 1987.

M.J.N. Priestley et D.N. Grant : Viscous damping in seismic design and analysis. *Journal of Earthquake Engineering*, 9(spec02):229–255, 2005.

M.J.N. Priestley, F. Seible et G.M. Calvi : *Seismic design and retrofit of bridges.* John Wiley & Sons, 1996.

R. Radulovic, O.T. Bruhns et J. Mosler : Effective 3d failure simulations by combining the advantages of embedded strong discontinuity approaches and classical interface elements. *Engineering Fracture Mechanics*, 78(12):2470–2485, 2011.

F. Ragueneau : *Fonctionnement dynamique des structures en béton.* Thèse de doctorat, Ecole Normale Supérieure de Cachan, 1999.

F. Ragueneau, N. Dominguez et A. Ibrahimbegovic : Thermodynamic-based interface model for cohesive brittle materials: application to bond slip in rc structures. *Computer Methods in Applied Mechanics and Engineering*, 195(52):7249–7263, 2006.

Lord Rayleigh : See articles 192a, 234 and 235. *In The Theory of Sound*, volume 1. Dover New York, 1877.

H.W. Reinhardt et G.L. Balazs : Steel-concrete interfaces: experimental aspects. *Studies in Applied Mechanics*, 42:255–279, 1995.

B. Richard, F. Ragueneau, L. Adelaïde et C. Cremona : A multi-fiber approach for modeling corroded reinforced concrete structures. *European Journal of Mechanics-A/Solids*, 30(6):950–961, 2011.

C. Rospars et D. Chauvel : Ceos. fr experimental programme and reference specimen tests results. *European Journal of Environmental and Civil Engineering*, 18(7):738–753, 2014.

J.G. Rots, B. Belletti et S. Invernizzi : Robust modeling of rc structures with an ?event-by-event? strategy. *Engineering Fracture Mechanics*, 75(3):590–614, 2008.

E. Schlangen : *Experimental and numerical analysis of fracture processes in concrete.* Thèse de doctorat, Delft University of Technology, Delft, The Netherlands, 1993.

J.F. Semblat, A. Patrón-Solares, M.F. Escoffier et A. Aouameur : Structures à amortissement non classique: caractérisation vibratoire par modes propres complexes. *Revue française de génie civil*, 5(8):1133–1157, 2001.

J.C. Simo, J. Oliver et F. Armero : An analysis of strong discontinuities induced by strain-softening in rate-independent inelastic solids. *Computational mechanics*, 12(5):277–296, 1993.

A. Simone, D. Wells et L.J. Sluys : From continuous to discontinuous failure in a gradient-enhanced continuum damage model. *Computer Methods in Applied Mechanics and Engineering*, 192(41):4581–4607, 2003.

E. Spacone, F.C. Filippou et F.F. Taucer : Fibre beam-column model for non-linear analysis of r/c frames: Part i. formulation. *Earthquake engineering and structural dynamics*, 25(7):711–726, 1996.

A. Sulaimani, K. Kaleemullah, I.A. Basunbul et M. Rasheeduzzafar : Influence of corrosion and cracking on bond behaviour and strength of reinforced concrete members. *ACI Structure Journal*, 87:220–231, 1990.

F. Taucer, E. Spacone et F.C. Filippou : *A fiber beam-column element for seismic response analysis of reinforced concrete structures*, volume 91. Earthquake Engineering Research Center, College of Engineering, University of California Berkekey, California, 1991.

H. Varum : *Seismic assessment, strengthening and repair of existing buildings.* Thèse de doctorat, Civil engineering department, University of Aveiro, 2003.

M. Vassaux, B. Richard, F. Ragueneau, A. Millard et A. Delaplace : Lattice models applied to cyclic behavior description of quasi-brittle materials: advantages of implicit integration. *International Journal for Numerical and Analytical Methods in Geomechanics*, 39 (7):775–798, 2015.

L.J. Walpole : Fourth-rank tensors of the thirty-two crystal classes: multiplication tables. *In Proceedings of the Royal Society of London A: Mathematical, Physical and Engineering Sciences*, volume 391, pages 149–179. The Royal Society, 1984.

J.S. Willans et M.D. Harrison : A toolset supported approach for designing and testing virtual environment interaction techniques. *International Journal of Human-Computer Studies*, 55(2):145–165, 2001.

S Yazdani et HL Schreyer : Combined plasticity and damage mechanics model for plain concrete. *Journal of engineering mechanics*, 116(7):1435–1450, 1990.

K. Zandi Hanjari, D. Coronelli et K. Lundgren : Bond capacity of severely corroded bars with corroded stirrups. *Magazine of concrete Research*, 63(12):953–968, 2011.

Y. Zhang, R. Lackner, M. Zeiml et H.A. Mang : Strong discontinuity embedded approach with standard sos formulation: Element formulation, energy-based crack-tracking strategy, and validations. *Computer Methods in Applied Mechanics and Engineering*, 287:335–366, 2015.